Technical Report

Discrimination, Detection, Depth, Location, and Wave Propagation Studies Using Intermediate Period Surface Waves in the Middles East, Central Asia, and the Far East

Approved for public release; distribution is unlimited.

July 2003

Anatoli L. Levshin
Michael H. Ritzwoller

Prepared by:

University of Colorado
Department of Physics
Campus Box 390
Boulder, CO 80309-0390

20031017 131

DESTRUCTION NOTICE

DISTRIBUTION LIST UPDATE

This mailer is provided to enable DTRA to maintain current distribution lists for reports. (We would appreciate you providing the requested information.)

❑ Add the individual listed to your distribution list.

❑ Delete the cited organization/individual.

❑ Change of address.

Note:
Please return the mailing label from the document so that any additions, changes, corrections or deletions can be made easily. For distribution cancellation or more information call DTRA/IMMI (703 767-4726.

NAME: _____

ORGANIZATION: _____

OLD ADDRESS	NEW ADDRESS
_____	_____
_____	_____
_____	_____

TELEPHONE NUMBER: (   ) _____

DTRA PUBLICATION NUMBER/TITLE	CHANGES/DELETIONS/ADDITONS, etc.
	(Attach Sheet if more Space is Required)
_____	_____
_____	_____
_____	_____

DTRA or other GOVERNMENT CONTRACT NUMBER: _____

CERTIFICATION of NEED-TO-KNOW BY GOVERNMENT SPONSOR (if other than DTRA):

SPONSORING ORGANIZATION: _____

CONTRACTING OFFICER or REPRESENTATIVE: _____

SIGNATURE: _____

DEFENSE THREAT REDUCTION AGENCY
ATTN: IMMI
8725 John J. Kingman Road, MS-6201
Ft Belvoir, VA 22060-6201

REPORT DOCUMENTATION PAGE

Public reporting burden for this collection of information is estimated to average 1 hour per response, including the time for reviewing instructions, searching existing data sources, gathering and maintaining the data needed, and completing and reviewing the collection of information. Send comments regarding this burden, estimate or any other aspect of this collection of information, including suggestions for reducing this burden, to Washington Headquarters Services, Directorate for Information Operations and Reports, 1215 Jefferson Davis Highway, Suite 1204, Arlington, VA 22202-4302, and to the Office of Management and Budget, Paperwork Reduction Project (0704-0188), Washington, DC 20503.

1. AGENCY USE ONLY (Leave blank)	2. REPORT DATE	3. REPORT TYPE AND DATES COVERED
	July 2003	Technical 971015 - 001231

4. TITLE AND SUBTITLE

Discrimination, Detection, Depth, Location, and Wave Propagation Studies Using Intermediate Period Surface Waves in the Middle East, Central Asia, and the Far East

5. FUNDING NUMBERS

C – DSWA01-97-C-0157
PE - RDT&E
PR - CD
TA - CD
WU - DH56068, DH65170

6. AUTHOR(S)
Anatoli L. Levshin and Michael H. Ritzwoller

7. PERFORMING ORGANIZATION NAME(S) AND ADDRESS(ES)
University of Colorado
Department of Physics
Campus Box 390
Boulder, CO 80309-0390

8. PERFORMING ORGANIZATION REPORT NUMBER

153-5418

9. SPONSORING/MONITORING AGENCY NAME(S) AND ADDRESS(ES)
Defense Threat Reduction Agency
8725 John J. Kingman Road, MS-6201
Fort Belvoir, VA 22060-6201
TDCN/Dainty

10. SPONSORING/MONITORING AGENCY REPORT NUMBER

DTRA-TR-01-28

11. SUPPLEMENTARY NOTES
This Work was sponsored by the Defense Threat Reduction Agency under RDT&E RMC codes B 4613 R CD CD 56068 5P50 A 25904D and B 4698 C CD CD 65170 5P5D A 25904D.

12a. DISTRIBUTION/AVAILABILITY STATEMENT
Approved for public release; distribution is unlimited.

12b. DISTRIBUTION CODE

13. ABSTRACT (Maximum 200 words)
The objective of this research was to construct surface wave group velocity maps at intermediate periods for the Near East, Central Asia and the Far East and to estimate the possibility of using these maps to extract weak surface wave signals and measure their amplitude spectra. To reach these goals we acquired broadband digital records of more than 1600 events that occurred in and around Eurasia during the period 1976-1998 and recorded by about 170 stations of global and regional networks, and PASSCAL deployments. All data were processed by seismic analysts using the frequency-time analysis package developed at the Univ. of Colorado. Altogether more than 23,000 dispersion curves of Rayleigh waves and 18,500 dispersion curves of Love waves were obtained. We developed a new method for tomographic inversion of these measurements. We studied effects of source group time delays and off-path propagation on tomographic images. The resolution of group velocity maps is spatially variable and is between 200 and 400 km in W. China, C. Asia, Afghanistan, Pakistan, Iran and N. India. The imprints of a number of known tectonic structures are observed in the maps. Of particular note are the signatures of sedimentary basins at periods of 15-25 s and crustal thickness variations at longer periods. The group velocity maps obtained are already being used for the identification and extraction of surface-wave packets, and in inversions of lithosperic models. We used these maps to design source-station tuned phase-matched filters. These filters were successfully applied for recovering weak surface signals from several nuclear explosions in China and N. India. We investigated the possibility of using surface wave amplitude spectra for discriminating nuclear explosions and got positive results for several seismic events near the Lop Nor.

14. SUBJECT TERMS

Surface Waves	Central Asia	Group Velocity
Tomography	Southern Asia	

15. NUMBER OF PAGES
150

16. PRICE CODE

17. SECURITY CLASSIFICATION OF REPORT	18. SECURITY CLASSIFICATION OF THIS PAGE	19. SECURITY CLASSIFICATION OF ABSTRACT	20. LIMITATION OF ABSTRACT
UNCLASSIFIED	UNCLASSIFIED	UNCLASSIFIED	SAR

Summary

Objectives.

In this effort to improve the U.S. ability to monitor seismic activity in the Middle East, Central Asia, and the Far East we had the following objectives:
1. To acquire digital records of seismic surface waves crossing the Middle East, Central Asia, and the Far East;
2. To measure group velocity dispersion of fundamental Rayleigh and Love waves in the range of periods between 10 s and 40 s;
3. To construct group velocity maps for these regions by means of tomographic inversion;
4. To estimate the possibility of using these maps for extracting weak surface wave signals by means of phase-matched filtering and for measuring their amplitude spectra;
5. To estimate effects of the off-path propagation on surface wave group velocity maps.

Motivations.

Surface waves compose the longest and largest amplitude parts of broad band seismic waveforms generated both by explosions and shallow earthquakes. In addition, they contain most of the low frequency information radiated by seismic sources. Measurements of the properties of surface waves have been important for evaluating source mechanisms, estimating yields, and helping to discriminate nuclear explosions from naturally occurring earthquakes. Surface wave measurements have been widely used by national and international organizations charged with monitoring and verifying various nuclear test treaties. Under the CTBT, effort has shifted from teleseismic monitoring of a threshold yield targeted on a few well-defined locations to identifying and characterizing signals from weak nuclear explosions and earthquakes. These activities use potentially very noisy and incomplete regional data following events that may be distributed widely in space. Emphasis has shifted from yield estimation to trying to discriminate explosions from naturally occurring earthquakes. There is also the need to locate small events using sparse regional networks in complex tectonic environments with the accuracy and precision demanded by the CTBT.

Within the context of the CTBT, the use and interpretation of information from surface waves has grown in significance. There are two general uses of surface waves under the CTBT. First, the comparison of the amplitudes of surface waves and body waves remains the most reliable regional discriminant, an example of which is the well known $m_b : M_s$ discriminant (e.g., Stevens and Day, 1985). Second, broad band surface wave dispersion provides important information used in estimating 3-D seismic models of the crust and uppermost mantle which are necessary to obtain accurate locations for small events for which only regional data may be available. The success of both applications depends on obtaining reliable surface wave dispersion measurements and representing these measurements in a useful form, usually as group or phase velocity maps.

The measurement of the group velocity of Rayleigh and Love waves is performed on the envelope of the surface wave packet and can be robustly measured across a broad frequency band, from several seconds to hundreds of seconds period (e.g., Dziewonski *et al.*, 1969; Levshin *et al.*, 1972;

Cara, 1973; Kodera *et al.*, 1976; Russell *et al.*, 1988; Levshin *et al.*, 1989, 1992; Ritzwoller *et al.*, 1995). A recent experiment by a number of research groups in the U.S. revealed general agreement among the various methods and codes used to measure group velocities (Walter and Ritzwoller, 1998). Phase velocity measurements are typically obtained by wave form fitting (e.g., Woodhouse and Dziewonski, 1984) or by differencing phase spectra obtained at adjacent stations or from nearby events. There are three key reasons why group velocities have been considered more useful in nuclear monitoring than phase velocities. First, absolute phase velocity measurements are strongly affected by initial source phase (e.g., Knopoff and Schwab, 1968; Muyzert and Snieder, 1996), which may be poorly known or completely unknown for small events. Group velocities are much less sensitive to source characteristics (e.g., Levshin *et al.*, 1999). Second, phase velocities are difficult to estimate unambiguously below about 30 s period. Finally, although multi-station and multi-event differential phase measurements are largely unaffected by source phase, they are typically too sparsely distributed to be of general use in constructing tomographic maps. With a few notable exceptions, surface wave data processing for use in nuclear monitoring has concentrated on estimating velocities rather than wave amplitudes, polarizations, or scattering. If the emphasis on constructing 3-D models to improve regional location capabilities continues into the future, it is likely that a larger share of future efforts will be devoted to short period phase velocity estimation and the use of more complicated wave field effects to constrain 3-D models, such as polarization anomalies (e.g., Levshin *et al.*, 1994; Laske, 1995), and scattering (e.g., Pollitz, 1994).

The estimation of dispersion maps by tomography (e.g., Ditmar and Yanovskaya, 1987; Yanovskaya and Ditmar, 1990) is now commonplace, and new methods such as kriging (e.g., Schultz *et al.*, 1998) have emerged. Dispersion maps on a variety of scales have appeared in the last several years. For example, there are global phase velocity maps (e.g., Laske and Masters, 1996; Trampert and Woodhouse, 1996; Zhang and Lay, 1996; Ekström *et al.*, 1997; van Heijst and Woodhouse, 1999) as well as regional studies across Eurasia (e.g., Wu *et al.*, 1994, 1997; Curtis *et al.*, 1998; Griot *et al.*, 1998; Ritzwoller and Levshin, 1998; Ritzwoller *et al.*, 1998; Yanovskaya and Antonova, 2000) and elsewhere (e.g., Antarctica: Vdovin, 1999; Ritzwoller *et al.*, 2001; South America: Vdovin *et al.*, 1999; Arctic: Levshin *et al.*, 2001).

Advances in surface wave methodology continue to emerge both on regional (e.g., Stevens and McLaughlin, 1997) and global scales (e.g., Wang and Dahlen, 1995; Wang *et al.*, 1998). Barmin *et al.* (2001) developed a tomographic method for constructing both isotropic and azimuthally anisotropic surface wave maps. Although their algorithm is based on a regular grid it extends naturally to irregular grids and recent advances in the construction and use of irregular grids in tomography (e.g., Sambridge *et al.*, 1995; Spakman and Bijwaard, 1998). Irregular grids are most useful when the spatial distribution of data is inhomogeneous, as is common in regional surface wave tomography. Other researchers have demonstrated that broad band group and phase velocity maps can be simultaneously inverted for 3-D structure on both regional (e.g., Villaseñor *et al.*, 2001) and global scales (e.g., Stevens and McLaughlin, 2001). In addition, Villaseñor *et al.* (2001) established that the resulting model of the mantle agrees well with a recent model constructed with teleseismic body wave travel times (e.g., Spakman and Bijwaard, 1998).

Tomographic maps have four principal applications: to detect and extract surface waves from noisy records, to help discriminate nuclear explosions from other sources of seismic energy, to characterize sources, and to be used as data in inversion for the shear velocity structure of the crust and uppermost mantle.

First, the focus of the CTBT on small events makes the detection of seismic signals and the

extraction of useful information a crucial task. The detection and extraction of surface waves is facilitated by using phase-matched filters (e.g., Herrin and Goforth, 1977), which are designed to compensate for the dispersion of the surface wave train. To perform optimally, these filters need to be tuned regionally with group velocity delays which may be efficiently summarized as group travel time correction surfaces for each monitoring station.

Second, an important application of surface wave observations is in the discrimination of nuclear explosions from numerous other natural and human-made seismic phenomena. The surface wave magnitude in combination with the body wave magnitude obtained for each event is then used as part of the well known $m_b : M_s$ discriminant. After the surface wave has been extracted from the observed wave form, the amplitude is typically measured in a window centered around 20 s period from which the surface wave magnitude M_s is inferred. The exact procedure varies depending on the monitoring agency. There has been considerable debate concerning the appropriate distance correction to use in computing M_s (e.g., Marshall and Basham, 1972; Herak and Herak, 1993), and for paths less than $\sim 20°$ it is common practice not to use surface wave amplitude measurements. The effect has been to constrain M_s to relatively large events for which surface waves are well observed beyond epicentral distances of 20°. The prototype International Data Center (pIDC) recently adopted a new M_s - distance relation of Rezapour and Pearce (1998) which appears to justify the use of surface wave amplitudes at all distances below 100 degrees and, hence, extends M_s to smaller events. The procedure for estimating M_s at the pIDC is described in detail by Stevens and McLaughlin (2001). They show that the automated methods that they developed and that are now in place at the pIDC demonstrate a detection threshold approximately one magnitude unit lower than those of other global networks that use visual detection of surface waves. They also argue that continuing improvements in 3-D earth models will advance surface wave identification and reduce the magnitude threshold further. Observational efforts aimed at producing period group velocity maps at periods well below 20 s, such as those of Pasyanos et al. (2001) and Mokhtar et al. (2001), hold out the hope to reduce the period at which M_s is measured to below 20 s. The effect envisioned will be to reduce the size of events further for which reliable M_s measurements can be obtained. Levshin and Ritzwoller (2001) sound a cautionary note by demonstrating how spectral amplitudes below 20 s period vary strongly on the relatively small scales across the Kirghyz Seismic Network (KNET).

The third application of surface wave observations relevant to monitoring the CTBT concerns source characterization, because source depth and the source mechanism may together form a useful discriminant. For example, events that are deeper than 2-3 km below the Earth's surface are most probably natural phenomena. The difficulty is in discriminating very shallow natural events from explosions. Bukchin et al. (2001) argue that source depth and both the isotropic and nonisotropic components of the moment tensor can be estimated if body wave polarization data and surface wave amplitudes are considered simultaneously. They test the hypothesis that events without an isotropic component are earthquakes and near-surface events that have a significant isotropic component are explosions. To do this they analize data following events on and near the Lop Nor test site in China.

The fourth and final application of surface wave dispersion data is in improving and focusing regional models. The inversion of broad band regional surface wave maps can provide a more detailed picture of the earth's lithosphere than can emerge from globally propagating surface waves or observations of teleseismic body waves alone. By ray tracing through such models, it is possible to construct body wave travel time correction surfaces for a set of monitoring stations. These correction surfaces can improve location estimates of weak seismic events (e.g., Villaseñor

et al., 2000). This is especially important in regions of complex structure, where locations based on global models or coarse regional models are invariably biased in the absence of good azimuthal coverage.

This report presents the technique and results of constructing group velocity maps. It outlines the three major applications of surface wave data to monitoring the CTBT, namely extracting seismic signals, measuring spectral amplitudes, and source characterization.

Organization and Main Results.

To satisfy the objectives discussed above, we acquired broadband digital records following more than 1,600 events that occurred in and around Eurasia from 1976–1998 and were recorded by about 170 stations of global digital networks (GDSN, GSN, GEOSCOPE, GEOFON), regional networks (MEDNET, CDSN, KNET, KAZNET), and PASSCAL deployments (Tibet, Saudi Arabia). All information was converted into CSS-3.0 formatted event volumes and processed by seismic analysts in a semi-automatic regime using the frequency-time analysis package developed at CU. All resulting measurements of group velocities and other surface wave characteristics were preserved in a format which is an extension of the CSS-3.0 format. Altogether more than 23,000 dispersion curves of Rayleigh waves and 18,500 dispersion curves of Love waves were obtained.

1. To convert these measurements into tomographic maps we developed a new tomographic method which has several features making it preferable to existing tomographic techniques for our purposes: a) spherical geometry; b) the region of inference is defined by an arbitrary simple closed curve; c) regularization is applied to provide spatial smoothness (with a specified correlation length) plus model amplitude constraints, both spatially variable and adaptive, depending on data density; d) azimuthal anisotropy may optionally be estimated. This method is described in detail in Section 1 of this report.

2. The tomographic technique we used does not take into account several factors which in principle may produce distortion or blurring of obtained tomographic images. One of these is neglecting the source group time delays. The methodology and results of studying this effect are presented in Section 2. The main conclusion of this section is that corrections for source group time delays are small for short periods and shallow events and may be neglected in group velocity measurements for periods less than 75 s and source depths less than 25 km.

3. Another unaccounted factor is off-path propagation of surface waves in a laterally inhomogeneous Earth. The evaluation of possible deviations of surface waves from great circle paths and of corresponding group velocity errors is given in Section 3. We arrived at the conclusion that, at least for periods around 20 s and above, the effects of the off-path propagation are not significant for surface wave paths which length is less than ~ 5,000 km. For many longer paths deviations from the great circle are significant. Our experience showed that the long paths are important for stabilizing tomographic inversion. By this reason the further studies are needed to evaluate the distorting effects produced by these deviations on tomographic maps.

4. The resulting maps of Rayleigh and Love waves for a set of periods between 16 s and 40 s for the region between 10° and 50° N and 20° and 140°E are described in Section 4. The resolution of these maps is spatially variable depending on the ray coverage and is optimal in western China, the Central Asian Republics, Afghanistan, Pakistan, Iran, and Northern India. The imprints of a number of known geological and tectonic structures are observed in the group velocity maps. Of

particular note are the signatures of numerous sedimentary basins at short periods (15-25 s) and crustal thickness variations at longer periods (~ 40 s). The obtained group-velocity maps are being used for the identification and extraction of surface-wave packets, and as data in inversions for crustal and upper mantle models. The group velocity maps for periods shorter than 14-16 s are not completely reliable across the region due to the poor coverage. Special efforts supported by the current Contract DTRA01-00-C-026 are in progress now to collect additional short-period surface wave data in the range of periods between 8 and 15 s.

5. We used group-velocity maps that we obtained to construct surface wave Travel Time Correction Surfaces (TTCS) for a set of stations in Eurasia. Then we evaluated the reliability of the maps and TTCS by means of two synthetic experiments described in Section 5. In the first experiment, we evaluated how the effects of unmodeled sub-scale inhomogeneities present in an input model (e.g., sedimentary basins, surface or Moho topography) and how random noise, which is always present in real measurements, distorts the TTSCs computed from estimated tomographic maps. In the second experiment, we estimated errors in the TTSCs produced by azimuthal anisotropy unmodeled in the tomographic maps. Results of these experiments are described in Section 5. Synthetic experiments show that in areas with dense ray coverage the spatial resolution of these maps is on the order of 250 - 350 km. The amplitude bias is no more than 10%. We estimated that the accuracy of group velocity maps and TTCSs for the part of the region to the north of 25°N is typically better than 0.03-0.04 km/s. The unmodeled 2% azimuthal anisotropy across such large areas as the Tibetan plateau does not generate significant errors in group velocity maps and TTCSs constructed from them.

6. The constructed TTCSs were used to design source-station phase-matched filters for extracting weak surface wave signals from seismic records (Section 6). These filters were successfully applied for recovering weak surface signals from several nuclear explosions in China and Northern India. The amplitude spectra of extracted surface waves were evaluated. These and other applications lead us to conclude that this method shows considerable promise as a surface wave detector and could yield high quality surface wave measurements automatically. It appears feasible to obtain automated spectral amplitude measurements for events in Central and Southern Asia with M_s down to as low as 3.5 - 4.0.

7. Together with a group of seismologists from the International Institute of Earthquake Prediction Theory and Mathematical Geophysics, Russian Academy of Sciences, we investigated the possibility of using surface wave amplitude spectra for discriminating nuclear explosion and screening surface wave data (Section 7). The discriminant is based on the assumption that events without an isotropic component of the seismic tensor are earthquakes, and near-surface events having a significant isotropic component are explosions. Results obtained for several seismic events (earthquakes and explosions) near the Lop Nor are encouraging, but a much larger data set of earthquakes must be considered to determine the false alarm rate (i.e., the percentage of earthquakes with surface wave amplitudes consistent with a substantial isotropic component of the moment tensor).

Acknowledgements

CONVERSION TABLE

Conversion Factors for U.S. Customary to metric (SI) units of measurement.

MULTIPLY ⟶ BY ⟶ TO GET
TO GET ⟵ BY ⟵ DIVIDE

angstrom	1.000 000 x E -10	meters (m)
atmosphere (normal)	1.013 25 x E +2	kilo pascal (kPa)
bar	1.000 000 x E +2	kilo pascal (kPa)
barn	1.000 000 x E -28	meter^2 (m^2)
British thermal unit (thermochemical)	1.054 350 x E +3	joule (J)
calorie (thermochemical)	4.184 000	joule (J)
cal (thermochemical/cm^2)	4.184 000 x E -2	mega joule/m^2 (MJ/m^2)
curie	3.700 000 x E +1	*giga bacquerel (GBq)
degree (angle)	1.745 329 x E -2	radian (rad)
degree Fahrenheit	$t_k = (t°f + 459.67)/1.8$	degree kelvin (K)
electron volt	1.602 19 x E -19	joule (J)
erg	1.000 000 x E -7	joule (J)
erg/second	1.000 000 x E -7	watt (W)
foot	3.048 000 x E -1	meter (m)
foot-pound-force	1.355 818	joule (J)
gallon (U.S. liquid)	3.785 412 x E -3	meter^3 (m^3)
inch	2.540 000 x E -2	meter (m)
jerk	1.000 000 x E +9	joule (J)
joule/kilogram (J/kg) radiation dose absorbed	1.000 000	Gray (Gy)
kilotons	4.183	terajoules
kip (1000 lbf)	4.448 222 x E +3	newton (N)
kip/inch^2 (ksi)	6.894 757 x E +3	kilo pascal (kPa)
ktap	1.000 000 x E +2	newton-second/m^2 (N-s/m^2)
micron	1.000 000 x E -6	meter (m)
mil	2.540 000 x E -5	meter (m)
mile (international)	1.609 344 x E +3	meter (m)
ounce	2.834 952 x E -2	kilogram (kg)
pound-force (lbs avoirdupois)	4.448 222	newton (N)
pound-force inch	1.129 848 x E -1	newton-meter (N-m)
pound-force/inch	1.751 268 x E +2	newton/meter (N/m)
pound-force/foot^2	4.788 026 x E -2	kilo pascal (kPa)
pound-force/inch^2 (psi)	6.894 757	kilo pascal (kPa)
pound-mass (lbm avoirdupois)	4.535 924 x E -1	kilogram (kg)
pound-mass-foot^2 (moment of inertia)	4.214 011 x E -2	kilogram-meter^2 (kg-m^2)
pound-mass/foot^3	1.601 846 x E +1	kilogram-meter^3 (kg/m^3)
rad (radiation dose absorbed)	1.000 000 x E -2	**Gray (Gy)
roentgen	2.579 760 x E -4	coulomb/kilogram (C/kg)
shake	1.000 000 x E -8	second (s)
slug	1.459 390 x E +1	kilogram (kg)
torr (mm Hg, 0° C)	1.333 22 x E -1	kilo pascal (kPa)

*The bacquerel (Bq) is the SI unit of radioactivity; 1 Bq = 1 event/s.
**The Gray (GY) is the SI unit of absorbed radiation.

Table of Contents

Table of Contents (Continued)

Table of Contents (Continued)

Table of Contents (Continued)

Figures

Figures (Continued)

Figures (Continued)

Figures (Continued)

Tables

Section 1
A Fast and Reliable Method for Surface Wave Tomography

1.1 Introduction.

We present and discuss a method to invert surface wave dispersion measurements (frequency dependent group or phase velocity) on regional or global scales to produce two dimensional (2-D) isotropic and azimuthally anisotropic maps of surface wave velocities. Such "tomographic" maps represent a local spatial average of the phase or group velocity at each location on the map and summarize large volumes of surface wave dispersion information in a form that is both useful and easily transportable. Dispersion information in this form can be applied naturally to a number of problems relevant to monitoring the Comprehensive Nuclear Test Ban Treaty (CTBT); for example, (1) to create phase-matched filters (e.g., Herrin & Goforth, 1977; Russell *et al.*, 1988; Leach *et al.*, 1998; Levshin & Ritzwoller, 2001) designed to detect weak surface wave signals immersed in ambient and signal-generated noise as a basis for spectral amplitude measurements essential to discriminate explosions from earthquakes (e.g., Stevens & Day, 1985; Stevens & McLaughlin, 1997) and (2) in inversions to estimate the shear velocity structure of the crust and upper mantle (e.g., Villaseñor *et al.*, 2001) which is useful to improve regional event locations. The method we discuss here is designed to produce accurate and detailed regional surface wave maps efficiently and reliably, as well as to provide information about the quality of the maps. The method may be applied, perhaps with a few extensions, to other 2-D inverse problems such as P_n and S_n tomography (e.g., Levshin *et al.*, 2001).

We note, as a preface to further discussion, that the relationship between observed seismic waveforms and an earth model is not linear. Thus, the problem of using surface wave data to constrain the structure of the crust and upper mantle is nonlinear. In surface wave inversions, however, the inverse problem is typically divided into two parts: a nearly linear part to estimate 2-D dispersion maps and a nonlinear part in which the dispersion maps are used to infer earth structure. It is the nearly linear part that we call surface wave tomography and that is the subject of this section. Some surface wave inversion methods linearize the relation between the seismic waveforms and an earth model (e.g., Nolet, 1987; Snieder, 1988; Marquering *et al.*, 1996) and iteratively estimate the earth model. Therefore, these methods do not estimate dispersion maps on the way to constructing structural models. We take the path through the dispersion maps for the following reasons.

- Surface wave dispersion maps, like a seismic model, summarize large volumes of data in a compact form, but remain closer to the data than the models.
- They are less prone to subjective decisions made during inversion and contain fewer assumptions (both hidden and explicit).
- Because of the foregoing, dispersion maps are more likely than models to be consumed and utilized by other researchers.
- Dispersion maps are directly applicable to detect and extract surface waves from potentially noisy records, which is important in discriminating explosions from earthquakes for CTBT monitoring.

On the negative side, dispersion maps contain only part of the information about earth structure in the seismogram, are the products of inversions themselves, and contain uncertainties due to both observational and theoretical errors.

There are a number of surface wave tomographic techniques currently in use by several research groups around the world. These techniques differ in geometry (i.e., Cartesian versus spherical), model parameterization (e.g., global versus local basis functions), certain theoretical assumptions (particularly about wave paths and scattering), the regularization scheme, and whether azimuthal anisotropy can be estimated simultaneously with the isotropic velocities. Because surface wave tomographic inversions are invariably ill-posed, the regularization scheme is the focal point of any inversion method. There is a large, general literature on ill-posed linear or linearized inversions that applies directly to the surface wave problem (e.g., Tikhonov, 1963; Backus and Gilbert, 1968, 1970; Franklin, 1970; Aki & Richards, 1980; Tarantola and Valette, 1982; Tarantola, 1987; Menke, 1989; Parker, 1994; Trampert, 1998). We do not intend to extend this literature, rather the purpose of this section is to describe one useful path through the large number of options available to an inversion method. Our method appears to provide robust and reliable dispersion maps on both global and regional scales.

The surface wave tomographic method we describe here has the following characteristics.

- **Geometry:** spherical;
- **Scale:** the region of inference is defined by an arbitrary simple closed curve;
- **Parameterization:** nodes are spaced at approximately constant distances from one another, interpolation is based on the three nearest neighbors;
- **Theoretical Assumptions:** surface waves are treated as rays sampling an infinitesimal zone along the great circle linking source and receiver, scattering is completely ignored;
- **Regularization:** application of spatial smoothness (with a specified correlation length) plus model amplitude constraints, both spatially variable and adaptive, depending on data density;
- **Azimuthal Anisotropy:** may optionally be estimated with the isotropic velocities.

The theoretical assumptions that we make are common in most of surface wave seismology. The method we describe generalizes naturally to non-great circular paths, if they are known, with finite extended Fresnel zones (e.g., Pulliam & Snieder, 1998). The incorporation of these generalizations into surface wave tomographic methods is an area of active research at this time. The use of the scattered wavefield (the surface wave coda) is also an area of active research (e.g., Pollitz, 1994; Friederich, 1998), but usually occurs within the context of the production of a 3-D model rather than 2-D dispersion maps.

The choices of parameterization and regularization require further comment.

1.1.1 Parameterization.

There are four common types of basis functions used to parameterize velocities in surface wave tomography: (1) integral kernels (the Backus-Gilbert approach), (2) a truncated basis (e.g., polynomial, wavelet, or spectral basis functions), (3) blocks, and (4) nodes (e.g., Tarantola and Nersessian, 1984). In each of these cases, the tomographic model is represented by a finite number

of unknowns. Blocks and nodes are local whereas wavelets and polynomials are global basis functions. (To the best of our knowledge, wavelets have not yet been used in surface wave tomography.) Backus-Gilbert kernels are typically intermediary between these extremes. Blocks are 2-D objects of arbitrary shape with constant velocities and are typically packed densely in the region of study. They are typically regularly shaped or sized, but there are notable exceptions (e.g., Spakman and Bijwaard, 1998; Spakman and Bijwaard, 2001). Nodes are discrete spatial points, not regions. A nodal model is, therefore, defined at a finite number of discrete points and values in the intervening spaces are determined by a specific interpolation algorithm in the inversion matrix and travel-time accumulation codes. Nodes are not necessarily spaced regularly. The ability to adapt the characteristics of these basis functions to the data distribution and other a priori information is a desirable characteristic of any parameterization, and is typically easier with local than with global basis functions. Blocks can be thought of as nodes with a particularly simple interpolation scheme. Thus, we use nodes rather than blocks because of their greater generality.

To date, most surface wave travel time tomographic methods have been designed for global application and have utilized truncated spherical harmonics or 2-D B-splines as basis functions to represent the velocity distribution (e.g., Nakanishi and Anderson, 1982; Montagner and Tanimoto, 1991; Trampert & Woodhouse, 1995, 1996; Ekström et al., 1997; Laske and Masters, 1996; Zhang and Lay, 1996). There are two notable exceptions. The first is the work of Ditmar and Yanovskaya (1987) and Yanovskaya and Ditmar (1990) who developed a 2-D Backus-Gilbert approach utilizing first-spatial gradient smoothness constraints for regional application. This method has been extensively used in group velocity tomography (e.g., Levshin et al. 1989; Wu & Levshin, 1994; Wu et al., 1997; Ritzwoller & Levshin, 1998; Ritzwoller et al., 1998; Vdovin et al., 1999) for studies at local and continental scales. The main problem is that the method has been developed in Cartesian coordinates and sphericity is approximated by an inexact earth flattening transformation (Yanovskaya, 1982; Jobert & Jobert, 1983) which works well only if the region of study is sufficiently small (roughly less than one-tenth of the Earth's surface). Yanovskaya and Antonova (2000) recently extended the method to a spherical geometry, however. The second is the irregular block method of Spakman and Bijwaard (2001).

We prefer local to global basis functions due to the simplicity of applying local damping constraints, the ability to estimate regions of completely general shape and size, and the ease by which one can intermix regions with different grid spacings. For example, with local basis functions it is straightforward to allow damping to vary spatially, but it is much harder to target damping spatially with global basis functions. This spatially targeted damping is a highly desirable feature, particularly if data distribution is inhomogeneous.

1.1.2 Regularization.

The term 'regularization', as we use it, refers to constraints placed explicitly on the estimated model during inversion. These constraints appear in the "penalty function" that is explicitly minimized in the inversion. We prefer this term to 'damping' but take the terms to be roughly synonymous and will use them interchangeably. Regularization commonly involves the application of some combination of constraints on model amplitude, the magnitude of the perturbation from a reference state, and on the amplitude of the first and/or second spatial gradients of the model. It is typically the way in which a priori information about the estimated model is applied and how the effects of inversion instabilities are minimized. The strength of regularization or damping

is usually something specified by the user of a tomographic code, but may vary in an adaptive way with information about data quantity, quality, and distribution and about the reliability of the reference model or other a priori information. As alluded to above, the practical difference between local and global basis functions manifests itself in how regularization constraints (e.g., smoothness) are applied as well as the physical meaning of these constraints.

As described in Section 1.2, the regularization scheme that we have effected involves a penalty function composed of a spatial smoothing function with a user defined correlation length and a spatially variable constraint on the amplitude of the perturbation from a reference state. The weight of each component of the penalty function is user specified, but the total strength of the model norm constraint varies with path density. Our experience indicates that Laplacian or Gaussian smoothing methods are preferable to gradient smoothing methods. The first-spatial gradient attempts to produce models that are locally flat, not smooth or of small amplitude. This works well if data are homogeneously distributed, but tends to extend large amplitude features into regions with poor data coverage and conflicts with amplitude penalties if applied simultaneously. The model amplitude constraint smoothly blends the estimated model into a background reference in regions of low data density, such as the areas on the fringe the region under study. In such areas the path density is very low, and the velocity perturbations will be automatically overdamped due to amplitude constraints. The dependence on data density is also user specified.

1.2 Surface Wave Tomography.

Using ray theory, the forward problem for surface wave tomography consists of predicting a frequency dependent travel time, $t_{R/L}(\omega)$, for both Rayleigh (R) and Love (L) waves from a set of 2-D phase or group velocity maps, $c(\mathbf{r}, \omega)$:

$$t_{R/L}(\omega) = \int_p c_{R/L}^{-1}(\mathbf{r}, \omega) ds, \tag{1}$$

where $\mathbf{r} = [\theta, \phi]$ is the surface position vector, θ and ϕ are co-latitude and longitude, and p specifies the wave path. The dispersion maps are nonlinearly related to the seismic structure of the earth, $\mathcal{M}(\mathbf{r}, z)$, where for simplicity of presentation we have assumed isotropy, and $\mathcal{M}(\mathbf{r}, z) = [v_s(z), v_p(z), \rho(z)](\mathbf{r})$ is the position dependent structure vector composed of the shear and compressional velocities and density. Henceforth, we drop the R/L subscript and, for the purposes of discussion here, do not explicitly discriminate between group and phase velocities or their integral kernels.

By surface wave tomography we mean the use of a set of observed travel times $t^{obs}(\omega)$ for many different paths p to infer a group or phase velocity map, c(r), at frequency ω. We assume that

$$t^{obs}(\omega) = t(\omega) + \epsilon(\omega),$$

where ϵ is an observational error for a given path. The problem is linear if the paths p are known. Fermat's Principle states that the travel time of a ray is stationary with respect to small changes in the ray location. Thus, the wave path will approximate that of a spherically symmetric model, which is a great-circle linking source and receiver. This approximation will be successful if the magnitude of lateral heterogeneity in the dispersion maps is small enough to produce path perturbations smaller than the desired resolution.

4

1.2.1 The Forward Problem.

Because surface wave travel times are inversely related to velocities, we manipulate Equation (1) as follows. Using a 2-D reference map, $c_o(\mathbf{r})$, the travel time perturbation relative to the prediction from $c_o(\mathbf{r})$ is:

$$\delta t \;=\; t - t_o = \int_p \frac{ds}{c} - \int_p \frac{ds}{c_o} = \int_p \frac{m}{c_o} ds \tag{2}$$

$$m \;=\; \frac{c_o - c}{c} \tag{3}$$

where we have suppressed the $\mathbf{r} = [\theta, \phi]$ dependence throughout and have assumed that the ray paths are known and are identical for both c and c_o.

For an anisotropic solid with a vertical axis of symmetry, the surface wave velocities depend on the location $\mathbf{r}$ and the local azimuth ψ of the ray. In the case of a slightly anisotropic medium, Smith and Dahlen (1973) show that phase or group velocities can be approximated as:

$$c(\mathbf{r}) \;=\; c_I(\mathbf{r}) + c_A(\mathbf{r}) \tag{4}$$

$$c_I(\mathbf{r}) \;=\; A_0(\mathbf{r}) \tag{5}$$

$$\begin{aligned} c_A(\mathbf{r}) \;=\;& A_1(\mathbf{r})\cos(2\psi) + A_2(\mathbf{r})\sin(2\psi) + \\ & A_3(\mathbf{r})\cos(4\psi) + A_4(\mathbf{r})\sin(4\psi) \;, \end{aligned} \tag{6}$$

where c_I is the isotropic part of velocity, c_A is the anisotropic part, A_0 is the isotropic coefficient, and $A_1, \ldots, A_4$ are anisotropic coefficients. If we assume that $|c_A/c_I| \ll 1$ so that $(1 + c_A/c_I)^{-1} \approx (1 - c_A/c_I)$, and if the reference model c_o is purely isotropic, then by substituting equations (4) - (6) into (3) we get:

$$m \;\approx\; \frac{c_o - c_I}{c_I} - \frac{c_A}{c_I} - \left(\frac{c_A}{c_I}\right)\left(\frac{c_o - c}{c_I}\right) \;\approx\; \frac{c_o - c_I}{c_I} - \frac{c_A}{c_I^2}c_o, \tag{7}$$

where the latter equality holds if $|c_A/c_I| \ll 1$ as before. Equation (7) can be rewritten as:

$$m(\mathbf{r}, \psi) = \sum_{k=0}^{n} \gamma_k(\psi) m_k(\mathbf{r}), \tag{8}$$

where n should be 0, 2 or 4 for a purely isotropic model, a 2ψ anisotropic model, or a 4ψ anisotropic model, respectively, and γ_k and m_k are defined as follows:

$$\begin{aligned} \gamma_0(\psi) &= 1 & m_0(\mathbf{r}) &= \left(c_o(\mathbf{r}) - c_I(\mathbf{r})\right)/c_I(\mathbf{r}) \\ \gamma_1(\psi) &= -\cos(2\psi) & m_1(\mathbf{r}) &= A_1(\mathbf{r})c_o(\mathbf{r})/c_I^2(\mathbf{r}) \\ \gamma_2(\psi) &= -\sin(2\psi) & m_2(\mathbf{r}) &= A_2(\mathbf{r})c_o(\mathbf{r})/c_I^2(\mathbf{r}) \\ \gamma_3(\psi) &= -\cos(4\psi) & m_3(\mathbf{r}) &= A_3(\mathbf{r})c_o(\mathbf{r})/c_I^2(\mathbf{r}) \\ \gamma_4(\psi) &= -\sin(4\psi) & m_4(\mathbf{r}) &= A_4(\mathbf{r})c_o(\mathbf{r})/c_I^2(\mathbf{r}). \end{aligned} \tag{9}$$

1.2.2 The Inverse Problem.

Our goal is to estimate the vector function $\mathbf{m}(\mathbf{r}) = [m_0(\mathbf{r}), \ldots, m_n(\mathbf{r})]$ using a set of observed travel time residuals d relative to the reference model $c_\mathrm{o}(\mathbf{r})$:

$$d = \delta t^{obs} = \quad t^{obs} - t_\mathrm{o} = \int_p \frac{m}{c_\mathrm{o}} ds + \epsilon \tag{10}$$

From $\mathbf{m}(\mathbf{r})$ we can reconstruct $c_I, A_1, \ldots, A_4$ for substitution into Equations (4) - (6):

$$c_I \quad = \quad \frac{c_\mathrm{o}}{1 + m_0} \tag{11}$$

$$A_k \quad = \quad \frac{m_k}{1 + m_0} c_I \quad (k \neq 0). \tag{12}$$

We define the linear functionals G_i as:

$$G_i(\mathbf{m}) = \sum_{k=0}^{n} \int_{p_i} \left(\gamma_k \left(\psi(\mathbf{r}) \right) c_\mathrm{o}^{-1}(\mathbf{r}) \right) m_k(\mathbf{r}) ds, \tag{13}$$

By substituting Equations (8) and (13) into Equation (10) for each path index ($1 \leq i \leq N$) we obtain the following:

$$d_i = \delta t_i^{obs} = G_i(\mathbf{m}) + \epsilon_i . \tag{14}$$

To estimate $\mathbf{m}$ we choose to minimize the following penalty function:

$$(\mathbf{G}(\mathbf{m}) - \mathbf{d})^T \mathbf{C}^{-1} (\mathbf{G}(\mathbf{m}) - \mathbf{d}) + \sum_{k=0}^{n} \alpha_k^2 ||F_k(\mathbf{m})||^2 + \sum_{k=0}^{n} \beta_k^2 ||H_k(\mathbf{m})||^2, \tag{15}$$

where $\mathbf{G}$ is a vector of the functionals G_i. For an arbitrary function $f(\mathbf{r})$ the norm is defined as:
$$||f(\mathbf{r})||^2 = \int_S f^2(\mathbf{r}) d\mathbf{r} .$$

The first term of the penalty function represents data misfit ($\mathbf{C}$ is the *a priori* covariance matrix of observational errors ϵ_i). The second term is the spatial smoothing condition such that

$$F_k(\mathbf{m}) = m_k(\mathbf{r}) - \int_S S_k(\mathbf{r}, \mathbf{r}') m_k(\mathbf{r}') d\mathbf{r}' , \tag{16}$$

where S_k is a smoothing kernel defined as follows:

$$S_k(\mathbf{r}, \mathbf{r}') = K_{0k} \exp \left(-\frac{|\mathbf{r} - \mathbf{r}'|^2}{2\sigma_k^2} \right) \tag{17}$$

$$\int_S S_k(\mathbf{r}, \mathbf{r}') d\mathbf{r}' = 1, \tag{18}$$

and σ_k is spatial smoothing width or correlation length. The minimization of the expression in Equation (16) explicitly ensures that the estimated model will approximate a smoothed version of the model.

The final term in the penalty function penalizes the weighted norm of the model,

$$H_k(\mathbf{m}) = \mathcal{H}(\rho(\mathbf{r}), \chi(\mathbf{r})) m_k, \tag{19}$$

6
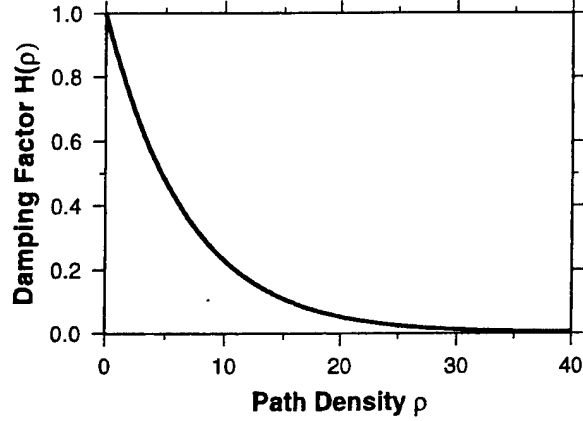
Figure 1. Example of the model norm weighting function, $\mathcal{H}(\rho)$ that we commonly use; e.g., as Figure 5. Here we choose the constant $\lambda \sim 0.147$ so that when path density (ρ) is less than about 20 paths per 50,000 km^2 damping toward the input reference model becomes increasingly strong.

where $\mathcal{H}$ is a weighting function that depends on local path density ρ for isotropic structure and a measure of local azimuthal distribution χ for azimuthal anisotropy. Thus, for $k = 0$, $\mathcal{H} = \mathcal{H}(\rho)$ and for $k = 1, \ldots, 4$, $\mathcal{H} = \mathcal{H}(\chi)$. Path density is defined as the number of paths intersecting a circle of fixed radius with center at the point $\mathbf{r}$. For isotropic structure, we choose $\mathcal{H}$ to approach zero where path density is suitably high and unity in areas of poor path coverage. The function $\mathcal{H}(\rho)$ can be chosen in various ways. We use $\mathcal{H} = \exp(-\lambda\rho)$, where λ is a user defined constant. An example is shown in Figure 1. To damp azimuthal anisotropy in regions with poor azimuthal coverage, we define $\chi(\theta, \phi)$ to measure the azimuthal distribution of ray paths at point (θ, ϕ). To find χ we construct a histogram of azimuthal distribution of ray paths in the vicinity of (θ, ϕ) for a fixed number n of azimuthal bins in the interval between $0°$ and $180°$, and evaluate the function

$$\chi = \frac{\sum\limits_{i=1}^{n} f_i}{n \max\limits_{i} f_i},$$

(20)

where f_i is the density of azimuths in the ith bin. Values of χ are in the range $1/n \leq \chi \leq 1$. $\chi \approx 1$ characterizes an almost uniform distribution of azimuths, and $\chi \approx 1/n$ is an indicator of the predominance of a single azimuthal direction (large azimuthal gap). We assume that the anisotropic coefficients cannot be determined reliably in regions where χ is less than ~ 0.3. Examples of a χ map and the histogram of azimuthal density, $f(\psi)$, are given in Section 1.3.4 (Figure 7c,d).

Because $\mathbf{m}$ is a perturbation from a reference state, the effect of the third term in the penalty function is to merge the estimated model smoothly and continuously into the isotropic reference state in regions of poor data coverage. In regions of good coverage, this term has no effect so that the only regularization is the smoothness constraint represented by the second term in expression (15).
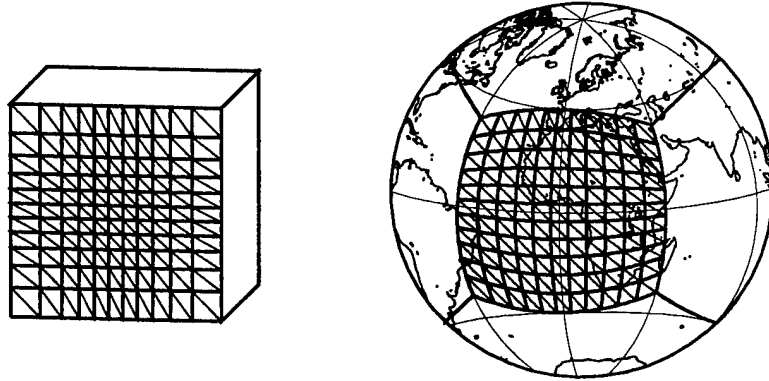
Figure 2. An example of the Delaunay triangulation on a sphere by defining a variable triangular grid on a reference cube and performing a central projection of the grid onto the sphere.

The user supplied regularization constants, α_k and β_k, define the relative strengths of the three terms in the penalty function. The smoothing width or correlation length σ_k is also specified by the user. These parameters should be varied systematically in applying the method. In practice, we often estimate the isotropic and anisotropic maps simultaneously. In this case we normally use slightly different values of all three constants α_k, β_k, σ_k for the isotropic and anisotropic maps to make anisotropic maps more smooth. Typically $\alpha_1 = \alpha_2$ and $\alpha_3 = \alpha_4$, $\sigma_1 = \sigma_2$, $\sigma_3 = \sigma_4$, and $\beta_k = \beta$.

1.2.3 Discretization.

The discretization of the Equations in the preceding Section involves two steps: (1) the formation of a discrete grid and the evaluation of the model on this grid and (2) the discretization of the penalty function. We discuss each in turn.

1.2.3.1 Grid, Nearest Neighbors, and Interpolation.
The goal is to generate a discrete grid with nodes that are approximately constantly spaced on a sphere such that nearest neighbors can be identified and the model evaluated at these points quickly. Significant advances in nonconstant grid generation have been made in recent years by several researchers (e.g., Sambridge, 1995; Spakman & Bijwaard, 1998), particularly for application in 3-D body wave tomography. The tomographic method that we describe is applicable irrespective of grid. However, because path coverage for regional surface waves tends to be less variable than for body waves and surface wave tomography is only in 2-D (e.g., Bijwaard et al., 1998; Van der Hilst et al., 1997; Grand et al., 1997; Zhou, 1996), we find that a constant grid is sufficient for our purposes. Generalization to nonconstant grids for surface wave tomography is, however, a useful direction for future research (e.g., Spakman and Bijwaard, 2001).

We create a nearly constant grid on a sphere by performing a central projection onto the sphere of a grid on a reference cube, such that the cube and the sphere share a common center. The advantage of using this reference cube is that nearest neighbors on each of the six faces of the

cube are identified trivially. Efficient neighbor identification for interpolation during model evaluation is important for travel time accumulation, which occurs during the construction of the inversion matrix, and in the application of the smoothness constraint. Thus, this method is computationally very efficient because it imposes a natural ordering for the nodes on the sphere, which avoids the need for the creation and use of an adjacency matrix (e.g., Sloan, 1987; Sambridge et al., 1995). To ensure that the distances between nodes on the sphere are approximately constant, the grid on the reference cube must be non-constant. Without providing the details, Figure 2 demonstrates the mapping between the face of a cube and the spherical shell related to the face. The current method of grid generation guarantees that the areas defined by adjacent quadruples of nodes on the sphere differ by no more than 10% from the average area. One could produce a mapping with smaller variation in these areas, but this is good enough for our purposes.

The value of the model at each location on the sphere is evaluated from the values at the three nearest nodes. This is done by constructing Delaunay triangles from the set of nodes on the sphere (e.g., Aurenhammer, 1991; Braun and Sambridge, 1997). Each triangle defines a flat plane between the three nodes at the vertices on the plane which is nearly the tangent plane to the sphere. We define a local Cartesian coordinate system on this plane and determine the distances between the point of interest and the three defining nodes approximately. Typical internodal distances, even for global inversions, are 200 km or less, so this local Cartesian approximation is accurate enough for our purposes. Three-point linear interpolation is used to evaluate the model within each Delaunay triangle. Thus, the value of the model at some arbitrary point $\mathbf{r}$ can be expressed as the weighted sum of the values at the three neighboring nodes:

$$m_k(\mathbf{r}) = \sum_{j=1}^{M} m_k(\mathbf{r}_j) w_j(\mathbf{r}),\tag{21}$$

where $\mathbf{r}_j$ are the locations of the M nodes (vortices of triangles) defining the model. The weights $w_j(\mathbf{r})$ are non-zero only inside the triangles surrounding $\mathbf{r}_j$ and linearly depend on two local coordinates inside the Delaunay triangle enclosing $\mathbf{r}$. The weights $w_j(\mathbf{r})$ form the set of the local basis functions such that the values of the basis functions range from 0 to 1 with a maximum value of 1 at the point $\mathbf{r}_j$.

1.2.3.2 The Inversion Matrix. To construct the inversion matrix, we have to substitute Equation (21) into expression (15). After integrating, the penalty function can be rewritten in matrix form as the sum of two quadratic forms,

$$(\mathbf{Gm} - \mathbf{d})^T \mathbf{C}^{-1} (\mathbf{Gm} - \mathbf{d}) + \mathbf{m}^T \mathbf{Qm},\tag{22}$$

in which the second term is the regularization condition that includes both smoothness and model norm constraints. Let N be the number of data, n be the isotropic/anisotropic index (0 for isotropic, 2 for isotropic plus 2ψ anisotropic, 4 for isotropic plus both 2ψ and 4ψ anisotropic), and M be the number of nodes defining the model such that $k = 0, \ldots, n$, $i = 1, \ldots, N$, $j = 1, \ldots, M$.

Let us define now our discrete model as a vector $\mathbf{m}$ in the following way:

$$\mathbf{m} = (m_0(\mathbf{r}_1), m_0(\mathbf{r}_2), \ldots m_0(\mathbf{r}_M), \ldots, m_n(\mathbf{r}_1), m_n(\mathbf{r}_2), \ldots m_n(\mathbf{r}_M))^T .$$

Without changing notation we discretize $\mathbf{G}$ to create a $N \times (n+1)M$ matrix in the following way.

Let $\mathbf{G}$ to be composed of a set of n submatrices, $\mathbf{U}^k$,

$$\mathbf{G} = \begin{bmatrix} \mathbf{U}^0 \end{bmatrix} \qquad (n = 0)$$
$$\mathbf{G} = \begin{bmatrix} \mathbf{U}^0 \vdots \mathbf{U}^1 \vdots \mathbf{U}^2 \end{bmatrix} \qquad (n = 2) \qquad (23)$$
$$\mathbf{G} = \begin{bmatrix} \mathbf{U}^0 \vdots \mathbf{U}^1 \vdots \mathbf{U}^2 \vdots \mathbf{U}^3 \vdots \mathbf{U}^4 \end{bmatrix} \quad (n = 4)$$

where $\mathbf{U}^k$ is defined as follows:

$$U_{ij}^k = \int_{p_i} \left(\gamma_k \left(\psi \right) c_0^{-1}(\mathbf{r}) \right) w_j \left(\mathbf{r} \right) ds. \qquad (24)$$

The $(n+1)M \times (n+1)M$ regularization matrix $\mathbf{Q}$ is the result of discrete numerical integration of the last two terms in Equation (15), and can be determined in the following way:

$$\mathbf{Q} = \mathbf{F}^T \mathbf{F} + \mathbf{H}^T \mathbf{H}, \qquad (25)$$

where the smoothing constraint is incorporated within the $(n+1)M \times (n+1)M$ block-diagonal matrix $\mathbf{F}$ as follows:

$$\mathbf{F} = \begin{bmatrix} \alpha_0 \mathbf{F}^0 & \dots & 0 & \dots & 0 \\ \vdots & \vdots & \vdots & \vdots & \vdots \\ 0 & \dots & \alpha_k \mathbf{F}^k & \dots & 0 \\ \vdots & \vdots & \vdots & \vdots & 0 \\ 0 & \dots & 0 & \dots & \alpha_n \mathbf{F}^n \end{bmatrix} \qquad (26)$$

The $M \times M$ matrices $\mathbf{F}^k = \left(F_{jj'}^k \right)$ $(k = 0, \dots, n; \; j, j' = 1, \dots, M)$ are:

$$F_{jj'}^k = \begin{cases} 1 & j = j' \\ -S_k(\mathbf{r}_j, \mathbf{r}_{j'})/p_k & j \neq j' \end{cases} , \quad p_k = \sum_{j'} S_k(\mathbf{r}_j, \mathbf{r}_{j'}). \qquad (27)$$

The model norm constraint is encoded within the $(n+1)M \times (n+1)M$ matrix $\mathbf{H}$ which consists of $(n+1)$ diagonal matrices $\mathbf{H}^k = \left(H_{jj'}^k \right)$:

$$\mathbf{H} = \begin{bmatrix} \beta_0 \mathbf{H}^0 & \dots & 0 & \dots & 0 \\ \vdots & \vdots & \vdots & \vdots & \vdots \\ 0 & \dots & \beta_k \mathbf{H}^k & \dots & 0 \\ \vdots & \vdots & \vdots & \vdots & \vdots \\ 0 & \dots & 0 & \dots & \beta_n \mathbf{H}^n \end{bmatrix} \qquad (28)$$

where

$$H_{jj'}^k = \begin{cases} \mathcal{H}\left(\rho(\mathbf{r}_j), \chi(\mathbf{r}_j) \right) & j = j' \\ 0 & j \neq j' \end{cases} \qquad (29)$$

With these definitions the forward problem for the travel time perturbation relative to an isotropic reference model is:

$$\delta\mathbf{t} = \mathbf{Gm}, \qquad (30)$$

10

and the estimated model is:

$$\hat{\mathbf{m}} = \mathbf{G}^\dagger \mathbf{C}^{-1} \delta \mathbf{t} \tag{31}$$

where the inversion operator, $\mathbf{G}^\dagger$, is defined as follows:

$$\mathbf{G}^\dagger = \left(\mathbf{G}^T \mathbf{C}^{-1} \mathbf{G} + \mathbf{Q}\right)^{-1} \mathbf{G}^T \tag{32}$$

1.2.4 Resolution Analysis.

We agree with Leveque *et al.* (1993) who argue that the estimation of the resolution matrix is generally preferable to checkerboard tests such as those performed by Ritzwoller and Levshin (1998). Note that from Equations (30) - (32):

$$\hat{\mathbf{m}} = \mathbf{G}^\dagger \mathbf{C}^{-1} \delta \mathbf{t} = \left(\mathbf{G}^\dagger \mathbf{C}^{-1} \mathbf{G}\right) \mathbf{m} = \mathcal{R}\mathbf{m} \tag{33}$$

$$\mathcal{R} = \left(\mathbf{G}^T \mathbf{C}^{-1} \mathbf{G} + \mathbf{Q}\right)^{-1} \mathbf{G}^T \mathbf{C}^{-1} \mathbf{G}. \tag{34}$$

The matrix $\mathcal{R}$ is the resolution matrix. In this application, each row of $\mathcal{R}$ is a resolution map defining the resolution at one spatial node. Thus, the resolution matrix is very large and the information it contains is somewhat difficult to utilize. We attempt to summarize the information in each resolution map by estimating two scalar quantities at each point: spatial resolution and ampltidue bias.

To estimate spatial resolution we fit a cone to each resolution map. This cone approximates closely the response of the tomographic procedure to a δ-like perturbation at the target node. Figure 3a shows a δ-like input perturbation (the local basic function) at the specified spatial location. Figure 3b displays the resolution map for that spatial location for the 50 s Rayleigh wave. The cone that best-fits the resolution surface for this point is shown in Figure 3c and the difference between the fit cone and the resolution map appears in Figure 3d. We define the resolution σ_R as the radius of the base of the fit cone. This value may be interpreted as the minimum distance at which two δ-shaped input anomalies (i.e., Figure 3a) can be resolved on a tomographic map. Of course, resolution cannot be less than 2ℓ, where ℓ is the distance between the nodes. In the example in Figure 3, nodes are separated by 2 equatorial degrees (~ 222 km). Therefore, if σ_R is estimated to be less than 2ℓ or 444 km, we redefine resolution as $\sigma_R = 2\ell = 444$ km.

It is also useful to know how reliably the amplitude of the estimated anomalies may be determined. To do this, we apply the appropriate row of the resolution matrix (Equation 33) associated with node (θ_0, ϕ_0) to a test model consisting of a cylinder of unit height with a diameter equal to $2\sigma_R$ centered at (θ_0, ϕ_0). We then define the amplitude of the fit surface as the average amplitude within σ_R of the center of the input cylinder. The relative difference between the input and estimated amplitudes is then taken as the amplitude bias estimate for this point on the map.

Examples of the estimated resolution and amplitude bias are shown in Figure 4 for the 20 s Rayleigh wave. Across much of Eurasia, the 20 s Rayleigh wave data yields nearly optimal resolution for a 2° × 2° grid spacing; about 450 km. Amplitude bias at the estimated resolution is typically within about ±10% at each spatial point. Near the periphery of the map where data coverage degrades, estimates of spatial resolution become unreliable but amplitude bias grows rapidly. Thus, amplitude bias is a more reliable means of estimating the reliability of dispersion maps in regions of extremely poor data coverage using the method we describe here.

11
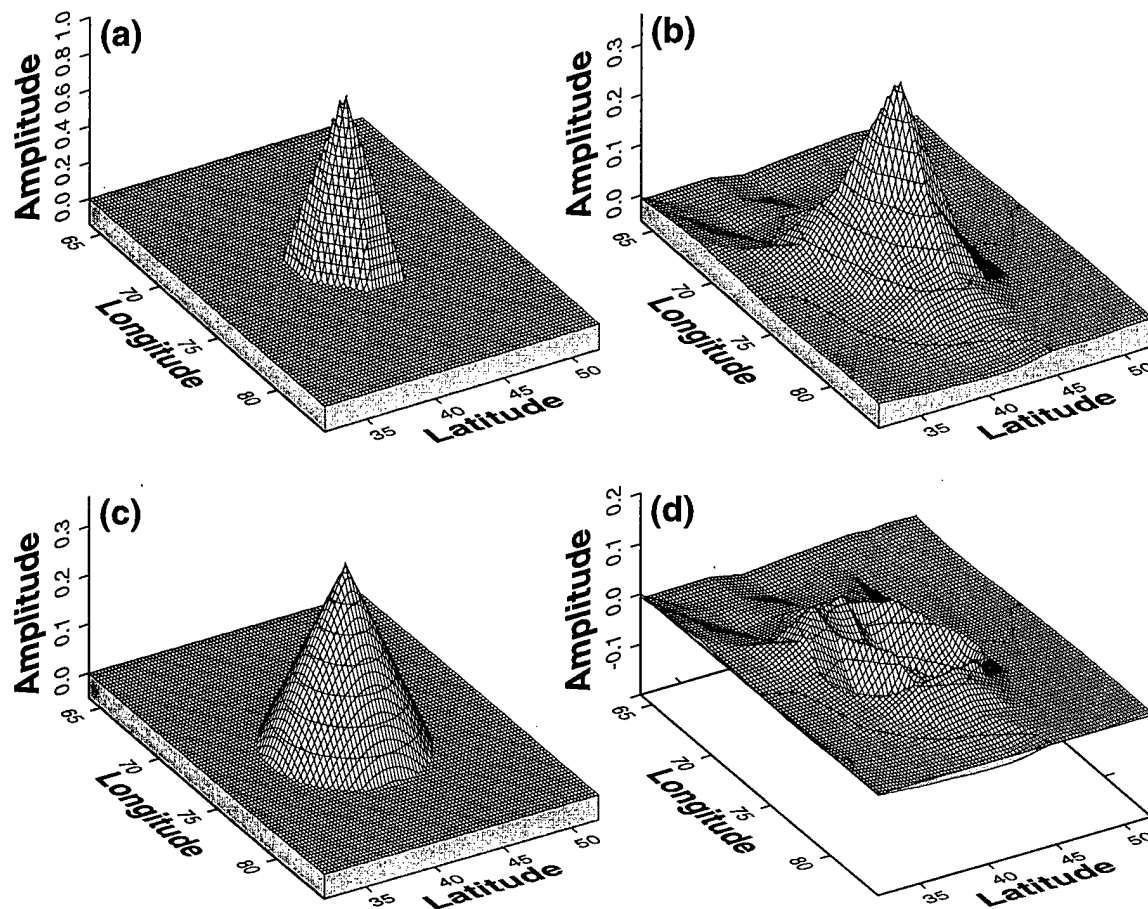
Figure 3. Graphical description of the resolution analysis. a) Minimum sized function that can be estimated with a 2° × 2° grid. The function is centered at 42°N latitude and 73° E longitude. (b) The row of the resolution matrix (a resolution map) for the point specified in (a) for the 50 s Rayleigh wave. (c) The cone that best fits the row of the resolution matrix shown in (b). A comparison of (a) with (b) and (c) demonstrates the spatial spreading produced in the tomographic procedure. (d) The difference between the resolution map and the best fitting cone.
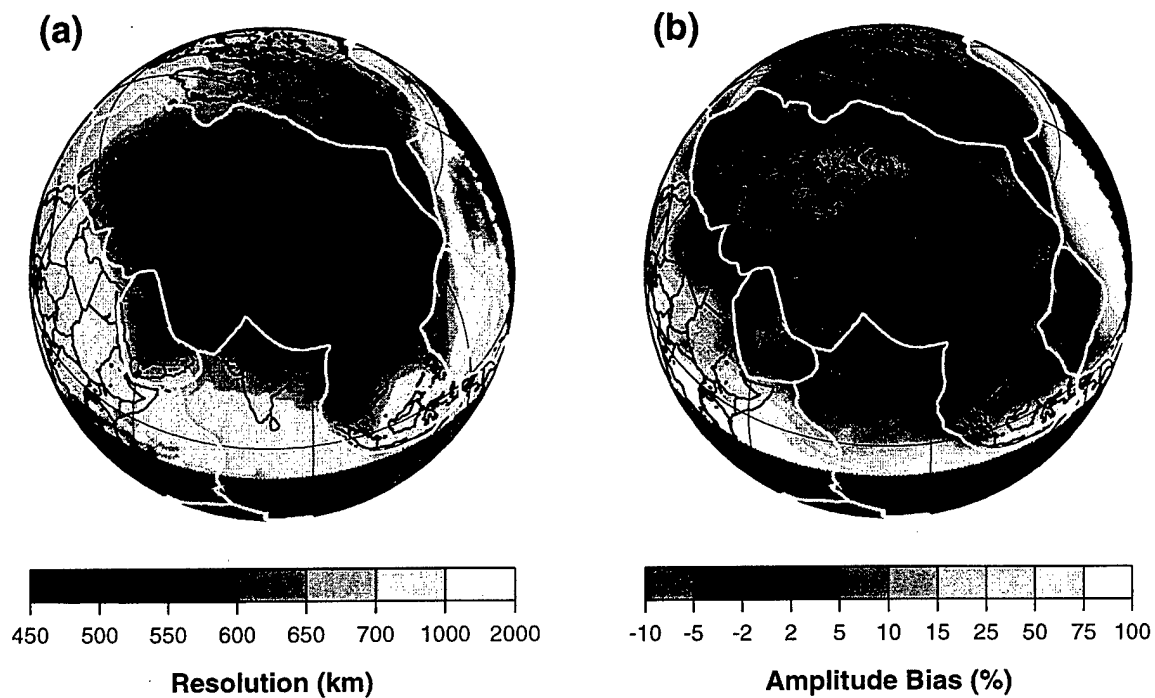
Figure 4. (a) Spatial resolution in km for the 20 s Rayleigh wave across Eurasia. Resolution depends on data coverage. In the central part of Eurasia the resolution is high (~ 450 − 500 km) in areas of high path density and degrades rapidly on the periphery of the region where path density (Figure 5d) is low. (b) Amplitude bias for Rayleigh waves at 20 s period. Units of amplitude bias are percent such that 0% means that the cylindrical test function's amplitude has been fully recovered upon inversion. Amplitude bias across the region varies between about ±10% depending on path coverage.

13

1.2.5 Computational Requirements.

The following formulas summarize computational time (550 MHz, DEC Alpha) and memory requirements for a purely isotropic inversion:

$$t \sim 68 \left(\frac{k}{d}\right)^4 \text{ hours} \qquad \text{(computational time in hours)} \qquad (35)$$

$$M \sim 29 \left(\frac{k}{d}\right)^4 \text{ Gb} \qquad \text{(memory usage in Gb),} \qquad (36)$$

where k is the fraction of the earth's surface covered and d is the distance between nodes in equatorial degrees. For Eurasian tomography, about half of the earth's surface is covered ($k \sim 0.5$) and $d = 2$ degrees $= 222$ km, thus $t \sim 15$ minutes and $M \sim 115$ Mb.

1.3 Examples of Applications.

1.3.1 Preliminaries.

The technique described above has been extensively tested using different cell sizes, regularization parameters, and data sets from different regions of the world: Eurasia, Antarctica, South America, and the Arctic. The two conditions necessary for constructing reliable tomographic images are preliminary outlier rejection (data "cleaning") and a careful choice of regularization (or damping) parameters appropriate for a given path coverage.

Data cleaning is based on a two part process. First, we identify outliers in a preliminary way by clustering measurements into summary rays. Second, the resulting data are inverted for an overdamped, smooth tomographic map and outliers are then identified by comparing observed group travel times with those predicted from the smooth map. The usual percentage of the rejected measurements is about 2-3% of all observations.

The choice of regularization parameters is made after several iterations using different combinations of the parameters α_k, β_k, σ_k. The criteria for choosing the best combination are subjective and are based on common sense and some a priori information about the region under study. We select a combination of parameters that produces a map free from aphysical features like speckling, streaking, and other artifacts and that also reveals the well known features of the region (sedimentary basins, mountain ranges, etc.) appropriate for the type of map under construction. Ritzwoller & Levshin (1998) describe this procedure in some detail. For example, a typical combination of parameters selected for an isotropic inversion of the 20 s Rayleigh wave data for Eurasia on a $2° \times 2°$ grid is: $\alpha_0 = 800$, $\beta_0 = 1$, and $\sigma_0 = 200$. The resulting maps are relatively insensitive to small (20-30%) changes in the damping parameters. Similar robustness of maps of azimuthal anisotropy to changes in the anisotropy damping parameters was demonstrated by Vdovin (1999) for Antarctica, but in other areas of the world both the pattern and the amplitude of anisotropy change strongly with damping (e.g., Eurasia and the Arctic, Levshin et al., 2001) as discussed further in Section 1.3.4.

1.3.2 Regional Isotropic Group Velocity Maps.

Regional group and phase velocity maps have been produced by a number of researchers (e.g., Suetsugu and Nakanishi, 1985; Curtis *et al.*, 1998; Ritzwoller *et al.*, 1998; and many others). Using the protocol described in Section 1.3.1, we have recently constructed a set of isotropic group velocity maps of Eurasia and surrounding areas for Rayleigh and Love waves from 15 s to 200 s period. An example for the 20 s Rayleigh wave is shown in Figure 5a. As input data we used 12900 Rayleigh group velocity measurements obtained from records of both global (GSN, GEOSCOPE) and regional (CDSN, CSN, USNSN, MEDNET, Kirgiz and Kazak networks) networks. The basic characteristics of the measurement procedure, data control and weighting are described in detail in Ritzwoller & Levshin (1998). Because 20 s Rayleigh waves are most sensitive to upper crustal velocities, the corresponding group velocity map clearly shows the significant sedimentary basins across Eurasia and on the periphery of the Arctic Ocean as low velocity anomalies (e.g., Barents Sea shelf, western Siberian sedimentary complex, Pre-Caspian, South Caspian, Black Sea, Tadzhik Depression, the Tarim Basin, Dzhungarian Basin, Ganges Fan and Delta, etc.) There is qualitative agreement between the observed group velocity map and the prediction of a hybrid model composed of crustal structure from the model CRUST5.1 (Mooney *et al.*, 1998) and mantle velocities from the model S16B30 (Masters *et al.*, 1996). The comparison is shown in Figures 5b,c. The estimated r.m.s. group velocity misfit at 20 s period is significantly less for our maps (0.08 km/s) than for the map computed from the model CRUST5.1/S16B30 (0.14 km/s). The numbers for the 50 s Rayleigh wave are correspondingly 0.05 km/s and 0.16 km/s. Similar results are reported by Ritzwoller and Levshin (1998) which used the tomographic method of Ditmar & Yanovskaya (1987).

1.3.3 Global Isotropic Phase Velocity Maps.

The tomographic method described above identifies the region of interest by requiring the user to define a simle closed curve on the sphere and identify a single point outside the contour that distinguishes the inside from the outside of the region of interest. If the contour is a very small circle surrounding the point, then the region of interest becomes nearly the entire sphere. In this way, our method can be used to produce global tomographic maps on a regular grid. An example is shown in Figure 6a, in which we have inverted the 100 s Rayleigh wave phase velocity data of Trampert and Woodhouse (1995, 1996). Trampert and Woodhouse's map is shown in Figure 6b, where they used spherical harmonics up through degree and order 40. The major features of these maps are nearly identical. We have chosen the damping parameters, however, to accentuate smaller scale features than those apparent in the spherical harmonic parameterization. There is much signal remaining in the data set of Trampert and Woodhouse to be fit by smaller scale features than those apparent in Figure 6b. For example, the rms misfit to Trampert and Woodhouse's data produced by the map in Figure 6a is about 8.1 s compared with the 10.8 s produced by the spherical harmonic map in Figure 6b; about a 40% reduction in variance.

1.3.4 Azimuthal Anisotropy.

We follow the majority of the studies of azimuthal anisotropy and our discussion above (Equations (4) - (6)) by parameterizing azimuthal anisotropy for group velocity as:

$$U(\mathbf{r}, \psi) = U_0(\mathbf{r}) + U_1(\mathbf{r}) \cos 2\psi + U_2(\mathbf{r}) \sin 2\psi + U_3(\mathbf{r}) \cos 4\psi + U_4(\mathbf{r}) \sin 4\psi, \qquad (37)$$
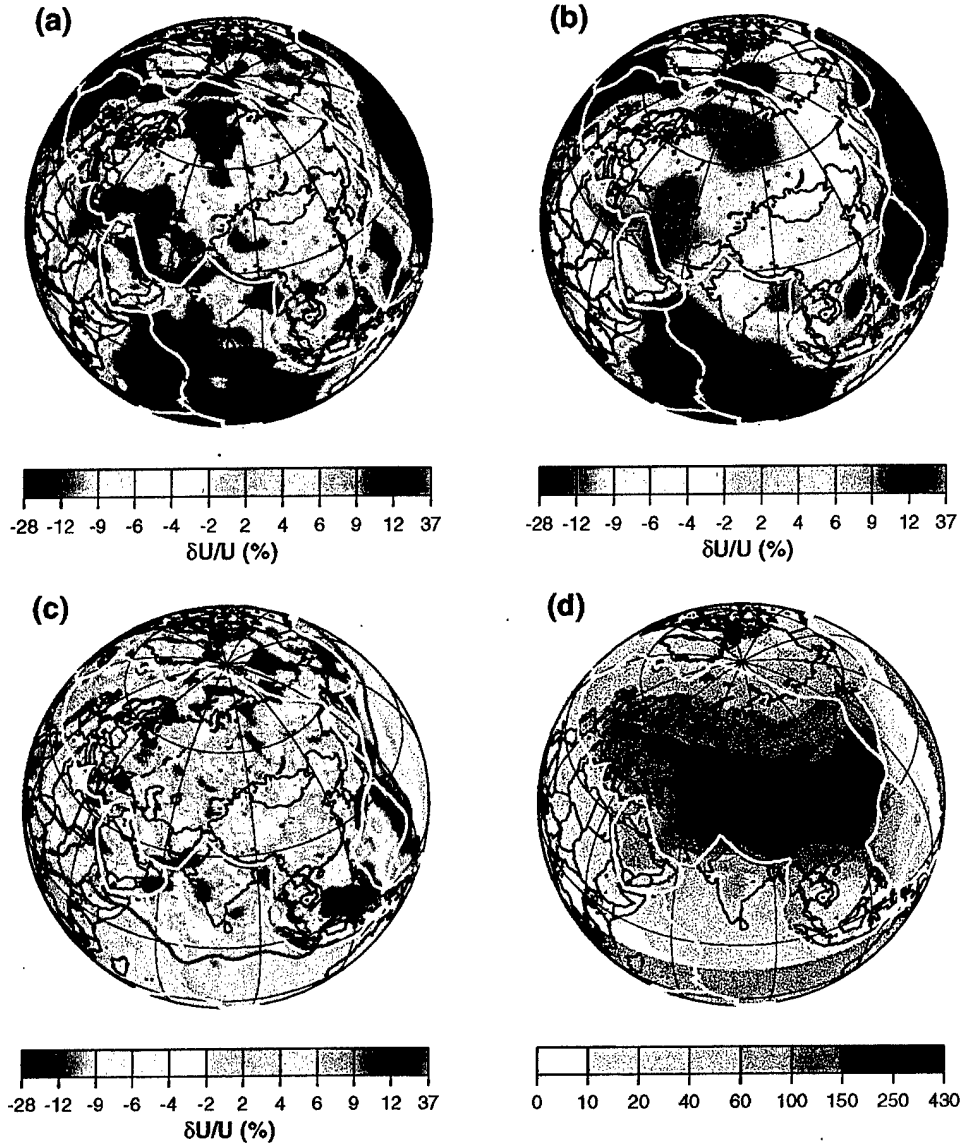
Figure 5. (a) The group velocity map across Eurasia for the 20 s Rayleigh wave using the method described in this section. A 2° × 2° grid is used. (b) The group velocity map computed from the smoothed version of the model CRUST5.1/S16B30. Maps (a) and (b) are plotted in percent relative to the same average velocity. (c) The difference between maps (a) and (b) relative to the same average in (a) and (b). (d) Path density, defined as the number of rays intersecting a 2° square cell ($\sim 50,000$ km^2).

(a)   **(b)**

-5.1 -3.5 -2.2 -1.5 -1.0 -0.5 0.5 1.0 1.5 2.0 3.0 5.0   -5.1 -3.5 -2.2 -1.5 -1.0 -0.5 0.5 1.0 1.5 2.0 3.0 5.0
$\delta C/C$ (%) $\delta C/C$ (%)
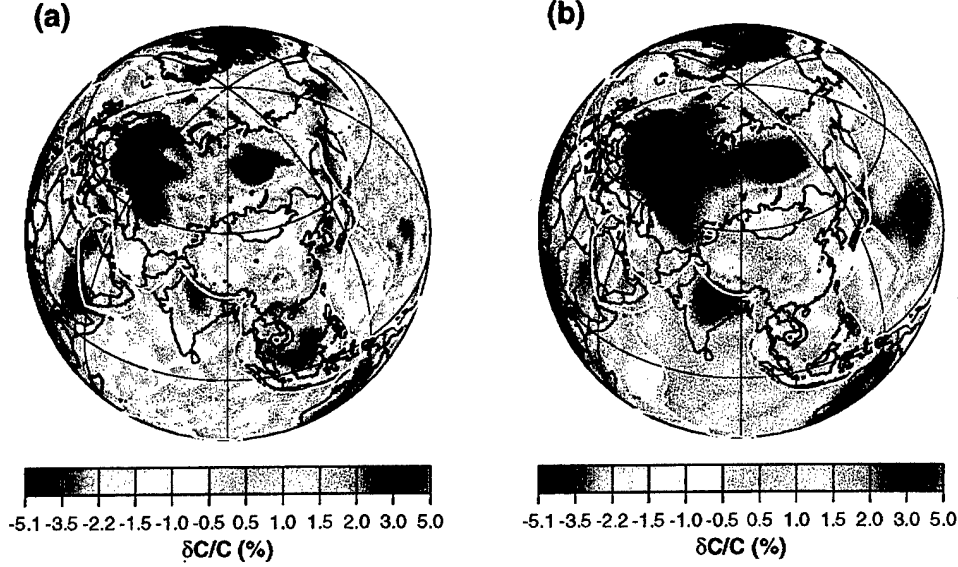
Figure 6. (a) Global 100 s Rayleigh wave phase velocity map estimated with the procedure described in this section using the data of Trampert and Woodhouse (1995, 1996). (b) Trampert and Woodhouse's map using a degree 40 spherical harmonic parameterization using the same data as in (a).

where U_0 is isotropic group velocity at spatial point $\mathbf{r} = (\theta, \phi)$, U_1 and U_2 define the 2ψ part of azimuthal anisotropy, and U_3 and U_4 the 4ψ part of azimuthal anisotropy.

Figure 7 presents examples of the 2ψ component of group velocity azimuthal anisotropy for the 50 s Rayleigh wave across Antarctica and the surrounding oceans. We took the approximately 2200 observations and divided them into two separate sets of about 1100 measurements each which we then inverted separately for the two maps in Figure 7a,b. Both maps display spatially smooth anisotropy patterns, and the fast axes at many locations tend to be parallel to the directions of plate motions. The main features of the maps are similar, but there are differences in detail. In order to quantify the correlation between these two 2ψ maps we use the coherence function defined by Griot *et al.* [1998] which takes into account differences in the fast axes directions $(\alpha_1(\theta, \phi), \alpha_2(\theta, \phi))$ and the amplitudes $(A_1(\theta, \phi), A_2(\theta, \phi); A = (U_1^2 + U_2^2)^{1/2})$ of the two maps. The coherence K as a function of rotation angle α, varying between $-90°$ and $90°$, is defined as follows:

$$K(\alpha) = \frac{\sum_\theta \sum_\phi A_1(\theta, \phi)\, A_2(\theta, \phi)\, \sin\theta\, \exp\left(-\frac{(\alpha_1(\theta, \phi) - \alpha_2(\theta, \phi) + \alpha)^2}{2 D_{cor}^2}\right)}{\left(\sum_\theta \sum_\phi \sin\theta\, A_1^2(\theta, \phi)\right)^{1/2} \left(\sum_\theta \sum_\phi \sin\theta\, A_2^2(\theta, \phi)\right)^{1/2}}. \tag{38}$$

Here D_{cor} is the uncertainty in the anisotropic direction, and was set to equal $10°$. The resulting curve is shown in Figure 8. It is evident that the two maps are correlated, and the average absolute difference in orientation of the fast axes across the maps is less than $20°$. The low value

17
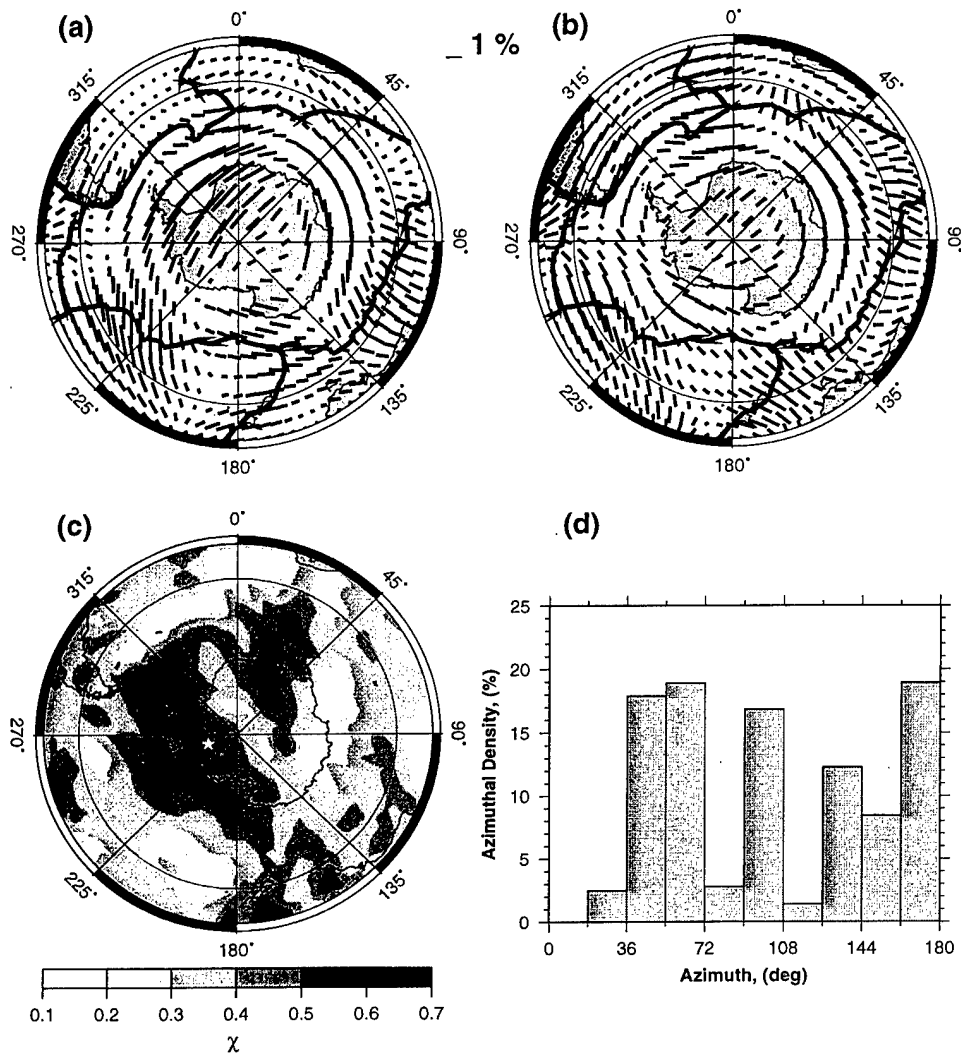
Figure 7. (a) and (b). The 2ψ component of the 50 s Rayleigh wave group velocity anisotropy across Antarctica and the surrounding oceans. Results from two equal data subsets of about 1100 measurements each are shown for comparison. (c) Distribution of the function $\chi(\theta, \phi)$ characterizing the azimuthal coverage for the whole set of 2200 Rayleigh wave paths. (d) Histogram of azimuthal distribution at the fixed point $\theta = 173°$ (83°S), $\phi = 267°$ (93°W) shown by the star in (c).

18
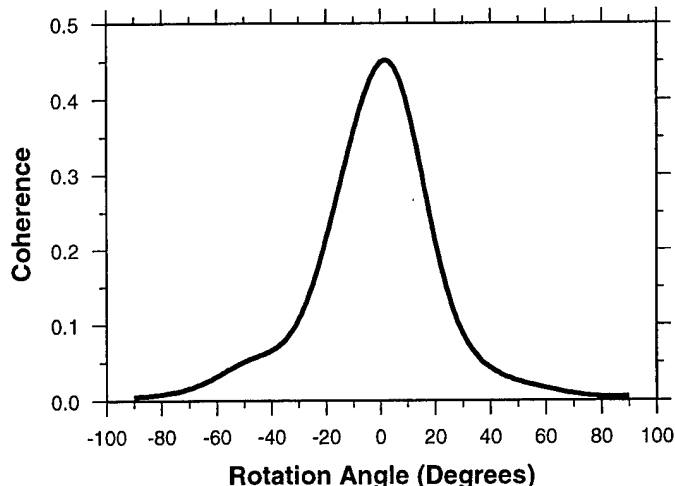
Figure 8. Coherence as defined by Griot *et al.* (1998) between the two 2ψ anisotropy maps shown in Figure 7.

of the maximum coherence (~ 0.45) reflects differences in amplitudes of the anisotropic coefficients between the two maps.

The azimuthal coverage of the region is illustrated by Figure 7c where the behavior of the function $\chi(\theta, \phi)$ defined by Equation (20) is shown. The area in which $\chi > 0.3$ covers about 60% of the region. An example of a histogram of azimuthal distribution for a single point is shown in Figure 7d. In the vicinity of this point, $\chi = 0.53$ which indicates a small azimuthal gap and acceptable azimuthal coverage.

The estimated maps, in addition, correlate fairly well with the global phase velocity maps of Trampert and Woodhouse (1996), particularly for the Rayleigh 50 s and 100 s period maps, but there are notable differences.

In summary, across Antarctica and the surrounding oceans azimuthal anisotropy appears to be a fairly robust observable. Across Eurasia and the Arctic this is not true, however. We find that similar data subsetting and arbitrary changes in damping and parameterization can produce substantial changes in both the pattern and amplitude of the estimated anisotropy (e.g., Levshin *et al.*, 2001). Although azimuthal anisotropy can be rapidly and efficiently estimated with the algorithm described above, it remains a difficult target to estimate reliably with surface wave data, particularly in continental regions.

1.4 Conclusions.

We have described a rapid method for constructing surface wave tomographic maps on local, regional or global scales. Extensive testing of this technique on data sets obtained from a variety of regions around the globe have confirmed its efficiency in producing detailed and reliable surface wave group and phase velocity tomographic maps together with useful measures of map quality.

19

Section 2
Source Effects on Surface Wave Group Travel Times and Group Velocity Maps

2.1 Introduction.

Surface wave tomographic studies are commonly based on phase and group velocity dispersion measurements (e.g., Zhang & Tanimoto, 1993; Wu & Levshin, 1994; Trampert & Woodhouse, 1995; Laske & Masters, 1996; Curtis & Woodhouse, 1997; Wu et al., 1997; Ritzwoller & Levshin, 1998; Ritzwoller et al., 1998). Two distinct approaches to such measurements are in practice today. The first is based on direct measurements of surface wave functionals such as phase and group velocities, particle motion (ellipticity, polarization), and amplitudes as functions of period (e.g., Knopoff, 1972). The second is based on waveform fitting (e.g., Woodhouse & Dziewonski, 1984; Nolet, 1987; Snieder, 1988) in which phase velocity curves, phase velocity maps, or seismic models of the Earth are iteratively improved by comparing synthetic waveforms to observations.

In the first, and more traditional, approach apparent surface wave velocities may be distorted by the effect of the so-called 'source phase' (e.g., Knopoff & Schwab, 1968). The source phase is the phase of a complex excitation function produced by convolving the components of the strain tensor carried by a given surface wave and evaluated at the source depth with the elements of the moment tensor. This function is one of several factors that define the surface wave spectrum (e.g., Gilbert, 1976; Aki & Richards, 1980). The nature of this excitation function, and consequently its phase, depends on frequency, source mechanism, depth, and the seismic structure of the medium near to the source. Source phase is an initial phase that introduces a temporal shift in the measurement of a phase time and, hence, a perturbation in phase velocity. We call this shift the 'source phase time' (SPT) shift. In addition, there is an associated shift in group time which produces a perturbation in group velocity. 'Source group time (SGT)' shift is related to the frequency derivative of source phase. If source phase is nearly frequency independent, SGT is very small.

It is commonly reported (e.g., Knopoff & Schwab, 1968) that at periods below about 50 s, source phase depends only weakly on frequency and, hence, SGT shifts at these periods are usually neglected in most group velocity studies. This is, in fact, one of the features that commends the use of group velocity measurements over phase velocities at relatively short periods. Group velocity measurements are not as strongly contaminated by source effects and it is believed that group velocity measurements can be made and used without a knowledge of the source mechanism.

In contrast, the need to introduce SPT corrections into phase velocity measurements has long been recognized (e.g., Knopoff & Schwab, 1968; Panza et al., 1973) and is now a part of most processing routines. If the source mechanism and a regional model of the medium near to the source are known, it is possible to compute the necessary phase corrections and to remove them from phase measurements leaving only perturbations in phase produced during the propagation of the wave. The main difficulty in applying source phase corrections is the inherent inaccuracy of estimates of the source depth and mechanism. This information is commonly taken from global

catalogs such as the Harvard Centroid Moment Tensor (CMT) catalog (e.g., Dziewonski et al., 1981). The accuracy of depth and moment tensor estimates presented in such catalogs depends strongly on the magnitude, spatial location, and depth of an event. The relative accuracy of depth estimates is particularly poor for crustal events in coarsely instrumented regions. Muyzert & Snieder (1996) analyzed the effect of uncertainties in source depth and source mechanism on phase velocity corrections and found that this effect is significant, especially for Rayleigh waves.

Although group velocities probably remain somewhat less used than phase velocities they are commonly utilized in the analysis of small regional events, in seismic verification research (e.g., Stevens & Day, 1985), and, recently, at long periods for the study of the crust and upper mantle (e.g, Ritzwoller & Levshin, 1998). There are several different techniques for obtaining such measurements; all involve direct measurements made on the observed seismogram and use some kind of windowing of the observed signals in the time, frequency, or a time-frequency domains to suppress interference from unwanted signals (e.g., Landisman et al., 1969; Dziewonski et al., 1969; Knopoff, 1972; Levshin et al., 1972, 1989, 1992; Russell et al., 1988; Ritzwoller et al., 1995). No a priori model of the medium of propagation is needed for such measurements, and most of these methods do not include any model fitting procedures. Source corrections for group velocity measurements are commonly considered to be negligibly small and have not been applied to observed group velocities in most of related studies. Exceptions are Cara & Hatzfeld (1976) who noted that SGT is zero only for particular source mechanisms and Jimenez at al. (1989) in which the authors analyzed the importance of such corrections in determining selected source mechanisms. Calcagnile et al. (1982) and Vdovin et al. (1999) aplied SGT corrections in their structural studies. However, taking into account the growing use of broadband group velocity data in modern surface wave tomographic studies aimed at obtaining detailed and reliable 3D structure of the Earth's lithosphere, we believe that it would be useful to investigate the accuracy of the approach neglecting SGT corrections. We will limit our discussion to Rayleigh waves, as our calculations have shown that for Love waves the SGT is negligible in the period band (10 - 200 s) and source depth range (0 - 200 km). We also ignore here effects caused by the finite duration and finite size of earthquake sources. These effects are usually strongly diminished by using CMT centroid estimates (Dziewonski et al., 1981) as the source time and spatial coordinates instead of hypocenter determinations. The estimates of possible bias in group velocity tomographic maps introduced by errors in event locations were presented earlier in Ritzwoller & Levshin (1998).

The goal of this section is to evaluate the possible effects of source group time (SGT) on group velocity measurements and tomographic maps constructed by inverting Rayleigh wave group velocity data. We will estimate the range of periods and source depths for which corrections due to SGT are negligible or practically nonessential in comparison with the inherent inaccuracy of the group velocity measurements and CMT solutions.

2.2 Theoretical Background.

The asymptotic formalisms defining surface wave waveforms and spectra in laterally homogeneous media and smoothly laterally inhomogeneous media are summarized briefly in the Appendix A. The expressions for the source phase and the source group time shift for a given surface mode in a laterally homogeneous halfspace are given by formulas (A2.16, A2.17, A2.22, A2.23). In the case of a smooth laterally inhomogeneous medium, these functions are described by similar formulas.

To estimate the validity of these asymptotic formulas, we computed a set of theoretical

21

seismograms of the fundamental Rayleigh wave for several events from the Harvard CMT catalog at several stations of the Global Seismic Network. We used a nonasymptotic normal mode representation of the seismic wave field in a spherically symmetric isotropic earth model (Gilbert & Dziewonski, 1975). After converting seismograms to the spectral domain and correcting unwrapped phase spectra for the phase delay due to propagation, we found source phases and source group times for different source-station geometries. Figure 9 demonstrates the similarity of the SGT obtained from the normal mode synthetics with results of calculations using the asymptotic formulas for the same combination of earth and source parameters, and the source-receiver geometries. All calculations are performed for three events from the Harvard CMT catalog (1 - 1/01/96, Sulawesi; 2 - 10/09/96, Cyprus; 3 - 10/23/96, Philippines) at two recording stations in Eurasia (OBN and PAB). Differences between asymptotic and nonasymptotic c urves are negligibly small (less than 3 s) in all cases. The asymptotic description of SGT is accurate enough for our purposes in the whole period range, as the difference between the asymptotic and nonasymptotic SGT values is less than 2-3 s everywhere.

Averaging results of similar calculations for four different events and ten stations provided the statistical support for this conclusion. The rms values of this difference change from 0.3 s at 40 s period to 2 s at 200 s period. This means that for an epicentral distance of 3000 km at period 100 s, the error in estimating group velocity using the asymptotic formalism is on the order of 0.15%, and for 6000 km on the order of 0.08%, which is at least one order of magnitude less than measurement errors (Ritzwoller & Levshin, 1998), One should note that the stationary phase approach described in the Appendix (formulas A2.18 - A2.21) is not valid at frequencies where the amplitude spectrum is changing rapidly (e.g., Pekeris, 1948), such as near nodes in the radiation pattern or near so called 'spectral holes' where spectral amplitudes sharply decrease. Such changes are usually accompanied by a jump of π in phase. This means that the phase derivative with frequency does not exist locally. As a result, the numerical implementation of the asymptotic formalism can produce the physically unreasonable values of SGT near the π phase jumps. Such nonphysical values of SGT do not appear in measurements made on the normal mode synthetics due to averaging with frequency in the measuring procedure. The group times determined from the observed seismograms are also free from such physically unrealistic anomalies. This means that we need to be careful to exclude such singularities in the SGT corrections from consideration in our study.

2.3 Effects of Source Mechanism and Depth on Source Group Time Delays of Rayleigh Waves.

As shown in the Appendix, SGT depends on several factors. For a given model of a laterally homogeneous or smooth laterally inhomogeneous medium, SGT is a function of the period T, the source depth h, the source mechanism (i.e., seismic moment tensor $\mathbf{M}$), and the source-receiver geometry; namely, the angle ψ between the strike of the fault and the direction from the epicenter to a station. Because the last factor varies widely from station to station and from event to event, we will consider the pattern of SGT for all possible values of ψ ($0° \leq \psi < 360°$) as a function of T and h. We will limit ourselves to consider only double-couple source mechanisms.

As an organizational device we use a triangle of source mechanisms suggested by Kaverina et al., (1996). This condensed representation allows us to map all possible double-couple type mechanisms irrespective of the strike orientation, using the values of the plunges for their P, T, and N axes, into an area limited by an isosceles triangle (Figure 10). Vertices N, T, and S

22
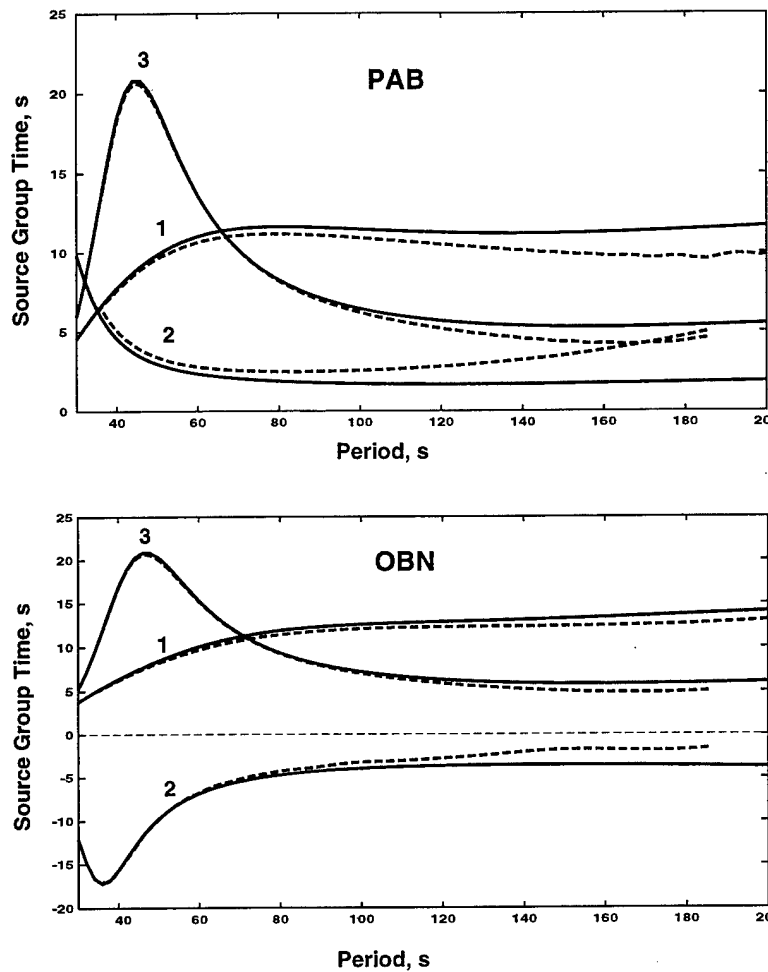
Figure 9. Comparison of two types of computed source group time curves. Curves of the first type (solid lines) are from the asymptotic formalism in the Appendix A. Curves of the second type (dashed lines) are found by the spectral analysis of synthetic seismograms obtained by nonasymptotic normal mode summation.
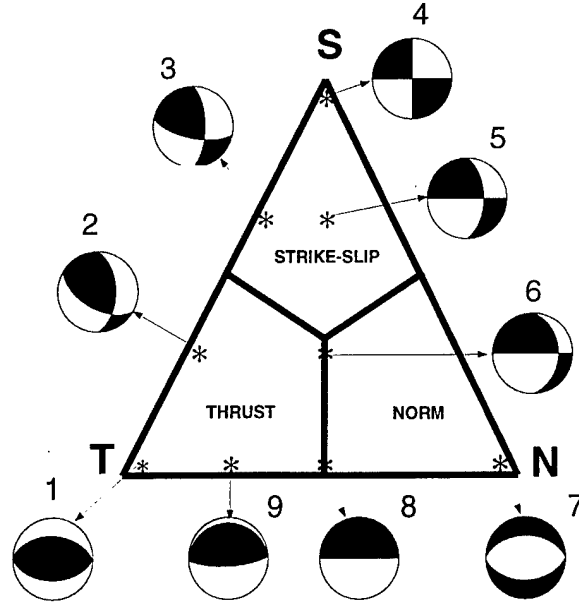
Figure 10. Triangle representation of source mechanisms. Stars indicate positions of selected mechanisms inside the triangle (Kaverina *et al.*, 1996). T, S, N denote thrust, strike-slip, and normal.

(Figure 10) of this triangle correspond, respectively, to a normal fault, a thrust fault along the 45°-dipping plane, and a pure strike-slip fault along a vertical plane. Bisectors divide this triangle into three parts according to the predominant type of mechanism, as labeled on Figure 10.

Selected types of mechanisms, whose positions inside the triangle are indicated by asterisks, are shown on the same figure. Because a change in the sign of the slip direction does not change the absolute value of the SGT, it is sufficient to consider mechanisms belonging to the left half of the triangle.

To estimate how different source mechanisms are represented in world seismicity and in a subset of events used for the Eurasian surface wave tomography (Ritzwoller & Levshin, 1998), we show in Figure 11 maps of the density of events inside the source triangle for several source depth intervals: 0 - 20 km, 20 - 40 km, 40 - 60 km, and 60 - 100 km from the CMT catalog and from the tomographic subset. Event density is defined in percent as $N_c(x,y)/N_d^i$, where $N_c(x,y)$ is the number of events in a circle of fixed radius with a center at the point (x,y) inside the triangle, and N_d^i is (the number of events inside the i-th depth interval) × (the relative area of the circle). The size of the chosen circles and the number of events for each depth interval are shown in the figure.

Both sets of diagrams show that for shallow source depths, strike-slip and normal events are as common as thrust events. When the source depth increases, the dominant type of mechanism is a thrust. Earthquakes with mechanisms in the central part of the triangle are rare.

Before we start to analyze effects of source mechanisms on source group times we should note that mechanisms 1, 4, and 7 at the vertices of the triangle present extreme (degenerative) cases

24

CMT Catalog 77-97   **CU Eurasia 88-96**

DEPTHS

0 - 20 km   6181   382

20 - 40 km   2643   207

40 - 60 km   1439   70

60 - 100 km   974   10

0   2   6   10   20   50
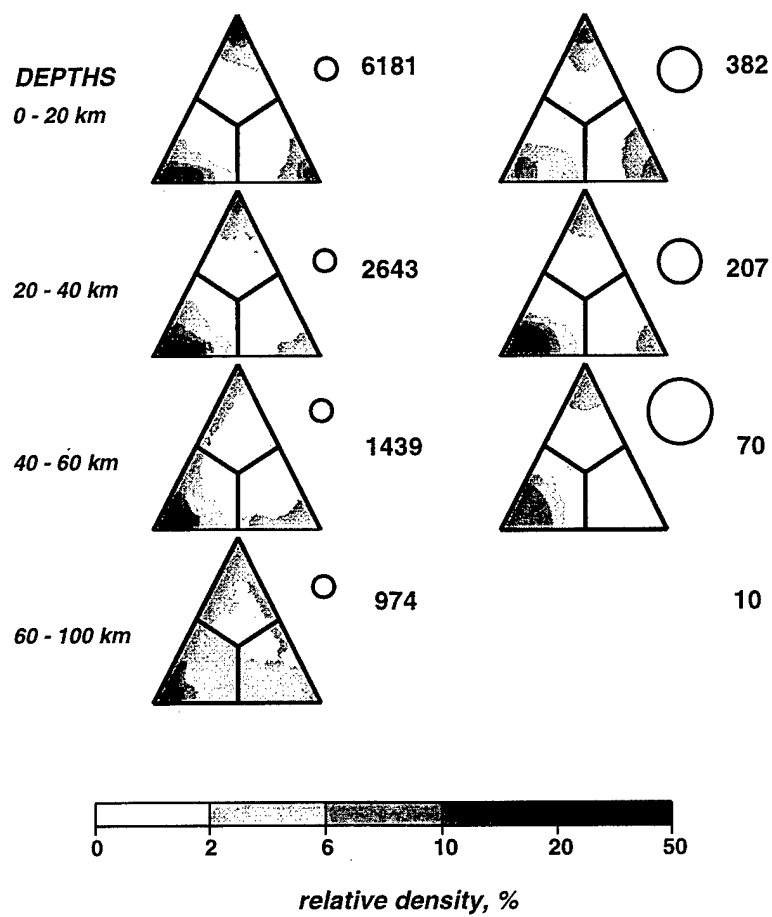
relative density, %

Figure 11. Maps of the relative density of events inside the triangle for several source depth intervals.

25
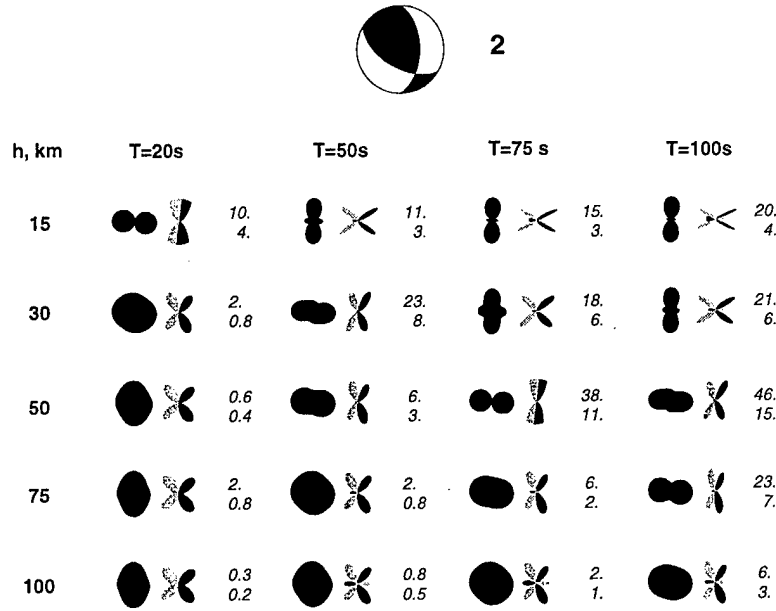
Figure 12. Amplitude radiation patterns and $SGT(\psi)$ diagrams of Rayleigh waves for source mechanism 2 shown on the top of the figure, at four different periods and five different source depths.

for which source phase does not change with frequency (except the jumps in π at the nodes of the radiation pattern). Consequently, the SGTs for these sources are zero independent of the azimuth of radiation. However, even in the near vicinity of these points inside of triangle we find significant nonzero SGT. Figure 12 displays normalized amplitude radiation patterns and patterns of the $SGT(\psi)$ for the fundamental Rayleigh wave in a slightly modified PREM model (Dziewonski & Anderson, 1981) in which the water layer is replaced by a layer of soft sediments. Each figure corresponds to one of three selected source mechanisms indicated by numbers 2, 3, and 9 in Figure 10. The selection is based on the conclusions regarding the prevailing types of the source mechanisms among events with known CMT solutions and degeneracy at the vertices mentioned above. The associated focal mechanisms ('beachball' images) are shown at the top of each figure. The left column for each period-depth pair represents amplitudes normalized by the maximum value with azimuth, the middle column represents the SGT pattern (black filling is for positive values and grey filling is for negative values). The third column presents normalization information.

We observe a great diversity of SGT patterns for different periods, source depths and mechanisms. They are much more complex than amplitude radiation patterns for two main reasons. First, as mentioned earlier, the source phase may have a jump of π with period near the nodal planes of radiation. Second, the phase changes with period may be much more rapid than the amplitude changes at some azimuthal directions.

A fault with a dominant vertical slip ('beachballs' 1, 7, 8, and 9 in Figure 10) is characterized by zero or relatively small SGT values for practically all period-depth pairs. Strike-slip and thrust

26
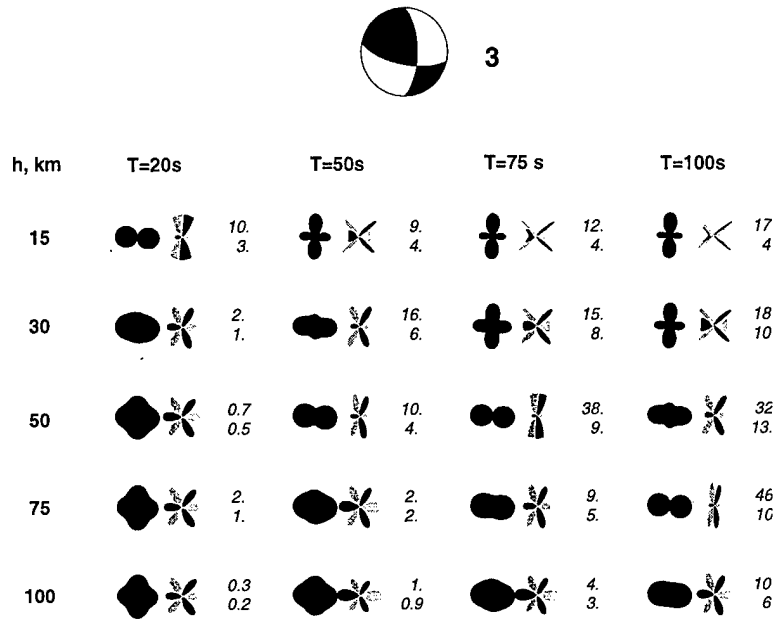
Figure 13. Same as Figure 12, but for source mechanism 3.
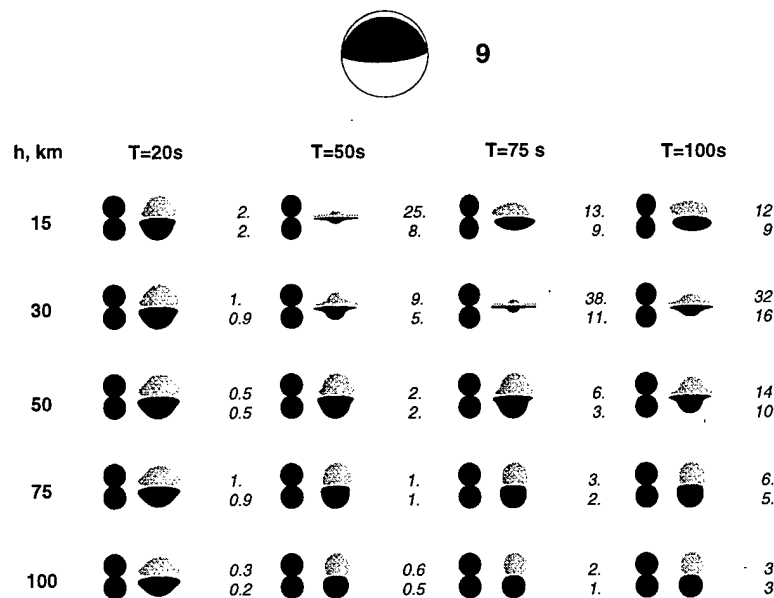
Figure 14. Same as Figure 12, but for source mechanism 9.
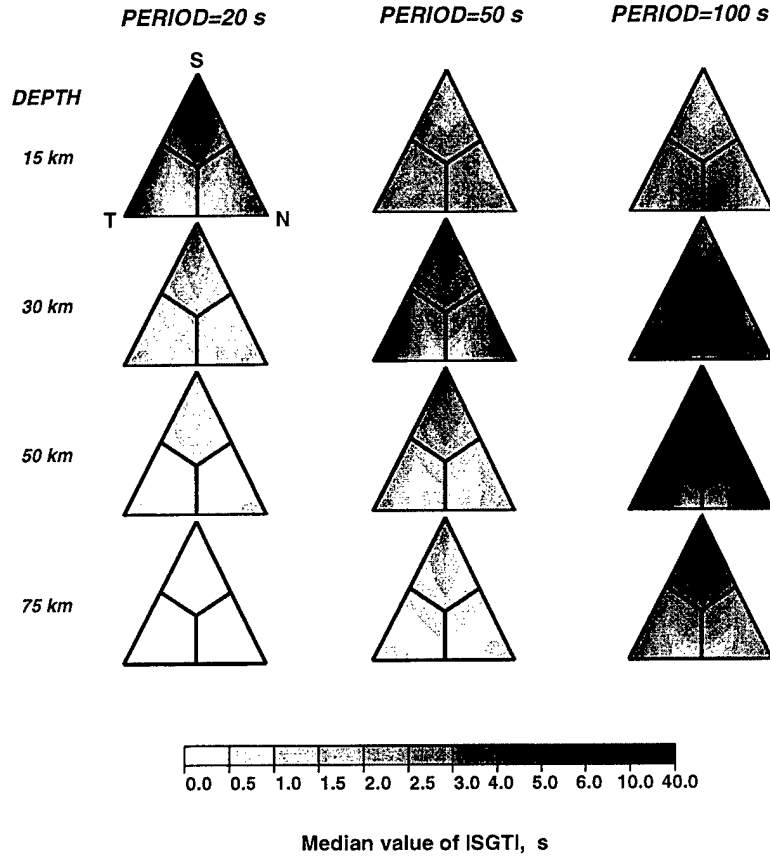
Figure 15. Maps of median values, $\bar{S}$, of $|SGT(\psi)|$ across the source triangle for periods 20, 50, and 100 s. Median values for periods 20 and 50 s are below 12 s and decrease as the source depth increases. For the 100 s period median values are above 10 s for a significant part of the source triangle and increase with depth.

faults along inclined fault planes have the most significant SGT at periods above 75 s.

The average characteristics of SGT for different periods and source depths may be summarized in different ways. We found the median values, $\bar{S}$, of the magnitude of the source group time as a function of azimuth ψ incremented by 1° to be a useful average. We mapped $\bar{S}$ across the whole source triangle for a set of periods and depths. The resulting maps are shown in Figure 15.

For periods less than about 75 s, median values are less than 10 s for essentially all depths and source mechanisms and decrease with depth. For periods of 75 s and above, there are areas inside the source triangle with relatively high median values, especially for strike-slip faults along inclined planes at depths greater than 50 km.

A more general conclusion about typical values of the magnitude of the source group time is obtained by finding and averaging median values $\bar{S}$ for all events in the CMT catalog sorted by the depth into four source depth intervals, namely, 0 - 20, 20 - 40, 40 - 75, and 75 - 200 km. The resulting curves for the four source depth intervals are shown in Figure 16. Very similar curves
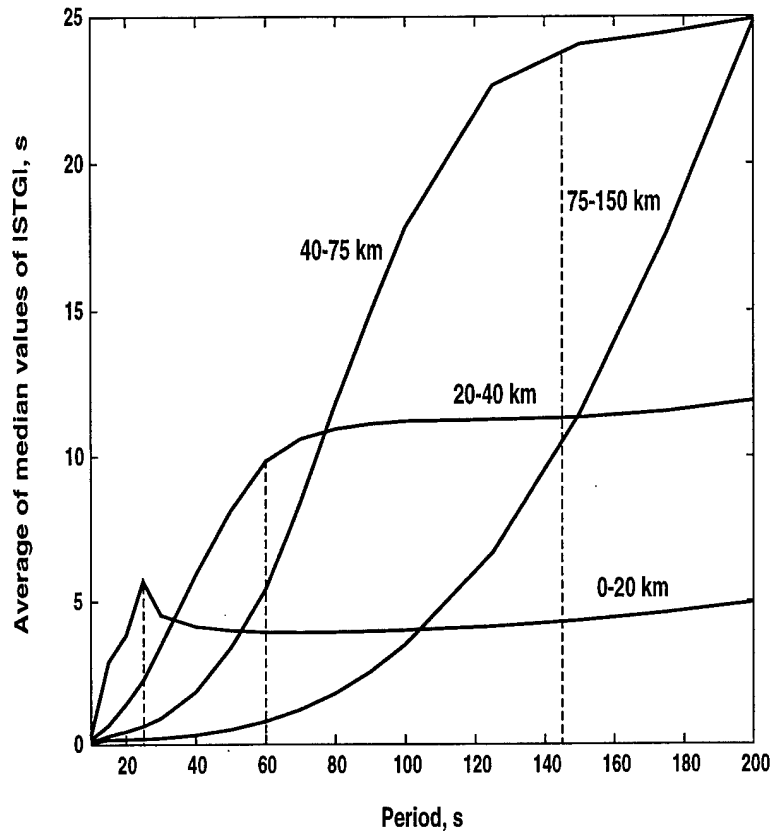
Figure 16. Averages of median values of $|SGT(\psi)|$ for events at different depth intervals (all events from the Harvard CMT catalog for January 1977-November 1997). The dashed lines divide parts of curves with different dependence on period: fast growth with increasing period to the left of the dashed line, and slow changes to the right of this line.

are obtained for events used for Eurasian tomography.

The behavior of all four curves is similar. They are characterized at short periods by a rapid increase in average median value (AMV) with period, followed, after passing through a narrow inflection zone, by much slower changes. Shallow events (with source depths less than 20 km) are characterized by an AMV less than 5 s and the central period of the inflection zone at about 20 s. The AMV for events with source depths between 20 and 40 km is less than 12 s everywhere, grows rapidly with period, and stabilizes at a level of about 12 s at periods longer than 60 s. · Events at depths between 40 and 75 km are characterized by an AMV below 10 s for periods below 75 s, rising to 20-25 s at periods above 100 s. For deeper events (75-100 km), the 10 s level of the AMV is reached at a period of about 140 s, and the 25 s level at 200 s period (the right end of period range considered.) Notice that events with depths greater than 40 km, which produce large SGT, are relatively rare in data sets which are normally used for fundamental mode group velocity measurements, such as events in the CMT catalog or the Eurasian tomography data set. This is illustrated by Figure 17 which presents histograms of source depths for events from the CMT catalog and events used for group velocity tomography of Eurasia for source depths less

29

than 200 km.

2.4 Distortions of Tomographic Images Due to Neglecting SGT.

As we have shown in the previous section, SGT corrections are appreciable, especially at periods more than 75 s and for source depths more than 25 km. As they are usually neglected in tomographic studies, it is important to understand the level of bias produced in tomographic group velocity maps by neglecting SGT corrections. We performed several synthetic tests to estimate this bias. In these tests we used the same set of Rayleigh wave paths as in the tomographic inversion performed by Ritzwoller & Levshin (1998). Instead of the observed group velocity we assigned to each ray the same fixed value of group velocity and then corrected it for the predicted group time shift. Thus for the ith ray and the period T_j we have

$$\mathcal{U}_i(T_j) = \Delta_i/[(\Delta_i/\mathcal{U}_r(T_j)) - S_i(T_j)],$$

where Δ_i is the length of the ith ray in km, and $\mathcal{U}_r(T_j)$ is the fixed reference velocity.

As discussed in Section 2.2, the asymptotic formalism does not provide an accurate description of the wave field near nodes of source radiation patterns and inside of 'spectral holes'. As a result, calculations based on asymptotic formulas (A2.22-A2.23) may predict for certain azimuths and periods unreasonably large and physically unjustified magnitudes of the SGT. To deal with this problem we introduced some *ad hoc*, but reasonable, empirical rules to identify and discard or reduce erroneous SGT corrections. These rules are based on using a parameter describing the distribution of magnitudes of SGT for a given source in the entire azimuth range, $0° \le \psi < 360°$, to calibrate the predicted value for a given ray. We chose the median value, $\bar{S}$, of the magnitude of the SGT correction, $|SGT(\psi)|$, with ψ incremented by $1°$ degree to be this parameter. If the predicted magnitude of the SGT for a given ray and period is above some multiple of $\bar{S}$, the SGT correction is discarded and the observation is rejected. If the predicted magnitude of SGT is less than this limit but still above some smaller multiple of $\bar{S}$, the magnitude of SGT will be reduced to this smaller multiple but the sign of predicted SGT will be preserved. In formal terms these rules are: (1) the observation for the ith ray at period T_j is rejected if $|SGT_i(T_j)| \ge K_1\bar{S}(T_j)$, (2) the magnitude of $SGT_i(T_j)$ is reduced to $K_2\bar{S}(T_j)$ if $K_2\bar{S}(T_j) < |SGT_i(T_j)| < K_1\bar{S}(T_j)$. We chose coefficients K_1 and K_2 to equal, respectively, 5 and 3. The application of such rules to our data caused the rejection of 1-2% of the observations and a reduction in the SGT corrections to yield a change in the values of the group velocities for another 3-4% of all observations.

Tomographic images for this synthetic input data set demonstrate the level of group velocity anomalies produced by uncorrected source group times. Figures 18a-b present such images for the Eurasian tomography Rayleigh wave data at periods 20 s and 50 s. The maximal anomalies for 20 s are of the order of 2.5%, for 50 s are less than 2%, and for 100 s are less than 5%. Significant anomalies dominantly are confined to the periphery of the maps (Western Pacific Arc, the Philippine Sea, Indochina). Even at 100 s period, anomalies across most of Eurasia are less than 1%. The maximum signal related to the lateral inhomogeneity of the crust and the upper mantle is on the order of 20% for 20 s - 50 s period, and 5 - 8% for 100 s period (Ritzwoller & Levshin, 1998). This means that by neglecting SGT we do not significantly distort the tomographic images, except in marginal areas at long periods. This is understandable because SGT corrections vary in sign and magnitude from one seismic zone to another, and their effect averages nearly to zero for internal regions crossed by many differently oriented paths. Only for the rim of Eurasia,
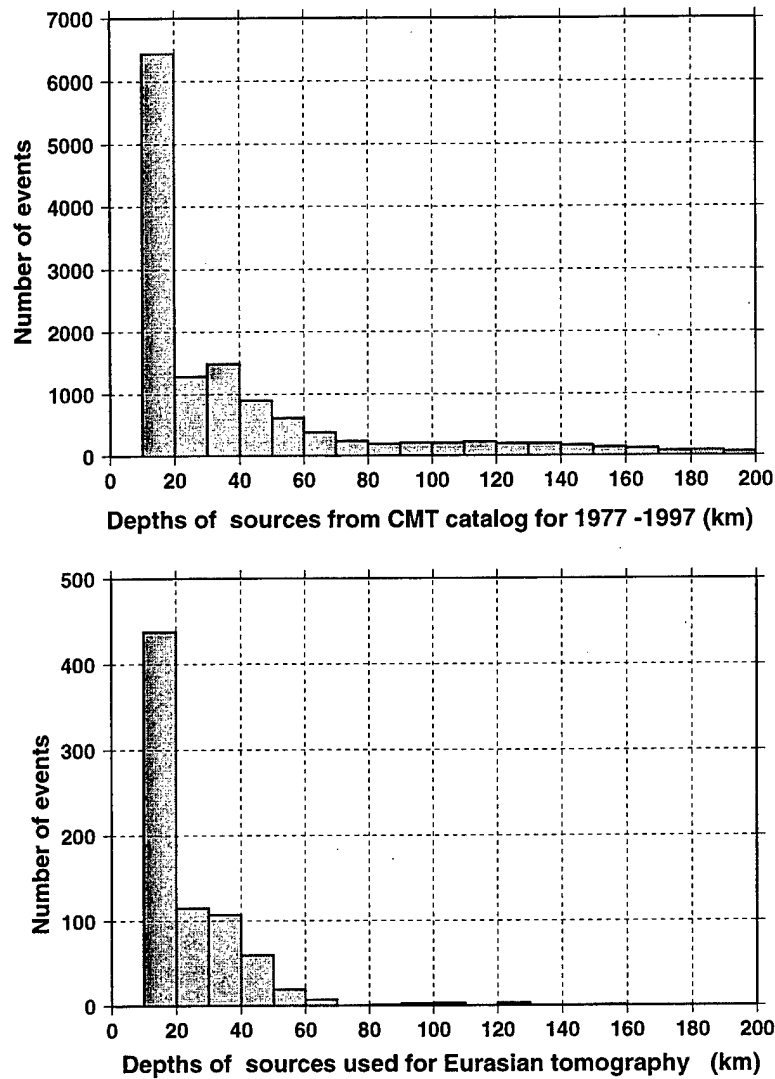
Figure 17. Histograms of source depths in the depth interval 0 - 200 km. (Top) For all events from the Harvard CMT catalog from January 1977 to November 1997. (Bottom) For events used for Eurasian surface wave tomography (Ritzwoller & Levshin, 1998). The fraction of events with depths greater than 40 km used in surface wave tomographic studies is much smaller than in the CMT catalog.

31

where most of paths begin or terminate, and the number of crossing paths is very small, are the effects of uncorrected SGT relatively important. This is especially true at long periods.

2.5 Sensitivity of SGT Corrections to Source Characteristics.

As shown at Section 2.3 the magnitude of SGT can easily be above 10 - 15 s for periods above 75 s and source depths larger than 25 km. This means that some of observed group velocities uncorrected for SGT may be appreciably distorted. At the same time the tomographic experiment based on the Eurasian tomographic data set discussed in Section 2.4 demonstrated the existence of appreciable bias due to uncorrected SGT at the rim of the continent. These results imply that it may be advisable to apply SGT corrections in group velocity studies.

To evaluate the practical importance of applying SGT corrections we consider data obtained from adjacent ray paths (Ritzwoller & Levshin, 1998). Measurements whose path endpoints lie within 2% of the path length are grouped to produce a 'cluster' of dispersion curves. Averaging the curves composing the cluster provides an average cluster dispersion curve. To exemplify the effects of uncorrected SGT on group velocity measurements we selected several clusters of seismic events and several recording stations. For each event and station we compared group velocity curves obtained with and without corrections for SGT. As an example, we show in Figure 19 the rms values of group velocity deviations relative to the average values for two station-event pairs: Eastern Iran to Arti, Russia (ARU), and Kuril Islands to Obninsk, Russia (OBN). In the first case the cluster consists of four events, and in the second case sixteen events. In the first case, SGT corrections increase the rms difference between the measured group velocities in the cluster across wide range of periods. Evidently, introducing SGT corrections increases the level of noise in our data for this cluster of events. In the second case, the introduction of the corrections slightly decreases the rms differences.

More general estimates may be obtained if we average similar results for all clusters present in our Rayleigh wave data for Eurasia. The number of such clusters is quite large (e.g., around 4500 at 40 s period). We compared the average rms deviations between individual group velocities and their cluster averages for corrected and uncorrected data and found the differences between the average rms for all clusters to be very small; namely, less than 0.005 km/s for the entire range of periods. Such small differences are statistically insignificant, being evidently much less than measurement errors and observational errors due to the inaccuracy in the spatial and temporal locations of earthquakes provided by the CMT catalog and measurement errors (Ritzwoller & Levshin, 1998). In addition, there is no systematic decrease of the average rms deviations when SGT corrections are introduced for subsets of data with different ranges of source depths.

The absence of improvements in group velocity cluster rms statistics after introducing SGT corrections requires explanation. We estimated the sensitivity of possible SGT corrections to random errors in source depth and source mechanism. Muyzert and Snieder (1996) took a similar approach for source phase time corrections. Figure 20 demonstrates the magnitude of changes of SGT for two earthquakes from the CMT catalog: on 10/18/1996 in Japan with centroid depth of 22 km (top), and on 1/01/1996 in the Philippines with a centroid depth of 33 km (bottom) for a fixed azimuth (135°) far from the nodal direction of the Rayleigh wave radiation pattern for both events. Figure 20a shows changes in $SGT(T)$ when the depth of the source is changed by ± 10 km. The radiation pattern for 50 s and the azimuthal direction for which the $SGT(T)$ is presented are shown in the upper left corner of each subfigure, and the source mechanisms are
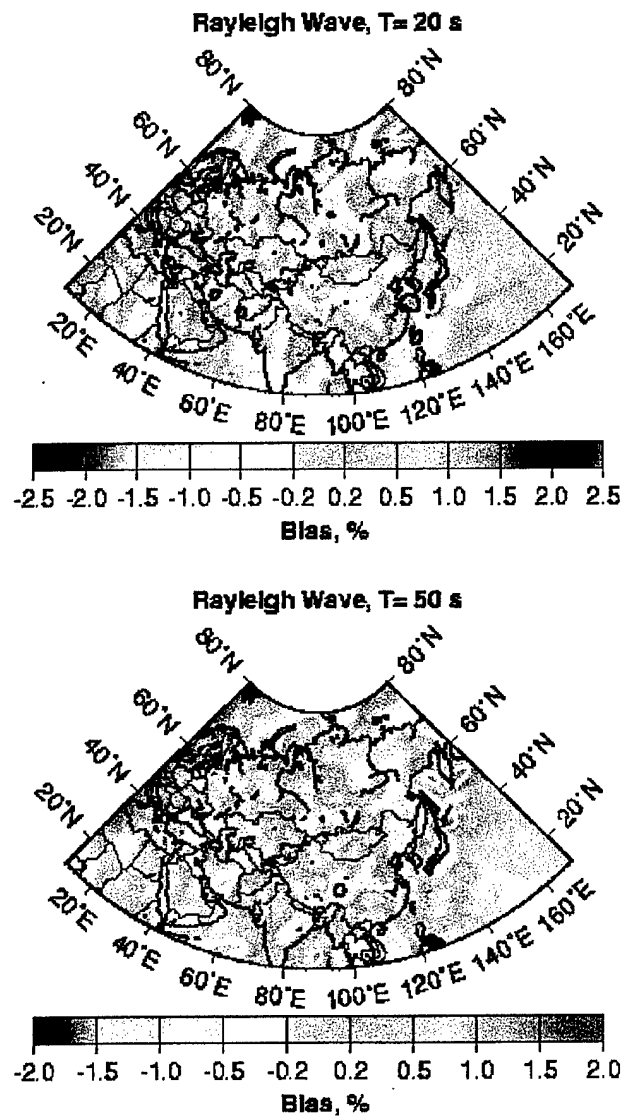
Figure 18. Bias produced by neglecting source group time shift in Eurasian tomographic studies (Ritzwoller & Levshin, 1998.) Significant bias (above 1% of the reference velocity) appears predominantly near the rim of the continent at long periods.
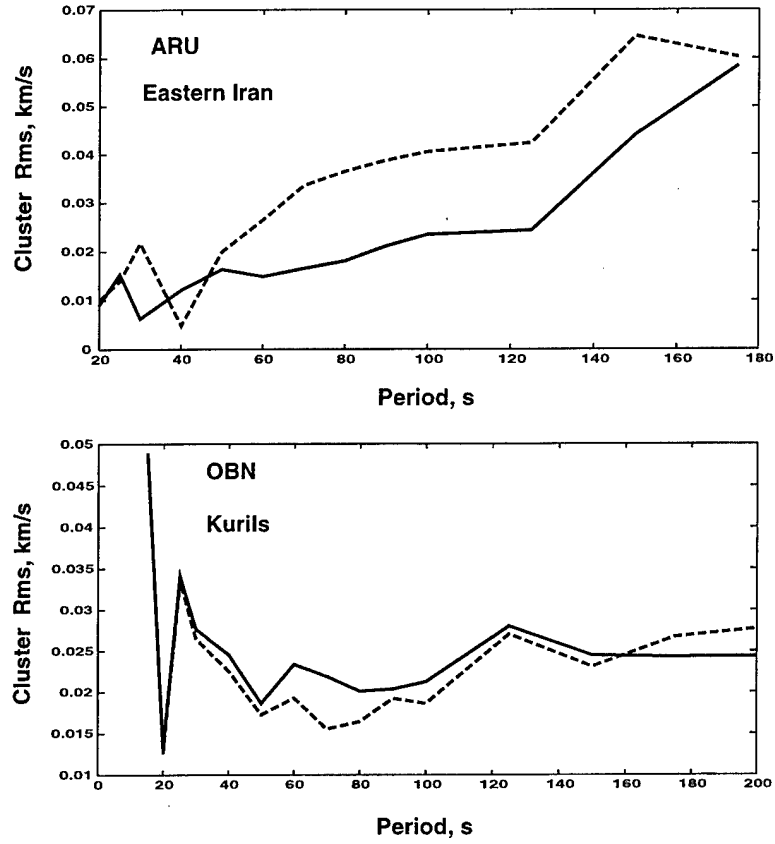
Figure 19. Comparison of rms group velocity deviations from the average Rayleigh wave group velocity curve for two clusters of measurements. (Top) Events in Eastern Iran recorded at the station ARU (Arti, Russia). (Bottom) Events near the Kuril Islands recorded at the station OBN (Obninsk, Russia). Solid lines are for group velocity measurements without source group time corrections applied, and dashed lines are obtained after corrections. No significant decrease in rms due to corrections for SGT is observed.
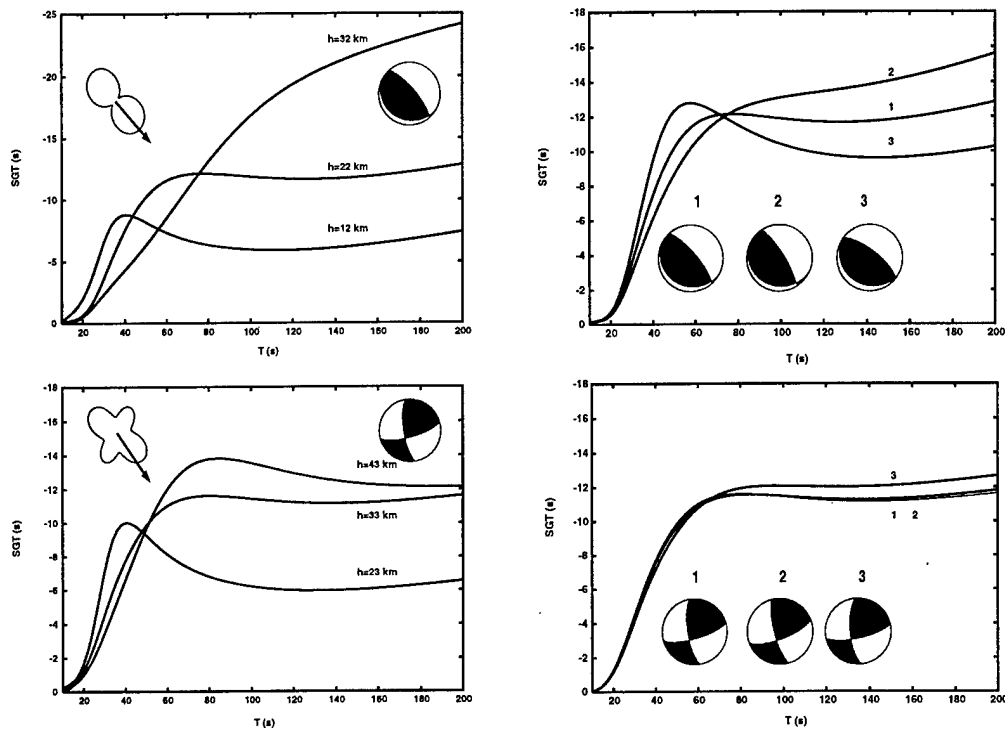
Figure 20. The effects of errors in source depth and moment tensor on SGT for different periods.

shown in the upper right corners. It is evident from this figure that a realistic uncertainty on the order of 10 km in the source depth may produce an effect comparable in size to the magnitude of the SGT correction itself. Figure 20b shows the effect of 20% changes in the values of the components of the moment tensor for these two events (the zero trace of the moment tensor is preserved). Two earthquakes are selected from the CMT catalog: (top) on 10/18/1996, 10h26m at Japan with a centroid depth of 22 km, and (bottom) on 1/01/1996, 22h42m at the Philippines with a centroid depth of 33 km for a fixed azimuth (135°). The left side corresponds to the case when the depth of the source is changed by ±10 km. The source mechanisms are shown at the upper right corners. Significant changes of SGT values due to changes in source depth are seen. The right side corresponds to the case when values of moment tensor components are changed by 20%. Corresponding variations of the source mechanism are shown. Changes of SGT values caused by perturbations of the moment tensor are relatively small

In this case the effect on the SGT is less significant, especially for the second event. Similar numerical experiments with other events lead us to conclude that SGT is strongly sensitive to errors in depth and only weakly sensitive to errors in the moment tensor. It should to be remembered, that this problem is exacerbated by the fact that for many seismic events the data used for finding the CMT solution do not provide adequate depth resolution, and the source centroid depth in the CMT catalog is fixed at 15 km.

It is evident from our experiments that deviations of the real source depth from the CMT value by $\pm 5 - 10$ km probably produce errors in the SGT that vitiate the corrections. Unless source depth is very well known, then, the efficacy of the SGT corrections is compromised and a positive effect of the application of the corrections is far from guaranteed.

2.6 Conclusions.

In this study, we estimated the possible effect of source group time (SGT) on group velocity measurements for fundamental Rayleigh waves generated by double couple type seismic events. We have studied the dependence of this effect on period (10 s - 100 s), source mechanism, and depth (15 km - 100 km). We found that there is a great variability in azimuthal patterns and magnitude of SGT depending on these three factors. Statistics of certain salient functionals that characterize the dependence of SGT on different factors were presented, e.g., the median values of SGT magnitude as a function of azimuth from epicenter to station for different periods, source depths and mechanisms.

The main conclusions of our study are as follows.

1. SGT corrections may be neglected in group velocity measurement for periods less than 75 s and source depths less than 25 km. For longer periods and especially for deeper events SGT corrections are appreciable.

2. The perturbations produced by uncorrected SGT in tomographic inversions of Rayleigh wave group velocity data for the Eurasian continent are generally very small (less than 1% of the unperturbed values), but appreciable perturbations (up to 1-2% for 50 s period and up to 5% for 100 s period) are found near the edge of the continent where ray coverage is poor.

3. SGT corrections are very sensitive to errors in the source depth. If extremely accurate depth determination are available the SGT corrections should be applied at periods above 75 s, especially for events deeper than 25 km. However, taking into account the accuracy of most CMT solutions for earthquake depth and the magnitude of observational errors in measuring group velocities, at present SGT corrections are practically nonessential for group velocity tomographic studies.

Section 3
Effects the Off-Path Propagation on Surface Wave Tomography

3.1 Introduction.

The technique for surface wave tomography described in Section 1 is based on the assumption
that surface waves propagate along the great circle paths connecting epicenters and stations. This
assumption has been used in practically all tomographic studies using surface waves (e.g.,
Woodhouse & Dziewonski, 1984; Montagner & Tanimoto, 1991; Zhang & Lay, 1996; Curtis &
Woodhouse, 1997; Ekstrom *et al.*; Curtis *et al.*, 1998). At the same time, it is well known from
theoretical studies (Woodhouse, 1974; Babich & Chikhachev, 1975; Babich *et al.*, 1976; Levshin,
1985; Levshin *et al.*, 1989; Dahlen & Tromp, 1998) as well as from observations of surface wave
polarization (Levshin *et al.*, 1992, 1994; Pollitz & Hennet, 1993; Laske & Masters, 1996) and
array measurements of azimuthal deflections of surface wave fronts (e.g., Capon, 1970; Bungum &
Capon, 1974; Sobel & von Seggern, 1978, Levshin & Berteussen, 1979; Lerner-Lam & Park, 1989)
that in many cases surface wave paths may significantly deviate from great circles. To study the
effect of these deviations on our surface wave tomographic images in the frame of surface wave ray
theory, we carried out several numerical experiments designed to estimate maximum ray
deviations expected for the Eurasian data set which we used for tomographic inversion. These
experiments included the following stages.

1. Constructing 3D model of the region under study using the set of CU Rayleigh and Love group
velocity maps for periods in the range 15-200 s and global phase velocity maps in the range of
periods from 40 to 200 s provided by Harvard and Utrecht Universities.
2. Calculating phase velocities of Rayleigh waves across the region from the 3D model.
3. Tracing Rayleigh wave rays with given end points from the CU Eurasian data set through the
phase velocity maps. We estimated maximum off-path deviation of the "real" rays from assumed
great circle paths and found corresponding statistics.
4. Calculating average group velocities along the "real" paths using group velocity maps for the
3D model. We obtained the statistics of differences between average group velocities along great
circle paths and "real" paths.

Our analysis of these statistics shows that significant off-path deviations and significant changes
in phase and group velocities occur only for a small percentage of ray paths, mostly with a length
of path above 5,000 km.

3.2 Constructing the 3D Model and Surface Wave Phase Velocity Maps.

Constructing the 3D model from the CU group velocity maps and global phase velocity maps for
a set of periods is described in detail in (Ritzwoller & Shapiro, 2001) as a part of work done under
the contract DTRA 01-99-C-0019. This is done on a regular grid (usually 2x2 degrees). Local
group and phase velocity curves for Rayleigh and Love waves are found for each point of a grid by
extracting velocity values from tomographic maps. Then, the 1D shear velocity structure is found
at each knot of the grid by the Monte Carlo inversion of these curves. Some constraints on P-wave

velocity and density distribution are applied. The median solution found, as a result of the Monte Carlo search is taken as a 1D model at a given point of the grid. Phase and group velocities are calculated at each knot for a set of periods T_j and are then combined in model-predicted phase and group velocity maps $C_j(\varphi, \lambda)$ and $U_j(\varphi, \lambda)$ where φ and λ are latitude and longitude.

3.3 Ray Tracing.

The algorithm developed by Prof. T. Yanovskaya (St.-Petersburg University, Russia), and kindly provided to us by her, was used after some modifications to trace surface wave rays through the set of the 2D phase velocity maps. We selected periods 20 s and 40 s as representative examples for our goals. The mentioned algorithm is a shooting technique which uses the Runge-Kutta integration of 2D ray equations to find the ray starting at the epicenter and coming to the station. The iterative procedure stops if the tentative ray passes close enough to the station, normally at the distance less than 1 km. In some cases, due to the existence of local shadow zones this distance may be increased up to 16 km (still inside the surface wave Fresnel zone for all considered periods). Integration of slowness (inverse of phase velocity $C_j(\varphi, \lambda)$) along the ray, gives a phase travel time t_{ijC} for the ith ray and jth period. The apparent phase velocity for this ray is defined as $C_{ij}^{app} = r_i/t_{ijC}$ where r_{ij} is a length of a great circle path for the ith ray. Projecting this ray on the group velocity map for the same period and integrating the group velocity slowness $1/U_j(\varphi, \lambda)$ along the ray we find a group travel time t_{ijU} for the same ray. The ratio $U_{ij}^{app} = r_{ij}/t_{ijU}$ defines the apparent group velocity for this ray which will be used in tomographic inversion. The relative difference between the apparent group velocity and the group velocity along the great circle path also characterizes the possible distortion of tomographic images.

3.4 Examples and Statistics of Off-path Deviations.

As stated above, we traced a significant subset of the surface wave ray paths used in our group velocity tomography across the phase velocity maps for periods 20 and 40 s. Figures 21 and 22 demonstrate deviations of Rayleigh wave ray paths from great circles in two regions with high lateral gradients of phase velocities, namely Southern Asia and Japan.

The presence of the Tibetan plateau in the first case and of the ocean-continent boundary in the second case and related strong lateral changes of the crustal thickness should have some effect on ray behavior. However, we see that the deviations from great circle paths for a set of rays going parallel to the Tibetan plateau (Figure 21) and to the Japan coast (Figure 22) are relatively small (mostly less than 100 km) for both periods. For rays going in other directions the deviations are practically zero. The length of rays in these examples is less than 2,500 km. When the length of ray increases, deviations may be more significant. Figure 23 demonstrates such deviations for rays whose length is between 5,000 and 10,000 km. For the 20 s period the maximum deviations may be as big as 300 or 400 km. Especially strong deviations are found for those rays whose great circle path crosses big sedimentary depressions (like the Eastern Mediterranean Sea or Black Sea). All deviations decrease with increasing period.

To estimate how typical are these significant deviations of rays from the great circle path and how they depend on the path length, we present several statistics. Figure 24 shows magnitude distribution of maximum deviations for 20 s and 40 s. Figure 25 demonstrates the distance dependence of the maximum deviation for the same periods. Almost all maximum deviations are
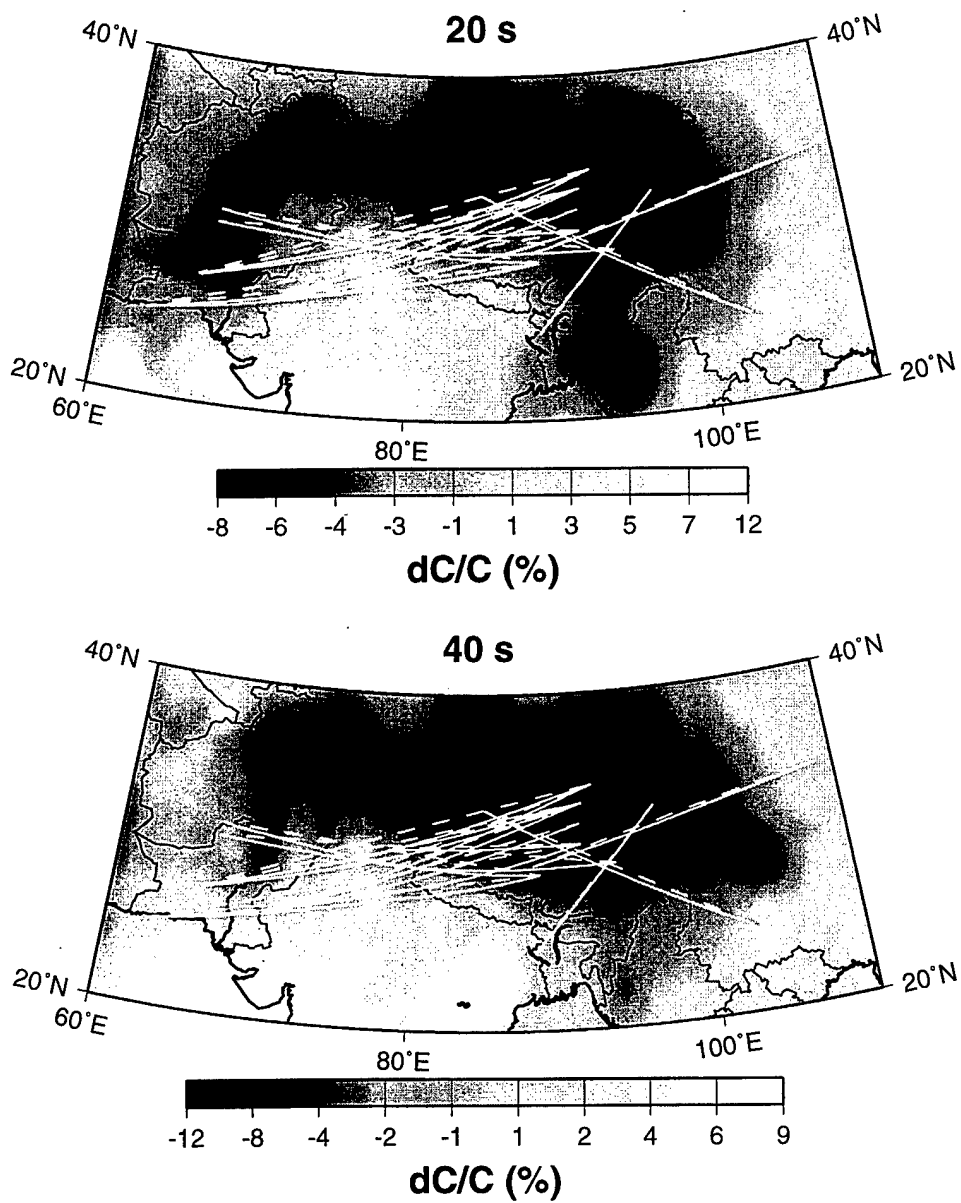
Figure 21. Examples of Rayleigh ray deviations from great circle paths in Southern Asia. Continuous lines are rays traced across the phase velocity map for a given period. Dashed lines are great circle paths.
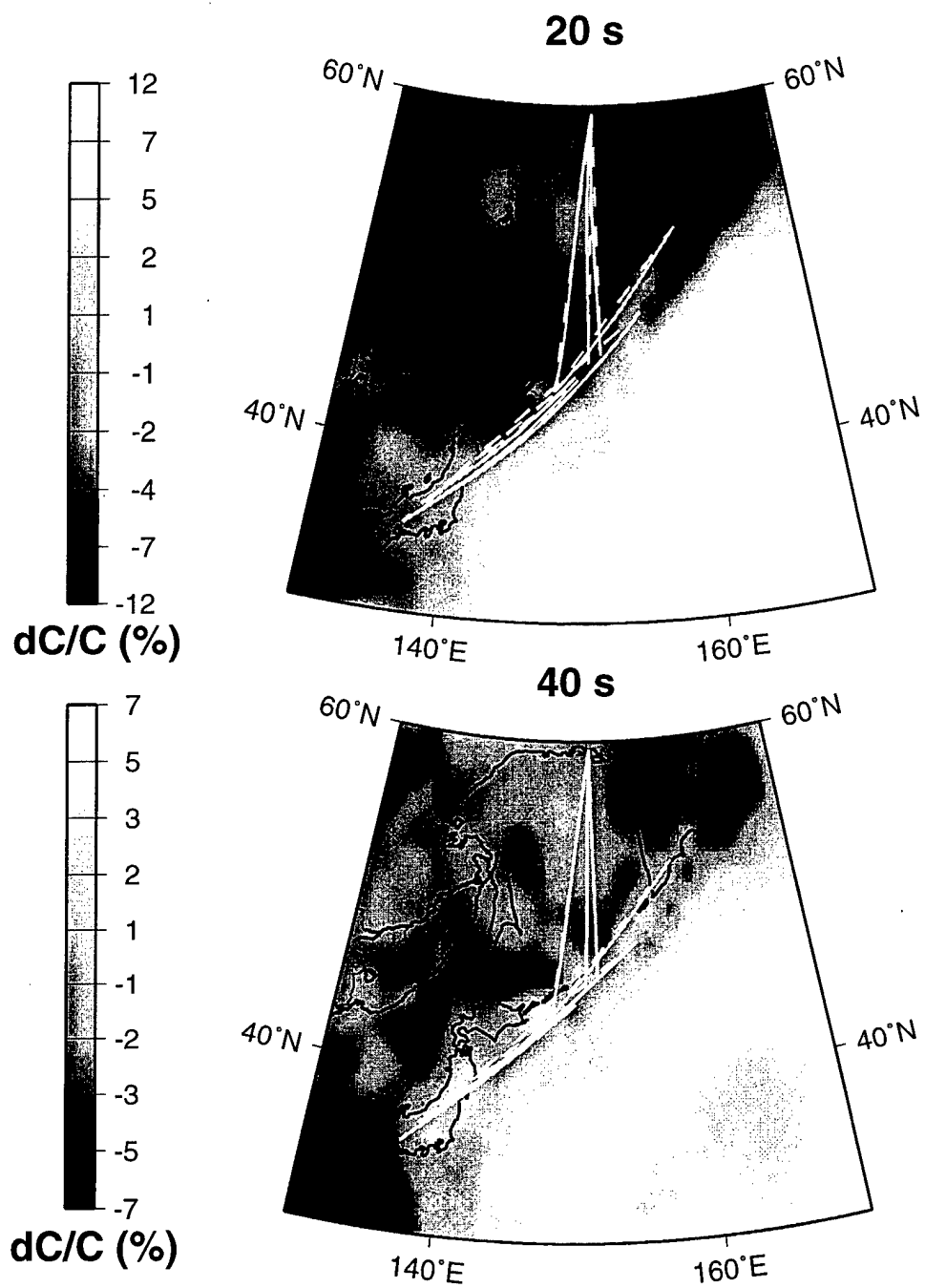
Figure 22. The same as in Figure 21 but for the coast of Japan.

20 s

40 s

dC/C (%)
-20 -15 -10 -5 -1 1 3 6 10 15
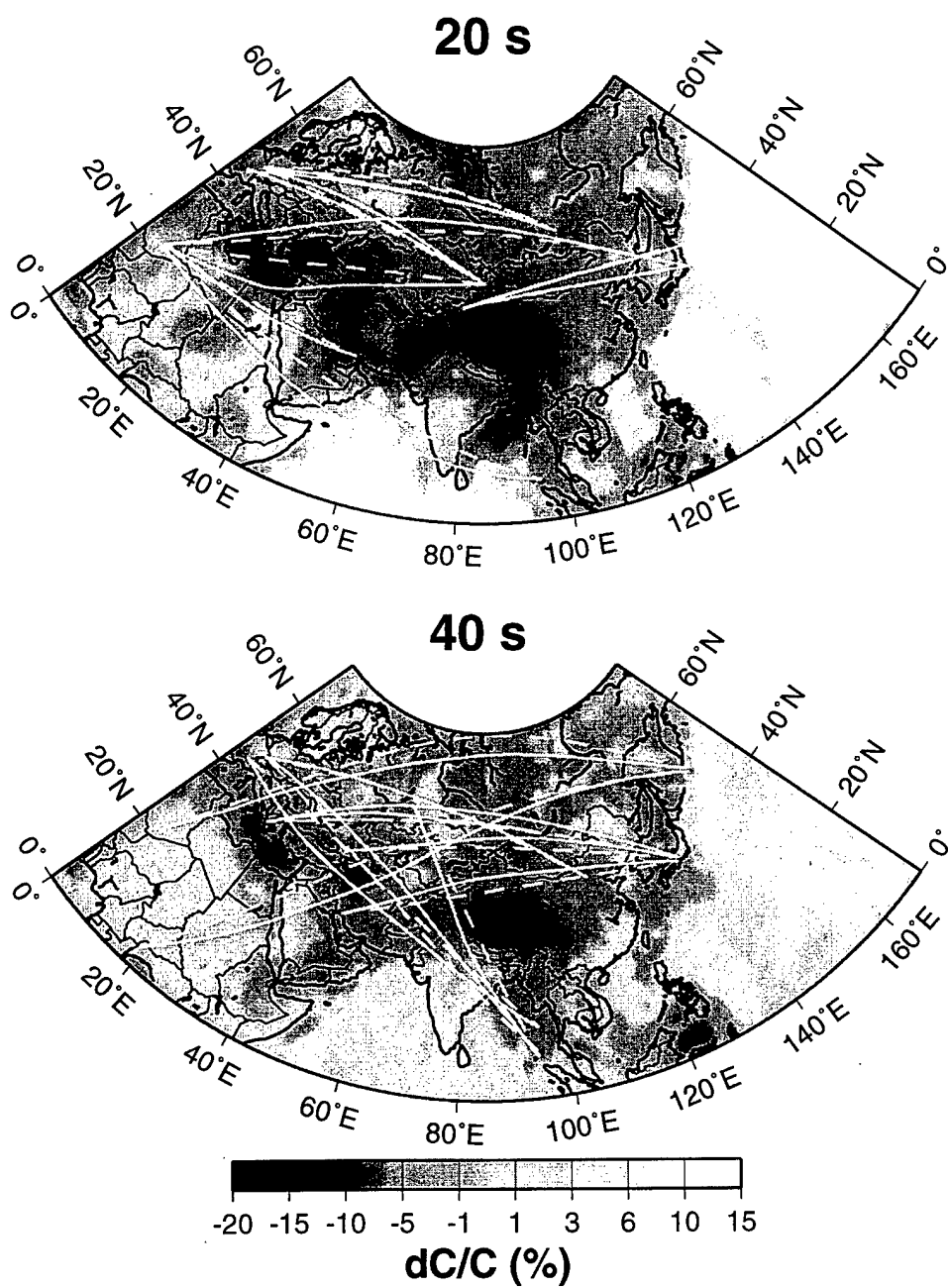
Figure 23. Examples of surface ray deviations for long ray paths (> 5,000 km.)
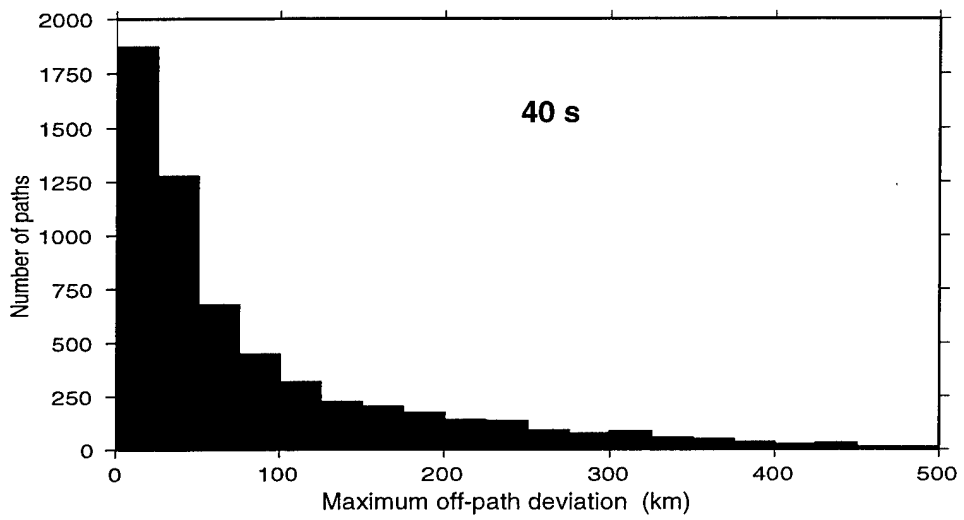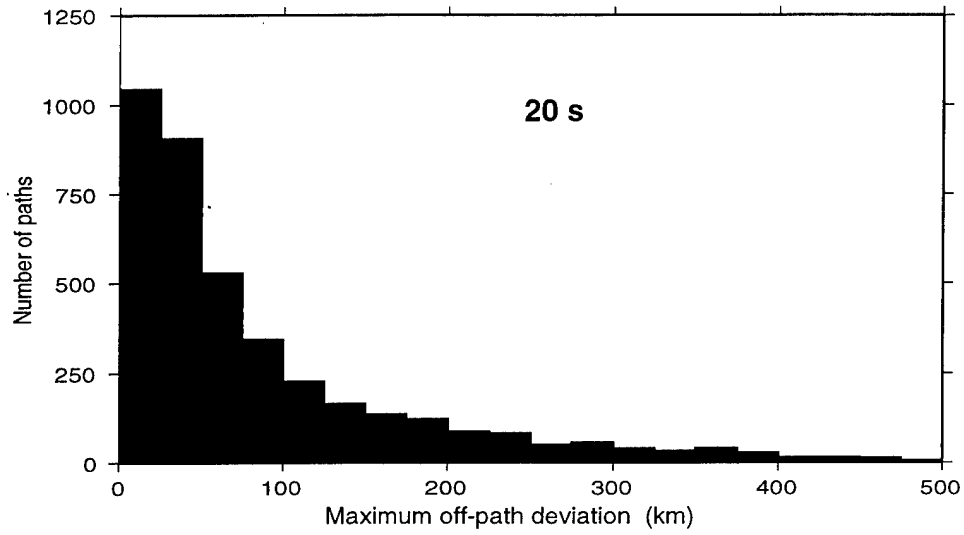
Figure 24. Histogram of maximum off-path deviations for Rayleigh waves at 20 and 40 s period.

less than 3% of the path length, and in average are in the order of 0.5 − 1%. The deviations of apparent group velocity along rays from the same velocity measured along the great circles are shown in Figure 26. We can see that these deviations are, as a rule, very small (less than 0.5% for most of the rays, and more than 1% only for a very few rays.)

Each surface wave tomographic study is characterized by its spatial resolution, depending on the density and azimuthal distribution of the ray coverage, and by random and systematic errors depending on accuracy of measurements and event locations, as well on underlaying theoretical assumptions. A detailed discussion of these factors is presented by Ritzwoller & Levshin, 1998. In our case, the spatial resolution for most of the region under study is 200 km or worse, and the accuracy of our maps is in the order of 1-2% of group velocity. We come to the conclusion that in the considered range of periods, deviations of surface wave rays from great circles cannot cause significant distortions which will change characteristic features of our maps, their accuracy and spatial resolution. To get a quantitative estimate of possible distortions, we are developing a new tomographic code which will allow for an iterative improvement of images by accounting for off-path propagation.

3.5 Conclusions.

The off-path propagation effects are small for the relatively short paths (shorter ∼ 5,000 km), but may be essential for many longer rays. Our experience shows that the long paths are important for stabilizing tomographic inversion. Their relative contribution grows with period. More work has to be done to estimate possible distortions such as blurring or defocusing of group velocity maps due to deviation of these long paths from the great circle. There are yet several questions to answer:
(1) Are the phase velocity maps predicted by the 3D model obtained in result of group velocity inversion adequate for the ray tracing?
(2) How strongly does the contribution of the long paths with significant off-path deviations distort the tomographic images?
(3) What is the range of periods for which such distortions are practically important?
To answer these questions we are developing an iterative technique of tomographic inversion taking into account possible effects of off-path propagation.
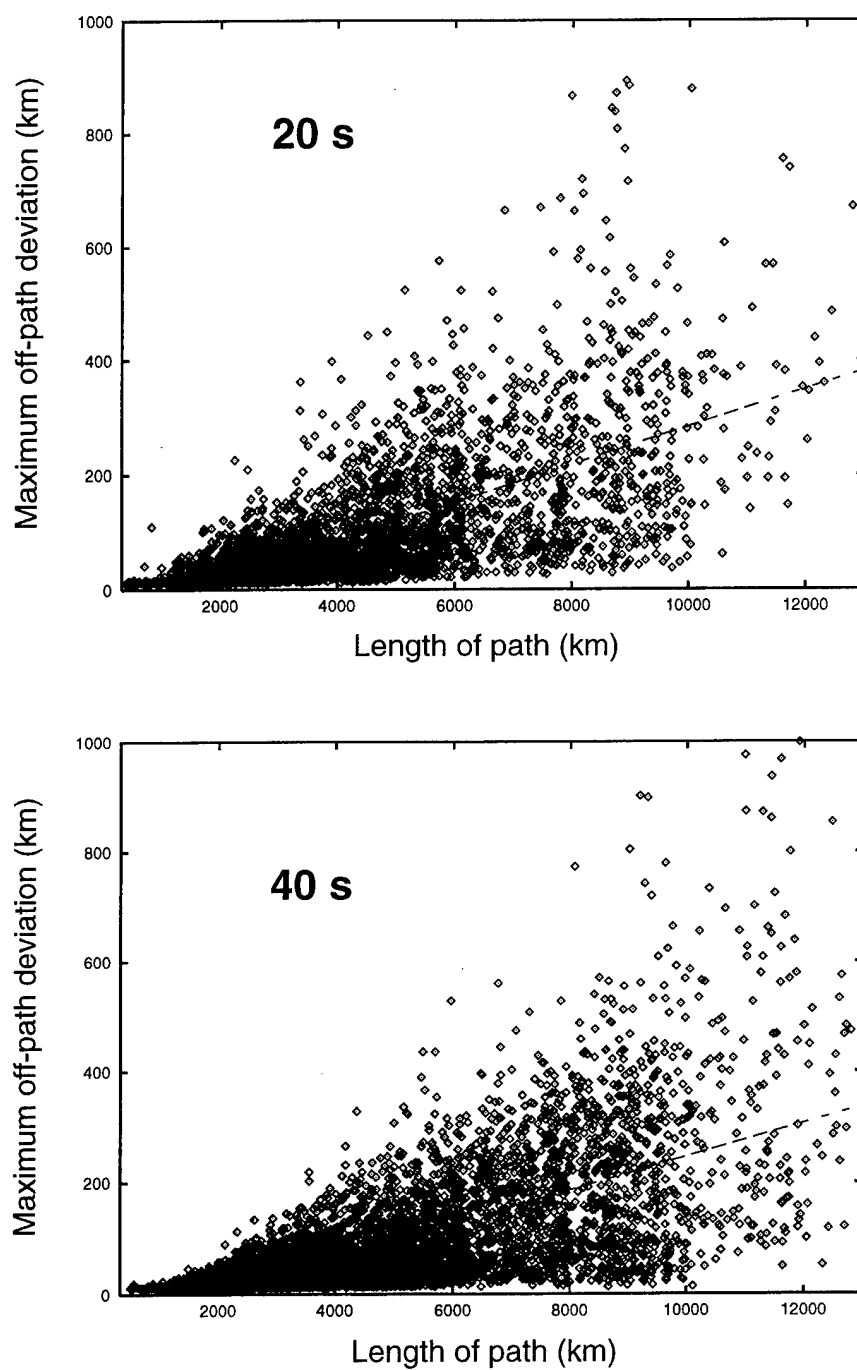
Figure 25. Maximum off-path deviations of Rayleigh waves as a function of the length of path. The straight line characterizes the average maximum deviation.
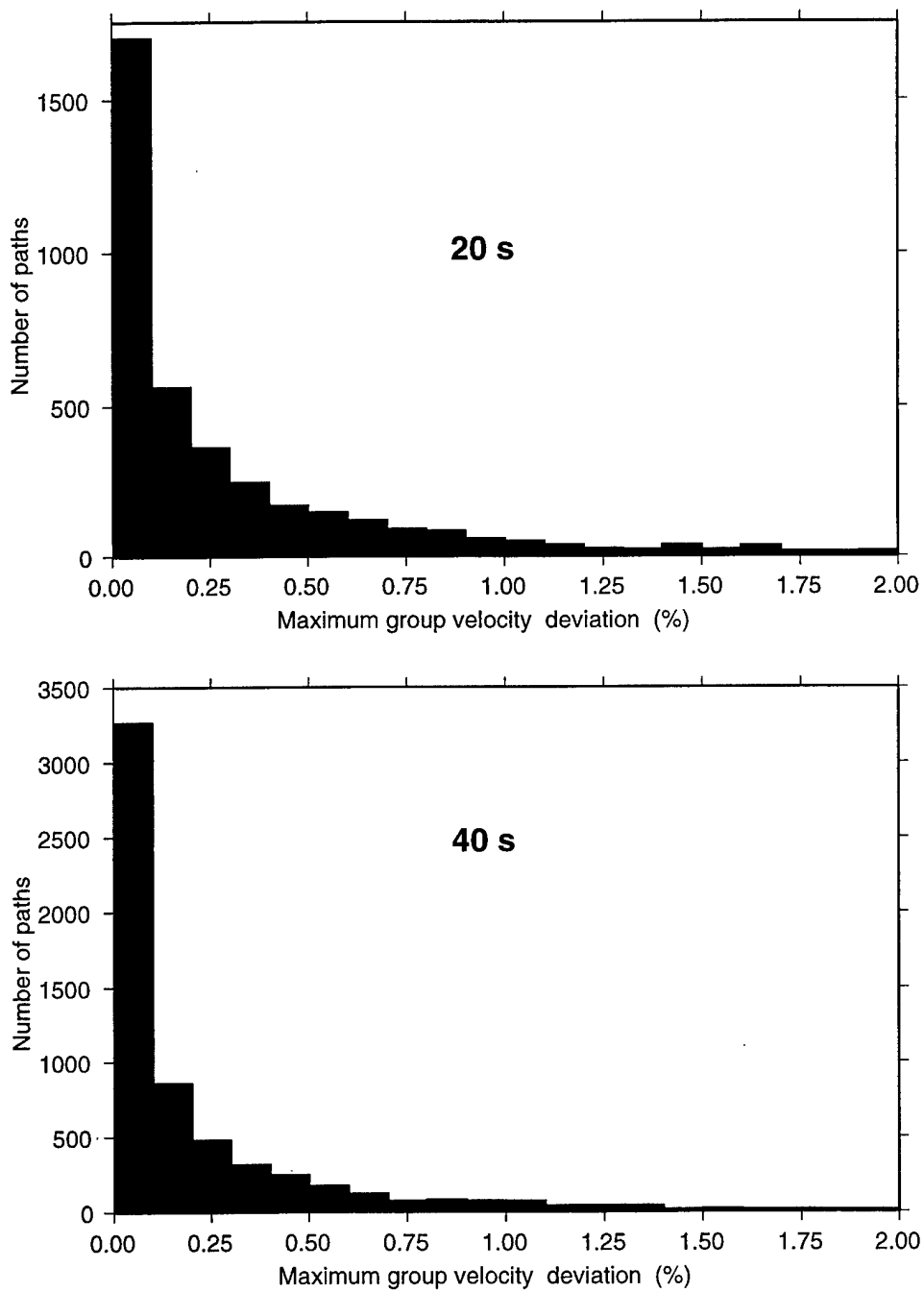
Figure 26. Histogram of relative differences between group velocities along the "real" and great circle paths for Rayleigh waves at 20 and 40 s periods.

Section 4
Group Velocity Measurements and Maps in Central Asia, Near East, and the Far East

4.1 Introduction.

This section presents the results of a study of intermediate period (10 - 40 s) Rayleigh and Love wave dispersion across Southern Eurasia. The region studied encompasses latitudes from 10°N to 50°N and longitudes from 20°E to 140°E. The focus of this section is on the estimation, presentation, assessment, and interpretation of group velocity maps.

There are two main motivations for this study. First, accurate high resolution intermediate period group velocity maps are useful in monitoring clandestine nuclear tests. These maps guide the identification and extraction of surface waveforms that emanate from small seismic events. The estimation of surface wave magnitude, M_s, near 20 s period is thereby facilitated for use as part of, for example, the $M_s : m_b$ method of discriminating underground explosions from earthquakes (e.g., Stevens and Day, 1985). In addition, the existence of group velocity maps below 20 s period should allow for the development of a regional surface wave magnitude scale based on a shorter reference period (<20 s) so that the discriminant could be applied to smaller earthquakes and explosions. Second, regional intermediate period dispersion maps provide new constraints on the shear velocity structure of the crust and on crustal thickness. As Das and Nolet (1995) have pointed out, because surface wave sensitivities compress into the crust at the short period end of our study (<25 s), group velocity maps below 25 s period are particularly important to help resolve Moho depth from the average shear velocity of the lower crust in seismic inversions.

There have been numerous studies of surface wave dispersion across the studied region within the past 20 years (e.g., Chen and Molnar, 1975; Knopoff and Fouda, 1975; Bird and Toksoz, 1977; Chun and Yoshii, 1977; Patton, 1980; Pines et al., 1980; Knopoff and Chang, 1981; Wier, 1982; Romanowicz, 1982; Feng et al., 1983; Jobert et al., 1985; Brandon and Romanowicz, 1986; Lyon-Caen, 1986; Kozhevnikov and Barmin, 1989; Bourjot and Romanowicz, 1992; Kozhevnikov et al., 1992; Levshin et al., 1992; Wu and Levshin, 1994; Levshin et al., 1994; Levshin and Ritzwoller, 1995; Ritzwoller et al., 1996b; Wu et al., 1997; Curtis & Woodhouse, 1997; Griot et al., 1997). Most of these studies concentrated on Tibet and were nontomographic, multistation or multievent phase velocity studies. None of the studies, other than our own, produced group velocity maps at the periods of the present study. There have also been other studies on larger scales and at longer periods that have produced dispersion maps (usually phase velocities) across the studied region; e.g., Feng and Teng (1983), Montagner and Tanimoto (1991); Trampert and Woodhouse (1995), Laske and Masters (1996), Zhang (1997), Ekström et al. (1997), Curtis et al. (1998). Ritzwoller and Levshin (1998) presented Rayleigh and Love wave group velocity maps on a larger spatial scale (all of Eurasia) and for a broader period band than considered here (20 - 200 s versus 10 s - 40 s).

In this section, we discuss our attempts to improve resolution in the region of study and to extend the group velocity images to relatively short periods (i.e., periods less than 30 s). The success of these attempts depends on two key factors. The first factor is the accurate identification and

extraction of the direct surface wave arrival from amidst scattered energy at the short period end of the study. The second factor is the use of data not typically employed in larger-scale studies. These include data from regional networks and arrays and data from events smaller in magnitude than those used on a continental scale (i.e., $M_s \leq 5.0$).

Surface wave scattering grows quickly in severity below 30 s period, especially in structurally complex regions such as the region of study, and causes three main problems. First, it strongly attenuates surface waves, particularly at and below 15 s to 20 s period. This means that at the shortest periods of this study dispersion measurements can be obtained only from relatively localized paths, and this negatively affects path coverage and resolution. This is why path coverage and resolution are worst at the short period end of the study, and is the reason we do not present group velocity maps below about 15 s period. Second, it obscures the "direct" arrival and, in fact, if scattering is strong enough, it may be questionable if there is a direct arrival at all. The tendency is, then, to identify the scattered energy as the direct arrival and, thereby, bias the group velocity estimates. For this reason, an analyst has overseen every measurement in this study using frequency-time analysis to identify and separate the direct arrival from scattered energy. If scattering is sufficiently strong to obscure the direct arrival, the analyst truncates the dispersion measurements at periods that are long enough to overcome the ambiguity. This procedure is far from foolproof, but it helps to hold erroneous measurements to a minimum so that they can be identified as outliers. Finally, the direct arrival may follow a path significantly different from a great circle. This phenomenon is not scattering as such, but is rather a characteristic of surface waves at all periods that simply becomes more pronounced as periods shorten. As we stated in Section 3, in the present study we ignore it and identify every path with the great-circle linking the earthquake and the seismic receiver.

The use of short-path (<2,000 km) measurements helps to reduce the period range of the study and improves resolution. The addition of data from much longer paths to the regional measurements improves the homogeneity of ray path coverage and provides crossing paths, both of which improve resolution and reduce sensitivity to event mislocation.

4.2 Data, Measurement, and Surface Wave Tomography.

We have accumulated broadband digital records of more than 1,600 events that occurred in and around Eurasia in 1976-1998 and were recorded by about 170 stations of global digital networks (DGSN, GSN, GEOSCOPE, GEOFON), regional networks (MEDNET, CDSN, KNET, KAZNET), PASSCAL deployments (Tibet, Saudi Arabia). All data and corresponding event and station information were converted into CSS-3a formatted event volumes and processed by seismic analysts in a semi-automatic regime using the frequency-time analysis package developed at CU.

We used the Frequency-Time Analysis (FTAN) method (e.g., Levshin *et al.*, 1972; Russell *et al.*, 1988; Levshin *et al.*, 1992; Ritzwoller *et al.*, 1995) to obtain group travel time, phase travel time, and spectral amplitude measurements. Group velocity and phase velocity were then computed from these travel times and distances between the receiver and the CMT location (Dziewonski *et al.*, 1981), when it exists, or the receiver and the PDE location otherwise. As part of FTAN, an analyst interactively designed a group velocity-period filter to reduce contamination from other waves and coda, chose the frequency band for each measurement, and assigned a qualitative grade (A - F) to each measurement. All resulting measurements of group velocities and other surface wave characteristics were preserved in a format which is an extension of the CSS-3a format.

Altogether more than 23,000 dispersion curves of Rayleigh waves and 18,500 dispersion curves of Love waves were obtained.

These numbers include data from about 250 relatively small events $(4.0 < M_s \leq 5.0)$ that occurred mostly in the studied region and that we processed, mainly at KNET, KAZNET, and the PASSCAL deployments in Saudi Arabia and Tibet. Not all small events are processed at all four networks. Figure 27 presents the locations of stations and events used in this study.

The resulting data set exhibits considerable redundancy, which allows for consistency tests, outlier rejection, and the estimation of measurement uncertainties. Broadband regional network data, such as those from KNET, KAZNET, or PASSCAL deployments are particularly useful for these purposes because they facilitate the "clustering" of measurements from similar paths. Paths are considered to be similar if their starting and ending points both lie within 2% of the path length from one another. For example, for an event 2,000 km from KNET, we would cluster measurements from KNET stations that lie within about ~40 km of one other. Typically, measurements from two to three stations within KNET cluster for such short paths, but more stations within KNET cluster for longer paths. About one-third of all measurements form part of some cluster. If a measurement at a specified period and wave type results from a cluster, the uncertainty assigned to it is the standard deviation of the measurements that compose that cluster (at that period and wave type). For measurements that are not part of some cluster, we assigned the average of the standard deviations at that period and wave type taken over all clusters. The average measurement uncertainties estimated in this way are about 0.025 km/s at 20 s period and above, but are larger at shorter periods particularly for Love waves (Figure 28). Measurement uncertainties increase below 20 s due to scattering, mostly from sedimentary basins. This indicates that the analysts have not been as successful in identifying the direct arrival accurately below 20 s period.

We employed the algorithm described in the Section 1 to construct the group velocity maps using the group velocity curves that emerged from the cluster analysis applied to measurements made with the frequency-time analysis (FTAN).

4.3 Resolution Analysis.

The resolution of the each group velocity map depends strongly on geographical location. Experience shows that all three of the following should be satisfied to produce a resolution of 5° or better: high path density, good azimuthal coverage, and a significant number of paths shorter than ~3000 km. In this section, we present the results of an analysis of resolution and bias and show that, on average, resolution across the studied region is about 2°-3° at periods of 20 s and above but degrades sharply below 20 s period. Figure 29 shows the reason for this degradation. Most measurements below 20 s period are from paths entirely contained within the studied region which are not sufficiently pervasive or uniform in their distribution to provide good resolution across all of the region of study.

Figure 30 displays examples of path density in terms of the number of paths that intersect each square 2° cell (~50,000 km^2). Path densities are highest in the interior of the studied region, usually maximizing near KNET, and decrease toward the south at all periods (particularly in India, the Bay of Bengal, the Arabian Sea, and north-eastern Africa) and towards the north below 20 s period. Below about 20 s period, because most of the measurements are from paths contained entirely within the region of the study. Station and event distribution within the

48
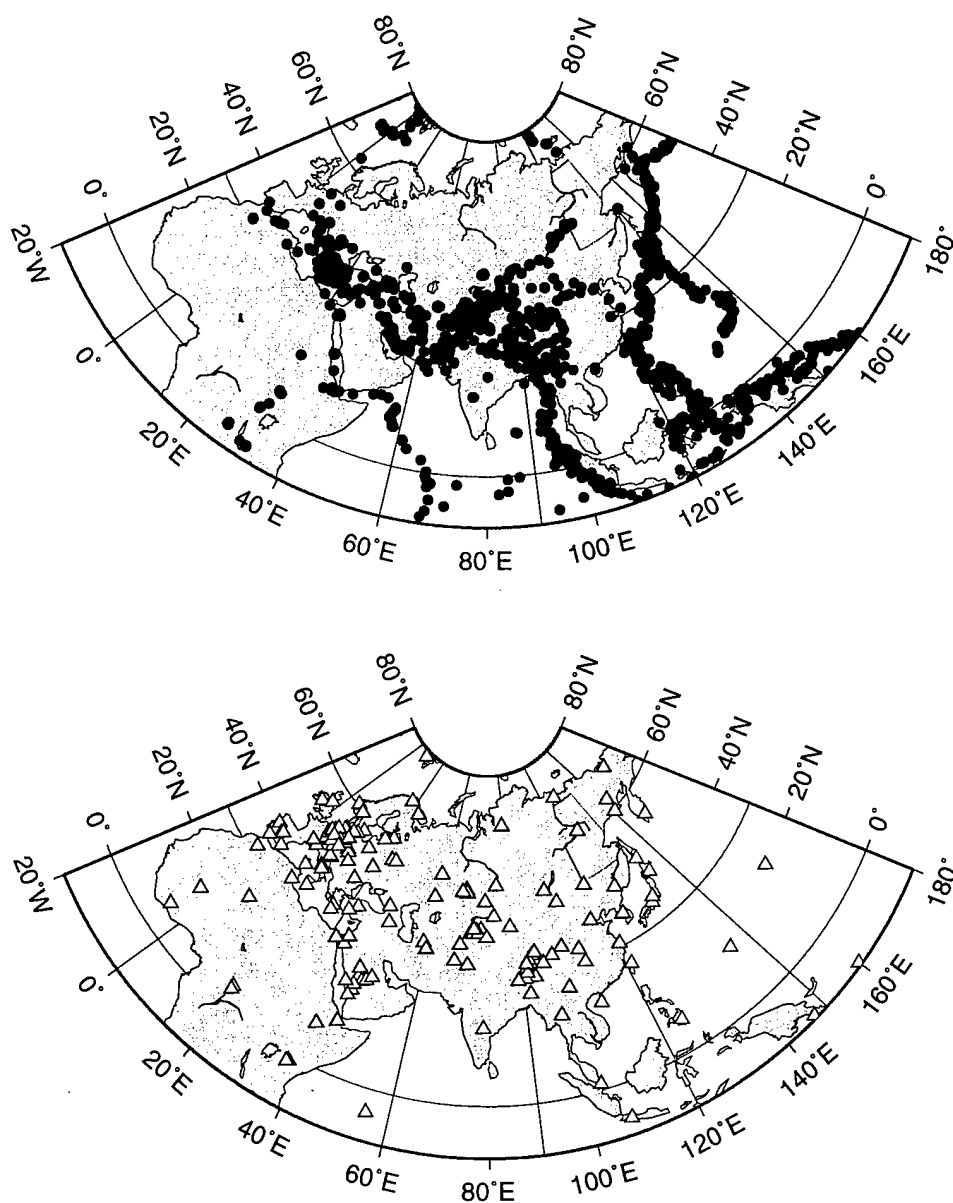
Figure 27. The locations of the events and stations used in this study. (Top) Events. (Bottom) Stations.
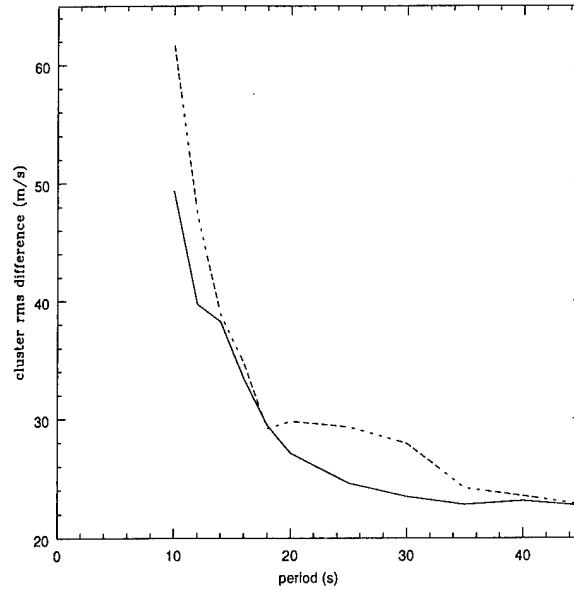
Figure 28. Average measurement uncertainty estimated from the cluster analysis. Solid line - Rayleigh wave, dashed line - Love wave.

studied region control the path distribution, and path distribution is less homogeneous than at longer periods. For example, at 12 s period, there are few paths constraining India, the Persian Gulf region, or the Caspian region. Accurate group velocity maps cannot be constructed at this period except in isolated parts of central Asia. In addition, the azimuthal distribution of paths below 20 s period is less complete than at longer periods. Below 20 s period, measurements made at KNET from events in western China (to the southeast of KNET), in southern Iran (to the southwest of KNET), and the Saudi Arabian Network from evens in the Hindu Kush and western China dominate path distribution. At 20 s period and above, measurements from the paths that begin or end outside of the studied region come into play, and this improves coverage appreciably. Because path coverage is so variable in period and geographical location, it is important to refer to the resolution analyses presented in this section to use or interpret the estimated group velocity maps.

Roughly speaking, resolution is latitudinally banded and optimizes between about 22°N and 45°N. However, event distribution does impart a somewhat higher resolution in the eastern part of the studied region. Resolution is worst in the south, particularly in the Bay of Bengal, central and southern India, the Arabian Sea, and north-eastern Africa (Egypt, Sudan). These are the regions most poorly resolved at all periods, consistent with the observations of path distribution. In particular, it will be very difficult to improve resolution substantially in India without the installation of new seismic stations. At present, the entire subcontinent is constrained by only the single Geoscope station at Hyderabad. The current event and station distribution produces surface waves that effectively skirt India. Our attempts to improve coverage across the subcontinent by using events in the Andaman Sea measured at the Saudi Arabian Network have been only partially successful. The fact that this network is no longer in operation further

Rayleigh Waves

Love Waves
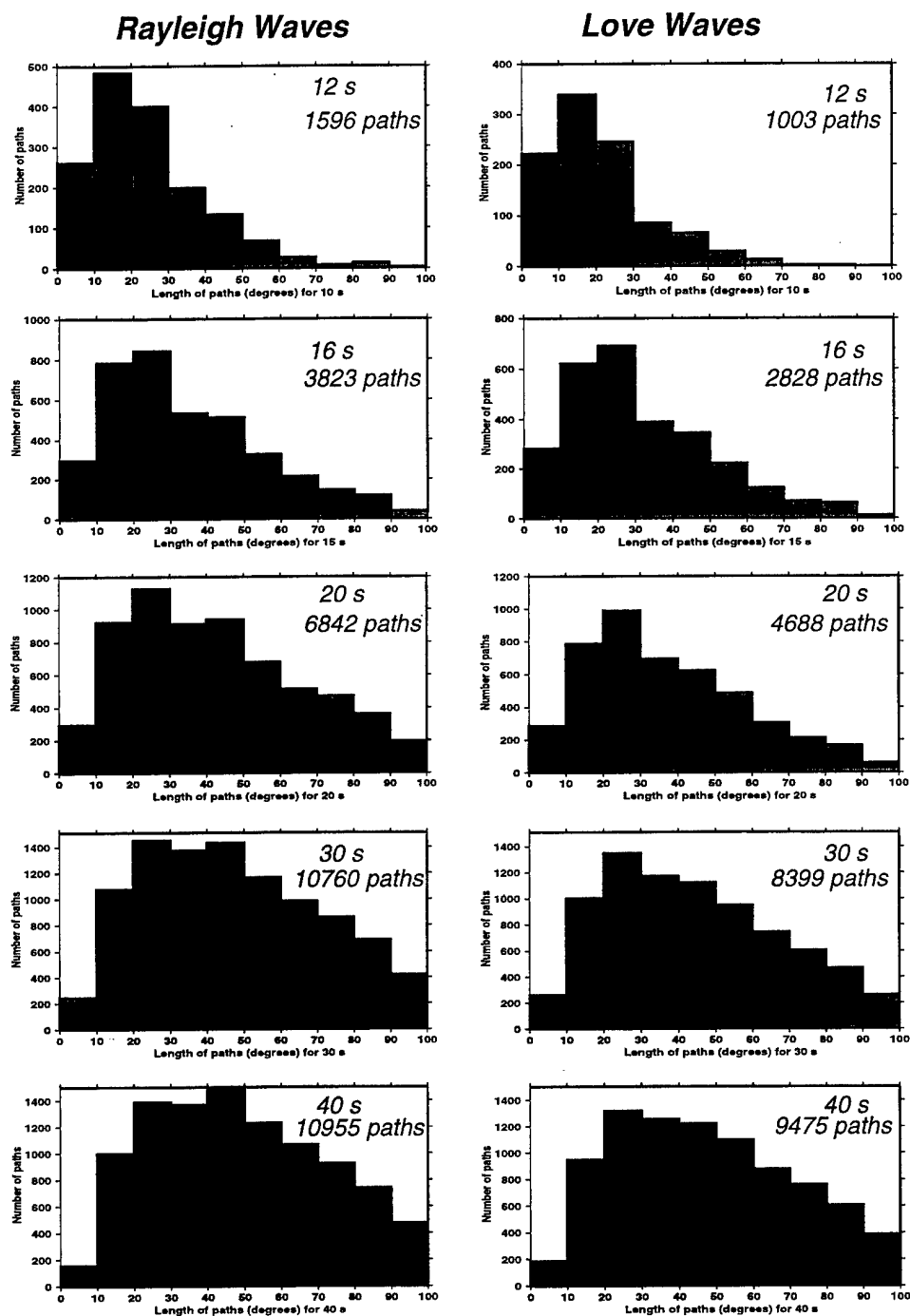
Figure 29. Histograms displaying the number of dispersion measurements (after the cluster analysis) for the paths that intersect the studied region, as a function of path length, segregated by period, ranging from 12 - 40 s. Left column: Rayleigh waves; Right column: Love waves.

51
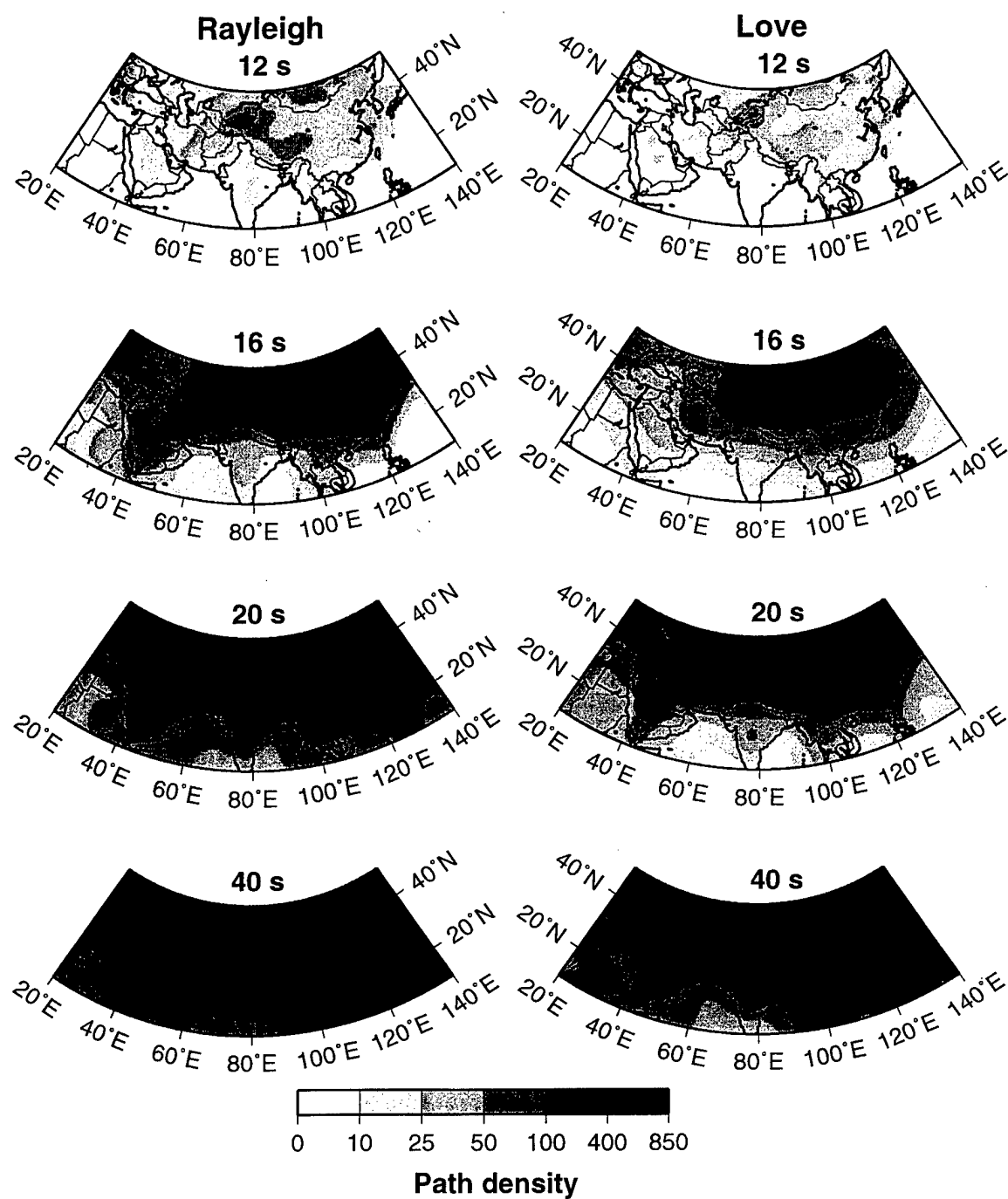
Figure 30. Path density for Rayleigh and Love waves at the four indicated periods. Path density is defined as the number of rays intersecting a 2° square cell (~50,000 km²).

exacerbates the situation. From the resolution analysis we estimate that the average resolution across the studied region lies between about 2.5° and 4.0° at 20 s and above, but degrades rather sharply below 20 s period (Figure 31), especially for Love waves. The amplitude bias defined in Section 1 is shown in Figure 32. The most significant bias (more than 20%) is observed for the southern part of the region with pure ray coverage at short periods. The bias increases sharply for the most of the region below 20 s.

An assumption at the heart of resolution analyses is that the resolution and accuracy of the estimated dispersion maps are dominated by known quantities that can be simulated in the resolution analysis; namely, measurement uncertainties, path coverage, and the weighting and damping used in the inversion. However, theoretical errors, which may be largely of unknown character and magnitude, also affect resolution and bias. Such errors include (1) event mislocations, (2) source group time shifts, (3) azimuthal anisotropy, and (4) off-great-circle propagation.

(1) Ritzwoller and Levshin (1998) demonstrated that using measurements from paths that begin and/or end outside of the studied region reduces sensitivity to event mislocations in the region of study, and biases imparted are not expected to be larger than about 0.5%.
(2) We have showed in Section 2 that group source time shifts do not have to be modeled at the periods of this study but are significant at longer periods.
(3) Crustal anisotropy is poorly understood in the region of study. We are unaware of evidence of coherent large-scale anisotropy in the crust in the studied region. Therefore, we believe that anisotropy is a serious problem only for longer period waves that are sensitive to anisotropy in the upper mantle. The results of synthetic experiments (Section 5) show the weak effect of anisotropy across the Tibetan plateau on resulting group-velocity maps. However, Ritzwoller & Levshin (1998) and Vdovin et al. (1997) demonstrated how large-scale patterns of azimuthal anisotropy in the uppermost mantle bias group velocity maps above 40 s period.
(4) We believe that the most significant effects of theoretical errors on intermediate period surface waves are due to off-great-circle propagation. The effect of off-great-circle propagation is largely to smear the estimated maps, rather than to introduce completely spurious features. However, because measurement uncertainties are approximately constant with periods above 20 s, scattering and off-great-circle propagation are probably most severe at and below about 20 s where waves are very sensitive to the large velocity anomalies caused by sedimentary basins. Indeed, the low velocity anomalies associated with certain adjacent sedimentary basins on the 16 s group velocity maps in Figures 34 and 36 tend to blend together (e.g., northern and southern Caspian Basins) somewhat more strongly than would be implied by the resolution estimates in Figure 31. Low velocity features associated with mountain roots on the 30 s and 40 s Rayleigh wave maps, for example, appear to be better separated. For these reasons, we believe that the resolution analyses accurately represent uncertainties in the estimated group velocity maps above about 20 s period but are somewhat optimistic near large sedimentary basins on the short period maps.

4.4 Group Velocity Maps.

Using the tomographic method described in Section 1, we construct group velocity maps for Rayleigh and Love waves from 16 s to 40 s period. We consider maps at periods below 14 to 16 s still not very reliable due to insufficient density of ray coverage. Special efforts supported by the current contract DTRA01-00-C-026 are in progress to significantly improve the coverage at shorter periods in Western China, Northern India, Pakistan and nearby.
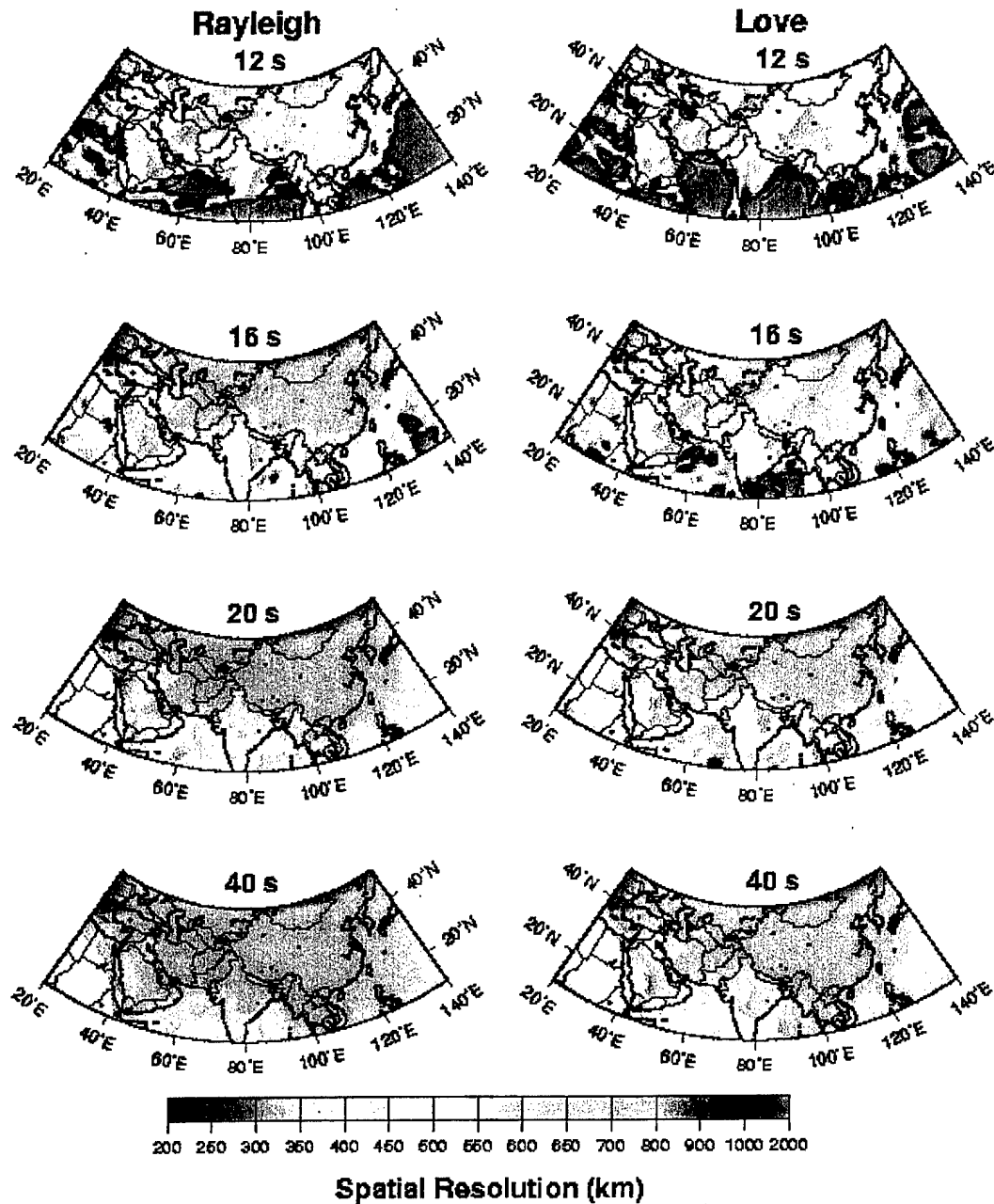
Figure 31. Spatial resolution for Rayleigh and Love waves at the indicated periods. Resolution units are km.
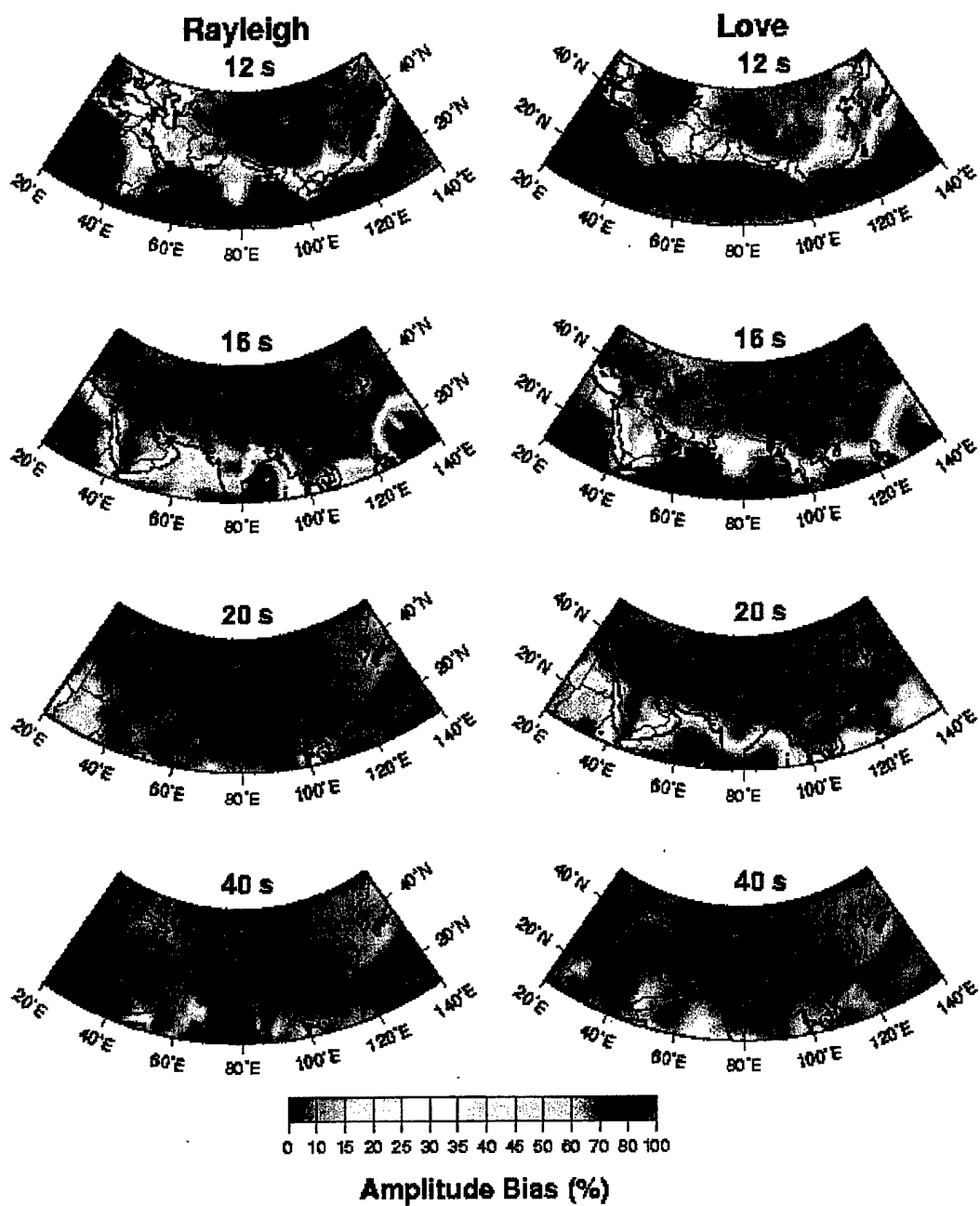
Figure 32. Bias for Rayleigh and Love waves at the indicated periods. Bias units are %.
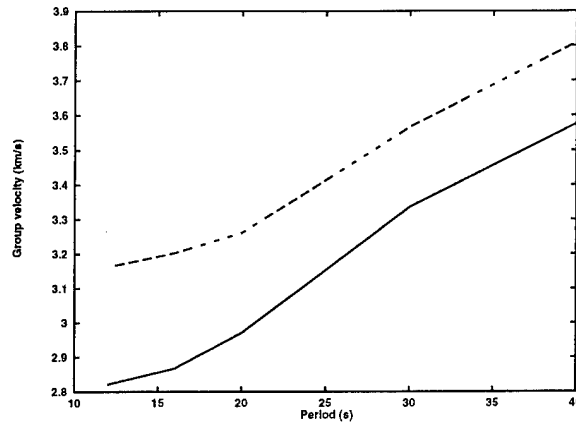
Figure 33. Average group velocity curves across the region of study (latitude, 10°N - 50°N, longitude, 20°E - 140°E) for our estimated group velocity maps. Solid line - Rayleigh wave, dashed line - Love wave.

Figures 34 - 37 display a sampling of the estimated group velocity maps. These maps represent lateral group velocity variations relative to the regional averages shown in the same figures. Figures 38- 39 show more detailed Rayleigh and Love wave group velocity maps for the Near East and Central Asia at periods 12 and 16 s, and Figures 40 and 41 present Rayleigh and Love group velocity maps for the Far East at periods 12, 16, 20, and 40 s.

4.5 Discussion.

We have argued that the effects of theoretical errors are small compared to the main features that appear in the estimated group velocity maps and that the resolution analyses fairly accurately represent the precision of the measurements except at the shortest periods near to large sedimentary basins. For these reasons, it is worthwhile discussing the group velocity maps further. A number of the features in the group velocity maps shown in Figures 34- 40 are worthy of further note here. Interpretation of these maps must be predicated upon the results of the resolution analysis found in Figures 4.5 and 4.6. Place names for Near East, Central and Southern Asia are presented in Figure 42 partially segregated by geological type. Sedimentary basins are taken from 3SMAC (Nataf and Ricard, 1996; Kunin *et al.*, 1987).

At the short period end of the study (12 - 25 s), the group velocity maps show the imprint of sedimentary basins and continental platforms and shields. This is because the group velocities at these periods are dominantly sensitive to shear velocities in the upper crust which are, of course, very low in sedimentary basins and high in shield or platform regions. As an example, consider the 20 s Rayleigh and Love wave maps in Figures 34- 40. The 20 s Love wave samples are somewhat shallower than the Rayleigh wave at the same period. This provides greater sensitivity to sedimentary features, but at this period their sensitivities in continental regions are not substantially different and the maps are seen to be quite similar. Low velocity features are all associated with known sedimentary basins. Most of the basins listed in Figure 42 are coincident

56

Rayleigh Waves

16 s

dU/U (%)

Average 2.892 km/s

20 s

dU/U (%)

Average 2.971 km/s
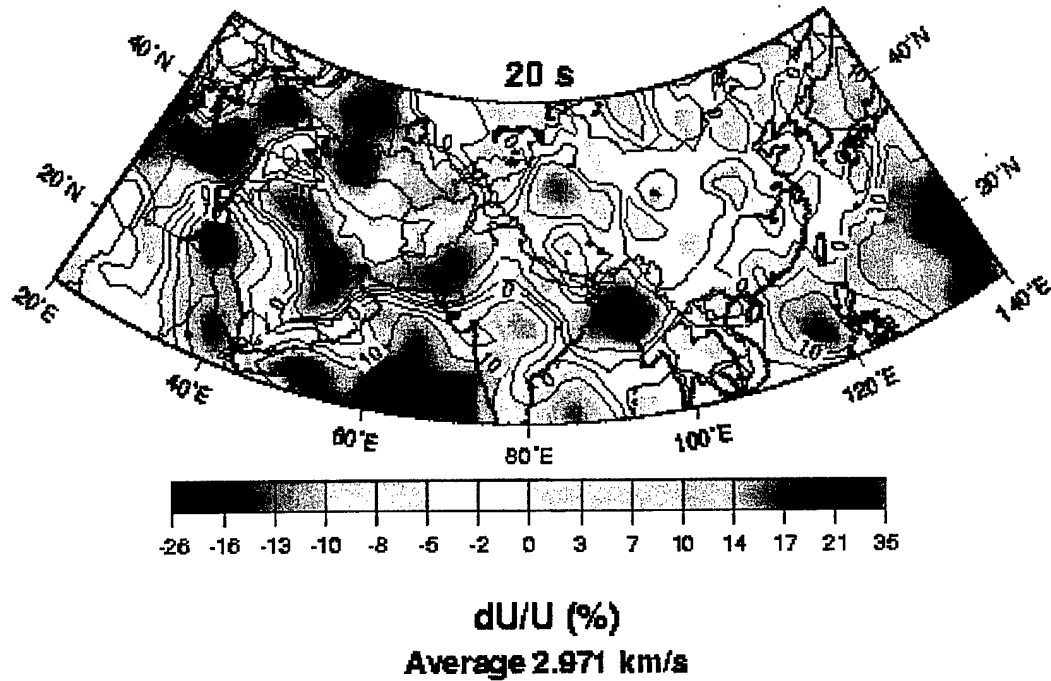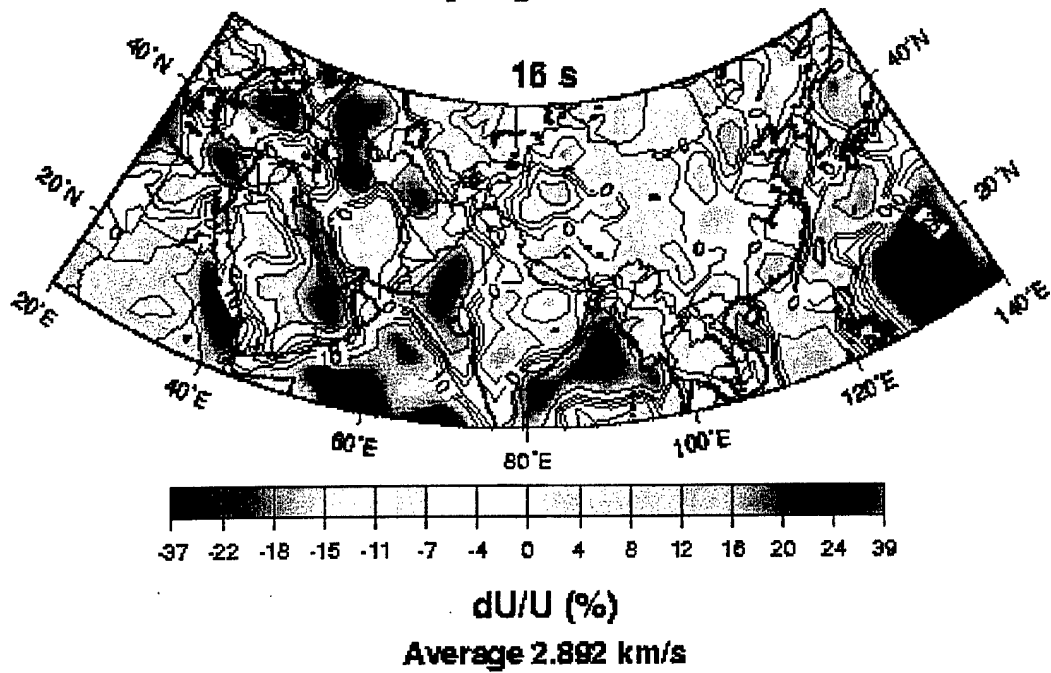
Figure 34. Estimated Rayleigh wave group velocity maps at the periods 16 and 20 s.

57
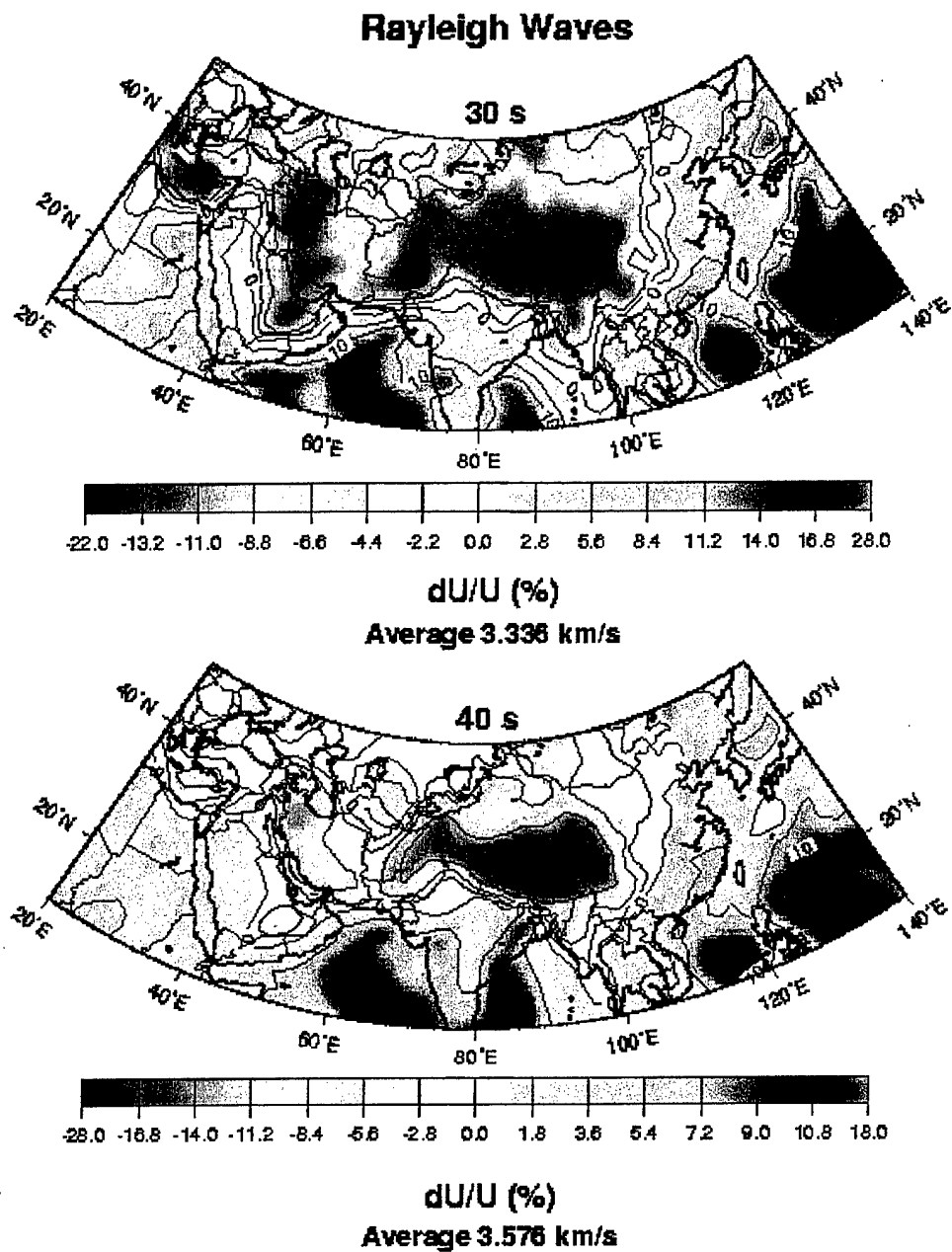
Rayleigh Waves

Figure 35. Estimated Rayleigh wave group velocity maps at the periods 30 and 40 s.
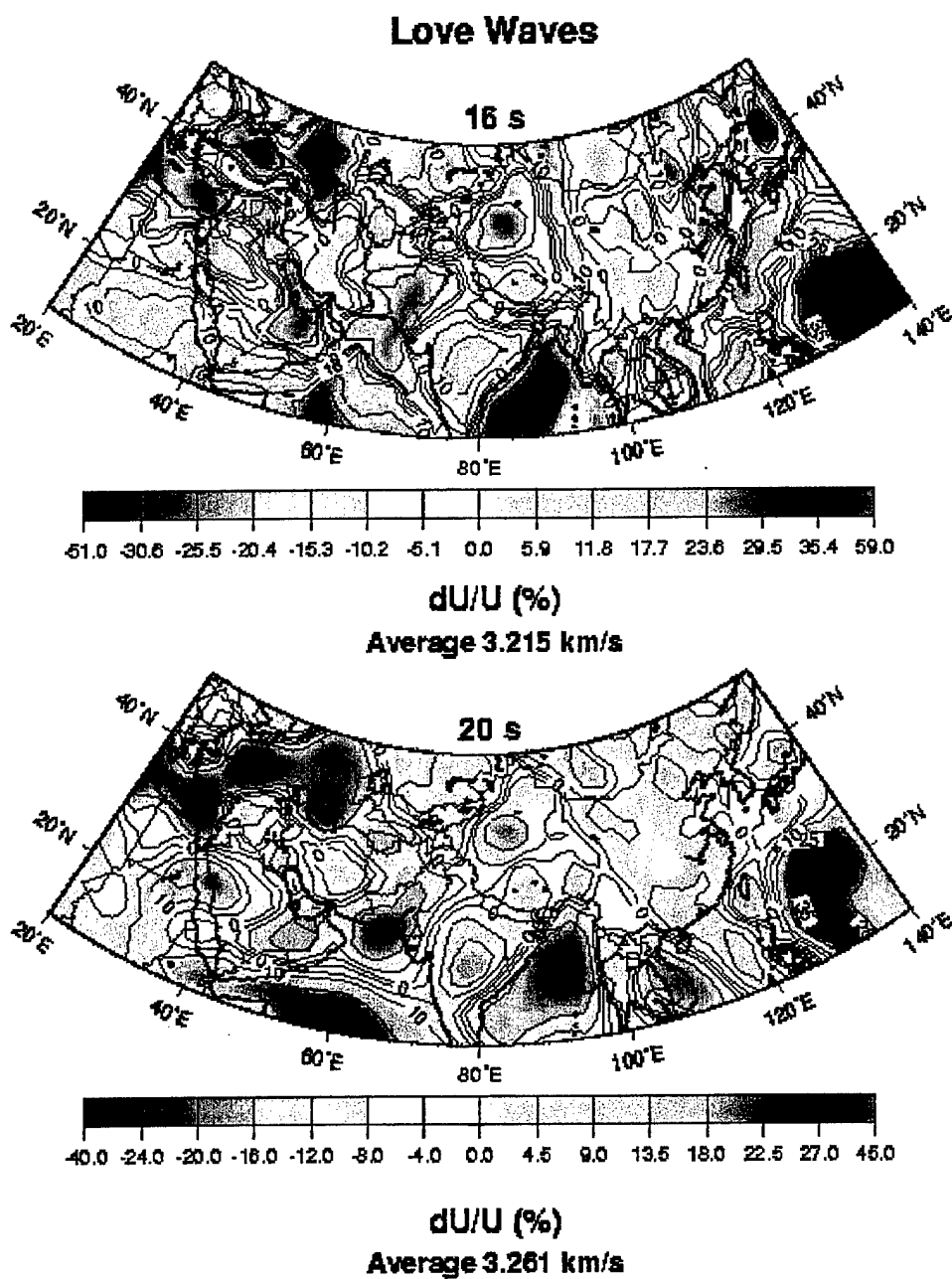
Figure 36. Estimated Love wave group velocity maps at the periods 16 and 20 s.
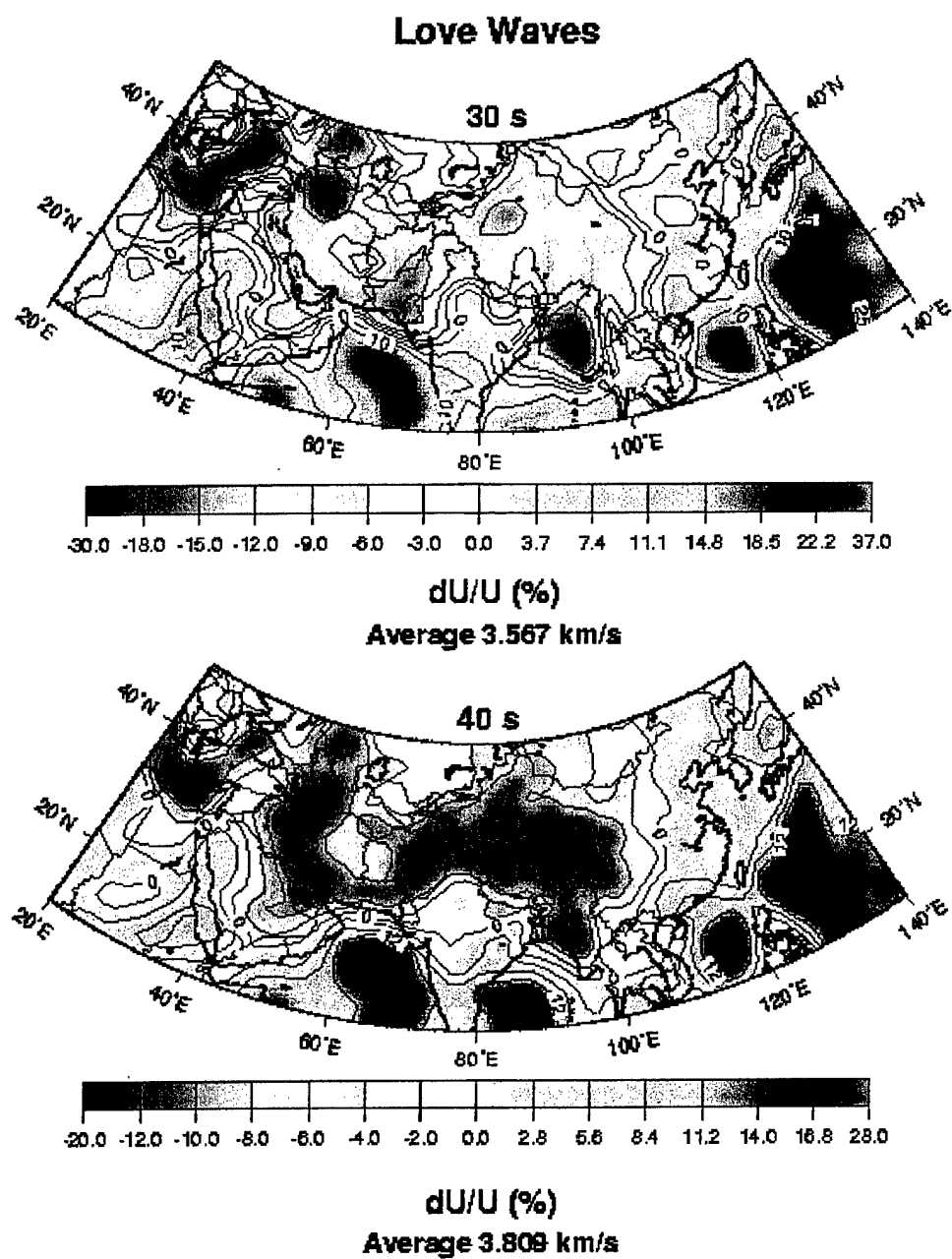
Love Waves

Figure 37. Estimated Love wave group velocity maps at the periods 30 and 40 s.
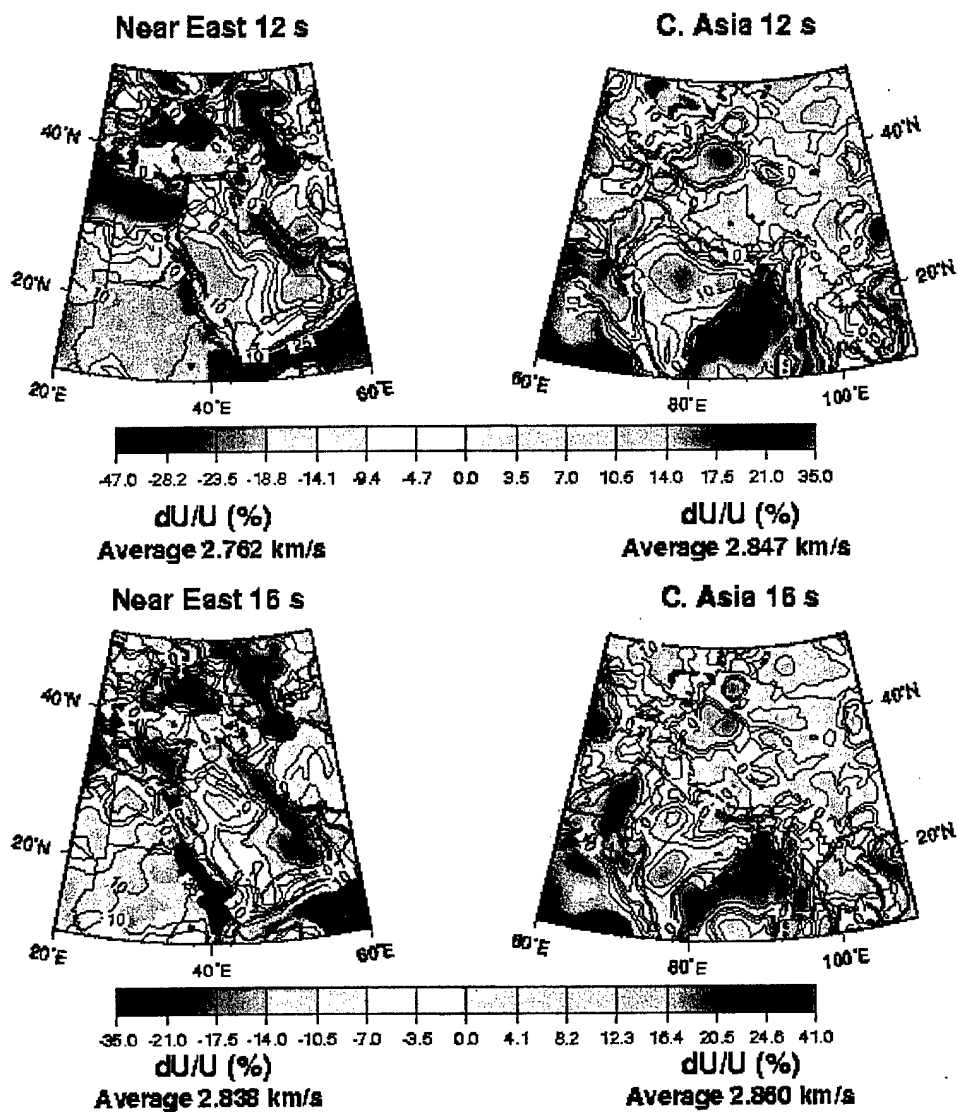
Figure 38. Estimated Rayleigh wave group velocity maps at the periods 12 and 16's for two subregions: Near East and Central Asia.

Love Waves

Near East 12 s

40°N
20°N
20°E   40°E   60°E

-52.0 -31.2 -28.0 -20.8 -15.6 -10.4 -5.2 0.0 3.5 7.0 10.5 14.0 17.5 21.0 35.0

dU/U (%)
Average 3.043 km/s

C. Asia 12 s

40°N
20°N
60°E   80°E   100°E

dU/U (%)
Average 3.083 km/s

Near East 16 s

40°N
20°N
20°E   40°E   60°E

-50.0 -30.0 -25.0 -20.0 -15.0 -10.0 -5.0 0.0 4.6 9.2 13.8 18.4 23.0 27.6 46.0

dU/U (%)
Average 3.144 km/s

C. Asia 16 s

40°N
20°N
80°E   80°E   100°E

dU/U (%)
Average 3.145 km/s
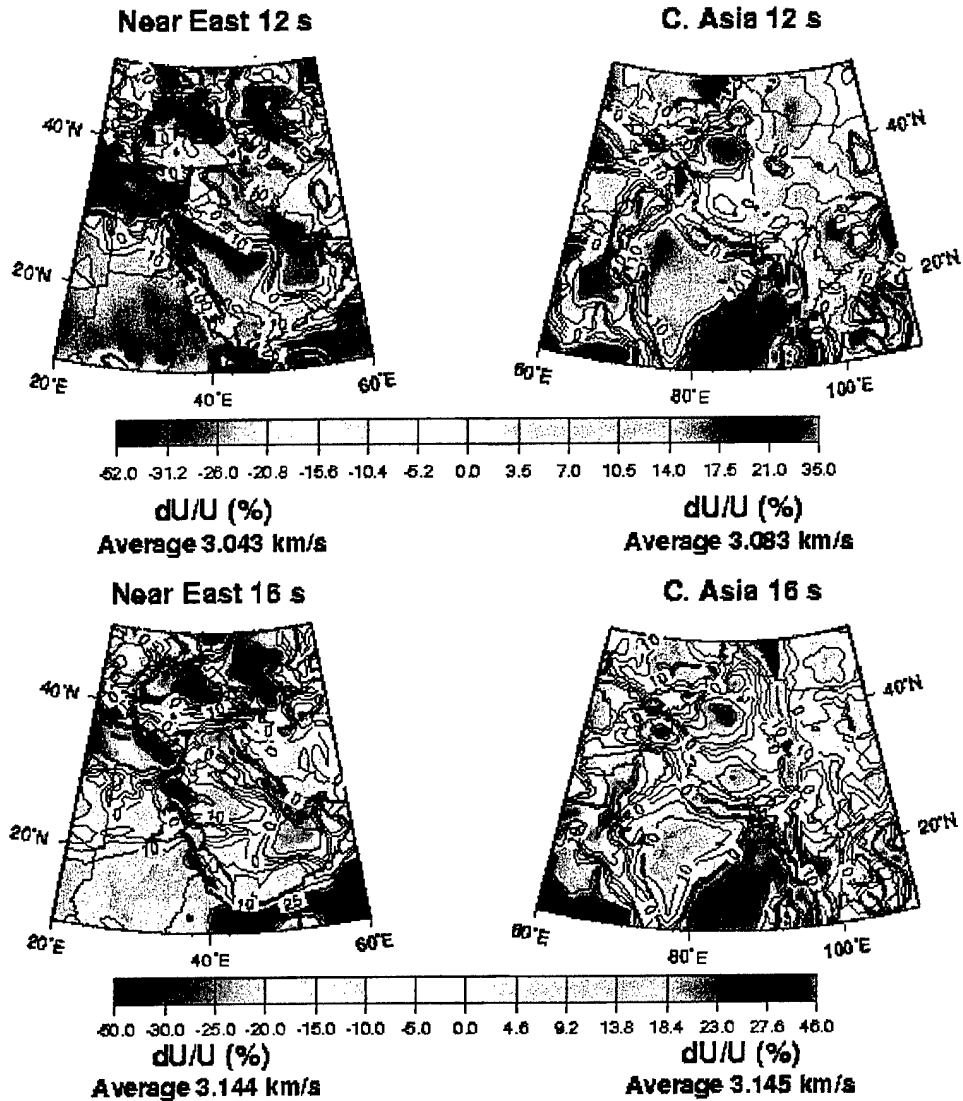
Figure 39. Estimated Love wave group velocity maps at the periods 12 and 16 s for two subregions: Near East and Central Asia.

62
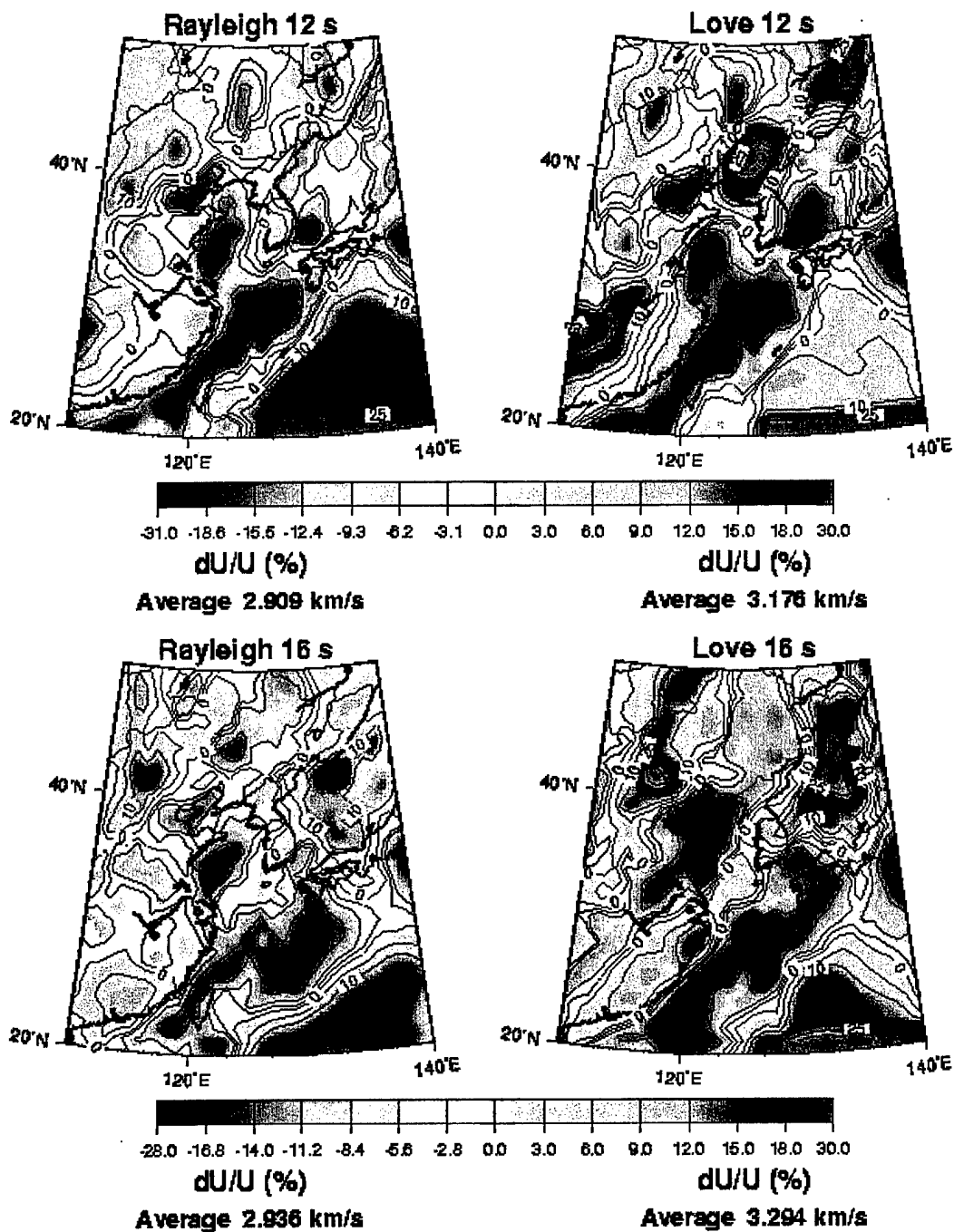
Figure 40. Estimated Rayleigh and Love wave group velocity maps at the periods 16 and 20 s for the Far East subregion.
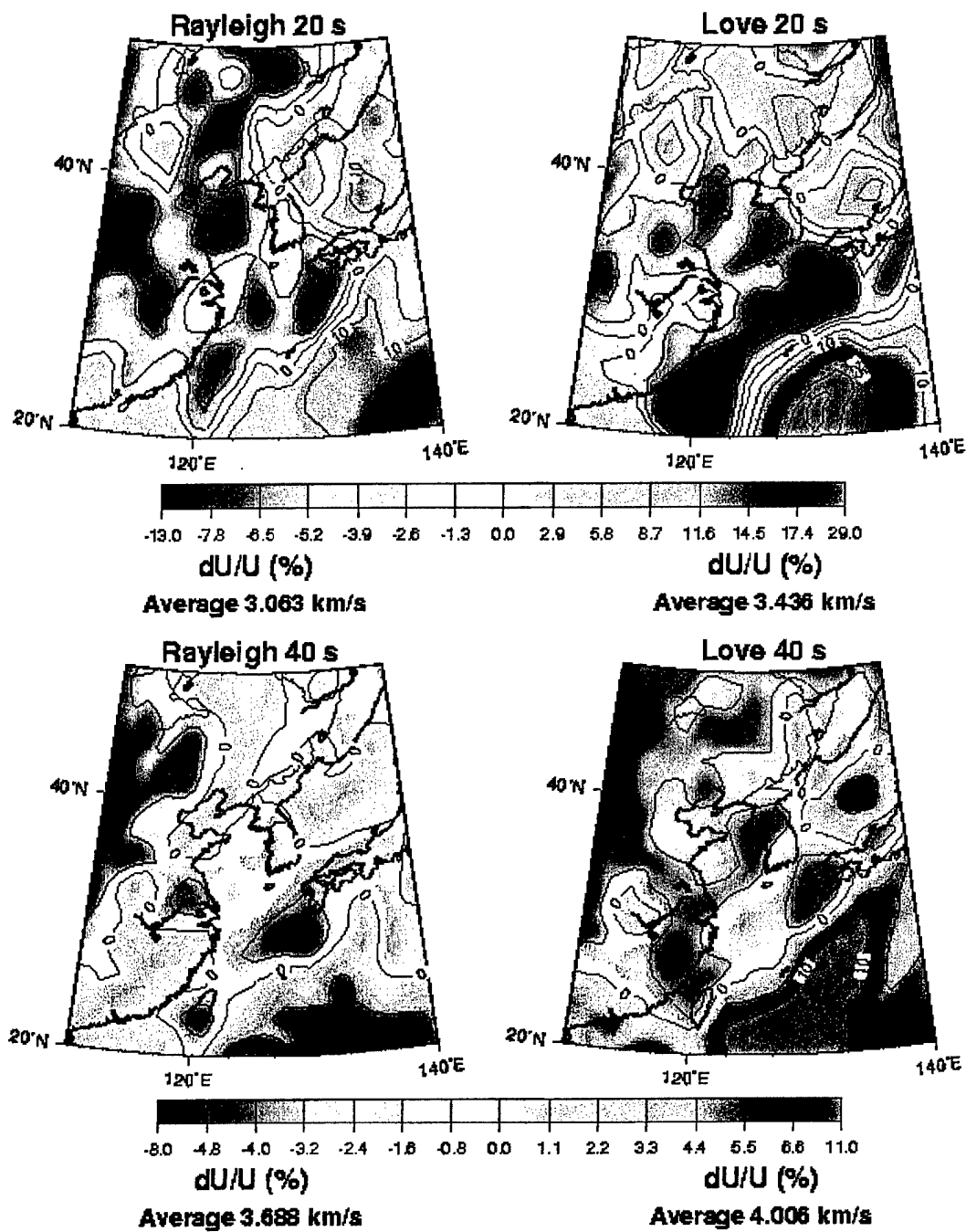
Figure 41. Estimated Rayleigh and Love wave group velocity maps at the periods 20 and 40 s for the Far East subregion.

64
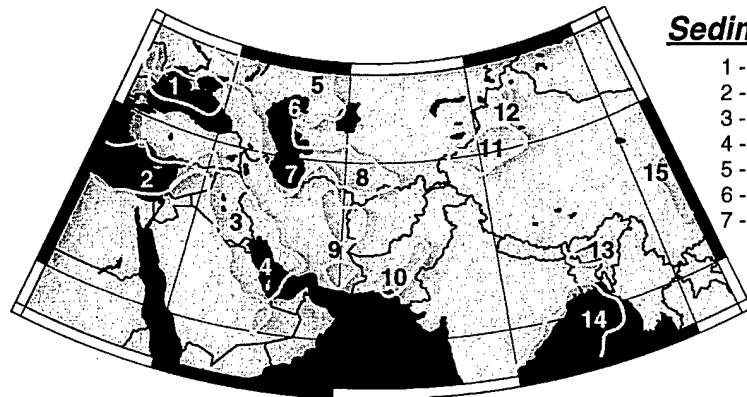
Sedimentary Basins

1 - Black Sea
2 - E. Mediterranean
3 - Iraq
4 - Persian Gulf
5 - Pri-Caspian
6 - N. Caspian
7 - S. Caspian
8 - Turkmen/Tajik
9 - E. Iran
10 - Indus
11 - Tarim
12 - Dzungarian
13 - Brahmaputra
14 - Ganges Fan
15 - Sechuan
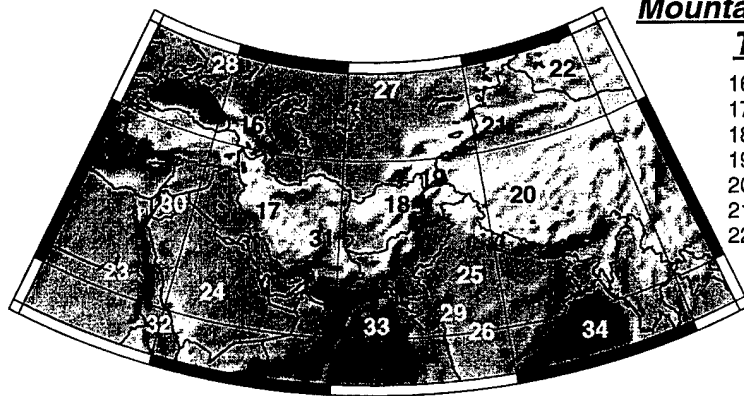
Mountains, Tectonic Features, etc.

16 - Caucasus.
17 - Zagros Mtns.
18 - Hindu Kush
19 - Pamir
20 - Tibet
21 - Tien Shan
22 - Altai
23 - Nubian Shield
24 - Arabian Platform
25 - N. Indian Platform
26 - Indian Shield
27 - Kazakh Platform
28 - E. Europen Platform
29 - Deccan Traps
30 - Jordanian Volc.
31 - Lut Block
32 - Red Sea
33 - Arabian Sea
34 - Bay of Bengal

Figure 42. Place names. Sedimentary basin outlines (5 km isopach) are taken from Nataf & Richard (1996). Surface topography is from ETOPO-5.

with a low velocity anomaly. The principal exceptions are the north eastern Iranian Basin and the Sechuan basin, both of which overlie high velocity crust (Lut Block, East China Block) that obscures the sedimentary signals. The most striking example of this in Eurasia is the Tunguska Basin in central Siberia which, displays fast velocities even though there is substantial sedimentary cover (Ritzwoller & Levshin, 1998). Sedimentary basins of the Far East (in the north-eastern China, the Yellow Sea, the East China Sea) are clearly seen in short-period Rayleigh and Love maps (Figure 40)

The discrepancies in the features observed on the short period maps between periods and wave types are largely attributable to resolution differences. For example, the low velocity anomaly in the Persian Gulf, southern Iran, and southern Pakistan halts abruptly at the coast on the 20 s Rayleigh wave map but extends into the Arabian Sea on the 16 s map. This is due to poor resolution on the 16 s map and should not be taken seriously. However, the 20 s Love wave displays a strong anomaly in the Bay of Bengal associated with the Ganges Fan which is more muted on the 20 s Rayleigh wave map. This discrepancy is probably real because the Love wave is simply much more sensitive to oceanic sediments.

High velocity features on the short period maps exist in central Iran (Lut Block), Kazakhstan (Kazakh Platform), India (northern Indian Platform and Indian Shield), eastern Tibet (particularly for Love waves), and are coincident with the Red Sea and the Nubian Shield in southern Egypt and the Sudan. A small tongue of high group velocities extends south from the Kazakh Platform to the Pamir (near the western syntaxis of the Indian-Eurasian plate boundary). These areas are known to be characterized by very high near surface velocities. The Deccan Traps are also coincident with high velocities for the short period Rayleigh waves. High velocities are typical for a significant part of the north China-Korean platform with very thin sedimentary cover.

At the long period end of this study, the group velocities are dominantly sensitive to deep crustal velocities and crustal thickness. This is particularly true for the Rayleigh waves that sample deeper at each period than the Love waves. Thick crust causes low group velocities. As an example, consider the 40 s Rayleigh and Love wave maps in Figures 4.9 and 4.11. By 40 s period, both types of waves possess considerable sensitivity to Moho depth, although the Love wave continues to have substantial sensitivity to upper crustal and sedimentary velocities. The effects of crustal thickness on the estimated group velocity maps are most striking under Tibet where the Moho extends to depths greater than 70 km. Low velocity anomalies are associated with Tibet, the Pamir, the Tien Shan, the Hindu Kush, the Altai Range in Mongolia, the Zagros Mountains in western Iran, and the Caucasus Mountains. The 40 s Love wave map continues to be imprinted with low velocities associated with the deepest basins; namely, the Tarim, the northern and southern Caspian, the Brahmaputra, the eastern Mediterranean, and the Persian Gulf. High velocities are associated at long periods with platforms and shields; namely, the northern Indian Platform, Indian Shield, Kazakh Platform, southeastern European Platform, and Nubian Shield. A high velocity anomaly also emerges coincident with the Dead Sea Rift volcanic province in Jordan.

In summary, a qualitative inspection of the group velocity maps in Figures 34 - 41 reveals the following.
(1) The observed group velocity features are repeatable in that similar features are observed at different periods and wave types which sample the Earth similarly.
(2) These repeatable features can be understood qualitatively in terms of known geological and tectonic structures, particularly sedimentary basins, continental platforms and shields, and crustal

66

thicknesses.

(3) Discrepancies that exist between the maps are largely attributable to differences in path coverage (resolution and bias).

(4) The features observed on the group velocity maps at 20 s period differ substantially from those observed at 40 s period because different crustal structures dominate the maps at these two periods.

Comment (4) indicates that it would be a mistake to use group velocity maps constructed around 40 s period and attempt to extrapolate them for use at much shorter periods. This is particularly true in Central Asia which is characterized by extremely thick crust and deep sedimentary basins.

Variance reductions to the observed group velocity measurements provided by CRUST5.1/S16B30 are large and positive for Rayleigh waves at 15 s and above and for Love waves at 20 s and above. Indeed, variance reductions are in excess of 80% for Rayleigh waves between 20 s and 40 s period and for Love waves between 25 s and 40 s. The degradation in misfit of CRUST5.1/S16B30 at shorter periods is largely due to the fact that several sedimentary basins are missing in the model and sedimentary velocities in existing basins are too low. As we discuss further below, measurement uncertainties and off-pure-path propagation also increase at short periods and these factors contribute to increase the misfit of both the observed and the model group velocity maps below 25 s period. The slight degradation in variance reduction for the 40 s Rayleigh wave is probably due to errors in crustal thickness in CRUST5.1. This is more clearly observed as a substantial increase in rms-misfit for the 40 s Rayleigh wave. The variance reduction degrades more subtly than the rms-misfit because signal levels due to crustal thickness variations increase along with the misfit.

At 25 s and beyond, the rms-misfits for Rayleigh and Love waves are nearly equal and lie between 0.04 - 0.05 km/s, on average about one-half of the misfit of CRUST5.1. Below 20 s period, misfit rises rapidly but remains about one-half of that of CRUST5.1. This rise is caused by two factors. First, measurements are harder to make accurately below 20 s period due to scattering. Analysts have a harder time constructing a frequency-time filter that reliably separates directly arriving surface waves from coda. Comparison with Figure 28 indicates that misfit is about twice the estimated standard deviation independent of period. Thus, about half of the misfit results from observational errors. Second, off-pure-path propagation becomes important below 20 s period. This phenomenon and event mislocation are the likely causes of the remainder of the misfit.

These observations allow us to conclude that the observed maps should prove superior in predicting group arrival times and should prove useful in calibrating crustal models. However, improvements at periods below 20 s are still needed. These periods may be necessary to provide better fits to the data. In addition, the resolution analyses indicate that there are parts of the studied region that remain poorly constrained at all periods.

4.6 Conclusions.

We have reported the results of a systematic study of intermediate period (10 s - 40 s) Rayleigh and Love wave dispersion across Central Asia, western China, and parts of the Middle East. We believe that this study represents a significant improvement in the understanding of intermediate period surface wave dispersion across the studied region for three reasons.. First, this study displays denser and more uniform data coverage and demonstrates higher resolution than previous studies performed on this scale and at these periods. Second, the group velocity maps

67

display the signatures of known geological and tectonic features never before revealed in surface wave studies on this scale. These group velocity maps provide entirely new constraints on sedimentary basins and crustal velocities and thicknesses. This lends credence to the maps and spurs interest in their use to infer information about the features that we observe. Third, the group velocity maps provide a significant improvement in fit to the observed dispersion curves. The group velocity maps presented here are already used to predict group travel times for the identification and extraction of surface wave packets, and as data in inversions for crustal upper mantle models (e.g., Ritzwoller *et al.*, 1999; Shapiro and Ritzwoller, 2001).

There are several key ingredients in order to estimate group velocity maps at these periods. First, there must be earthquakes and broadband instrumentation in the region of study. Second, dispersion measurements must be carefully performed to separate the direct arrival from scattering coda and other interfering waves. Third, data should be used from smaller earthquakes than those normally studied on continental or global scales (i.e., $M_s \leq 5.0$). Finally, the regional measurements should be combined with measurements made on a larger spatial scale. The inclusion of measurements on paths that propagate more broadly across Eurasia provides greater homogeneity of coverage and azimuthal distribution across the studied region and appreciably improves resolution and accuracy.

Section 5
Evaluation of Uncertainties and Bias in Surface Wave Tomographic Maps and Travel Time Correction Surfaces

5.1 Introduction.

Estimation of surface wave amplitudes plays an important role in the discrimination of explosions from earthquakes. For small seismic events surface wave signals are often too weak to be directly measured or even detected on seismograms. The most efficient technique for extracting such signals from ambient and signal- generated noise is phase-matched filtering (Herrin & Goforth, 1977; Russel et al., 1988; Stevens & McLaughlin, 1997; Leach et al., 1998; Levshin et al., 1998). Lateral inhomogeneity of the crust typical for tectonically active regions, such as Central and Southern Asia and the Near East, produces a variability in surface wave propagation from seismic sources to recording stations. To design efficient phase-matched filters, it is necessary to account for this diversity by tuning filters to a particular wave path. This can be done for each station using travel time correction surfaces (TTCSs) for a set of intermediate periods (10 - 30 s). TTCS may be constructed using regional group velocity tomographic maps for these periods obtained as a result of the tomographic inversion of numerous surface wave dispersion measurements (Levshin et al., 1996, 1997, 1998; Ritzwoller & Levshin, 1998; Ritzwoller et al., 1995, 1998, 1999; Vdovin et al., 1999). The efficiency of phase-matched filtering based on TTCSs strongly depends on the their quality and the quality of the group velocity maps used for their generation. One of the ways to estimate the quality is to use ground-truth events for which hypocenter parameters are well known (Harkrider et al., 1998). Unfortunately there is only a limited number of ground-truth events located in Central and Southern Asia (Engdahl, 1998). Most of them are nuclear explosions at well known test sites. Subsequently, the azimuthal coverage of wave paths for ground-truth events to the existing network of stations is quite poor, and does not provide sufficient information for verifying TTCSs.

However, it is evident that both TTCSs and group velocity maps would be more useful if their uncertainties could be estimated rigorously. The estimation of formal uncertainties is complicated by the fact that the level of uncertainty depends on the spatial length-scale of the modeled features as well as unknown theoretical errors and unmodeled structures. Our purpose is to take steps toward understanding uncertainties in both the tomographic maps and the TTCS constructed from them. All analyses are based on data coverage for 15 s - 20 s Rayleigh waves in Central and Southern Asia as the region of main CTBT monitoring efforts.

The new method to construct tomographic maps which was described in Section 1 permits estimation of resolution and scale-dependent amplitude bias corresponding to a given data coverage. Based on the resolution matrix formalism, this method produces more reliable estimates of the quality of the tomographic maps than the more popular checkerboard tests. Unfortunately, these estimates do not propagate naturally into uncertainties in predicted travel times. To gain insight into the uncertainties in the TTCSs, we performed two synthetic experiments to determine the effects of limited spatial resolution of the tomographic maps and unmodeled azimuthal anisotropy. In the first experiment we evaluate how the effects of unmodeled sub-scale inhomogeneities present in an input model (e.g., sedimentary basins, surface

or Moho topography) and random noise, which is always present in real measurements, distort the TTSCs computed from estimated tomographic maps. In the second experiment we estimate errors in the TTSCs produced by azimuthal anisotropy unmodeled in the tomographic maps. The comparison of predicted travel times with observed travel times for several nuclear explosions will be given in Section 6.

5.2 Examples of Tomographic Inversion of Surface Wave Dispersion Measurements.

Figure 43 and Figure 44 demonstrate new isotropic tomographic group velocity maps for the target region between 15° and 50° N, 25° and 105° E for Rayleigh and Love waves at the 15 s period obtained by this technique from surface wave dispersion measurements described at Ritzwoller & Levshin (1998), Ritzwoller et al. (1998). The numbers of independent paths used for the inversion are 3160 for Rayleigh waves, and 2160 for Love waves.

The same figures show the path density (defined as a number of rays crossing $2^o \times 2^o$ bin), estimated spatial resolution of these maps, and amplitude bias resulting from smoothing. We define the amplitude bias as the relative difference (in percents) between the amplitudes of the observed output anomaly and of the input local perturbation of the group velocity. Zero bias corresponds to the undistorted amplitude imaging. We see that the spatial resolution for the territory defined above is quite high. We resolve features of the size 250 - 300 km on Rayleigh wave maps almost everywhere to the north of latitude 30°N, except NW Iran. The resolution on Love wave maps is slightly worse but still better than 300-350 km virtually everywhere in the same territory. We are able to contour even relatively small sedimentary basins, like the Dzhungarian basin and some others, as slow velocity spots on group velocity maps. The amplitude bias characterizing these group velocity maps is rather small, less than 10%, except the southern part of the region characterized by poor ray coverage.

We used these maps as input to construct the travel time correction surfaces for several seismic stations deployed in this region and belonging to the IMS network, namely AAK (Kirgizstan), ABKT (Turkmenistan), BRVK, KURK, MAKZ (all in Kazakstan), LZH, WMQ (China), and TLY (Russia). Examples of TTCSs for four of these stations are shown in Figure 45 for the 15 s Rayleigh wave. These figures show group velocity corrections δU for the path from any point on the map to a given station. The predicted travel time t for a selected path is found using the formula:

$$t = r/(U_o + \delta U), \tag{39}$$

where r is the epicentral distance and U_o is the reference value obtained by averaging the group velocities across the input map. Both group velocity maps and TTCSs exhibit significant variations in surface wave group velocities and group travel times across the region.

5.3 Synthetic Experiments With Isotropic Tomographic Maps.

To estimate uncertainties in tomographic maps and TTCSs constructed from them due to unmodeled sub-scale heterogeneities and random noise in measurements, we performed the following numerical simulations:

70

CU Group Velocity

Path Density

Spatial Resolution

Amplitude Bias
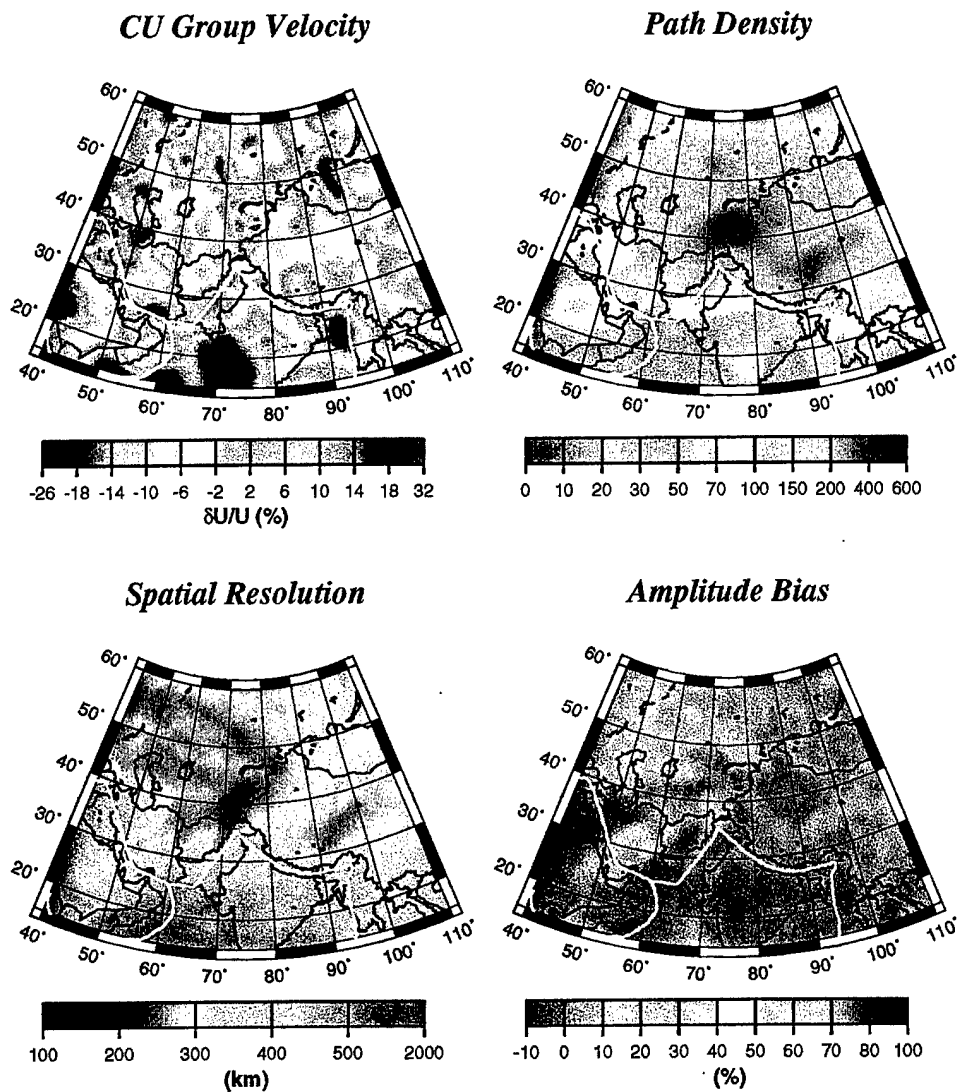
Figure 43. Estimated Rayleigh wave group velocity map and its assessment at the 15 s period. Path density is defined as the number of rays intersecting a 2° square cell.

71

CU Group Velocity

Path Density

Spatial Resolution

Amplitude Bias
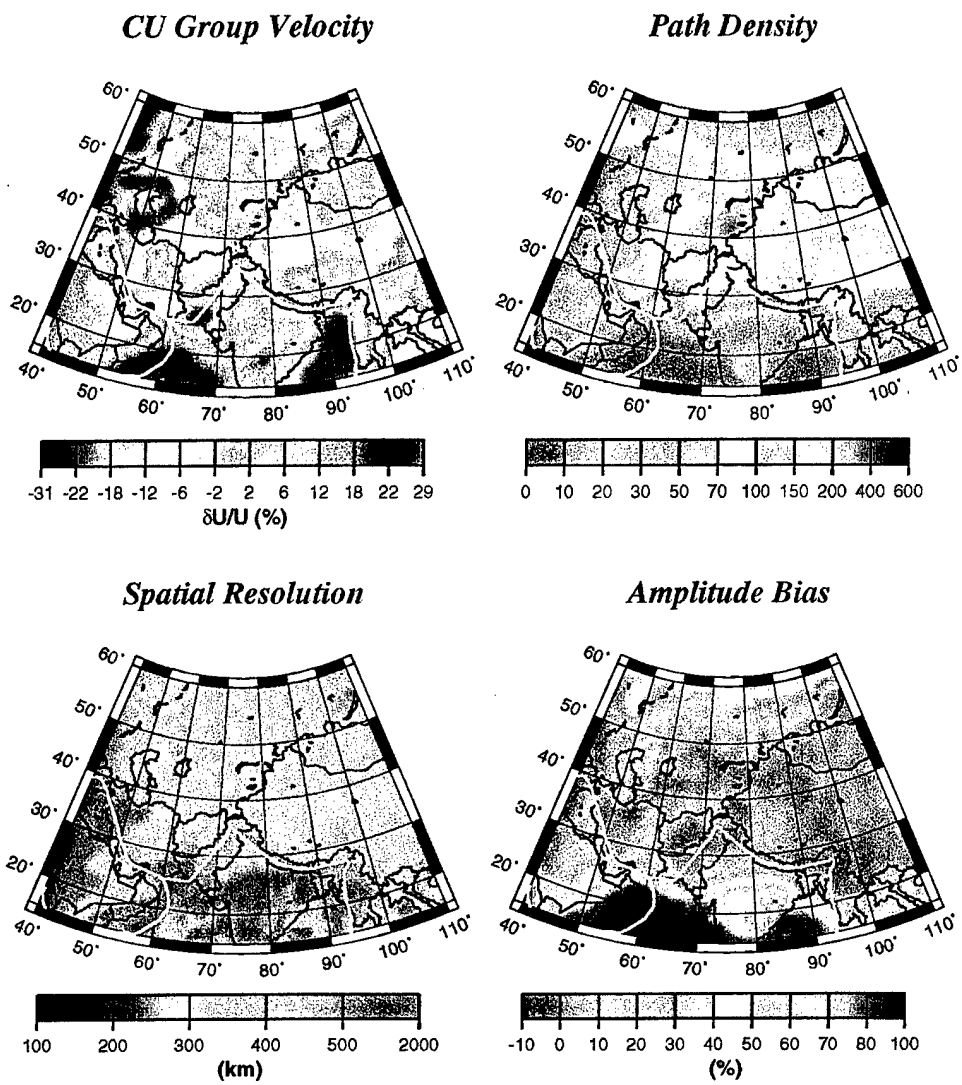
Figure 44. Same as Figure 43, but for the 15 s Love wave.

Group Velocity Correction Surfaces

15 s Rayleigh Wave

Reference Group Velocity 2.864 (km/s)
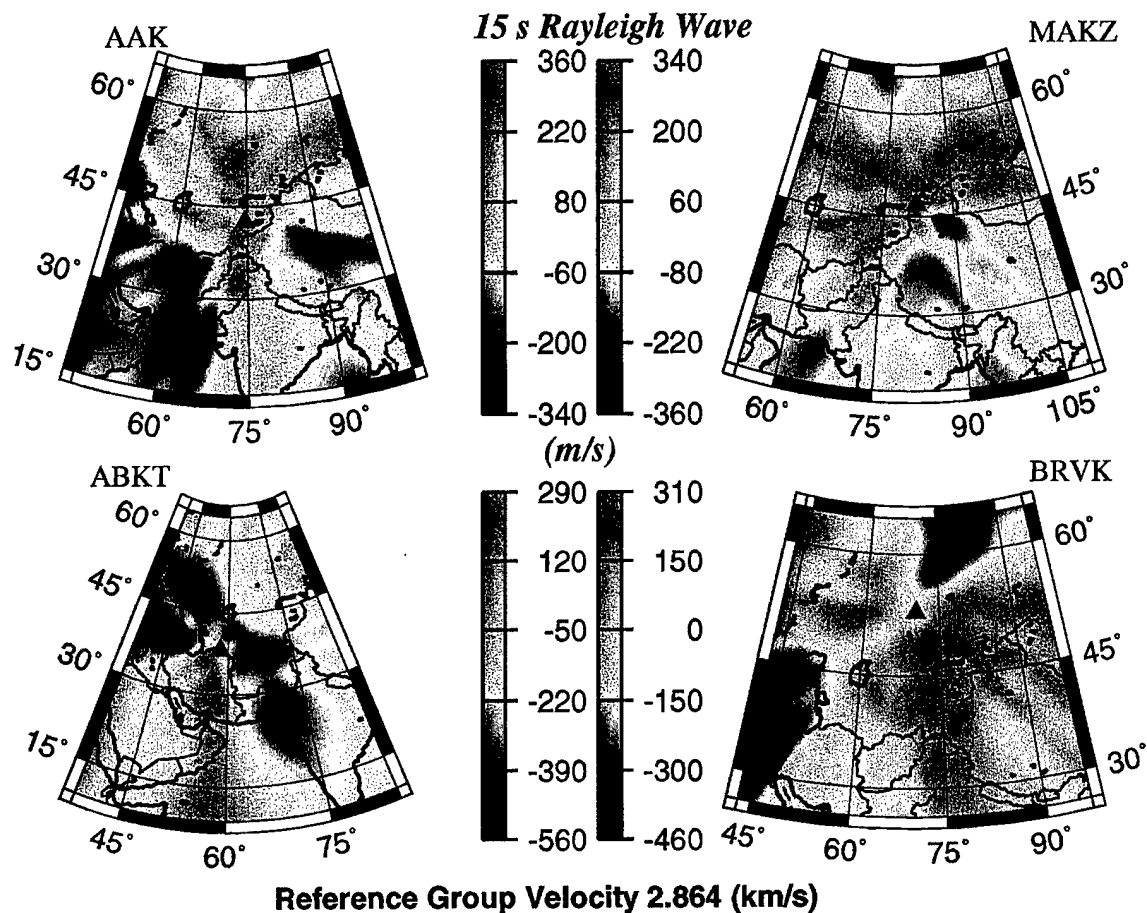
Figure 45. Group velocity correction surfaces for 4 stations in Central and Southern Asia for the 15 s Rayleigh wave. For each geographical point, maps define the group velocity perturbation that should be applied to a 20 s Rayleigh wave observed at a station if an event were located at the chosen point. Perturbations are relative to the reference value of the group velocity.

(1) the group velocity maps described above were considered as "exact" maps representing the real structure. We traced our set of rays across this model, assuming that waves follow great circle paths, and then introduced the random noise into the resulting average group velocities along each path. The rms of noise was selected to be equal to 0.03 km/s. This noise level is typical for group velocity observations along "clustered" paths (Ritzwoller & Levshin, 1998).
(2) This new set of "data" was then used as the input for the tomographic inversion code. We ran this code several times using different smoothing parameters and different background reference models: "exact" maps and maps predicted by the global crustal model of Mooney et al. (1998) . Smoothing parameters were chosen to get slightly "overdamped" tomographic maps. Resulting maps are distorted due to the random noise in input data, unaccounted sub-scale heterogeneity of the medium, and bias caused by the inhomogeneous path density. If we use our "exact" model as the background reference model in constructing the map, the distortion is caused only by the random noise and smoothing. In this case, the bias is minimized due to the rule for a local smoothing imbedded into our code: the less the path density the stronger the penalty for local deviation of a solution from the background model. The rms deviations of obtained maps from the "exact" ones are two or three times higher than the input noise level and slightly decrease with increase of smoothing. The rms deviation of "observed" group velocities from predicted by the constructed model is of the same order as the input noise level. In the realistic case of the absence of a good background model and nonhomogeneous path density, distortions become more significant.

Such an example is presented in Figure 46 where we used as the reference models group velocity maps predicted by the crustal global model of Mooney et al. (1998). This figure demonstrates difference between the input and constructed maps for the 15 s and 20 s Rayleigh waves and 20 s Love wave. The rms differences between the two maps are much higher than the level of random noise (of the order of 0.1-0.2 km/s), weakly depending on the smoothing parameter. The significant distortions correspond to the parts of the region characterized by poor coverage: the Caspian Sea, NW Iran, Oman Bay. At the same time, for most of the region, including all of Central Asia and Western China where the path coverage is good, the distortions are relatively small (1-2% of velocity values.) Note that the rms deviation of "observed" group velocities along individual paths from those predicted by the constructed model is only slightly higher than the input noise level. This was expected because distortions of the map caused by the poor coverage have almost no effect on group travel times. This example clearly demonstrates the importance of a reliable reference model when the path density is not homogeneous. In the absence of such a model, maps of spatial resolution and of amplitude bias should be used to outline poorly defined areas.
(3) We used these "noisy" and "overdamped" maps for constructing TTCSs, and compared them with TTCSs obtained from "exact" maps. Examples of differential TTCSs are presented in Figure 47. The rms values of differences between predicted and "exact" TTCSs vary from station to station mostly being of the same order of magnitude as the noise level (0.03-0.04 km/s). These values do not change significantly with changes of the smoothing parameters in tomographic inversion. The smallest differences are for the 20 s Rayleigh waves due to the highest density of paths. The largest differences are observed for the station ABKT in Turkmenistan due to the poor coverage of the western part of the region (NW Iran, Figure 47.)

Rayleigh Wave, 20 s

Reference Map

Difference

-36 -13 -9 -5 -3 -1 1 3 5 9 15 26 **(%)** -10 -8 -5 -3 -2 -1 1 2 3 5 8 10 **(%)**

Love Wave, 20 s

Reference Map

Difference

-36 -13 -9 -5 -3 -1 1 3 5 9 15 26 **(%)** -10 -8 -5 -3 -2 -1 1 2 3 5 8 10 **(%)**
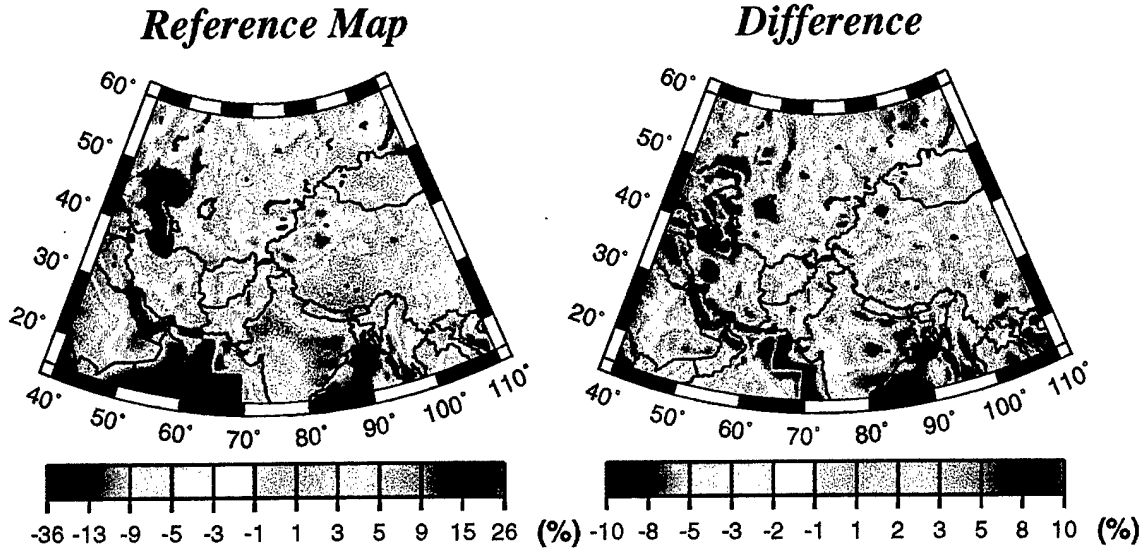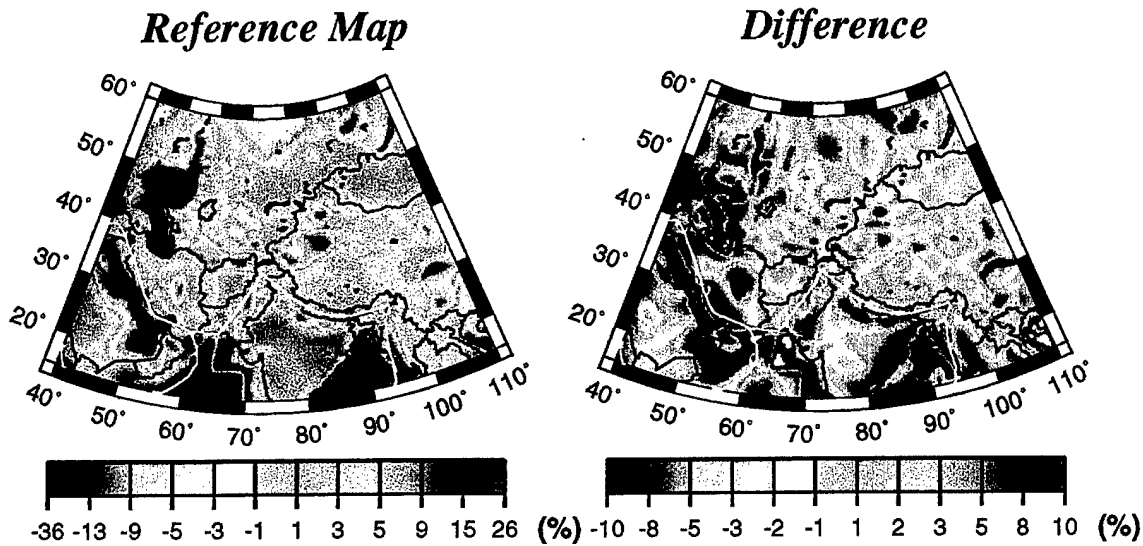
Figure 46. Synthetic example of errors in the constructed tomographic group velocity map for the 20 s Rayleigh and Love waves. Errors are due to the data noise, poor path density, and unmodeled sub-scale structures. The left map is an "exact" reference map. The right map is a relative difference (in percent) between the "exact" and constructed maps. The initial map for the tomographic inversion is predicted by the model CRUST5.1 (Mooney et al., 1998).
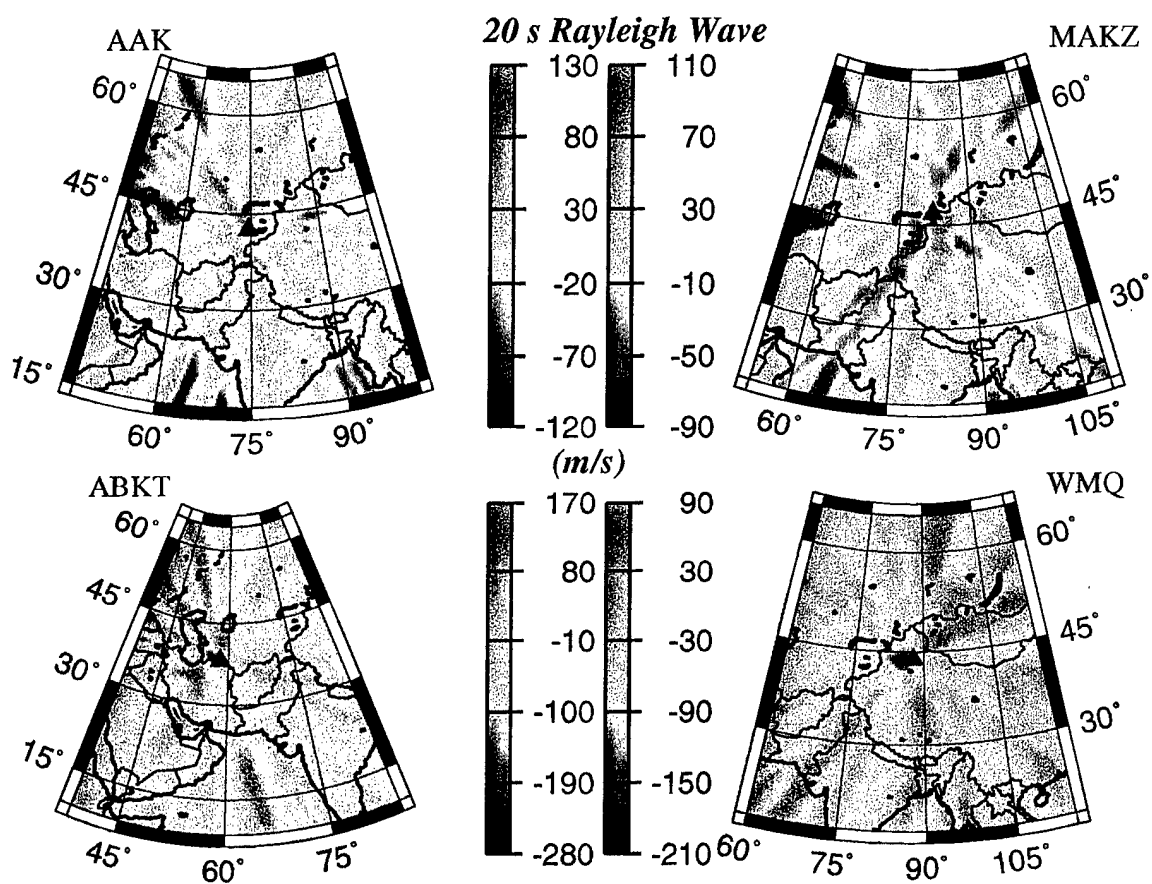
Figure 47. Errors in the travel time correction surfaces for the 20 s Rayleigh wave at four seismic stations. Errors (in ms) are obtained by subtraction of "exact" correction values of group velocity from values found using the maps shown in Figure 46.
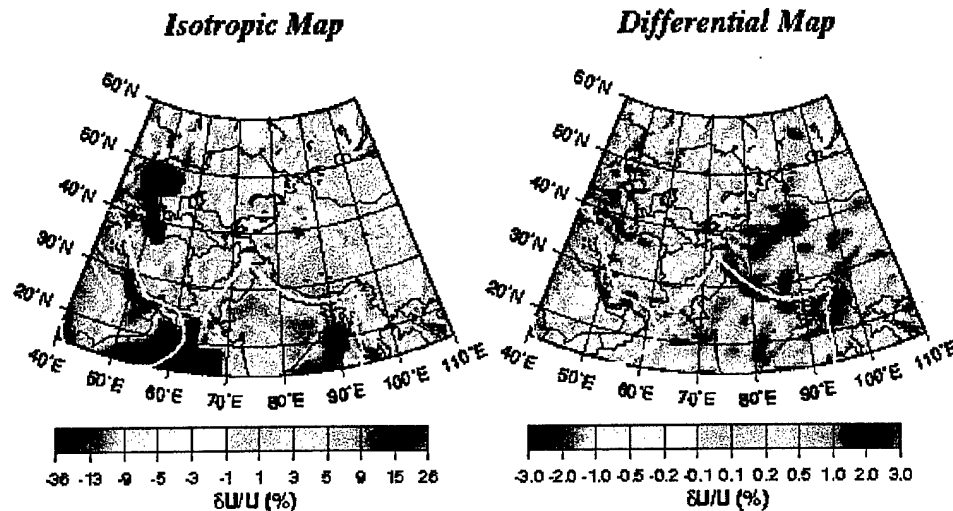
Figure 48. Errors in the group velocity map due to unmodeled azimuthal anisotropy introduced into the reference isotropic model for the Tibetan plateau. The left map is an isotropic reference map. The right map is a relative difference (in percent) between the "exact" and constructed maps. The initial map for the tomographic inversion is predicted by the model CRUST5.1 (Mooney et al., 1998).

5.4 Synthetic Experiments With Anisotropic Tomographic Maps.

Effects of unmodeled azimuthal anisotropy on tomographic maps and TTCSs were evaluated by the following way:

(1) We introduced 2% of the 2Ψ azimuthal anisotropy (Smith & Dahlen, 1973; Trampert & Woodhouse, 1995) into our "exact" maps across the Tibetan plateau , creating "exact anisotropic maps". Then, we traced rays across these maps to get a new "data" set for tomographic inversion. (2) We constructed a new set of isotropic tomographic maps using this new set of "data". The resulting maps are distorted due to the unaccounted effect of anisotropy. Differential maps demonstrating the differences between "real" and isotropic tomographic maps are shown in Figure 48. The differences between the "exact" isotropic map and the map constructed from "data" without modeling anisotropy are quite small for all reasonable values of the smoothing parameters. The rms of differences are on the order of 0.025-0.035 km/s, depending on the value of the smoothing parameter used in the inversion. The strongest differences are at some areas around Tibet and the poorly covered southern parts of the region. It is evident from this simulation that azimuthal anisotropy of this level cannot significantly distort the maps and TTCSs.

5.5 Conclusions.

The new technique for tomographic inversion of surface wave dispersion measurements provides necessary means for constructing travel time correction surfaces for selected stations and their

77

assessment in terms of spatial resolution and amplitude bias. The existing set of group velocity measurements across the Central Asia and Western China is sufficient for constructing reliable group velocity maps and TTCSs both for Rayleigh and Love waves at periods 15 s and longer. Synthetic experiments show that in areas with dense ray coverage the spatial resolution of these maps is on the order of 250 - 350 km and the amplitude bias is no more than 10accuracy of group velocity maps and TTCSs for the part of the region to the north of 25°N is typically better than 0.03-0.04 km/s. The unmodeled 2% azimuthal anisotropy across such large areas as the Tibetan plateau does not generate significant errors in group velocity maps and TTCSs constructed from them.

Section 6
Automated Detection, Extraction and Measurement of Regional Surface Waves

6.1 Introduction.

The $M_s : m_b$ discriminant and its regional variants are the most reliable transportable means of discriminating earthquakes from explosions. To measure surface wave amplitudes accurately in order to estimate M_s is very challenging for small events in which surface waves may not be readily identifiable in raw seismograms. To provide these amplitude measurements, it is crucial to be able to reliably detect small amplitude surface wave-packets and extract all and only the desired wave-packets reliably so that spectral amplitude measurements can be obtained.

We describe a surface wave detector and extractor designed to work on weak surface wave signals across Eurasia at intermediate periods (8 s - 40 s). It is founded on a long history of surface wave frequency-time analysis (e.g., Dziewonski *et al.*, 1969; Levshin *et al.*, 1972; Cara, 1973; Russell *et al.*, 1988; Levshin *et al.*, 1989, 1992). However, successful detection and wave-packet extraction are both dependent on the ability to make accurate predictions of surface wave arrival times at intermediate periods. Our method is based on the Rayleigh wave group travel time predictions from the recent broad-band group velocity maps of Ritzwoller and Levshin (1998) and Ritzwoller *et al.* (1998) and proceeds in three steps: signal compression, signal extraction or cleaning, and measurement.

First, the dispersed surface wave signals are compressed in time by applying an anti-dispersion or phase-matched filter defined from our group velocity maps. We refer to this as the "compressed signal". Second, the surface wave is then extracted by filtering "noise" temporally isolated from the time-compressed signal. This filtered signal is then redispersed by applying the inverse of the phase-matched filter. We refer to this wave-form as the 'filtered' or 'cleaned' signal. Finally, we adaptably estimate spectral amplitude as well as group and phase velocity on the filtered signal. After amplitudes are measured M_s is estimated using an empirical relation such as that recently presented by Rezapour and Pearce (1998).

The general methodology of matched filtering was developed previously by a number of other researchers (e.g., Herrin and Goforth, 1977; Stevens, 1986; Russell *et al.*, 1988; Stevens and McLaughlin, 1997). We introduce three innovations here: (1) the use of recent group velocity maps to define the matched-filters, (2) automation of the procedure, and (3) the use of the method as a detector.

We describe results of the application of this method to a set of nuclear explosions and earthquakes that occurred on or near the Chinese Lop Nor test site from 1992 through 1996 and one explosion on the Indian Rajasthan test site that occurred on May 11, 1998.

6.2 The Evaluation of the Travel Time Correction Surfaces.

The construction of group velocity maps and TTSCs was described in Sections 1, 4, and 5. Additional examples of TTSCs of the 20 s period Rayleigh waves for four stations in Central Asia are shown in Figure 49. Here we will discuss how well the travel times predicted by TTCS agree with observations. We note two things about the correction surfaces in Figure 45 and Figure 49. First, the corrections can be very large. For example, the 20 s Rayleigh wave from an event in the Caucasus 2500 km to AAK would experience a total group velocity perturbation of almost 400 m/s relative to the group velocity at AAK or a perturbation in arrival time of more than 2.5 minutes. Second, the correction surfaces at 20 s and 40 s are very different. This is because sedimentary basins control the 20 s map and crustal thickness controls the 40 s map.

Figures 50 - 52 provide information about how well the correction surfaces predict group velocity observations.

Figure 50 shows the overall rms-misfit for the Rayleigh waves from 15 s - 25 s period segregated by epicentral distance for observations made at four different stations. There is some indication of a diminishment of misfit with epicentral distance and misfit is highly variable between stations. Misfit also varies strongly as a function of wave path. More or less homogeneous paths are fit better than paths through complicated structures. Figure 51 and 52 exemplify this. Figure 51 presents the observed group velocities between about 8 s and 35 s period obtained for set of explosions and earthquakes on or near the Chinese Lop Nor test site, identified in Table 1. The error bars represent the standard deviations of the measurements obtained at a given station following several Lop Nor events. The number of events used for each station is listed in the upper right-hand corner of each panel. Comparison is made with predictions Ritzwoller *et al.* (1998) (solid line) and predictions from the hybrid crustal and mantle model CRUST5.1/S16B30 (dashed line).

Because of the strong structural variability in Central Asia, there are very different dispersion curves observed at the different stations. The trends of the observed dispersion curves agree fairly well with those predicted from our group velocity maps. In the case of ABKT, however, the agreement is very poor, presumably because the path from Lop Nor to Turkmenistan is along structural gradients which complicate the wave field in ways not represented by our group velocity maps (e.g., Levshin and Ritzwoller, 1995). Another comparison is presented in Figure 52 but in this case we have clustered the measurements made at five stations in KNET to estimate the error bars. Agreement is fairly good in this case. On average, rms-misfit is less than about 100 m/s near 20 s period, which amounts to an error in the predicted group travel time of less than 3%. The rms-misfit for the hybrid crustal and mantle model CRUST5.1/S16B30 (Masters *et al.*, 1996; Mooney *et al.*, 1998) is about twice this value.

6.3 Phase Matched Filter for Automated Detection, Extraction, and Measurement.

We describe here the method for detecting, extracting, and measuring surface waves. The method is entirely automated. We will describe the extraction and measurement first, assuming that the detection has been made and then will discuss the detector. To extract surface wave signals we use a phase-matched filter based on our group velocity correction surfaces and to detect weak signals we simply allow the filter to slide along the time axis. The method of extraction and
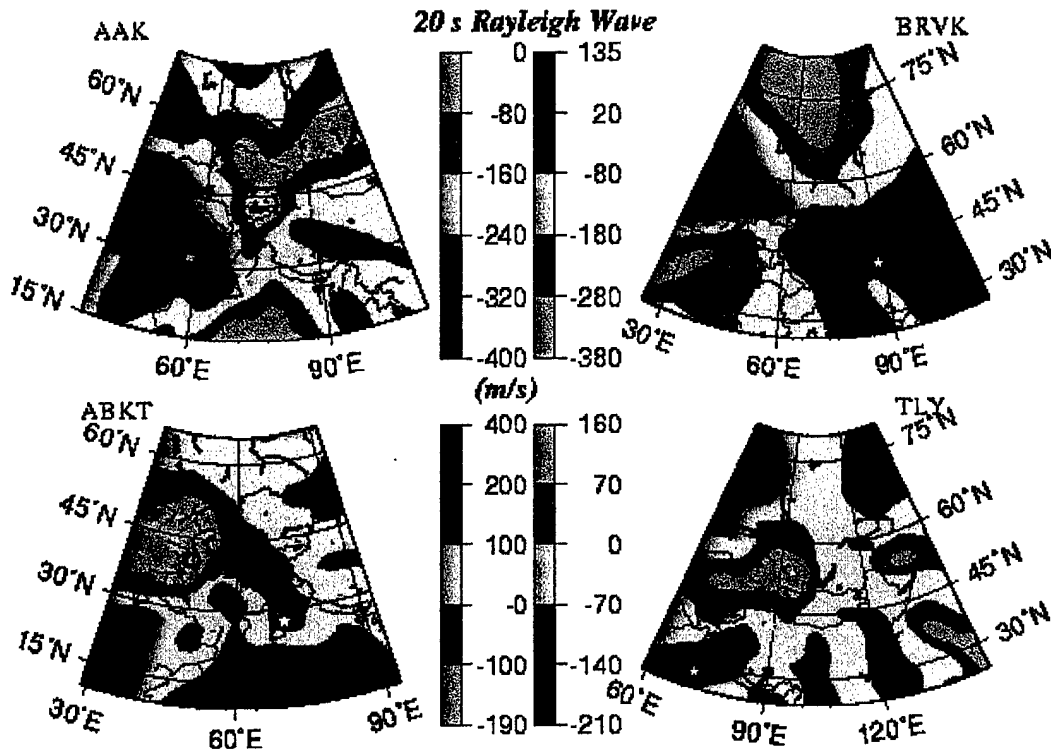
Figure 49. Group velocity correction surfaces for four stations in Central and Southern Asia for the 20 s Rayleigh wave. For each geographical point, the maps define the group velocity perturbation that should be applied to a 20 s Rayleigh wave observed at a station if an event were located at the chosen point. Perturbations are relative to the group velocity at the station. Units are m/s. The locations of the Chinese and Indian test sites are indicated with stars.

81
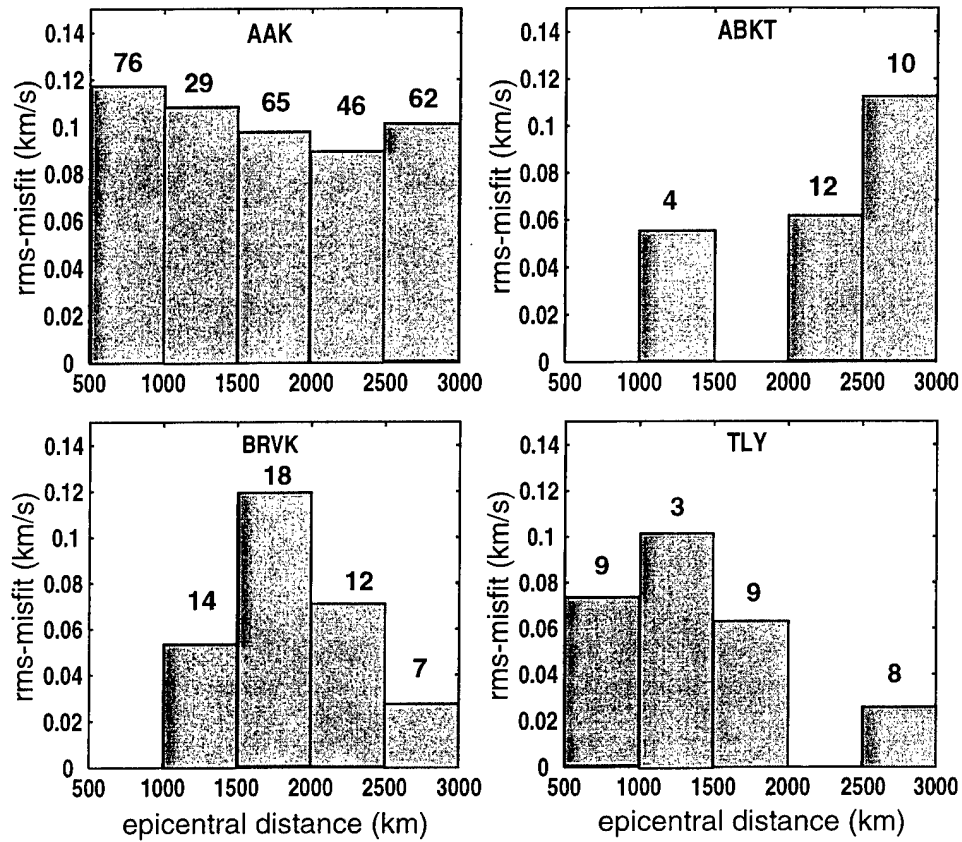
Figure 50. RMS-misfit between observed and predicted group velocities at four stations, plotted as a function of epicentral distance. Predicted group velocities are from Ritzwoller *et al.* (1998). The measurements are from a data base that includes earthquakes throughout Central and Southern Asia. The number of measurements per epicentral distance bin (summed over periods of 15 s, 20 s, and 25 s) is indicated above each histogram bar.
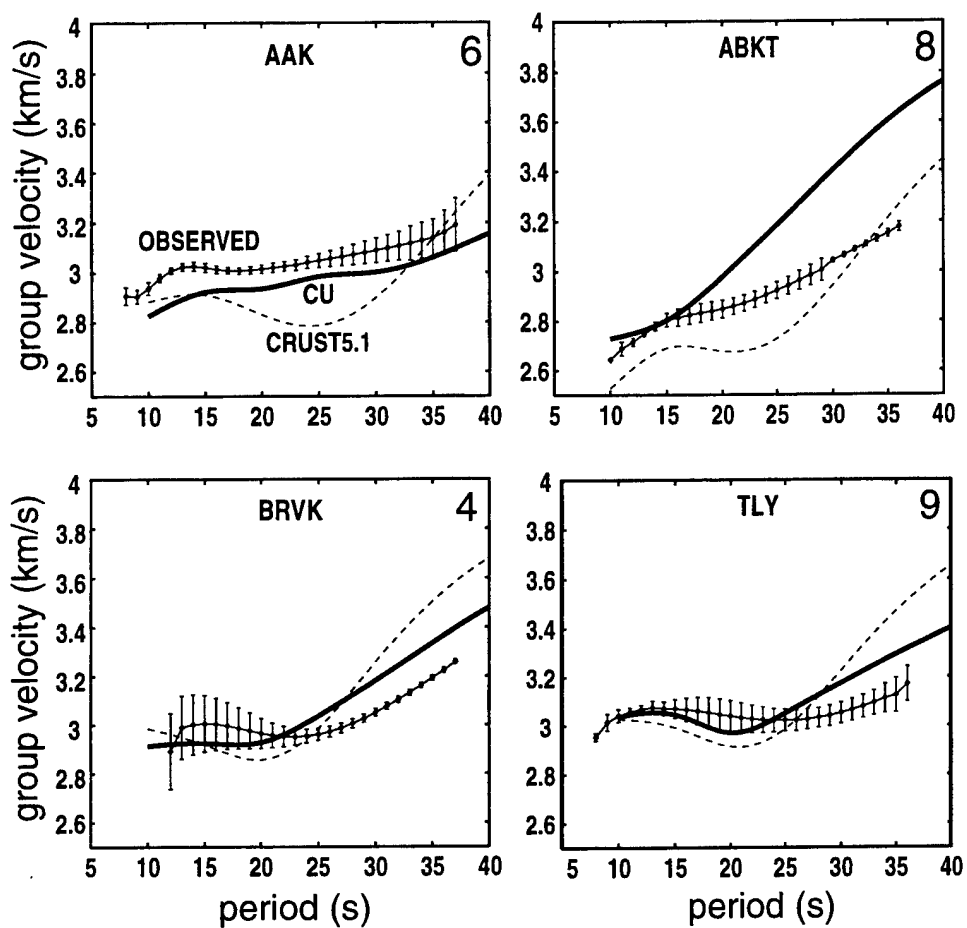
Figure 51. Comparison between observed and predicted group velocity curves. Group velocity measurements (error bars) at four stations in Central and Southern Asia following several nuclear explosions and earthquakes (Table 1) that occurred on or near the Lop Nor test site.
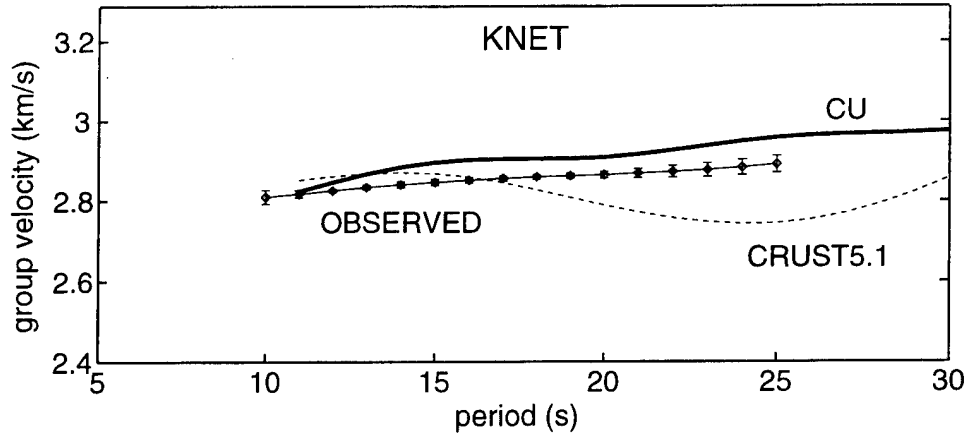
Figure 52. Like Figure 51, but for one of the Indian nuclear tests on May 11, 1998 observed at 5 stations of KNET.

Table 1. Events on or near the Lop Nor test site used in Figure 51

event type	date (mm/dd/yyyy)	time (Z)	m_b	M_s
explosion	5/21/1992	4:59:57.5	6.5	5.0
explosion	10/5/1993	1:59:56.6	5.9	4.7
explosion	6/10/1994	6:25:57.8	5.8	-
explosion	10/7/1994	3:25:58.1	6.0	-
explosion	5/15/1995	4:05:57.8	6.1	5.0
explosion	8/17/1995	0:59:57.7	6.0	-
explosion	6/8/1996	2:55:57.9	5.9	4.3
explosion	7/29/1996	1:48:57.8	4.9	-
earthquake	9/25/1992	7:59:59.9	5.0	-
earthquake	11/27/1992	16:09:09.1	5.3	4.8
earthquake	12/26/1994	16:58:46.1	4.6	-
earthquake	3/18/1995	18:02:36.6	5.2	-
earthquake	3/20/1996	2:11:21.9	4.8	

measurement is similar to that described by Levshin *et al.* (1992), but here it has been automated.

Assume that the coordinates of the epicenter and the epicentral distance Δ to the station are approximately known. Let the surface wave signal $s(t)$ be

$$s(t) = \pi^{-1} Re \int_{\omega_0}^{\omega_1} |S(\omega)| e^{i(\omega t - \Psi(\omega))} d\omega, \tag{40}$$

where the origin time is assumed to be at zero time, $\Psi(\omega) = k(\omega)\Delta = \omega\Delta/C(\omega)$ is the negative of the phase spectrum relative to the origin time, $C(\omega)$ is the phase velocity curve, k is wavenumber, and $|S(\omega)|$ is the amplitude spectrum of $s(t)$. The effects of dispersion on $s(t)$ are contained within the phase spectrum.

We wish to compress the signal by undispersing it in order to maximize the signal-to-noise ratio. To do this we would like to apply the correction $\psi(\omega) = \Psi(\omega)$, but typically we do not know the phase velocity or wavenumber curves reliably at periods below about 40 s. Thus, we must estimate the phase correction either from a 3-D model or from group velocity maps. The 3-D model approach is taken by Stevens and McLaughlin (2001). The advantage of this approach is discussed further below. Models, however, are not as well resolved as group velocity maps and the signal-to-noise enhancement of the matched filter will depend on the accuracy and resolution of the dispersion maps used to undisperse the surface waves. In order to optimize resolution, we use recent group velocity maps to build the matched filter. To do so, we must utilize the relation between group and phase velocities, $U = d\omega/dk, C = \omega/k$, from which we see that:

$$k(\omega) = k_\circ + \int_{\omega_\circ}^{\omega} \frac{d\omega'}{U(\omega')}, \tag{41}$$

where

$$k_\circ = \int_0^{\omega_\circ} \frac{d\omega'}{U(\omega')}. \tag{42}$$

$U(\omega)$ is the group velocity curve, and the phase correction is

$$\psi(\omega) = k(\omega)\Delta. \tag{43}$$

In practice, the continuous curve, $U(\omega)$, is obtained by spline interpolating the discrete curve $U(T_i)$ from the group velocity maps for frequencies $\omega \in (\omega_0, \omega_1)$, the low and high cut-off frequencies of a band-pass filter applied to the observed seismogram. We typically construct the discrete curve, $U(T_i)$, for each source - receiver pair from at a set of periods $T_i = 10, 15, 20, 25, 30, 35, 40$ s, set $2\pi/\omega_0 = 10$ s and $2\pi/\omega_1 = 40$ s, and taper quickly at the lower and higher frequencies. Using Equations (41) and (43) we compute the envelope function, $E(t)$, of the compressed or undispersed signal as follows:

$$E(t) = \pi^{-1} \left| \int_{\omega_0}^{\omega_1} |S(\omega)| \exp[i\omega t - i\Psi(\omega) + i\psi(\omega)] d\omega \right|. \tag{44}$$

If the source time is known we apply the phase correction given by Equation (44) described above to the spectrum of the observed seismogram and return to the time domain. If the group velocity curve is accurate this should have effectively undispersed the surface wave. We demonstrate this with applications to synthetic and real seismograms. Synthetics are computed by fundamental
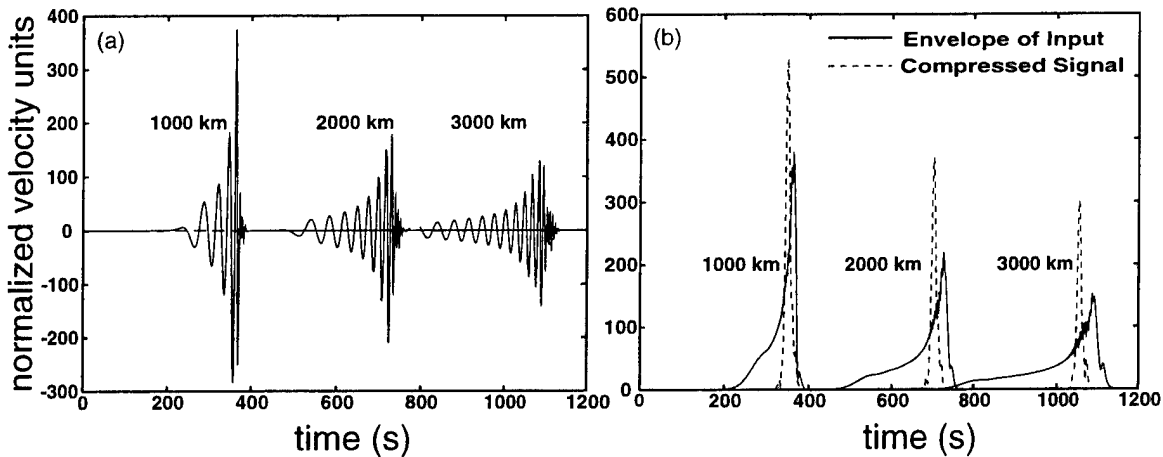
Figure 53. The synthetic example of the phase-matched filtering: (left) three synthetic Rayleigh waves computed for an explosive source at epicentral distances of 1000 km, 2000 km, and 3000 km; (right) the envelopes of the synthetic seismograms (solid lines) are compared with the envelopes of the compressed signals (dashed lines), $E(t)$, that result from the application of the phase-matched filter.

mode summation (e.g., Levshin et al., 1989) using a spherically symmetric model EUS. The velocities and Q values that define EUS are chosen to simulate stable, Eurasian structures. Compressed signals produced from the synthetic seismograms in Figure 53a are shown in Figure 53b. Signals from the real data following a large magnitude event (nuclear explosion at the Lop Nor test site on June 8, 1996, $m_b = 5.9$, $\Delta \sim 1200$ km to AAK) shown in 54a. The strong coda results from surface wave channeling by the Tarim Basin (Levshin and Ritzwoller, 1995). Compressed signals are contained in Figure 54b. Perfect compression would result in a sharply peaked function, as shown in the synthetic example. The example on real data is peaked, but not as sharply as the synthetic. Figure 53b shows that as the wave disperses, the amplitude of the compressed signal increases relative to the dispersed wave-form. Thus, the signal-to-noise enhancement of the compressed signal grows with distance.

The signal-to-noise enhancement at 1000 km in the synthetic example is about 20 - 30%, which is consistent with the $\sim 20\%$ enhancement observed on real data at 1200 km in Figure 54b.

To filter noise and unwanted signals we extract the compressed signal using a temporal window of fixed width centered on the peak of the compressed signal. The choice of the window width is ad hoc, but important. It should be broad enough to encompass the broadening of the compressed signal caused by the difference between the predicted and real dispersion curves, but narrow enough to filter out unwanted signals. Figure 50 demonstrates that for several stations in Central Asia using our entire surface wave data base, the rms-misfit is less than about 100 m/s and is roughly independent of range below 3000 km. We find that a time window centered at the peak of the compressed signal with a full width in time corresponding to a group velocity range of about 200 m/s is broad enough to work in most cases. More work is still required to calibrate this width, perhaps increasing it in structurally complex regions and decreasing it elsewhere. Finally,
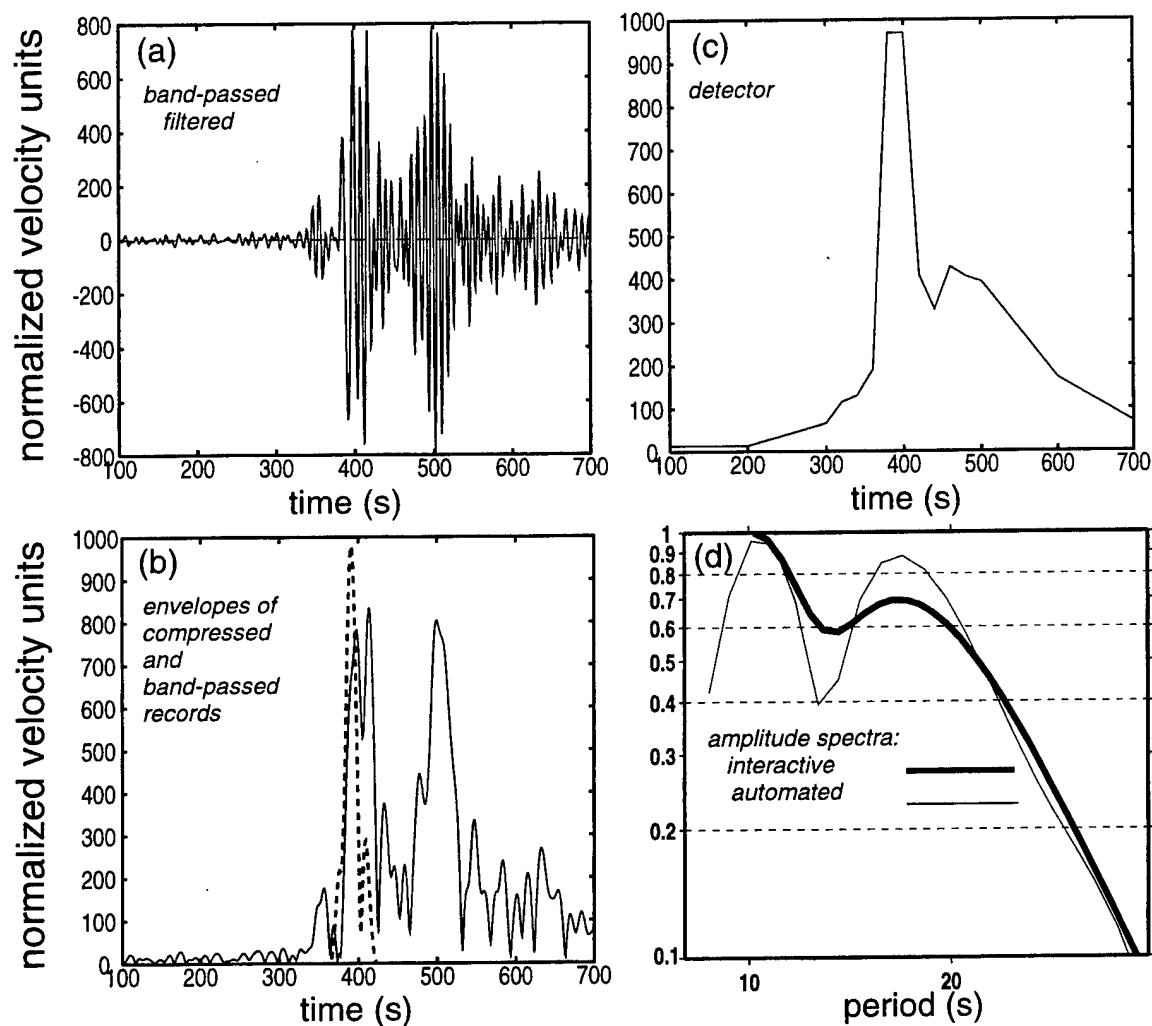
Figure 54. Demonstration of wave-form compression, detection, and spectral amplitude estimation of strong surface wave signals. (a) Band-passed (10 s - 40 s) vertical seismogram. (b) Comparison of the envelopes of the band-passed filtered seismogram (solid line) and the compressed signal (dashed line). (c) Peak amplitude of the envelope of the compressed signal, $D(t - t_0)$. (d) Rayleigh wave spectra found by automated frequency-time analysis and with human interaction during the frequency-time analysis.

we redisperse the extracted wave-form by applying the inverse of the matched-filter. Spectral amplitude as well as group and phase velocity are measured on the extracted wave-form exactly as described by Levshin *et al.* (1992) and Ritzwoller and Levshin (1998). In these papers, however, applications involved human interaction to control the wave-form extraction. This method is adaptive in that it finds the dispersion ridge and measures amplitudes and velocities on the ridge. Figure 54d shows an example of an automated spectral amplitude compared with the spectral amplitude estimated with human interaction to define the extraction filter. Discrepancies of 20% may exist below 20 s period, particularly near spectral holes.

In the description above we have glossed over an important subtlety. Knowledge of the phase correction, $\psi(\omega)$, requires us to know k_o, which in turn depends on an estimate of $U(\omega)$ to zero frequency. In fact, we estimate $U(\omega)$ only above some minimum frequency, ω_o. The result is that we only know $\psi(\omega)$ up to a constant of unknown value equal to $k_o\Delta$. Thus, the resulting envelope function will appear shifted in time by about $k_o\Delta$ from where it would appear if we knew the phase correction perfectly. The shift will always be toward shorter times relative to the location with the unknown constant included. Notice in Figure 53b that the location of the compressed signal marches to earlier times relative to the peak of the envelope of the uncompressed signal as the epicentral distance is increased. This uncertainty in the location of the envelope of the compressed signal is not a problem for most purposes, because we do not make any measurements on the compressed signal. Rather in our applications the compressed signal exists only to improve the detectability and to facilitate the extraction of the surface waves. All measurements are made when the signals have been uncompressed or redispersed. In the process of uncompression the time uncertainty that is introduced by compression is reversed and the extracted wave-form suffers no distortions in time. However, if the compressed signal would have resulted from a highly accurate phase correction, then the peak times of the compressed signal could be used to locate the event. Event location with weak surface wave signals probably is not a major desirable at this time. If it becomes important in the future and if 3-D models improve substantially in order to ensure the accuracy of the predicted phase velocity curves, then the model based method of Stevens and McLaughlin (2000) would be preferable to the method we discuss here.

If the source time is not known, the method we describe above may be naturally used to detect weak surface wave signals. We simply vary the source time, t_o, in a systematic way and plot the peak amplitude of the envelope of the compressed signal for each source time. We call this the detector time series, $D(t - t_o)$, which is a time series of amplitudes that will peak near the travel time of the compressed signal from the source. Signals with phase-content similar to the phase-matched filter are amplified and other signals are reduced. Figure 54c shows an example for a strong event. The signal-to-noise ratio (SNR) of this detection is about 75:1. Thus, the detector clearly has identified a signal. Strong detections need not be delta-like. The detector time series in Figure 54c displays a hump following the main detection caused by surface wave energy scattered into the Tarim Basin (Levshin and Ritzwoller, 1995). Figure 55 demonstrates that the detector based on our group velocity maps works much better than one based on the spherically symmetric model EUS. The signal-to-noise ratio of the detector time series is usually about 1.5 times higher using the group velocity maps than the model EUS.

6.4 Application to Weak Events.

The detection of strong events, such as the example in Figure 54, is straightforward. Detection and spectral estimation of weak events is the motivation of this study, however. We have applied
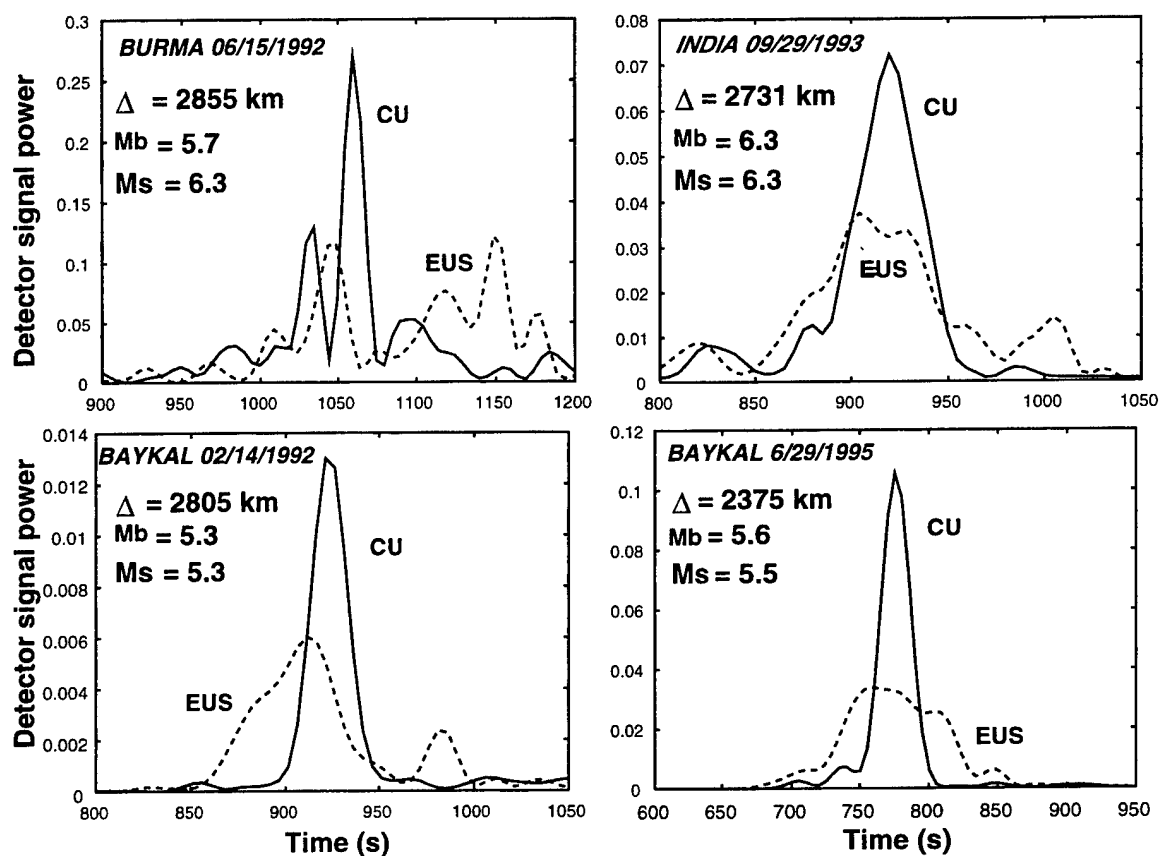
Figure 55. Comparison of the effectiveness of the automated detector based on two different group velocity correction surfaces: the group velocity maps of Ritzwoller *et al.* (1998) denoted as CU (solid lines) and the group velocity curve predicted by an average model of the crust and uppermost mantle for Eurasia denoted as EUS (dashed lines). All measurements are from the station AAK and the event location is indicated in each panel.

the detector/extractor/spectral estimator to broad-band records following a number of weak events at the Lop Nor, China test site and one of the nuclear explosions at the Indian Rajasthan test site that occurred on May 11, 1998.

Figure 56 shows the results for a nuclear test at Lop Nor with $m_b = 4.9$ that occurred on July 29, 1996. The M_s of this event is probably in the middle to high 3's, because, as Table 1 shows, the M_s for nuclear explosions at Lop Nor is usually more than a magnitude unit below m_b. As can be seen in Figure 56, the surface wave can barely be discerned on raw or band-passed records. However, the detection algorithm described above demonstrates a clear detection with a SNR of about 4:1 and the automated amplitude estimate is close to what is obtained with direct human interaction.

Figure 57 shows similar results for the Indian test (nuclear explosion at Rajasthan test site on May 11, 1998, $m_b = 5.1$, $\Delta \sim 1700$ km to KNET.) However, for the Indian test we have applied the method to five stations of KNET. The stations are located in structurally very different areas, and this apparently manifests itself as substantial differences in the observed amplitude spectra below about 18 s period. These differences are borne out when the measurements are obtained with human interaction. This highlights the difficulty in reducing the period at which M_s is measured below its current value of 20 s. Near receiver structural variations with spatial scales well below the resolution of group velocity maps or 3-D models can result in amplitude effects as large as 50% at periods below 15 s.

6.5 Conclusions.

We describe an automated surface wave detector and extractor designed to work on weak surface wave signals across Eurasia at intermediate periods (8 s - 40 s). The method is based on phase-matched filters defined by the Rayleigh wave group travel time predictions from the broad-band group velocity maps presented by Ritzwoller and Levshin (1998) and Ritzwoller *et al.* (1998). We describe preliminary results of the application of this method to a set of nuclear explosions and earthquakes in Central Asia. These and other applications lead us to conclude that this method shows considerable promise as a surface wave detector and of yielding high quality surface wave measurements automatically. It appears to be feasible to obtain automated spectral amplitude measurements for events in Central and Southern Asia with M_s down to as low as 3.5 - 4.0.

The method, however, requires further tuning and a more complete statistical evaluation. As discussed above, the extraction algorithm requires further work in that we need to calibrate the width of the temporal extraction window. The quality of the automated measurements and the SNR of the detection depend on the accuracy of the group velocity maps from which the phase-matched filter is defined. For example, more accurate maps allow sharper temporal filters to be applied which reduces bias in amplitude and velocity measurements caused by coda, multipathing, etc. The group velocity maps will continue to be improved and we anticipate improved performance when they are used. A more complete statistical evaluation of the automated spectral amplitude and velocity measurements relative to measurements obtained with human interaction would also be valuable.
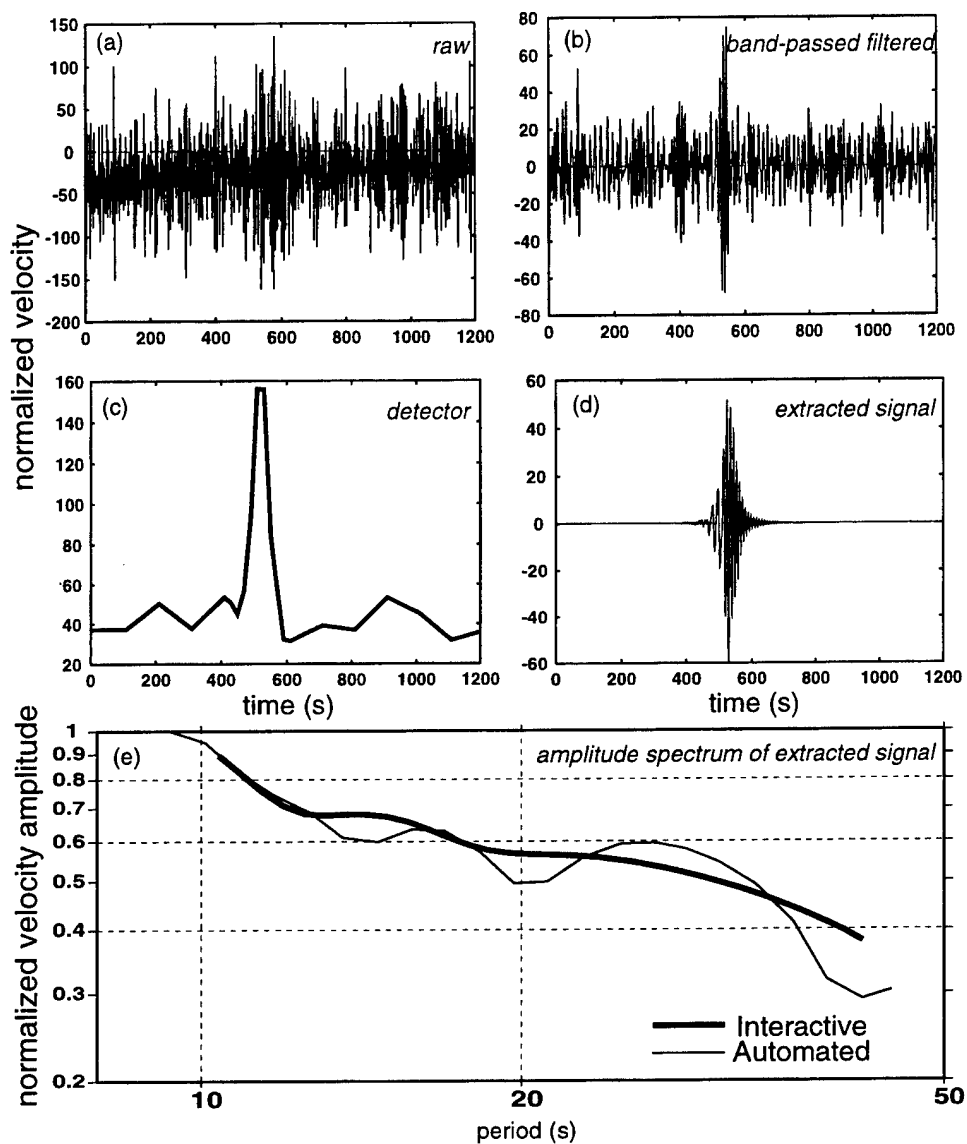
Figure 56. Demonstration of the detection, extraction, and spectral amplitude estimation of weak surface wave signals. (a) Raw vertical seismogram observed at TLY following a nuclear explosion at Lop Nor. (b) Band-passed (10 s - 40 s) seismogram. (c) Same as Figure 54c. (d) Extracted wave-form on which the spectral amplitude measurement is obtained. (e) Rayleigh wave spectra found by the automated frequency-time analysis and with human interaction during the frequency-time analysis.

91
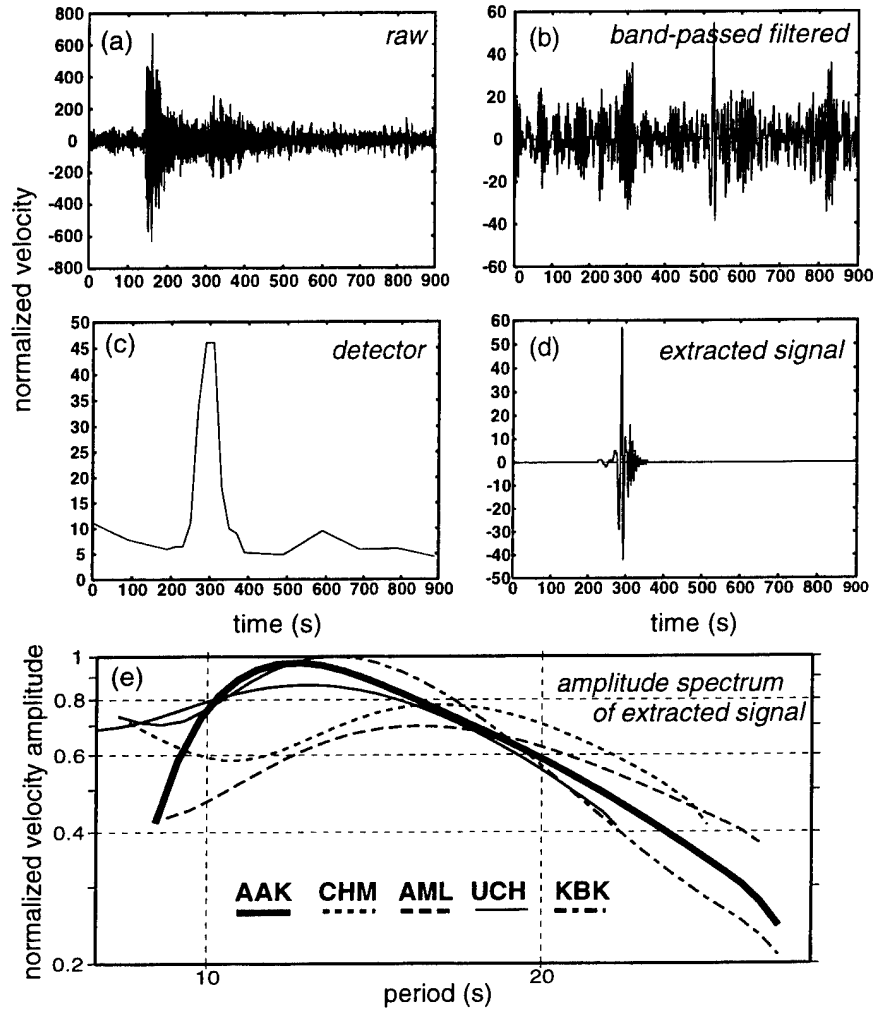
Figure 57. Same as Figure 56, but for a nuclear test in India. Nuclear explosion at the Rajasthan test site on May 11, 1998, $m_b = 5.1$, $\Delta \sim 1700$ km to KNET. The spectral amplitude measurements are at five KNET stations. Panels (a) - (d) are for AAK.

Section 7
Isotropic and Nonisotropic Components of Earthquakes and Nuclear Explosions on the Lop Nor Test Site, China

7.1 Introduction.

It has long been known that nearly all underground nuclear explosions have a significant component of nonisotropic seismic radiation (e.g., Press & Archambeau, 1962; Brune & Pomeroy, 1963; Aki & Tsai, 1972; Toksöz & Kehrer, 1972; Helle & Rygg, 1984; Wallace *et al.*, 1985; Walter & Patton, 1990). There appears to be general agreement that the long-period part of the nonisotropic radiation is caused by tectonic release due to existing tectonic stresses in the source region (Mueller & Murphy, 1971; Archambeau, 1972; Masse, 1981; Wallace *et al.*, 1985; Day & Stevens, 1986; Stevens, 1986; Day *et al.*, 1987; Patton, 1991; Stevens *et al.*, 1991; Harkrider *et al.*, 1994; Ekström and Richards, 1994; Li *et al.*, 1995).

Most of the experimental studies of tectonic release have concentrated on explosions at the Nevada Test Site and the test sites in Kazakhstan. Burger *et al.* (1986) described the long-period S wave radiation by tectonic release of explosions at Novaya Zemlya. Zhang (1994), Levshin & Ritzwoller (1995), and Wallace & Tinker (1996) studied Chinese nuclear explosions and found that most are accompanied by tectonic release. However, we are unaware of any detailed analysis of source mechanisms of these events.

Several authors have estimated the relative contributions of the nonisotropic (tectonic release) and isotropic (explosion) components to the resulting seismic moment tensor of explosions (see, for example, Ekström and Richards, 1994). As a rule these estimates have been performed using the assumption that both phenomena occur in the same small volume inside the Earth.

Although the determination of the source mechanism of earthquakes is a routine operation, only a few studies have evaluated the isotropic component of earthquake radiation. This is especially true for weak events that are of the primary interest for discrimination purposes. As is well known, a pure shear dislocation does not radiate an isotropic component. Subsequently, the natural tendency is to constrain the moment tensor solution with the assumption of a zero trace. However, from the point of view of discrimination it is important to determine if a significant isotropic component could appear in unconstrained moment tensor solutions due to some physical phenomena in the source region or due to inaccuracy of measurements and underlying assumptions.

In this section we will describe an approach of estimating the isotropic and nonisotropic components of the source mechanism and will apply this method to a small set of data for several earthquakes and explosions on the Lop Nor test site. The purpose is to determine whether the existence of a strong isotropic moment is consistent with the hypothesis that the event is an explosion. For each of the ten events we consider (7 explosions and 3 earthquakes, Figure 58, we obtain estimates of the isotropic and nonisotropic moments, characterize the tectonic release by estimating the moment tensor of the nonisotropic source, and estimate the depth of the equivalent double couple of the nonisotropic source. Our approach differs from those of previous studies in three main ways which are designed to focus the method on the discrimination problem: (1) we
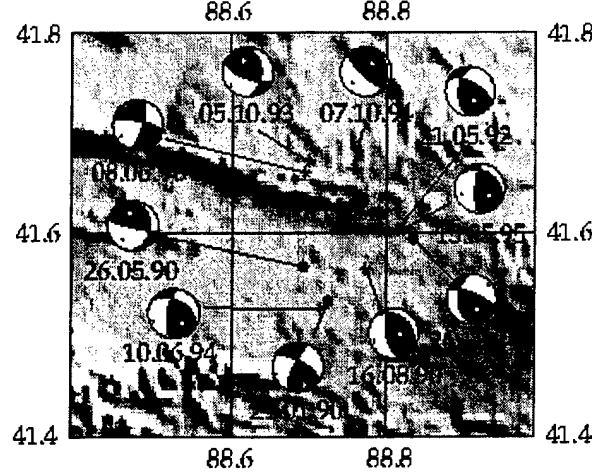
Figure 58. Epicenters and focal mechanisms of earthquakes (circles) and tectonic releases accompanying explosions (stars).

allow the depth of tectonic release for all events (earthquakes and explosions) to be variable and fix only the depth of the isotropic source near the surface, (2) we fit only the amplitude of the surface wave spectrum so the method, in principal, can be applied to much smaller events for which the interpretation of phase may be ambiguous, and (3) we minimize the misfit between synthetic and observed surface wave amplitude spectra jointly with fitting polarities of P-wave first arrivals.

Our approach is, therefore, based on the combination of an isotropic moment tensor at the surface, which models an explosive source, and a pure double couple at an estimated depth, which models tectonic release. We find it useful to express the seismic moment of the double-couple component, M_{0qu}, and the seismic moment of the isotropic component, M_{0ex}, as the total seismic moment M_0 and an angle φ which determines the ratio of the seismic moments of the isotropic and double couple components:

$$M_{0qu} = M_0 \cos \varphi \tag{45}$$

$$M_{0ex} = M_0 \sin \varphi \tag{46}$$

$$\tan \varphi = \frac{M_{0ex}}{M_{0qu}}. \tag{47}$$

We call φ the isotropic angle, for want of a better term, because $\varphi = 0$ corresponds to a pure earthquake and $\varphi = 90°$ corresponds to a pure explosion. With this notation and the assumption that the isotropic component of the source occurs at a known depth (usually at or near the surface), the source can then be characterized by six parameters: the seismic moment M_0, the isotropic angle φ, three angles (or two principal axes, **T** (tension) and **P** (compression)) determining the double couple focal mechanism, and the double-couple depth h.

We determine these source parameters by fitting the polarities of P-wave first arrivals jointly with

94

minimizing the misfit between synthetic and observed Love and Rayleigh surface wave amplitude spectra. We search for the optimal set of parameters by a systematic exploration of parameter space. To characterize the uncertainty of the source parameters, we calculate partial residual functions which describe the minimum misfit as a function of each varying parameter.

7.2 The Algorithm.

An instantaneous point source can be described by the moment tensor, a symmetric 3×3 matrix $\mathbf{M}$. Seismic moment, M_0, is defined by the equation $M_0 = \left(1/2\,\mathrm{tr}(\mathbf{M}^\mathrm{T}\mathbf{M})\right)^{1/2}$, where $\mathbf{M}^\mathrm{T}$ is the transposed moment tensor and $\mathrm{tr}(\mathbf{M}^\mathrm{T}\mathbf{M}) = \sum_{i,j=1}^{3} M_{ij}^2$. The moment tensor for any event can be presented in the form $\mathbf{M} = M_0\mathbf{m}$, where the matrix $\mathbf{m}$ is normalized by the condition $\mathrm{tr}(\mathbf{m}^\mathrm{T}\mathbf{m}) = 2$. We consider each event as a sum of an earthquake (0-trace moment tensor $\mathbf{M}_{qu}$) and an explosion (moment tensor $\mathbf{M}_{ex}$). The moment tensor $\mathbf{M}$ of such an event is given by the sum $\mathbf{M} = \mathbf{M}_{qu} + \mathbf{M}_{ex}$. If $\mathbf{I}$ be the 3×3 identity matrix, then $\mathbf{M}_{ex} = \sqrt{2/3}M_{0ex}\mathbf{I}$, where M_{0ex} is the seismic moment of the explosion. For the earthquake, $\mathbf{M}_{qu} = M_{0qu}\mathbf{m}$, where M_{0qu} is the seismic moment of the earthquake, and $\mathbf{m}$ is a normalized moment tensor that we will assume has the following characteristics: $\mathrm{tr}\,\mathbf{m} = 0$ and $\mathrm{tr}(\mathbf{m}^\mathrm{T}\mathbf{m}) = 2$. Thus, $\mathbf{m}$ represents a normalized double couple mechanism and we assume that $\mathbf{M}_{qu}$ represents a double couple source.

The tensors $\mathbf{M}_{ex}$ and $\mathbf{M}_{qu}$ are orthogonal in the sense we describe in the next paragraph. Thus, the total moment tensor is the sum of two orthogonal components, and the seismic moments of the explosion and earthquake components of the total moment can be expressed uniquely as total seismic moment M_0 and the isotropic angle φ between $\mathbf{M}$ and $\mathbf{M}_{qu}$, as given by Equations (45) - (47) above.

To show that $\mathbf{M}_{ex}$ and $\mathbf{M}_{qu}$ are orthogonal, consider the six dimensional linear Euclidean space of symmetric 3×3 matrices $\mathbf{M}$, and let the scalar product of two vectors $(\mathbf{M},\mathbf{N})$ be defined as $(\mathbf{M},\mathbf{N}) = \sum_{i,j} M_{ij}N_{ij} = \mathrm{tr}(\mathbf{M}^\mathrm{T}\mathbf{N})$. The isotropic tensors $\mathbf{M}_{ex}$ form a 1-D subspace which is orthogonal to the 5-D linear subspace of zero trace tensors $\mathbf{M}_{qu}$:

$$(\mathbf{M}_{qu}, \mathbf{M}_{ex}) = \sqrt{2/3}M_{0qu}M_{0ex}\mathrm{tr}(\mathbf{m}^\mathrm{T}\mathbf{I}) = \sqrt{2/3}M_{0qu}M_{0ex}\mathrm{tr}\,\mathbf{m} = 0. \tag{48}$$

Finally, the seismic moment of the combined event can be expressed by the formula:

$$\begin{aligned} M_0 = \sqrt{1/2\,(\mathbf{M},\mathbf{M})} &= \sqrt{1/2\left((\mathbf{M}_{qu} + \mathbf{M}_{ex}),(\mathbf{M}_{qu} + \mathbf{M}_{ex})\right)} = \\ &= \sqrt{1/2\,(\mathbf{M}_{qu},\mathbf{M}_{qu}) + 1/2\,(\mathbf{M}_{ex},\mathbf{M}_{ex})} = \sqrt{M_{0qu}^2 + M_{0ex}^2}. \end{aligned} \tag{49}$$

Our appoach then is to consider a seismic source as the combination of an isotropic tensor, modeling an explosion located at a zero depth, and a pure double couple point source at a depth h, modeling the tectonic release. Both explosions and earthquakes are considered as instantaneous sources. Such a source can be described by six parameters: isotropic angle φ, double couple depth h, three angles (strike, dip, slip) characterizing the focal mechanism or alternately the principal tension and compression axes $(\mathbf{T}, \mathbf{P})$, and the seismic moment M_0. We determine five of these parameters by a systematic exploration of the five dimensional parametric space, and the sixth parameter, M_0, by the least square minimization of the misfit between the observed and calculated surface wave amplitude spectra for every current combination of the other parameters.

Under the assumptions mentioned above, the relation between the surface wave displacement spectrum $u_i(\mathbf{x}, \omega)$ and the total moment tensor $\mathbf{M}$ can be expressed by the following formula

$$u_i(\mathbf{x}, \omega) = \frac{1}{i\omega} \left[M_{qu_{il}} \frac{\partial}{\partial y_{qu_l}} G_{ij}(\mathbf{x}, \mathbf{y}_{qu}, \omega) + M_{ex_{jl}} \frac{\partial}{\partial y_{ex_l}} G_{ij}(\mathbf{x}, \mathbf{y}_{ex}, \omega) \right], \tag{50}$$

where $i, j = 1, 2, 3$ and the summation convention for repeated indices is used. Here $G_{ij}(\mathbf{x}, \mathbf{y}, \omega)$ is the spectrum of the Green's function for the chosen model of the medium and the wave type (see Levshin, 1985; Bukchin, 1990), $\mathbf{y}$ is the source location, and $\mathbf{x}$ is the observation point. We assume that the explosion and earthquake have the same horizontal coordinates, but different depths: h for the earthquake and 0 for the explosion. Another important assumption is that the propagation medium has only weak lateral inhomogeneities so that the surface wave part of the Green's function is determined by structure near the source and receiver, by the average phase velocity along the path, and by geometrical spreading (Woodhouse, 1974; Babich et al., 1976; Levshin, 1985; Levshin et al., 1989). The amplitude spectrum $|u_i(\mathbf{x}, \omega)|$ defined by Equation (50) does not depend on the average phase velocity of the wave. Moreover, if lateral heterogeneities are sufficiently smooth, errors in source location do not affect the amplitude spectrum (Bukchin, 1990). Thus, we use only the amplitude spectra of surface waves to determine the source parameters. An example of fit to the surface wave amplitude spectra is shown in Figure 59.

Assuming that we know the relevant propagation characteristics of the medium, Equation (50) provides a system of equations for the 5 parameters defined above (φ, h, $\mathbf{T}$, $\mathbf{P}$). We define a grid in the space of these 5 parameters and use Equation (50) to calculate the amplitude spectra of the surface waves at the points of observation for every possible combination of values of the variable parameters. Comparison of the calculated and observed amplitude spectra gives us a surface wave residual $\varepsilon_{sw}^{(i)}$ for both Rayleigh and Love waves at each frequency ω. The index i runs through the entire set of observations. Specifically, it corresponds to a certain station, wave type, and frequency. Let $u^{(i)}(\mathbf{x}, \omega)$ be any observed value of the spectrum, $i = 1, \ldots, N$, and $\varepsilon_{sw}^{(i)}$ be the corresponding residual of $|u^{(i)}(\mathbf{x}, \omega)|$. We define the normalized amplitude residual by the formula

$$\varepsilon_{sw}(h, \varphi, \mathbf{T}, \mathbf{P}) = \left[\left(\sum_{i=1}^{N} \varepsilon^{(i)2}_{sw} \right) \bigg/ \left(\sum_{i=1}^{N} |u^{(i)}(\mathbf{x}, \omega)|^2 \right) \right]^{1/2}. \tag{51}$$

M_0 is found by the least square minimization of ε_{sw} for each combination of values of the five other variable parameters.

A well known problem in estimating moment tensors from surface waves is that the radiation pattern of surface wave amplitude spectra is symmetric with respect to the epicenter. Another uncertainty in moment tensor estimation appears when source depth is much less than the wavelength of the observed surface waves, in which case the surface waves provide only three linear constraints on the source parameters. To improve the resolution of the source parameters, we also use the polarities of P wave first arrivals. In calculating the radiation pattern of P waves for a set of source parameters, we assume that the waves radiated by the isotropic (i.e., explosion) and nonisotropic (i.e., tectonic release or earthquake) source arrive simultaneously. This assumption can be abolished if the observed signs of the P first arrivals would be substituted by polarities measured from long period P wave spectra (Bukchin et al., 1997). Before inversion we apply a smoothing procedure to the observed polarities as follows. A set of observed polarities (+1 for compression and −1 for dilatation) radiated in nearly the same direction is combined to form a single cluster and is assigned the mean of the cluster direction. If the number of one
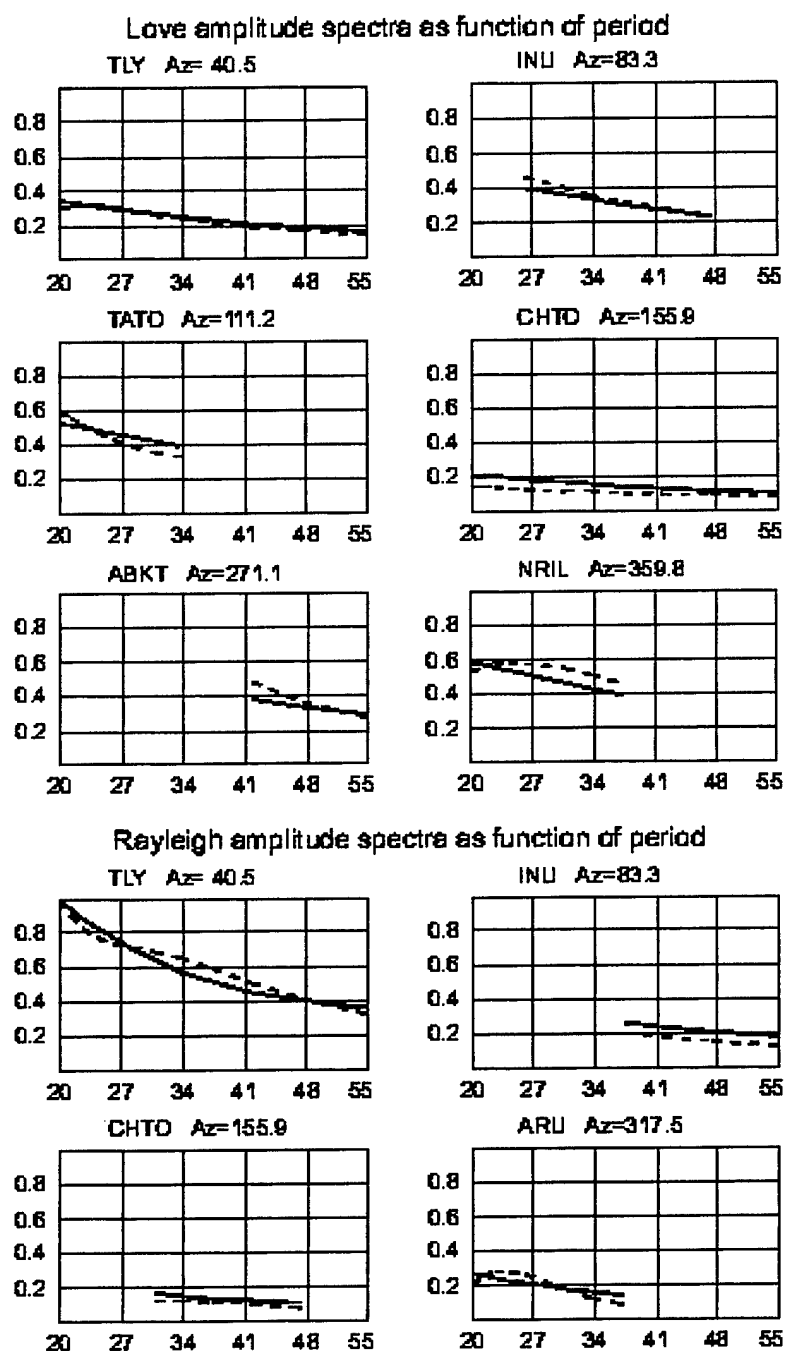
Figure 59. Comparison of observed (dashed lines) and computed (solid lines) Rayleigh and Love wave amplitude spectra for the explosion on 5 October, 1993. Stations' names and azimuths from the epicenter to the stations are provided. All spectra are normalized by the same value.

97

polarity in the cluster is significantly larger than the other, we prescribe this polarity to the mean direction. If neither of the two polarities dominate, then the entire cluster is discarded.

Using the misfit between the calculated and observed polarities, we calculate a joint residual of surface wave amplitude spectra and polarities of P wave first arrivals. Let ε_p be the residual of P wave first arrival polarities (the number of wrong polarities divided by the full number of observed polarities), we then define the joint residual ε by formula:

$$\varepsilon = 1 - (1 - \varepsilon_p)(1 - \varepsilon_{sw}) \tag{52}$$

If both residuals ε_p and ε_{sw} are small, then ε equals approximately to their sum. We consider the values of parameters that minimize ε as estimates of these parameters.

To evaluate the uncertainty of each of these source characteristics we calculate partial residual functions $\varepsilon_h(h), \varepsilon_\varphi(\varphi), \varepsilon_T(\mathbf{T}), \varepsilon_P(\mathbf{P})$ in the following way. For each value of a given parameter we find among all possible combinations of the other parameters such a value which provides the minimum of this function. Repeating the search for all possible values of the evaluated parameter we find one at which the corresponding residual function attains its minimum and take this value as an estimate of this parameter. The behavior of the residual function characterizes the uncertainty in determining the corresponding parameter.

7.3 Data and Data Processing.

We utilized IRIS and GEOSCOPE broadband digital seismograms and the ISC bulletins for 14 events that occurred on the Lop Nor test site in China from 1990 through 1996. Eight of these events are nuclear explosions, the other six are earthquakes. However, only 10 events with high signal-to-noise surface waves recorded at several stations were selected for study. The location of the selected events (7 explosions and 3 earthquakes) is given in Figure 58. The list of stations, with their distances and azimuths from Lop Nor test site are given in Table 2. In our calculations of the theoretical surface wave spectra we used three different models for (1) the structure for the source region, (2) the stations deployed in the stable continental regimes, and (3) the stations in the tectonic regions. For brevity we will call the corresponding models "Lop Nor", "Stable", and "Tectonic". The parameters for each model are presented in Table 3. For the Lop Nor model we used a regional velocity model for the four upper layers and the PREM model for deeper structure (see Lasserre et al., 2000). The Tectonic and Stable models are identical below first five layers. The column 4 in Table 2 indicates the model used for each station.

We estimated the source parameters using the spectra of Love and Rayleigh fundamental waves for periods ranging from 20 s to 70 s. Love and Rayleigh fundamental modes were extracted by using frequency-time analysis (FTAN) and floating filtering (e.g., Lander, 1989, and Levshin et al., 1994). We also analyzed the polarization of filtered surface waves using the technique described in Lander (1989), Paulssen et al., (1990), Levshin et al. (1992, 1994), and Levshin & Ritzwoller (1995). Only records in which the surface wave polarization pattern did not exhibit significant azimuthal anomalies ($\leq 15°$) were used for further analysis. Some examples of normalized amplitude spectra are shown in Figure 59. Note that the amplitude of the Love waves, which cannot be excited by a pure isotropic source, is comparable with the amplitude of the Rayleigh waves.

98

Table 2. Observed Seismograms and Models Used for Surface Wave Calculations for Each Station.

Station	Azimuth (o)	Distance (o)	Model
ABKT	271	24	Tectonic
ANTO	287	42	Tectonic
ARU	317	25	Stable
BNG	260	73	Stable
BRVK	319	17	Stable
CHTO	156	24	Stable
DPC	306	49	Stable
ENH	118	20	Stable
ERM	71	40	Stable
HIA	60	23	Stable
HYB	204	26	Stable
GNI	282	33	Tectonic
INU	83	38	Stable
KEV	333	42	Stable
KIV	290	34	Tectonic
KMI	140	20	Tectonic
KONO	320	50	Stable
LZH	111	13	Tectonic
MA2	43	42	Stable
MAJO	81	38	Stable
MDJ	70	29	Stable
NIL	242	15	Tectonic
NRIL	0	28	Stable
OBN	310	37	Stable
SEY	38	42	Stable
TATO	111	31	Stable
TLY	40	14	Tectonic
YAK	36	32	Stable

Table 3. Crustal and Upper Mantle Models Used for Surface Wave Calculations.

Lop Nor			
h(km)	V_p(km/s)	V_s(km/s)	ρ(g/cm^3)
1.1	5.08	2.9	2.26
5.8	5.90	3.5	2.59
14.1	6.06	3.57	2.65
30.9	6.51	3.77	2.83
8.1	8.09	4.47	3.38
20.0	8.07	4.46	3.38
35.0	7.99	4.37	3.37
35.0	7.97	4.36	3.37
35.0	7.95	4.34	3.36
35.0	7.93	4.33	3.36
45.0	8.56	4.60	3.45
45.0	8.65	4.64	3.48
45.0	8.74	4.67	3.50
45.0	8.82	4.70	3.53
50.0	9.22	4.95	3.76
50.0	9.47	5.09	3.82
50.0	9.73	5.23	3.88
50.0	9.98	5.38	3.94
50.0	10.14	5.46	3.98

Stable			
h(km)	V_p(km/s)	V_s(km/s)	ρ(g/cm^3)
19.0	6.14	3.55	2.74
19.0	6.58	3.80	3.00
12.0	8.20	4.65	3.32
10.0	8.17	4.62	3.34
10.0	8.14	4.57	3.35
10.0	8.10	4.51	3.36
10.0	8.07	4.46	3.37
10.0	8.02	4.41	3.38
25.0	7.93	4.37	3.39
25.0	7.85	4.35	3.41
25.0	7.89	4.36	3.43
25.0	7.98	4.38	3.46
25.0	8.10	4.42	3.48
25.0	8.21	4.46	3.50
50.0	8.38	4.54	3.53
50.0	8.62	4.68	3.58
50.0	8.87	4.85	3.62
50.0	9.15	5.04	3.69
50.0	9.45	5.21	3.82

Tectonic			
h(km)	V_p(km/s)	V_s(km/s)	ρ(g/cm^3)
20.0	6.14	3.55	2.74
20.0	6.80	3.93	3.00
10.0	8.10	4.51	3.32
10.0	8.10	4.51	3.34
10.0	8.10	4.51	3.35
10.0	8.10	4.51	3.36

h is the layer thickness

7.4 Results of Inversions.

A summary of the inversion results is given in Table 4.

Table 4. Information on the 10 Events Used in the Present Study.

Date	Event type	m_b	m_s	Number of records used	Double couple depth (km)	$M_0\ (N \cdot m)$	ψ (deg.)	φ (deg.)
21.01.90	earthquake	4.6	-	10	31	$0.15 \cdot 10^{17}$	72	0
26.05.90	earthquake	5.4	-	5	3	$0.42 \cdot 10^{16}$	52	0
26.12.94	earthquake	4.6	-	10	17	$0.15 \cdot 10^{16}$	56	0
16.08.90	explosion	6.2	-	7	1	$0.19 \cdot 10^{17}$	62	10-30
21.05.92	explosion	6.5	5.0	16	3	$0.62 \cdot 10^{17}$	64	10-15
05.10.93	explosion	5.9	4.7	10	0	$0.75 \cdot 10^{16}$	56	0-15
10.06.94	explosion	5.8	-	13	1	$0.52 \cdot 10^{16}$	64	20-40
07.10.94	explosion	6.0	-	11	1	$0.18 \cdot 10^{17}$	60	25-35
15.05.95	explosion	6.1	5.0	9	3	$0.15 \cdot 10^{17}$	62	40-60
08.06.96	explosion	5.9	4.3	12	3	$0.59 \cdot 10^{16}$	58	30-60

7.4.1 Double Couple Depths and Focal Mechanisms.

The focal mechanisms for the earthquakes and for the double couple components of the explosions are shown in Figure 58.

The double couple depth is well resolved for all events studied and varies from 0 to 3 km for the explosions and for the earthquakes we obtained depths of 3 km, 31 km, and 17 km. The partial residual function of double couple depth is presented in Figure 60 for all events. Figure 61 shows an example of the resolution of the double couple focal mechanism for the large explosion that occurred on October 5 1993 with $m_b = 5.9$ and $m_s = 4.7$. This figure displays the partial residual function of principal axes orientation. The principal compression axis is resolved better than the principal tension axis.

The number of surface wave records that we selected for the studied events was admittedly very small (see the column 5 in Table 4), particularly for the earthquakes on the test site. For some events, only a few polarities of P wave first arrivals were available. As a result, the double-couple focal mechanism was very well resolved only for the earthquake on 21.01.90, but for half of the events the principal compression axis, which trends in the SE-NW direction, was resolved well. Fortunately, Gao and Richards (1994) estimated focal mechanisms of several earthquakes in the vicinity of Lop Nor. Considering the focal mechanisms of the studied events, and the solutions obtained by Gao and Richards, we found that while focal mechanisms vary widely, there is a

Main tension axis

Main compression axis

0.13 0.14 0.15 0.16 0.17 0.18 0.19 0.20 0.21 0.22 0.23 0.24
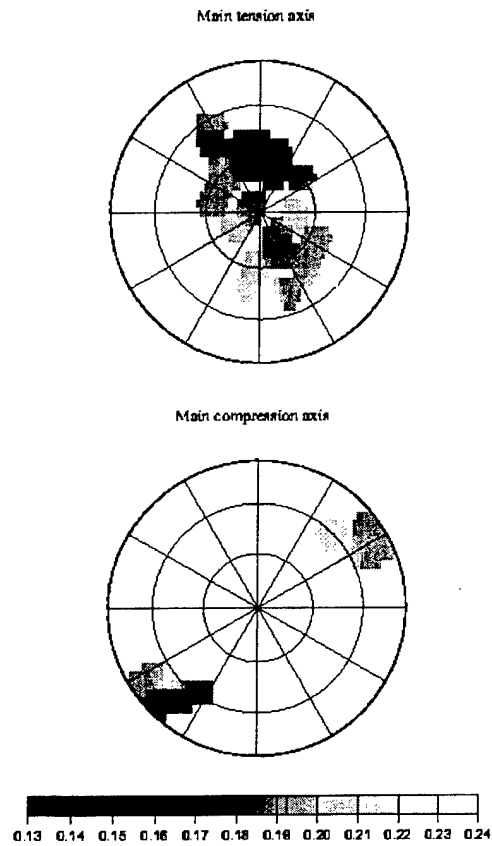
Figure 60. Partial residual functions of the orientation of the principal tension and compression axes for the double couple focal mechanism of the explosion on 5 October, 1993. The orientation of every axis is shown using a stereographic projection on the lower hemisphere.

102
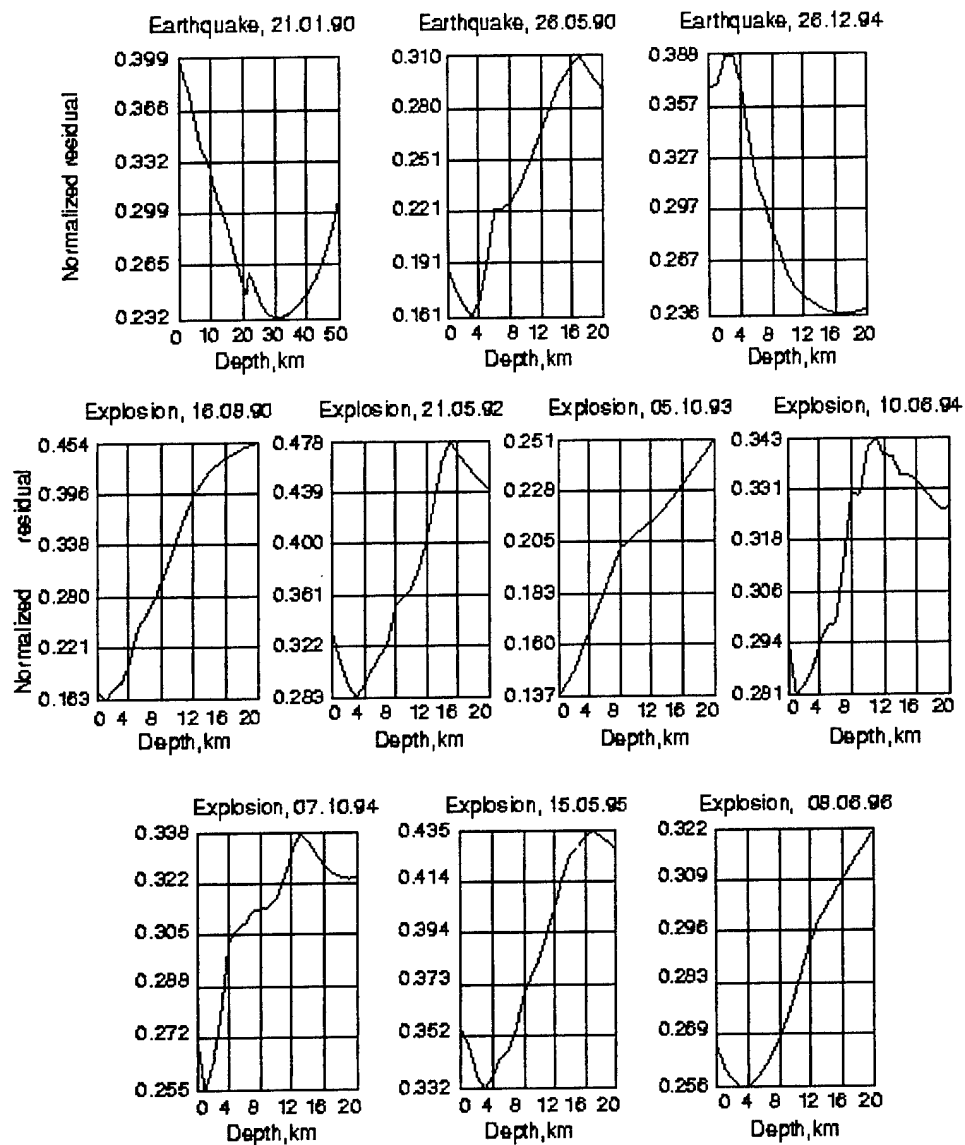
Figure 61. Partial residual functions of the double couple depth h.

moment tensor characteristic which is quite stable for all events. This characteristic is the orientation of the principal axes of the 2 × 2 minor of the moment tensor corresponding to the horizontal coordinates $\{M_{xx}, M_{xy}, M_{yx}, M_{yy}\}$. This minor describes the horizontal deformations on the horizontal plane. We found that for all events, horizontal compression is dominant, and the principal horizontal compression axis deviates from the average direction (with an azimuth of 60°) by no more than 12°. The direction of this axis for every event is given in the eighth column in Table 4.

7.4.2 Isotropic Component.

These observations allow us to improve the estimates of the isotropic angle φ by assuming that the orientation of the horizontal deformations is a stable characteristic for the region under study. The average direction of horizontal compression is deviated from the fault visible in Figure 58 by about 45°. With this assumption, we applied an *a priori* constraint on the possible double couple focal mechanisms. This constraint was formulated as a condition that the azimuth of the principal compression axis of the horizontal minor of the moment tensor cannot differ from 60° by more than ±45°. This constraint is weak, but reduces the number of possible focal mechanisms in half. Although the constraint is heuristic, we can present a special case when it is exact. This is when the deviatoric tectonic stresses in the region are horizontal and the direction mentioned above is the direction of principal compression. Then the constraint follows from the principle of positive deformation energy: $\sum_{i,j=1}^{3} S_{ij} M_{ij} \geq 0$, where **S** is the regional stress tensor, and **M** is moment tensor of event in the region.

When we applied this constraint, the resolution of the isotropic angle φ defining the seismic moments ratio was improved for three of the seven studied explosions (16.08.90, 05.10.93, and 08.06.96) but the mean of the curves did not vary appreciably. The curves of partial residual functions of the isotropic angle φ for all explosions are shown in Figure 62. Those for the three earthquakes are displayed in Figure 63. We also applied this method to two earthquakes that occurred in the Gansu province, China (Tianzhu, 1996, $M_s = 4.9$, depth 12 km, and Yongden, 1995, $M_s = 5.4$, depth 6 km) studied by Lasserre *et al.* (2000) under the assumption of a pure double couple source. The partial residual functions of the isotropic angle φ are also shown in Figure 63.

The explosions, with perhaps one exception (05.10.93), all display substantial non-zero isotropic angles φ ranging from about 10° to 50°, corresponding to M_{0ex}/M_{0qu} ranging from about 20% to 120%. In contrast, the isotropic angles for the earthquakes are all estimated to be approximately 0.

Figure 64 illustrates the effect of adding of an isotropic component to the double couple. source model for an explosion (on June 10 1994). Theoretical Rayleigh wave amplitude spectra and P wave first arrival polarities are compared here with observations for two different moment tensors. One (a,b) was obtained by minimizing the joint residual for a fixed zero isotropic angle (double couple source model). The other (c, d) is a result of a similar minimization, but for varying isotropic angle (30° is the estimated optimal value). The fit to P wave first arrival polarities is good for both source models, but the fit to Rayleigh wave amplitude spectra is much better in the case of a non-zero isotropic component.

Figure 65 illustrates the effect of adding of an isotropic component for the Youngden earthquake. Similar Figure 64, the results for two different moment tensors are presented here .One (a,b) was

104
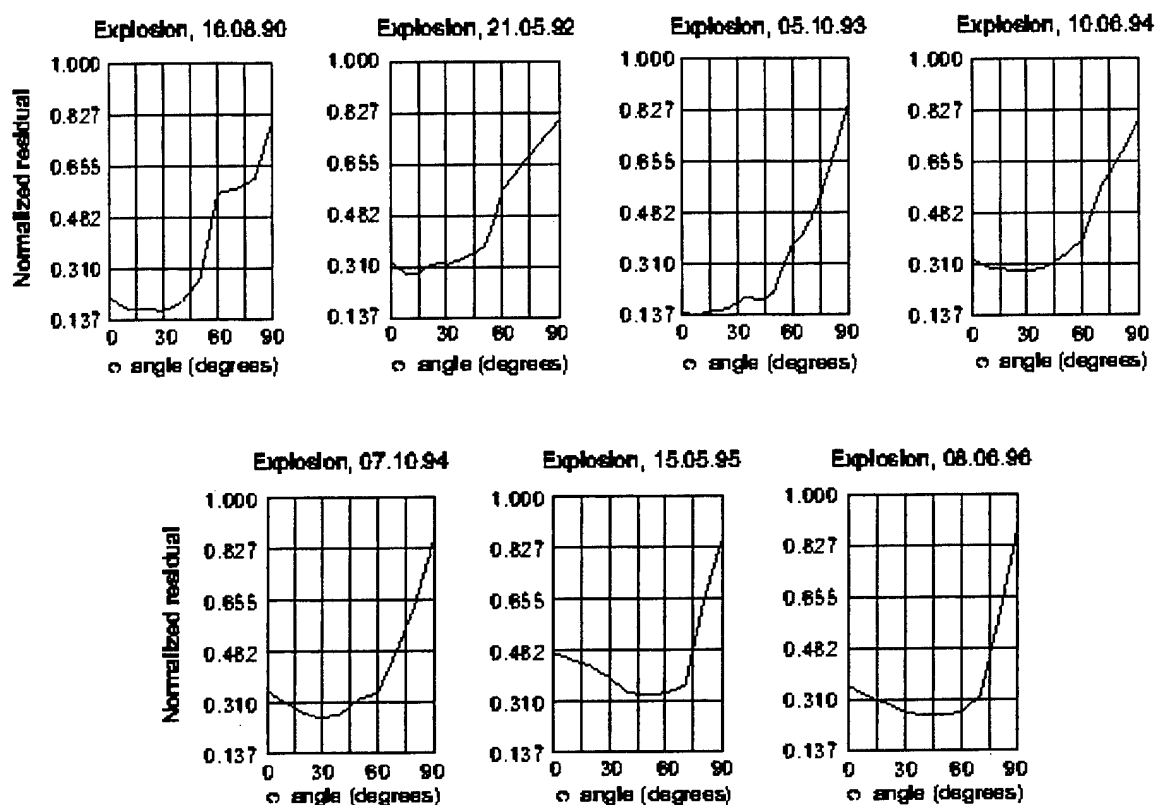
Figure 62. Partial residual functions of isotropic angle for studied explosions.
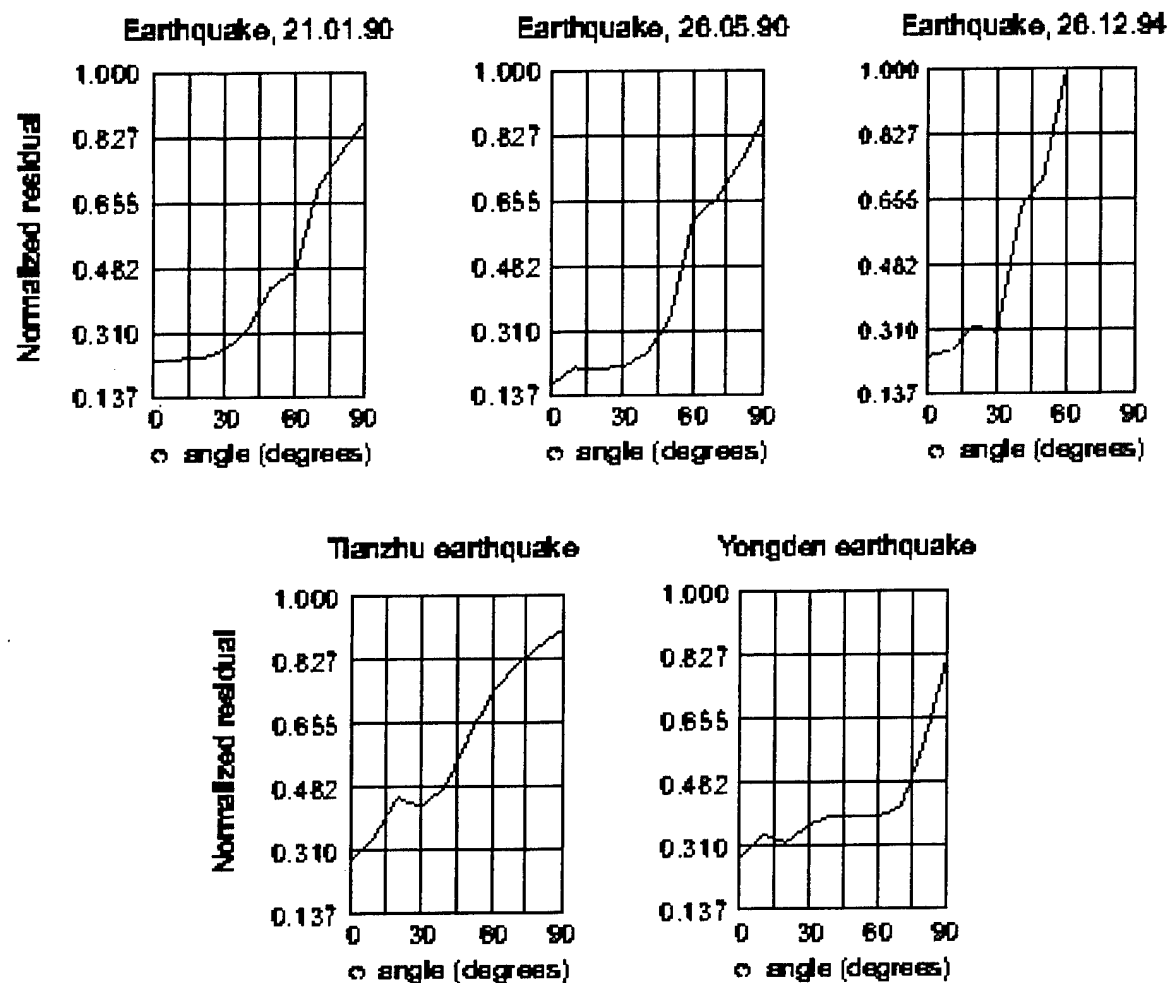
Figure 63. Partial residual functions of isotropic angle for studied earthquakes.

106
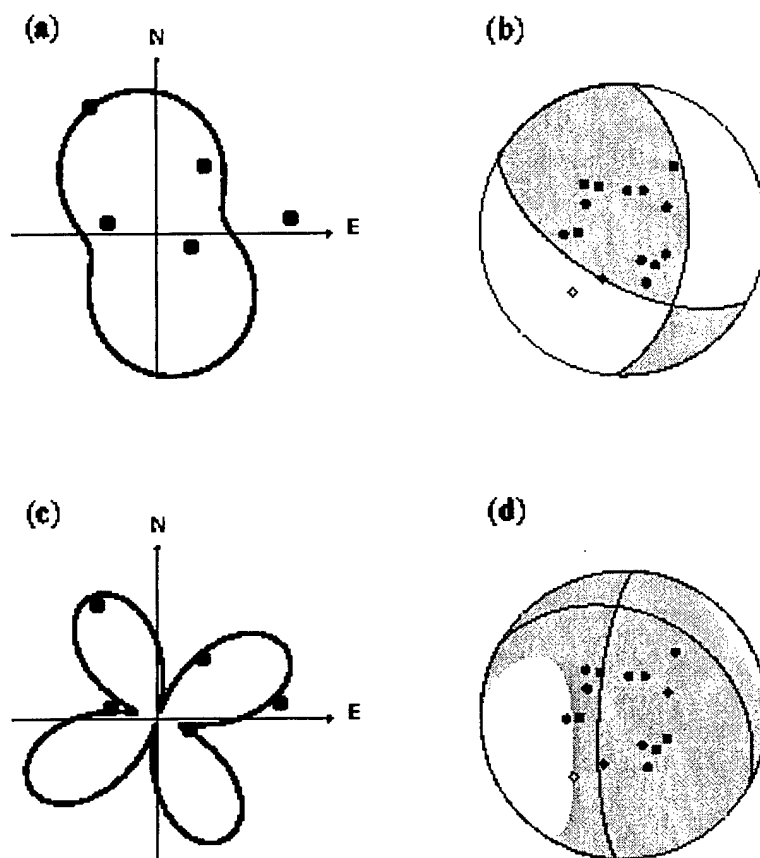
Figure 64. Comparison of observed Rayleigh wave spectral amplitudes at the 26 s period and polarities of first arrivals for the explosion on June 10, 1994 with those predicted for two different source models: (a, b) - pure double couple; (c,d) - non-zero isotropic component is added. (a,c) - observed (filled circles) and predicted (solid line) surface wave spectral amplitudes; (b,d) - observed positive (dark dots) and negative (white dots) P-wave polarities; predicted positive (shadowed areas) and negative (white areas) P-wave polarities.
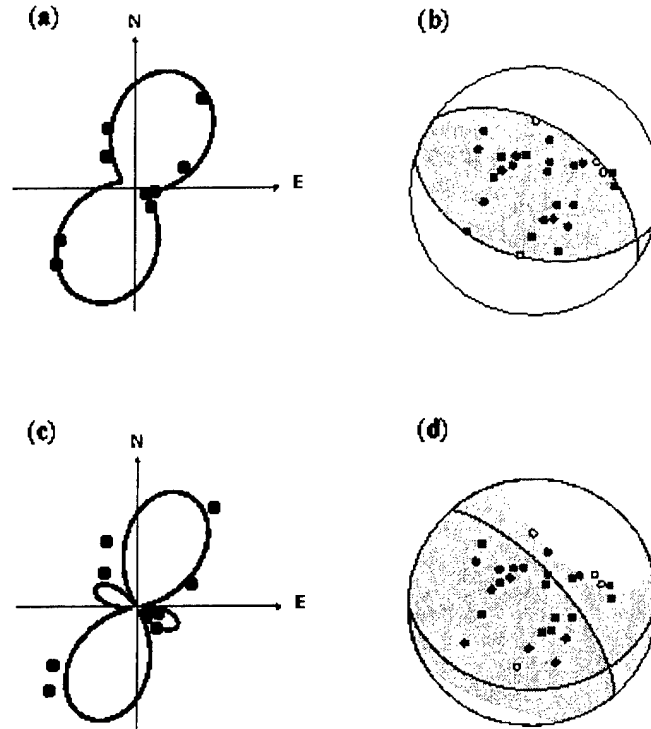
Figure 65. Same as Figure 64, but for the Yongden earthquake in Gansu province, China, on July 21, 1995 and the 50 s period.

obtained by minimizing the joint residual for a varying isotropic angle. The other (c, d) is a result of a similar minimization but for a fixed (30°) isotropic angle. In contrast with the previous case the fit is better for a pure double couple source.

7.5 Conclusions.

The results above are consistent with the hypothesis that motivates this study, numely, that for the events we analyzed on the Lop Nor test site surface wave amplitude spectra combined with polarities of P wave first arrivals can be used to discriminate explosions from earthquakes based on source characteristics alone (a combination of the double couple depth and the ratio of the isotropic to nonisotropic moments). Much more work remains to be done, however, to determine if the method can be applied to events with much smaller moments and if the method is transportable to other regions.

Section 8
Conclusions and Recommendations

8.1 Conclusions.

1. We have developed a method for rapidly constructing surface wave tomographic maps on local, regional or global scales together with useful measures of map quality. Extensive testing of this technique on data sets obtained from a variety of regions around the globe have confirmed its efficiency in producing detailed and reliable surface wave group and phase velocity tomographic maps.

2. We estimated the possible effect of source group time (SGT) on group velocity measurements for fundamental Rayleigh waves generated by double couple type seismic events. We have studied the dependence of this effect on period (10 s - 100 s), source mechanism, and depth (15 km - 100 km). We conclude that SGT corrections may be neglected in group velocity measurement for periods less than 75 s and source depths less than 25 km. For longer periods, and especially for deeper events, SGT corrections are appreciable.

3. We studied the off-path propagation, tracing the surface wave ray across predicted phase velocity maps. We found that the effects of off-path propagation are small for relatively short paths (shorter than ~ 5,000 km) but essential for a part of longer paths. These long paths are important for group velocity studies as they stabilize the tomographic inversion. Further work has to be done to estimate if the contribution of these deviating rays may produce significant distortions of tomographic maps in a certain period range. To answer this question we are developing an iterative technique for quantitative estimates of possible effects of off-path propagation.

4. We have reported the results of a systematic study of intermediate period (10 s - 40 s) Rayleigh and Love wave dispersion across Southern Eurasia (Near East, Central Asia, China, northern India and Indo-China, and the Far East). We believe that this study represents a significant improvement in the understanding of intermediate period surface wave dispersion across the studied region. First, this study displays denser and more uniform data coverage and demonstrates higher resolution than previous studies performed on this scale and at these periods. Second, our group velocity maps display the signatures of known geological and tectonic features never before revealed in surface wave studies on this scale. In particular, these maps provide entirely new constraints on sedimentary basins and crustal velocities and thicknesses. Finally, our group velocity maps provide a significant improvement in fit to the observed dispersion curves. The group velocity maps presented here are already being used to predict group travel times for the identification and extraction of surface wave packets. They are also being used as data in inversions for crustal and upper mantle models.

5. The new technique for tomographic inversion of surface wave dispersion measurements provides necessary means for constructing travel time correction surfaces for selected stations and their assessment in terms of spatial resolution and amplitude bias. The existing set of group velocity measurements across southern Eurasia is sufficient for constructing reliable group velocity maps and TTCSs both for Rayleigh and Love waves at periods 15 s and longer. Synthetic experiments

show that in areas with dense ray coverage the spatial resolution of group velocity maps is on the order of 250 - 350 km and the amplitude bias is no more than 10%. We estimate that the accuracy of group velocity maps and TTCSs for the part of the region to the north of 25°N is typically better than 0.03-0.04 km/s. The unmodeled 2% azimuthal anisotropy across such large areas as the Tibetan plateau does not generate significant errors in group velocity maps and TTCSs constructed from them.

6. We describe an automated surface wave detector and extractor designed to work on weak surface wave signals across Eurasia at intermediate periods (8 s - 40 s). The method is based on phase-matched filters defined by the Rayleigh wave group travel time predictions from the broad-band group velocity maps. Results of applying this method to a set of nuclear explosions and earthquakes in Central Asia lead us to conclude that this method shows considerable promise as a surface wave detector that yields high quality surface wave measurements automatically.

7. For the events we analyzed on the Lop Nor test site surface wave amplitude spectra combined with polarities of P wave first arrivals can be used to discriminate explosions from earthquakes based on source characteristics alone (a combination of the double couple depth and the ratio of the isotropic to nonisotropic moments). Much more work remains to be done, however, to determine if the method can be applied to events with much smaller moments. Further work can also determine if the method is transportable to other regions.

8.2 Recommendations.

On the basis of results obtained in this study, the following recommendations are made for future work:

(1) Further development of the methodology for constructing surface wave tomographic maps to account for off-path propagation effects.

(2) Augment the existing surface group velocity database in the short period range (8-15 s) by acquiring and processing surface wave data for relatively small events.

(3) Further testing of detection capabilities of an automated surface signal detector based on improved group velocity maps and travel time correction surfaces for different regions and different SNR relations.

(4) A more complete statistical evaluation of the spatial variability of surface wave amplitude spectra at short periods and its significance for measuring spectral magnitudes of weak signals.

(5) Further testing of the discriminant based on surface wave spectral and P-wave polarity measurements to determine if the method can be applied to events with much smaller moments and if the method is transportable to other regions.

Section 9
References

Aki, K., and P.G. Richards, Quantitative Seismology, 1980. **II**, W.H. Freeman and Co.. UNCLASSIFIED.

Aki, K. , and Y. Tsai, 1972. The mechanism of Love wave excitation by explosive sources. *J. Geoph. Res.*, **77**, 1452-1475. UNCLASSIFIED.

Archambeau, C. B., 1972. The theory of stress wave radiation from explosions in prestressed media. *Geophys. J.*, **29**, 329-366. UNCLASSIFIED.

Aurenhammer, F., 1991. Voronoi diagrams: A survey of fundamental geometric data structure, *Assoc. Comput. Mach. Comput. Surv.*, **23** (3), 345-405. UNCLASSIFIED.

Babich, V. M., and B. A. Chikhachev, 1975. Propagation of Love and Rayleigh waves in weakly inhomogeneous media, *Vestnik LGU*, No 1,32 - 38. UNCLASSIFIED.

Babich, V. M., B. A. Chikhachev, and T. B. Yanovskaya, 1976. Surface waves in a vertically inhomogeneous half-space with weak horizontal inhomogeneity, *Izv. AN SSSR, Fizika Zemli (Solid Earth)*, No 4, 24 - 31. UNCLASSIFIED.

Backus, G,. and J.F. Gilbert, 1968. Resolving power of gross earth data, *Geophys. J. R. Astron. Soc.*, **16**, 169-205. UNCLASSIFIED.

Backus, G,. and J.F. Gilbert, 1970. Uniqueness in the inversion of inaccurate gross earth data, *Philos. Trans. R. Soc. London, Ser. A*, **266**, 123-192. UNCLASSIFIED.

Barmin, M.P., M.H. Ritzwoller, and A.L. Levshin, 2001. A fast and reliable method for surface wave tomography, *Pure and Appl. Geophysics, Special volume on CTBT monitoring, Surface waves*, **158**, 1351-1375. UNCLASSIFIED.

Bijwaard, H., W. Spakman, and E.R. Engdahl, 1998. Closing the gap between regional and global travel time tomography, *J. Geophys. Res.*, **103**, 30055- 30078. UNCLASSIFIED.

Bourjot, L., and B. Romanowicz, 1992. Crust and upper mantle tomography in Tibet using surface waves, *Geophys. Res. Lett.*, **19**, 881-884. UNCLASSIFIED.

Brandon, C., and B. Romanowicz, 1986. A "no-lid" zone in the central Chang-Thang platform of Tibet: Evidence from pure path phase velocity measurements of long-period Rayleigh waves, *J. Geophys. Res.*, **91**, 6547-6564. UNCLASSIFIED.

Braun, J., and M. Sambridge, 1997. A numerical method for solving partial differential equations on highly irregular evolving grids, *Nature*, **376**, 665-660. UNCLASSIFIED.

Brune, J. N., and P. W. Pomeroy, 1963. Surface wave radiation patterns for under ground nuclear explosions and small-magnitude earthquakes. *J. Geophys. Res.*, **68**, 5005-5028. UNCLASSIFIED.

Bukchin, B.G., 1990. Determination of source parameters from surface waves recordings allowing for uncertainties in the properties of the medium, *Izv. Akad. Nauk SSSR, Fizika Zemli*, 25, 723-728. UNCLASSIFIED.

Bukchin, B.G., A.V. Lander, A.Z. Mostinsky, and V.I. Maksimov, 1997. Determination of seismic source parameters by analysis of coherence of body wave phases, In V.I. Keilis-Borok and G.M. Molchan (eds), *Theoretical Problems in Geophysics. Comput. Seismol.*, **29**, 3-17, 1997 (in Russian). English translation: *Comput. Seismology and Geodynamics*, **4**, AGU, 2001. UNCLASSIFIED.

Burger, R., T. Lay, T. Wallace, and L. Burdick, 1986. Evidence of tectonic release in long-period S waves from underground nuclear explosions at the Novaya Zemlya Test sites, *Bull. Seism. Soc. Am.*, **76**, 733-755. UNCLASSIFIED.

Bukchin, B.G., A.Z. Mostinsky, A.A. Egorkin, A.L. Levshin, and M.H. Ritzwoller, 2001. Isotropic and Nonisotropic Components of Earthquakes and Nuclear Explosions on the Lop Nor Test Site, China, *Pure and Appl. Geophysics, Special volume on CTBT monitoring, Surface waves*, **158**, 1497-1515. UNCLASSIFIED.

Bungum, H., and J. Capon, 1974. Coda pattern and multipath propagation of Rayleigh waves at NORSAR, *Physics Earth. planet. Interiors*, **9**, 111-127. UNCLASSIFIED.

Calcagnile, G., F. D'Ingeo, P. Farruga, and G. F. Panza, 1982. The lithosphere in the Central-Eastern Mediterranean area, *Pure and Applied Geophysics*, **120**, 389 - 406. UNCLASSIFIED.

Capon, J. , 1970. Analysis of Rayleigh-wave multipath propagation at LASA, *Bull. Seism. Soc. Amer.*, **60**, 1701-1731. UNCLASSIFIED.

Cara, M., 1973. Filtering of dispersed wave trains. *Geophys. J. R. astr. Soc.*, **33**, 65 - 80. UNCLASSIFIED.

Cara, M., and D. Hatzfeld, 1976. Vitesse de groupe de l'Onde de Rayleigh de part et d'autre de la ligne Açores-Gibraltar, *Ann. Geophys.*, **32**, 85 - 91. UNCLASSIFIED.

Chen, W.-P., and P. Molnar, 1975. Short-period Rayleigh wave dispersion across the Tibetan Plateau, *Bull. Seismol. Soc. Am.*, **65**, 1051-1057. UNCLASSIFIED.

Chun, K.Y, and T. Yoshii, 1977. Crustal structure of the Tibetan Plateau: A surface wave study, *Bull. Seismol. Soc. Amer.*, **67**, 735-750. UNCLASSIFIED.

Curtis, A., and J. Woodhouse, 1997. Crust and upper mantle shear velocity structure beneath the Tibetan plateau and surrounding regions from interevent surface wave phase velocity inversion, *J. Geophys. Res.*, **102**, 11789 - 11813. UNCLASSIFIED.

Curtis, A., J. Trampert, R. Snieder, and B. Dost, 1998. Eurasian fundamental mode surface wave phase velocities and their relationship with tectonic structures, *J. Geophys. Res.*, **103**, 26,919-26,947. UNCLASSIFIED.

Dahlen, F.A., and J. Tromp, 1998. *Theoretical global seismology*, Princeton Univers. Press, Princeton, NJ.UNCLASSIFIED.

Day, S.M., and J.L. Stevens, 1986. An explanation for apparent time delays in phase-reversed Rayleigh waves from underground nuclear explosions. *Geophys. Res. Lett.*, **13**, 1423-1425. UNCLASSIFIED.

Day, S.M., J.T. Cherry, N. Rimer, and J.L. Stevens, 1987. Nonlinear model of tectonic release from underground explosions. *Bull. Seism. Soc. Am.*, **77**, 996-1016. UNCLASSIFIED.

Ditmar, P.G., and T.B. Yanovskaya, 1987. Backus-Gilbert method for estimation of lateral variations of surface wave velocity, *Izv. Akad. Nauk SSSR, Fiz. Zeml*, **6**, 30-60, in Russian. UNCLASSIFIED.

Dziewonski, A. M., S. Bloch, and M. Landisman, 1969. A technique for the analysis of transient seismic signals, *Bull. Seism. Soc. Am.*, **59**, 427 - 444. UNCLASSIFIED.

Dziewonski, A. M., T.-A. Chou, and J. H. Woodhouse, 1981. Determination of earthquake source parameters from waveform data for studies of global and regional seismicity, *J. Geophys. Res.*, **86**, 2825 - 2852. UNCLASSIFIED.

Dziewonski, A. M., and D. L. Anderson, 1981. Preliminary reference Earth model, *Phys. Earth planet. Inter.*, **25**, 297 - 356. UNCLASSIFIED.

Ekström, G., J. Tromp, and E. W. F. Larson, 1997. Measurements and global models of surface wave propagation, *J. Geophys. Res.*, **102**, 8147 - 8158. UNCLASSIFIED.

Ekström, G., and P.G. Richards, 1994. Empirical measurements of tectonic moment release in nuclear explosions from teleseismic surface waves and body waves. *Geophys. J. Int.*, **117**, 120-140. UNCLASSIFIED.

Engdahl, E.R., 1998. Development of an archive of seismic ground truth events globally in support of monitoring under the CTBT, Proceedings of the 20th Seismic Research Symposium on Monitoring a CTBT, 11 - 15. UNCLASSIFIED.

Feng, C.C., and T. Teng, 1983. Three-dimensional crust and upper mantle structure of the Eurasian continent, *J. Geophys. Res.*, **88**, 2261-2272. UNCLASSIFIED.

Feng, R., J.S. Zhu, Y. Y. Ding, G.Y. Chen, Z.Q. He, S. B. Yang, H. N. Zhou, and K. Z. Sun, 1983. Crustal structure in China from surface waves, *Chin. Geophys.*, Engl. Transl., **2**, 273-289. UNCLASSIFIED.

Franklin, J.N., 1970. Well-posed stochastic extensions of ill-posed linear problems, *J. math. Analysis Applic.*, **31**, 682-716. UNCLASSIFIED.

Friederich, W., 1998. Propagation of seismic shear and surface waves in a laterally heterogeneous mantle by multiple forward scattering, *Geophys. J. Int.*, **136**, 180-204. UNCLASSIFIED.

Hadouche, O. and W. Zurn, 1992. On the structure of the crust and upper mantle beneath the Afro-Arabian region from surface wave dispersion, *Tectonophys.*, **209**, 179 - 196. UNCLASSIFIED.

Herak, M., and D. Herak, 1993. Distance dependence of M_s and calibrating function for 20 second Rayleigh waves, *Bull. Seism. Soc. Am.*, **83**, 1881 - 1892. UNCLASSIFIED.

Gao, L.-P., and P.G. Richards, 1994. Studies of earthquakes on and near the Lop Nor, China, nuclear test site. In *Proc. of the 16th Annual Seismic Research Symposium, 7-9 Sept. 1994*, 106-112, Phillips Lab., Directorate of Geophysics.UNCLASSIFIED.

Gilbert, F., and A.M. Dziewonski, 1975. An application of normal mode theory to the retrieval of structural parameters and source mechanisms from seismic spectra, *Philos. Trans. R. Soc. London A*, **278**, 187-269. UNCLASSIFIED.

Gilbert, F., 1976. The representation of seismic displacements in terms of travelling waves, *Geophys. J. R. astron. Soc*, **44**, 275 - 280. UNCLASSIFIED.

Grand, S.P., R.D. van der Hilst, and S. Widiyantoro, 1997. Global seismic tomography: a snapshot of convection in the Earth, *GSA Today*, **7**, 4, 1-7. UNCLASSIFIED.

Griot, D.A., J.P. Montagner, and P. Tapponier, 1998. Surface wave phase velocity tomography and azimuthal anisotropy in Central Asia, *J. Geophys. Res.*, **103**, 21,215-21,232. UNCLASSIFIED.

Harkrider, D.G., J.L. Stevens, and C.B. Archambeau, 1994. Theoretical Rayleigh and Love waves from an explosion in prestressed source regions. *Bull. Seism. Soc. Am.*, **84**, 1410-1442. UNCLASSIFIED.

Harkrider, D.G., and N.K. Yacoub, 1998. Evaluation of intermediate-period Rayleigh and Love wave global group velocity models, Proceedings of the 20th Seismic Research Symposium on Monitoring a CTBT, 453 - 457. UNCLASSIFIED.

Helle, H.B., and E. Rygg, 1984. Determination of tectonic release from surface waves generated by nuclear explosions in Eastern Kazakhstan, *Bull. Seism. Soc. Am.*, **74**, 1883-1898. UNCLASSIFIED.

Herrin, E., and T. Goforth, 1977. Phase-matched filters: Application to the study of Rayleigh waves, *Bull. Seism. Soc. Am*, **67**, 1259-1275. UNCLASSIFIED.

Jimenez, E., M. Cara, and D. Rouland, 1989. Focal mechanisms of moderate earthquakes from the analysis

of single-station three-component surface-wave records, *Bull. Seism. Soc. Am.*, **79**, 955 - 972. UNCLASSIFIED.

Jobert, N., and G. Jobert, 1983. An application of ray theory to the propagation of waves along a laterally heterogeneous spherical surface, *Geophys. Res. Lett.*, **10**, 1148-1151, 1983. UNCLASSIFIED.

Jobert, N., B. Journet, G. Jobert, A. Hirn, and S.-K. Zhong, 1985. Deep structure of southern Tibet inferred from the dispersion of Rayleigh waves through a long-period seismic network, *Nature*, **313**, 386-388. UNCLASSIFIED.

Kaverina, A. N., A. V. Lander, and A. G. Prozorov, 1996. Global creepex distribution and its relation to earthquake-source geometry and tectonic origin, *Geophys. J. Int.*, **125**, 249 - 255. UNCLASSIFIED.

Kim, W.-Y., V. V. Kazakov, A. G. Vanchugov, and D. W. Simpson, 1995. Broadband and array observations at low noise sites in Kazakhstan: Opportunities for seismic monitoring of a Comprehensive Test Ban Treaty, *Monitoring a Comprehensive Test Ban Treaty*, edited by E. S. Husebye and A.M. Dainty, pp. 467-482, Kluwer, Norwell, Mass. UNCLASSIFIED.

Kodera, K., C. De Villedary, and R. Gendrin, 1976. A new method for the numerical analysis of non-stationary signals, *Phys. Earth. Planet. Int.*, **12**, 142 - 150. UNCLASSIFIED.

Knopoff, L., and F.-S. Chang, 1981. Upper mantle structure under the Tibetan Plateau, in *Geological and Ecological Studies of the Qinghai-Xizang Plateau*, **1**, pp. 627-632, edited by Liu D.S., Gordon and Breach, New York. UNCLASSIFIED.

Knopoff, L., and A.A. Fouda, 1975. Upper mantle structure under the Arabian Peninsula, *Tectonophysics*, **26**, 121-134. UNCLASSIFIED.

Knopoff, L., and F. A. Schwab, 1968. Apparent initial phase of a source of Rayleigh waves, *J. Geophys. Res*, **73**, 755 - 760. UNCLASSIFIED.

Knopoff, L., 1972. Observation and inversion of surface wave dispersion, *Tectonophysics*, **13**, 497 - 519. UNCLASSIFIED.

Kozhevnikov, V. M., and M. P. Barmin, 1989. Dispersion curves of Rayleigh wave group velocities for several regions of the Asian continent, *Izv. Akad. Nauk SSSR, Fiz. Zemli*, no. 9, 16-25. UNCLASSIFIED.

Kozhevnikov, V. M., D. E. Lokshtanov, and M. P. Barmin, 1992. Shear-velocity structure of the lithosphere for nine large tectonic regions of the Asian continent, *Izv. Akad. Nauk SSSR, Fiz. Zemli*, no. 1, 61-70. UNCLASSIFIED.

Kunin, N. Y., *et al.*, 1987. Basement surface relief map, Inst. of Phys. of the Earth, Acad. of Sci., Minist. of Geol. of the USSR, Moscow. UNCLASSIFIED.

Lander, A.V., 1989. Frequency-time analysis. In: V.I. Keilis-Borok (Editor), *Seismic surface waves in a laterally inhomogeneous earth*. Kluwer Acad. Publ., Dordrecht, 153-163. UNCLASSIFIED.

Landisman, M., A. M. Dziewonski, and Y. Sato, 1969. Recent improvements in the analysis of surface wave observations, *Geophys. J. R. Astron. Soc.*, **17**, 369 - 403. UNCLASSIFIED.

Laske, G., and G. Masters, 1996. Constraints on global phase velocity maps from long-period polarization data, *J. Geophys. Res.*, **101**, 16,059 - 16,075. UNCLASSIFIED.

Lasserre, C., B. Bukchin, P. Bernard, P. Tapponier, Y. Gaudemer, A. Mostinsky, and Rong Dailu, 2001. Source parameters and tectonic origin of the June 1, 1996 Tianzhu ($M_w = 5.2$ and July 21, 1995 Yongden ($M_w = 5.6$) earthquakes, near Haiyuan fault (Gansu, China), *Geophys. J. Int*, **144**, 206-220. UNCLASSIFIED.

Lay, T. and H. Kanamori, 1985. Geometric effects of global lateral heterogeneity on long-period surface wave propagation, *J. Geophys. Res.*, **90**, 605-621. UNCLASSIFIED.

Leach, R.R., D.B. Harris, and W.R. Walter, 1998. Phase-matched filtering of after-shock sequences to detect Rayleigh waves in low SNR seismograms, *Proceedings of the 20th Annual Seismic Research Symposium on Monitoring a Comprehensive Test Ban Treaty*, DoD & DoE, 458-465. UNCLASSIFIED.

Lerner-Lam, A.L., and J. Park, 1989. Frequency-dependent refraction and multipathing of 10-100 second surface waves in the western Pacific, *Geophys. Res. Lett.*, **16**, 527-530. UNCLASSIFIED.

Leveque, J.-J., L. Rivera, and G.W. Wittlinger, 1993. On the use of checkerboard tests to assess the resolution of tomographic inversions, *Geophys. J. Int.*, **115**, 313-318. UNCLASSIFIED.

Levshin, A. L., V. F. Pisarenko, and G. A. Pogrebinsky, 1972. On a frequency-time analysis of oscillations, *Ann. Geophys.*, **28**, 211 - 218. UNCLASSIFIED.

Levshin, A. L., 1985. Effects of lateral inhomogeneities on surface wave amplitude measurements. *Ann.Geophys.*, **3**, No 4, 511 - 518. UNCLASSIFIED.

Levshin, A.L., T.B. Yanovskaya, A.V. Lander, B.G. Bukchin, M.P. Barmin, L.I. Ratnikova, and E.N. Its, 1989. *Seismic Surface Waves in Laterally Inhomogeneous Earth*, edited by V. I. Keilis-Borok, Kluwer. Publ., Dordrecht. UNCLASSIFIED.

Levshin, A. L., L. Ratnikova, and J. Berger, 1992. Peculiarities of surface wave propagation across Central Eurasia, *Bull. Seism. Soc. Am.*, **82**, 2464 - 2493. UNCLASSIFIED.

Levshin, A., M. Ritzwoller, and L. Ratnikova, 1994. The nature and cause of polarization anomalies of surface waves crossing Northern and Central Eurasia. *Geophys. Journal Int.*, **117**, 577-591. UNCLASSIFIED.

Levshin, A.L., M.H. Ritzwoller, M.P. Barmin, A. Villaseñor, and C.A. Padgett, 2000. New constraints on the Arctic crust and uppermost mantle: Surface wave group velocities, P_n, and S_n, *Phys. Earth. Planet. Int.*, **123**, 185-204. UNCLASSIFIED.

Levshin, A.L., M.H. Ritzwoller, and S.S. Smith, 1996. Group velocity variations across Eurasia, Proceedings of the 18th Seismic Research Symposium on Monitoring a CTBT, 70-79. UNCLASSIFIED.

Levshin, A.L., M.H. Ritzwoller, L.I. Ratnikova, M. Silitch, R. Kelly, and B. O'Sullivan, 1996. Intermediate period group velocity maps across Central Asia and parts of the Middle East, Proceedings of the 19th Seismic Research Symposium on Monitoring a CTBT, 67-76. UNCLASSIFIED.

Levshin, A.L., M.H. Ritzwoller, M.P. Barmin, L.I. Ratnikova, and C.A. Padget, 1998. Automated surface wave analysis using phase-matched filters from dispersion maps, Proceedings of the 20th Seismic Research Symposium on Monitoring a CTBT, 466-473. UNCLASSIFIED.

Levshin, A.L., M.H. Ritzwoller, and J.S. Resovsky, 1999, Source effects on surface wave group travel times and group velocity maps, Physics Earth and planet. Inter., **115**, 293-312. UNCLASSIFIED.

Levshin, A.L., M.P. Barmin, and M.H. Ritzwoller, 1999. Estimation of uncertainties and bias in surface wave tomographic maps and travel-time correction surfaces, Proceedings of the 21th Seismic Research Symposium: Technologies for Monitoring the Comprehensive Nuclear-Test-Ban Treaty, DOD/DOE, Las Vegas, 21-24 Sept.1999, 141-150. UNCLASSIFIED.

Levshin, A.L., M.H. Ritzwoller, B.G. Bukchin, A.Z. Mostinsky, and A.A. Egorkin, 2000. Isotropic and nonisotropic components of earthquakes and nuclear explosions on the Lop Nor test site, Proceedings, 22nd Seismic Research Symposium. UNCLASSIFIED.

Levshin, A.L., and M.H. Ritzwoller, 2001. Automated detection, extraction, and measurement of regional surface waves, *Pure and Appl. Geophysics, Special volume on CTBT monitoring, Surface waves*, **158**, 1531-1541. UNCLASSIFIED.

Li, Y., M.N. Toksoz, and W. Rodi, 1995. Source time functions of nuclear explosions and earthquakes in

central Asia determined using empirical Green's functions. *J. Geophys. Res.*, **100**, 659-674. UNCLASSIFIED.

Lyon-Caen, H., 1986. Comparison of the upper mantle shear wave velocity structure of the Indian Shield and the Tibetan Plateau and tectonic implications, *Geophys. J. R. Astron. Soc.*, **86**, 727-749. UNCLASSIFIED.

Marquering, H., R. Snieder, and G. Nolet, 1996. Waveform inversions and the significance of surface mode coupling, *Geophys. J. Int.*, **124**, 258-270. UNCLASSIFIED.

Marshall, P.D., and P.W. Basham, 1972. Discrimination between earthquakes and underground nuclear explosions employing an improved M_s scale, *Geophys. J. R. astr. Soc.*, **28**, 431-458. UNCLASSIFIED.

Masse, R.P., 1981. Review of seismic source models for underground nuclear explosions, *Bull. Seism. Soc. Am.*, **71**, 1249-1268. UNCLASSIFIED.

Masters, G., S. Johnson, G. Laske, and H. Bolton, 1996. A shear-velocity model of the mantle, *Phil. Trans. R. Soc. Lond. A*, **354**, 1385-1411. UNCLASSIFIED.

Menke, W., 1989. *Geophysical Data Analyses: Discrete Inverse Theory*, New York, Academic Press. UNCLASSIFIED.

Montagner, J.P., and T. Tanimoto, 1991. Global upper mantle tomography of seismic velocities and anisotropies, *J. Geophys. Res.*, **96**, 20,337 - 20,351. UNCLASSIFIED.

Mooney, W.D., G. Laske, and G. Masters, 1998. CRUST 5.1: A global crustal model at 5 degrees by 5 degrees, *J. Geophys. Res.*, **103**, 727-747. UNCLASSIFIED.

Mueller, R.A., and J.R. Murphy, 1971. Seismic characteristics of underground nuclear detonations. Part I: Seismic spectrum scaling, *Bull. Seism. Soc. Am.*, **61**, 1675-1692. UNCLASSIFIED.

Muyzert, E., and R. Snieder, 1996. The influence of errors in source parameters on phase velocity measurements of surface waves, *Bull. Seismol. Soc. Am.*, **86**, 1863 - 1872. UNCLASSIFIED.

Nakanishi, I., and D. L. Anderson, 1982. World-wide distribution of group velocity of mantle Rayleigh waves as determined by spherical harmonic inversion, *Bull. Seismol. Soc. Am.*, **72**, 1185-1194. UNCLASSIFIED.

Nataf, H.-C., and Y. Ricard, 1996. 3SMAC: An a priori tomographic model of the upper mantle based on geophysical modeling, *Phys. Earth Planet. Inter.*, **95**, 101-122. UNCLASSIFIED.

Nolet, G., 1987. Seismic wave propagation and seismic tomography, in *Seismic Tomography*, 1-23, Reidel, Dordrecht. UNCLASSIFIED.

Nolet, G., 1987. Waveform tomography, in *Seismic Tomography with Applications in Global Seismology and Exploration Geophysics*, edited by G. Nolet, D. Reidel, 301 - 322, Norwell, Mass. UNCLASSIFIED.

Panza, G.F. , F.A. Schwab, and L. Knopoff, 1973. Multimode surface waves for selected focal mechanisms. I. Dip-Slip sources on a vertical fault plane, *Geophys. J. R. astr. Soc.*, **34**, 265 - 278. UNCLASSIFIED.

Parker, R.L., 1994. *Geophysical Inverse Theory*, Princeton, NJ, Princeton University Press. UNCLASSIFIED.

Patton, H., 1980. Crustal and upper mantle structure of the Eurasian continent from the phase velocity and Q of surface waves. *Rev. Geophys.*, **18**, 605-625. UNCLASSIFIED.

Patton, H.J., 1991. Seismic moment estimation and the scaling of the long-period explosion source spectrum. In *Explosion Source Phenomenology, Geophysical Monograph 65, AGU*, ed. S.R. Taylor, H.J. Patton, and P.G. Richards , 171-184. UNCLASSIFIED.

Paulssen, H., Levshin, A.L., Lander, A.V., Snieder, R., 1990. Time and frequency dependent polarization analysis: anomalous surface wave observations in Iberia. *Geoph. J. Int.*, **103**, 483-496. UNCLASSIFIED.

Pavlis G., H. Al-Shukri, H. Mahdi, and D. Repin, 1994. JSP arrays and networks in Central Asia, *IRIS Newsl.*, **XIII** (2), 10-12. UNCLASSIFIED.

Pekeris, C. L., 1948. Theory of propagation of explosive sound in shallow water, *Geological Society of America Memoirs*, No. 27. UNCLASSIFIED.

Pines, I., T.-L. Teng, and R. Rosenthal, 1980. A surface wave dispersion study of the crustal and upper mantle structure of China, *J. Geophys. Res.*, **85**, 3829-3844. UNCLASSIFIED.

Pollitz, F.F., and C. G. Hennet, 1993. Analysis of Rayleigh wave refraction from three-component seismic spectra, *Geophys. J. Int.*, **113**, 629-650. UNCLASSIFIED.

Pollitz, F.F., 1994. Surface wave scattering from sharp lateral discontinuities, *J. Geophys. Res.*, **99**, 21,891-21,909. UNCLASSIFIED.

Press, F., and C. B. Archambeau, 1962. Release of tectonic strain by underground explosions. *J. Geophys. Res.*, **67**, 337-343. UNCLASSIFIED.

Pulliam, J., and R. Snieder, 1998. Ray perturbation theory, dynamic ray tracing and the determination of Fresnel zones, *Geoph. J. Int.*, **135**, 463-469. UNCLASSIFIED.

Quinlan, D.M., 1994. Datascope: A relational database system for scientists, *Eos Trans. AGU*, **75** (44), Fall Meet. Suppl., F431. UNCLASSIFIED.

Rezapour, M. and R.G. Pearce, 1998. Bias in surface wave magnitude M_s due to inadequate distance corrections, *Bull. Seism. Soc. Am.*, **88**, 43 - 61. UNCLASSIFIED.

Ritzwoller, M. H., A. L. Levshin, S. S. Smith, and C. S. Lee, 1995. Making accurate continental broadband surface wave measurements, in *Proceedings of the 17th Seismic Research Symposium on Monitoring a CTBT*, (ed. J. F. Lewkowicz, J. M. McPhetres, and D. T. Reiter), Phillips Lab., Hanscom AFB, Mass., 482 - 490. UNCLASSIFIED.

Ritzwoller, M.H., and A.L. Levshin, 1998. Eurasian Surface wave Tomography: Group velocities, *J. Geophys. Res.*, **103**, 4839-4878. UNCLASSIFIED.

Ritzwoller, M.H., A.L. Levshin, L.I. Ratnikova, and A. A. Egorkin-Jr, 1998. Intermediate Period Group Velocity Maps Across Central Asia, Western China, and Parts of the Middle East, *Geoph. J. Int.*, **134**, 315-328. UNCLASSIFIED.

Ritzwoller, M.H., M.P. Barmin, A. Villaseñor, A.L. Levshin, E.R. Engdahl, W. Spakman, and J. Trampert, 1999. Construction of a 3-D P and S model of the crust and upper mantle to improve regional locations in W. China, Central Asia, and parts of the Middle East, *Proceedings of the 21th Annual Seismic Research Symposium on Monitoring a Comprehensive Test Ban Treaty*, DoD & DoE, 656-665. UNCLASSIFIED.

Ritzwoller, M.H., N. Shapiro, A.L. Levshin, and G.M. Leahy, 2001. Crustal andupper mantle structure beneath Antarctica and surrounding oceans, submitted to *J. Geophys. Res.* UNCLASSIFIED.

Rodgers, A.J., W.R. Walter, R.J. Mellors, A.M.S. Al-Amri, and Y.S. Zhang, 1999. Lithospheric structure of the Arabian Shield and Platform from complete regional waveform modeling and surface wave group velocities, *Geophys. J. Int.*, **138**, 871-878. UNCLASSIFIED.

Romanowicz, B.A., 1982. Constraints on the structure of the Tibet Plateau from pure-path phase velocities of Love and Rayleigh waves, *J. Geophys. Res.*, **87**, 6865-6883. UNCLASSIFIED.

Russell, D.W., R.B. Herrman, and H. Hwang, 1988. Application of frequency-variable filters to surface wave amplitude analysis, *Bull. Seismol. Soc. Am.*, **78**, 339 - 354. UNCLASSIFIED.

Sambridge, M., J. Braun, and H. McQueen, 1995. Geophysical parameterization and interpolation of irregular data using natural neighbors, *Geophys. J. Int.*, **122**, 837-857. UNCLASSIFIED.

Shapiro, M.N., and M.H. Ritzwoller, 2001. Inversion of broad-band fundamental surface wave dispersion with a priori constraints, manuscript in preparation for submission to *Geophys. J. Int.* UNCLASSIFIED.

Schultz, C., S. Myers, J. Hipp, and C. Young, 1998. Nonstationary Bayesian Kriging: Application of spatial corrections to improve seismic detection, location, and identification, *Bull. Seism. Soc. Am.*, **88**, 1275 - 1288. UNCLASSIFIED.

Sloan, S.W., 1987. A fast algorithm for constructing Delaunay triangulation in the plane, *Adv. Eng. Software*, **9** (1), 34-55. UNCLASSIFIED.

Smith, M.L., and F.A. Dahlen, 1973. The azimuthal dependence of Love and Rayleigh wave propagation in a slightly anisotropic medium, *J. Geophys. Res.*, **78**, 3321-3333. UNCLASSIFIED.

Snieder, R. , 1988. Large-scale waveform inversions of surface waves for lateral heterogeneities, *J. Geophys. Res.*, **93**, 12055-65. UNCLASSIFIED.

Sobel, P.A., and D.H. von Seggern, 1978. Applications of surface wave ray tracing, *Bull. Seism. Soc. Amer.*, **68**, 1359-1380. UNCLASSIFIED.

Spakman, W., and H. Bijwaard, 1998. Irregular cell parametrization of tomographic problems, *Ann. Geophys.*, **16**, 18. UNCLASSIFIED.

Spakman, W., and H. Bijwaard, 2001. Irregular cell parametrization of tomographic inverse problems, *Pure and Appl. Geophys., Special volume on CTBT monitoring, Surface waves*, in press. UNCLASSIFIED.

Stevens, J.L., and S.M. Day, 1985. The physical basis of m_b : M_s and variable frequency magnitude methods for earthquake/explosion discrimination, *J. Geophys. Res.*, **90**, 3009 - 3020. UNCLASSIFIED.

Stevens, J.L., T.G. Barker, S.M. Day, K.L. McLaughlin, N. Rimer, and B. Shkoller, 1991. Simulation of teleseismic body waves, regional seismograms, and Rayleigh wave phase shifts using two-dimensional nonlinear models of explosion sources. In *Explosion Source Phenomenology, Geophysical Monograph* **65**, *AGU*, ed. S.R. Taylor, H.J. Patton, and P.G. Richards, 239-252.UNCLASSIFIED.

Stevens, J.L., 1986. Estimation of scalar moments from explosion-generated surface waves, *Bull.Seismol. Soc. Am.*, **76**, 123-151. UNCLASSIFIED.

Stevens, J.L., and K.L. McLaughlin, 1997. Improved methods for regionalized surface wave analysis, *Proceedings of the 17th Annual Seismic Research Symposium on Monitoring a CTBT*, 171-180. UNCLASSIFIED.

Stevens, J.L. and K.L. McLaughlin, 2001. Optimization of surface wave identification and measurement, *Pure and Appl. Geophys., Special volume on CTBT monitoring, Surface waves*, in press. UNCLASSIFIED.

Suetsugu, D., and I. Nakanishi, 1985. Surface waves tomography for the upper mantle beneath the Pacific ocean. Part I: Rayleigh wave phase velocity distribution, *J. Phys. Earth*, **33**, 345-368. UNCLASSIFIED.

Tarantola, A., 1987. *Inverse Problems Theory, Methods for Data Fitting and Model Parameter Estimation*, Amsterdam, Elsevier. UNCLASSIFIED.

Tarantola, A., and B. Valette, 1982. Generalized nonlinear inverse problems solved using the least squares criterion, *Revs. Geophys.*, **20** (2), 219-232. UNCLASSIFIED.

Tarantola, A., and A. Nersessian, 1984. Three-dimensional tomography without block, *Geophys. J. R. astr. Soc.*, **76**, 299-306. UNCLASSIFIED.

Tikhonov, A.N., 1963. On the solution of improperly posed problems and the method of regularization, *Dokl. Akad. Nauk SSSR*, **151**, 501. UNCLASSIFIED.

Toksöz, M.N. and H.H. Kehrer, 1972. Tectonic strain release by underground nuclear explosions and its effect on seismic discrimination, *Geophys. J. R. Astr. Soc.*, **31**, 141-161. UNCLASSIFIED.

Trampert, J., 1998. Global seismic tomography; the inverse problem and beyond, *Inverse Problems*, **14**, 371-385. UNCLASSIFIED.

Trampert, J., and J. Woodhouse, 1995. Global phase velocity maps of Love and Rayleigh waves between 40 and 150 seconds, *Geophys. J. Int.*, **122**, 675 - 690. UNCLASSIFIED.

Trampert, J., and J. Woodhouse, 1996. High resolution global phase velocity distributions, *Geophys. Res. Lett.*, **23**, 21-24. UNCLASSIFIED.

Trampert, J., and J. Woodhouse, 1996. Global azimuthal anisotropy, *Eur. Geophys. Soc. Newsl.*, **58**, 57. UNCLASSIFIED.

Tromp, J., and F. A. Dahlen, 1992. Variational principles for surface wave propagation on a laterally heterogeneous Earth, I, II, *Geophys. J. Int*, **109**, 581 - 598 and 599 - 619. UNCLASSIFIED.

van der Hilst, R.D, S. Widiyantoro, and E.R. Engdahl, 1997. Evidence for deep mantle circulation from global tomography, *Nature*, **386**, 578-584. UNCLASSIFIED.

van Heijst, J.J. and J.W. Woodhouse, 1999. Global high resolution phase velocity distribution of overtone and fundamental mode surface waves determined by mode branch stripping, *Geophys. J. Int.*, **137**, 601 - 620. UNCLASSIFIED.

Vdovin, O.Y., J.A. Rial, A.L. Levshin, and M.H. Ritzwoller, 1999. Group-velocity tomography of South America and the surrounding oceans, *Geoph. J. Int.*, **136**, 324-330. UNCLASSIFIED.

Vdovin, O.Y., 1999. Surface wave tomography of South America and Antarctica, *Ph. D. Thesis*, Department of Physics, University of Colorado at Boulder. UNCLASSIFIED.

Vernon, F., Mellors, R.J., J. Berger, A.M. Al-Amri, and J. Zollweg, 1996. Initial results from the deployment of broadband seismometers in the Saudi Arabian Shield, in *Proceedings of the 18th Seismic Research Symposium on Monitoring a CTBT*, edited by J.F. Lewkowicz, J.M. McPhetres, and D.T. Reiter, pp. 108-117, Phillips Lab., Hanscom AFB, Mass. UNCLASSIFIED.

Villaseñor, A., M.H. Ritzwoller, A.L. Levshin, M.P. Barmin, E.R. Engdahl, W. Spakman and J. Trampert, 2001. Shear velocity structure of central Eurasia from inversion of surface wave velocities, *Phys. Earth Planet. Inter.*, in press. UNCLASSIFIED.

Villaseñor, A., M.H. Ritzwoller, M.P. Barmin, E.R. Engdahl, and A.L. Levshin, 2000. Computation of travel times and station correction surfaces in Eurasia using three dimensional velocity models, *Proceedings of the 22nd Seismic Research Symposium on Monitoring a CTBT*. UNCLASSIFIED.

Wallace, T.C., D.V. Helmberger, and G.R. Engen, 1985. Evidence of tectonic release from underground nuclear explosions in long-period S waves. *Bull. Seism. Soc. Am.*, **76**, 123-151. UNCLASSIFIED.

Wallace, T.C., 1991. Body wave observations of tectonic release, In *Explosion Source Phenomenology, Geophysical Monograph* **65**, *AGU*, ed. S.R. Taylor, H.J. Patton, and P.G. Richards, 161-170. UNCLASSIFIED.

Wallace, T.C., and M.A. Tinker, 1996. The last nuclear weapons test? A brief review of the Chinese nuclear weapons program. *IRIS Newsletter,* **15**, N 3. UNCLASSIFIED.

Walter, W.R., and H.J. Patton, 1990. Tectonic release from SJVE, *Geophys. Res. Lett.*, **17**, 1517-1520. UNCLASSIFIED.

Wessel, P., and W.H.F. Smith, 1991. Free software helps map and display data. *Eos Trans. AGU*, **72**, 441. UNCLASSIFIED.

Wessel, P., and W.H.F. Smith, 1995. New version of the Generic Mapping Tools released, *Eos Trans. AGU*, **76**, 329. UNCLASSIFIED.

Wier, S., 1982. Surface wave dispersion and Earth structure in south-eastern China, *Geophys. J. R. astron. Soc.*, **69**, 33-47. UNCLASSIFIED.

Walter, W.R., and M.H. Ritzwoller, 1998. Summary report on the Workshop on the U.S. Use of Surface Waves for Monitoring the CTBT, UCRL-ID-131835, Lawrence Livermore National Laboratory, 16. UNCLASSIFIED.

Woodhouse, J. H., and A. M. Dziewonski, 1984. Mapping the upper mantle: Three-dimensional modeling of Earth structure by inversion of seismic waveforms, *J. Geophys. Res.*, **89**, 5953 - 5986. UNCLASSIFIED.

Woodhouse, J. H., 1974. Surface waves in the laterally varying layered structure, *Geophys. J. R. astron. Soc.*, **37**, 461-490. UNCLASSIFIED.

Wu, F.T., and A. Levshin, 1994. Surface wave group velocity tomography of East Asia, *Phys. Earth Planet. Int.*, **84**, 59-77. UNCLASSIFIED.

Wu, F.T., A.L. Levshin, and V.M. Kozhevnikov, 1997. Rayleigh wave group velocity tomography of Siberia, China, and the vicinity, *Pure & appl. Geophys.*, **149**, 447-473. UNCLASSIFIED.

Yanovskaya, T.B., and P.G. Ditmar, 1990. Smoothness criteria in surface wave tomography, *Geophys. J. Int.*, **102**, 63-72. UNCLASSIFIED.

Yanovskaya, T.B., and L.M. Antonova, 2000. Lateral variations in the structure of the crust and upper mantle in the Asia region from data on group velocities of Rayleigh waves. *Fizika Zemli, Izv. Russ. Acad. Sci.*, **36**, No.2, 121-128.UNCLASSIFIED.

Zhang, Y. S., & T. Tanimoto, 1993. High-resolution global upper mantle structure and plate tectonics, *J. Geophys. Res.*, **98**, 9793 - 9823. UNCLASSIFIED.

Zhang, Y.-S., and T. Lay, 1996. Global surface wave phase velocity variations, *J. Geophys. Res.*, **101**, 8415-8436. UNCLASSIFIED.

Zhang, Y.-S., 1997. Three-dimensional velocity structure beneath East Asia and its tectonic implication, *Mantle Dynamics and Plate Interactions in East Asia, Geophys. Monogr. Ser.*, edited by M.F.J. Flower and S.-L. Chung, AGU, Washington, D.C. UNCLASSIFIED.

Zhang, J., 1994. Polarization characteristics of seismic waves from the May 21, 1992 Lop Nor nuclear explosion using IRIS/GSN broadband data, In *Proc. of the 16th Annual Seismic Research Symposium, 7-9 Sept. 1994*, 393-397, Phillips Lab., Directorate of Geophysics. UNCLASSIFIED.

Zhou, H., 1996. A high-resolution P wave model for the top 1200 km of the mantle, *J. Geophys. Res.*, **101**, 27791-27810. UNCLASSIFIED.

Appendix A
Surface Wave Formalism

Laterally Homogeneous Medium

First consider surface wave propagation in a laterally homogeneous isotropic elastic halfspace. We use a source-centered cylindrical coordinate system (r, φ, z), $0 \leq r < \infty$, $0 \leq \varphi < 2\pi$, $0 \leq z < \infty$. Let a point source situated at the point $(0, 0, h)$ be described by the seismic moment tensor $\mathbf{M}H(t)$, where t is time, H is the step function, and $\mathbf{M}$ is a symmetrical second order tensor. The receiver is at the point $(r, \varphi, 0)$ on the free surface. The 1D model is characterized by a piece-wise continuous vector-function $\mathbf{m}(z)$, $\mathbf{m} = (\alpha, \beta, \rho)$, where α and β are P- and S-velocities and ρ is density. We assume that there exists a depth Z at which α and β reach their maximum values and are constant at depths $z \geq Z$. The displacement observed at the receiver is

$$\mathbf{d}(t, r, \varphi, h) = \frac{1}{2\pi} \int_{-\infty}^{\infty} \mathbf{D}(\omega, r, \varphi, h) \exp(i\omega t) d\omega, \tag{A.1}$$

where r is the epicentral distance, ϕ the epicentral azimuth, and h is the source depth. The displacement spectrum is the sum of body waves, leaking modes, and normal modes or surface waves:

$$\mathbf{D} = \mathbf{D_B} + \mathbf{D_L} + \mathbf{D_S}. \tag{A.2}$$

The surface wave spectrum may be further decomposed into fundamental and overtone modes depending on the radial order n of the mode, $\mathbf{D_S} = \sum_n \mathbf{D_S^{(n)}}$, where the fundamental surface wave has $n = 0$. Hereinafter we set $n = 0$ and suppress the index n. Let $\mathbf{e_r}, \mathbf{e_\varphi}, \mathbf{e_z}$ be the local unit vectors at the receiver, so $\mathbf{D_S} = D_r \mathbf{e_r} + D_\varphi \mathbf{e_\varphi} + D_z \mathbf{e_z}$, where the φ-direction is transverse to the great-circle linking source to receiver and the r-direction is radially outward from the source along the great-circle. Love waves are confined to the the φ-component of the seismogram and Rayleigh waves are found on the $r-$ and z-components. We, therefore, set $D_\varphi = D_L$, $D_r = D_{Rr}$, and $D_z = D_{Rz}$ where R represents Rayleigh waves and L represents Love waves. With these definitions it is well known (Aki & Richards, 1980; Levshin et $al.$, 1989) that the complex displacement spectrum of the fundamental surface waves may be asymptotically presented as

$$D_L(\omega, r, \varphi, h) = \frac{\exp(-i\pi/4)}{\omega\sqrt{8\pi r}} \frac{\exp(-ik_L(\omega)r)}{\sqrt{k_L(\omega)\mathcal{C}_L(\omega)\mathcal{U}_L(\omega)I_L(\omega)}} \mathcal{S}_L(\omega, r, \varphi, h), \tag{A.3}$$

$$D_{Rz}(\omega, r, \varphi, h) = \frac{\exp(-i3\pi/4)}{\omega\sqrt{8\pi r}} \frac{\exp(-ik_R(\omega)r)}{\sqrt{k_R(\omega)\mathcal{C}_R(\omega)\mathcal{U}_R(\omega)I_R(\omega)}} \mathcal{S}_R(\omega, r, \varphi, h) \tag{A.4}$$

$$D_{Rr}(\omega, r, \varphi, h) = \exp(-i\pi/2)D_{Rz}(\omega, r, \varphi, h)\epsilon(\omega), \tag{A.5}$$

if

$$k_L r >> 2\pi, k_R r >> 2\pi, r >> h. \tag{A.6}$$

Here $k_L(\omega)$ and $k_L(\omega)$ are horizontal wavenumbers, $\mathcal{C}_R(\omega) = \omega/k_r$ and $\mathcal{C}_L(\omega) = \omega/k_L$ are phase velocities, $\mathcal{U}_R(\omega) = (dk_R/d\omega)^{-1}$ and $\mathcal{U}_L(\omega) = (dk_L/d\omega)^{-1}$ are group velocities, and $\epsilon(\omega)$ is a real ellipticity factor. The integrals I_R and I_L are normalization integrals proportional to the kinetic energies of the corresponding waves and $\mathcal{S}_R$ and $\mathcal{S}_L$ are the source-excitation fucnctions defined below.

Let $U(\omega, z)$ and $V(\omega, z)$ be the 1D Rayleigh wave vertical and horizontal eigenfunctions of model $\mathbf{m}$, respectively, and let $W(\omega, z)$ be the 1D Love wave eigenfunction. With these definitions the normalization integrals are

$$I_R(\omega) = \int_0^\infty \rho(z) \left[U^2(\omega, z) + V^2(\omega, z)\right] dz, \tag{A.7}$$

$$I_L(\omega) = \int_0^\infty \rho(z)W^2(\omega, z)dz, \tag{A.8}$$

and the Rayleigh and Love wave source-excitation functions can be written

$$\mathcal{S}_R = U'(\omega,h)M_{zz} + k_R(\omega)V(\omega,h)\left[M_{xx}\cos^2\varphi + M_{xy}\sin 2\varphi + M_{yy}\sin^2\varphi\right] \tag{A.9}$$
$$-iV'(\omega,h)\left[M_{xz}\cos\varphi + M_{yz}\sin\varphi\right] + ik_R(w)U(\omega,h)\left[M_{xz}\cos\varphi + M_{yz}\sin\varphi\right],$$

$$\mathcal{S}_L = k_L(\omega)W(\omega,h)\left[M_{xx}\sin\varphi\cos\varphi - M_{xy}\cos 2\varphi - M_{yy}\sin\varphi\cos\varphi\right] \tag{A.10}$$
$$-iW'(\omega,h)\left[M_{xz}\sin\varphi - M_{yz}\cos\varphi\right],$$

where, for example, $U'(\omega,h)$ denotes the value of $dU(\omega,z)/dz$ evaluated at $z = h$.

It is seen from formulas (A.3) - (A.10) that the components of the complex displacement spectrum may be presented as

$$D_L = |D_L(\omega,r,\varphi,h)|\exp\left[i\Psi_L(\omega,r,\varphi,h)\right], \tag{A.11}$$
$$D_{Rz} = |D_R(\omega,r,\varphi,h)|\exp\left[i\Psi_R(\omega,r,\varphi,h)\right], \tag{A.12}$$
$$D_{Rr} = |D_R(\omega,r,\varphi,h)|\epsilon(\omega)\exp\left[i\left(\Psi_R(\omega,r,\varphi,h) - (\pi/2)\right)\right] \tag{A.13}$$

where the phase spectrum is

$$\Psi_L = -k_L(\omega)r - \pi/4 + \psi_L^S(\omega,\varphi,h), \tag{A.14}$$
$$\Psi_R = -k_R(\omega)r - 3\pi/4 + \psi_R^S(\omega,\varphi,h). \tag{A.15}$$

The source phases, ψ_L^S and ψ_R^S, are correspondingly

$$\psi_L^S = \tan^{-1}[\mathrm{Im}(\mathcal{S}_L)/\mathrm{Re}(\mathcal{S}_L)], \tag{A.16}$$
$$\psi_R^S = \tan^{-1}[\mathrm{Im}(\mathcal{S}_R)/\mathrm{Re}(\mathcal{S}_R)], \tag{A.17}$$

which are seen to be functions of frequency, source depth, and source-receiver geometry. Both functions are model-dependent because they depend on the ratio between the real and imaginary terms on right side of Equations (A.9) and (A.10) which include the model eigenfunctions and their first depth derivatives.

Group velocities derive from the application of the stationary phase approximation in converting the displacement spectrum into time-domain seismograms (e.g., Pekeris, 1948; Aki & Richards, 1980; Levshin et al., 1989). Following this approach, the observed group arrival times, $t_{\mathcal{U}_R}(\omega)$ and $t_{\mathcal{U}_L}(\omega)$, of the Rayleigh and Love waves at frequency ω follow from the frequency derivative of the phase spectrum:

$$0 = \frac{d(\omega t_{\mathcal{U}_R} + \Psi_R)}{d\omega} \rightarrow t_{\mathcal{U}_R} = \frac{r}{\mathcal{U}_R(\omega)} - \frac{d\psi_R^S}{d\omega}, \tag{A.18}$$

$$0 = \frac{d(\omega t_{\mathcal{U}_L} + \Psi_L)}{d\omega} \rightarrow t_{\mathcal{U}_L} = \frac{r}{\mathcal{U}_L(\omega)} - \frac{d\psi_L^S}{d\omega}. \tag{A.19}$$

The observed group velocities are

$$\mathcal{U}_R^{obs}(\omega) = \frac{r}{t_{\mathcal{U}_R}(\omega)} = r\left[\frac{r}{\mathcal{U}_R(\omega)} - T_R(\omega)\right]^{-1}, \tag{A.20}$$

$$\mathcal{U}_L^{obs}(\omega) = \frac{r}{t_{\mathcal{U}_L}(\omega)} = r\left[\frac{r}{\mathcal{U}_L(\omega)} - T_L(\omega)\right]^{-1}, \tag{A.21}$$

where we have defined the source group times (SGT), T_R and T_L, of the Rayleigh and Love waves as that part of the observed group arrival time that comes from the source phase:

$$T_L(\omega,r,\varphi,h) = \frac{d\psi_L^S}{d\omega}, \tag{A.22}$$

$$T_R(\omega,r,\varphi,h) = \frac{d\psi_R^S}{d\omega}. \tag{A.23}$$

A-3

Smoothly Laterally Inhomogeneous Medium

When the model **m** is a function of the horizontal coordinates r and φ, but changes in the elastic parameters, density, and boundary topography are relatively smooth, the formulas above can be generalized in the ray approximation (e.g., Woodhouse, 1974; Babich & Chikhachev, 1975; Babich et $al.$, 1976; Levshin, 1985; Levshin et $al.$, 1989; Tromp & Dahlen, 1992). According to this asymptotic theory, functions characterizing surface waves, such as $C_R, \mathcal{U}_R, k_R, U, V, I_R, \epsilon$ for Rayleigh waves, and $C_R, \mathcal{U}_R, k_L, W, I_L$ for Love waves, are defined by the local one-dimensional model corresponding to the structure under a given point at the free surface (r, φ). As a result, these functions become dependent on the horizontal coordinates (r, φ). Surface waves propagate along ray tubes whose geometry is defined by the scalar fields $C_L(\omega, r, \varphi), C_R(\omega, r, \varphi)$, respectively.

This approach leads to the following expressions for the Rayleigh and Love wave phase spectra (Levshin, 1985; Levshin et $al.$, 1989):

$$\Psi_R \;=\; -\omega \int_S \frac{ds}{C_R(\omega, s)} - 3\pi/4 + \psi_R^S(\omega, \phi_R(\omega, r, \varphi), h - z_0(0, 0)), \qquad (A.24)$$

$$\Psi_L \;=\; -\omega \int_S \frac{ds}{C_L(\omega, s)} - \pi/4 + \psi_L^S(\omega, \phi_L(\omega, r, \varphi), h - z_0(0, 0)), \qquad (A.25)$$

where ψ_L^S and ψ_L^S are defined in Equations (A.16) and (A.17). Source group times are found as in the spherical case by differentiating ψ_L^S and ψ_R^S by ω. The main difference here is that the emergence angle from the source for the ray that arrives at the receiver, ϕ_R or ϕ_L, may differ somewhat from the azimuth of the great-circle between source and receiver due to lateral refractions of rays caused by inhomogeneities in the medium of propagation.

Appendix B
Selected Bibliography

Ritzwoller, M.H., A.L. Levshin, L.I. Ratnikova, and A.A. Egorkin-Jr, 1998. Intermediate period group velocity maps across Central Asia, Western China, and parts of the Middle East, *Geoph. J. Int'l* , **134**, 315-328. UNCLASSIFIED.

Levshin, A.L., M.H. Ritzwoller, M.P. Barmin, L.I. Ratnikova, and C.A. Padgett, 1998. Automated surface wave analysis using phase-matched filters from dispersion maps, *Proceedings of the 20th Annual Seismic Research Symposium on Monitoring a CTBT*, DSWA/AFTAC/DOE, 451-460. UNCLASSIFIED.

Levshin, A.L., M.H. Ritzwoller, and J.S. Resovsky, 1999, Source effects on surface wave group travel times and group velocity maps, *Physics Earth and Planet. Interior*, **115**, 293-312. UNCLASSIFIED.

Levshin, A.L., M.P. Barmin, and M.H. Ritzwoller, 1999. Estimation of uncertainties and bias in surface wave tomographic maps and travel-time correction surfaces, *Proceedings of the 21th Seismic Research Symposium: Technologies for Monitoring the Comprehensive Nuclear-Test-Ban Treaty*, DOD/DOE, Las Vegas, 21-24 Sept. 1999, 141-150. UNCLASSIFIED.

Levshin, A.L., M.H. Ritzwoller, B.G. Bukchin, A.Z. Mostinsky, and A.A. Egorkin, 2001. Isotropic and nonisotropic components of earthquakes and nuclear explosions on the Lop Nor test site, *Proceedings of the 22nd Seismic Research Symposium*, DOD/DOE, New Orleans, 21 -24 Sept. 2000. UNCLASSIFIED.

Bukchin, B.G., A.Z. Mostinsky, A.A. Egorkin, A.L. Levshin, and M.H. Ritzwoller, 2001. Isotropic and nonisotropic components of earthquakes and nuclear explosions on the Lop Nor Test site, China, *Pure and Appl. Geophysics*, **158**,1497-1515. UNCLASSIFIED.

Levshin, A.L., and M.H. Ritzwoller, 2001. Automated detection, extraction, and measurement of regional surface waves, *Pure and Appl. Geophysics*, **158**, 1531-1545. UNCLASSIFIED.

Barmin, M.P., M.H. Ritzwoller, and A.L. Levshin, 2001. A fast and reliable method for surface wave tomography, *Pure and Appl. Geophysics*, **158**,1351-1375. UNCLASSIFIED.

DISTRIBUTION LIST

DTRA-TR-01-28

DEPARTMENT OF DEFENSE

DIRECTOR
DEFENSE INTELLIGENCE AGENCY
BUILDING 6000, BOLLING AFB
WASHINGTON, DC 20340 5100
    ATTN: DTIB

DIRECTOR
DEFENSE RESEARCH & ENGINEERING
WASHINGTON, DC 20301 3110
    ATTN: DDR&E, ROOM 3E808

DEFENSE TECHNICAL INFORMATION CENTER
8725 JOHN J. KINGMAN, RD SUITE 0944
FORT BELVOIR, VA 22060 6218
2 CYS   ATTN: DTIC/OCP

DEFENSE THREAT REDUCTION AGENCY
8725 JOHN J. KINGMAN, RD, MS 6201
FORT BELVOIR, VA 22060 6201
    ATTN: TDND, DR. A. DAINTY
    ATTN: TDND,LTC T. CARTLEDGE

OFFICE OF THE SECRETARY OF DEFENSE
NUCLEAR TREATY PROGRMS OFFICE
1515 WILSON BOULEVARD, SUITE 720
ARLINGTON, VA 22209
    ATTN: P. WAKEFIELD
    ATTN: DR. S. MANGINO

DEPARTMENT OF THE ARMY

US ARMY SMDC
SMDC-TC-YD
P.O. BOX 1500
HUNTSVILLE, AL 35807 3801
    ATTN: B. ANDRE

DEPARTMENT OF THE AIR FORCE

AIR FORCE RESEARCH LABORATORY
29 RANDOLPH ROAD
HANSCOM AFB, MA 01731
    ATTN: RESEARCH LIBRARY
    ATTN: VSBL, R. RAISTRICK

USAF AT USGS
2201 SUNRISE VALLEY DRIVE MS 951
RESTON, VA 20192
    ATTN: R. BLANDFORD
    ATTN: R. JIH

AIR FORCE TECHNICAL APPLICATIONS CTR
1030 S. HIGHWAY A1A
PATRICK AFB, FL 32925 3002
    ATTN: CA/STINFO
    ATTN: TTR, D. CLAUTER
    ATTN: CTI, DR. B. KEMERAIT
    ATTN: TT, DR. D. RUSSELL
    ATTN: TTR, F. SCHULT
    ATTN: TTR, G. ROTHE
    ATTN: TTR, V. HSU
    ATTN: DR. B. NGUYEN
    ATTN: DR. E. SMART
    ATTN: DR. G. WAGNER
    ATTN: DR. M. WOODS
    ATTN: DR. N. YACOUB

DEPARTMENT OF THE NAVY

NAVAL RESEARCH LABORATORY
4555 OVERLOOK AVE, SW, CODE 7643
WASHINGTON, DC 20375 0001
    ATTN: DR. D. DROB

DEPARTMENT OF ENERGY

NATIONAL NUCLEAR SECURITY
ADMINISTRATION
1000 INDEPENDENCE AVE SW
WASHINGTON, DC 20585 0420
    ATTN: L. CASEY
    ATTN: M. DENNY
    ATTN: G. KIERNAN

UNIVERSITY OF CALIFORNIA
LAWRENCE LIVERMORE NATIONAL LAB
P.O. BOX 808
LIVERMORE, CA 94551 9900
    ATTN: MS L205, DR. D. HARRIS
    ATTN: MS L208, TECHNICAL STAFF
    ATTN: MS 205, TECHNICAL STAFF

LOS ALAMOS NATIONAL LABORATORY
P.O. BOX 1663
LOS ALAMOS, NM 87545
    ATTN: MS C335, DR. S. R. TAYLOR
    ATTN: MS D460, FRANCESCA CHAVEZ
    ATTN: MS C335, TECHNICAL STAFF
    ATTN: MS D460, TECHNICAL STAFF
    ATTN: MS F665, TECHNICAL STAFF
    ATTN: MS D408, TECHNICAL STAFF
    ATTN: MS J577, TECHNICAL STAFF
    ATTN: MS D443, TECHNICAL STAFF

PACIFIC NORTHWEST NATIONAL LABORATORY
P.O. BOX 999
1 BATTELEE BOULEVARD
RICHLAND, WA 99352
    ATTN: MS P8-20, T. HEIMBIGNER
    ATTN: MS K8-29, DR. N. WOGMAN

SANDIA NATIONAL LABORATAORIES
MAIL SERVICES
P.O. BOX 5800
ALBUQUERQUE, NM 87185 1363
    ATTN: MS 1138 TECHNCIAL STAFF
        DEPARTMENT 6533

OTHER GOVERNMENT

DEPARTMENT OF STATE
2201 C STREET NW
WASHINGTON, DC 20520
    ATTN: R. MORROW, ROOM 5741

NATIONAL ARCHIVES & RECORDS
ADMINISTRATION
8601 ADELPHI ROAD, ROOM 3360
COLLEGE PARK, MD 20740 6001
2 CYS   ATTN: USER SERVICE BRACNH

US GEOLOGICAL SURVEY
ADVANCED SYSTEMS CENTER
MS 562
RESTON, VA 20192
    ATTN: W. LEITH

US GEOLOGICAL SURVEY
345 MIDDLEFIELD RD MS 977
MENLO PARK, CA 94025
    ATTN: S. DETWEILER
    ATTN: DR. W. MOONEY

DIRECTORY OF OTHER (LIBRARIES AND UNIVERSITIES)

BOSTON COLLEGE
INSTITUTE FOR SPACE RESEARCH
140 COMMONWEALTH AVENUE
CHESTNUT HILL, MA 02167
    ATTN: DR. D. HARKRIDER
    ATTN: B. SULLIVAN

BROWN UNIVERSITY
DEPARTMENT OF GEOLOGICAL SCIENCES
75 WATERMAN STREET
PROVIDENCE, RI 02912 1846
    ATTN: PROF. D. FORSYTH

CALIFORNIA INSTITUTE OF TECHNOLOGY
DIVISION OF GEOLOGY & PLANETARY SCIENCES
PASADENA, CA 91125
    ATTN: PROF. DONALD V. HELMBERGER
    ATTN: PROF. THOMAS AHRENS

UNIVERSITY OF CALIFORNIA BERKELEY
281 MCCONE HALL
BERKELY, CA 94720 2599
    ATTN: PROF. B. ROMANOWICZ
    ATTN: DR. D. DREGER

UNIVERSITY OF CALIFORNIA DAVIS
DAVIS, CA 95616
    ATTN: R.H. SHUMWAY, DIV
        STATISTICS

UNIVERSITY OF CALIFORNIA SAN DIEGO
LA JOLLA, CA 92093 0225
    ATTN: DR.L. DEGROOT - HEDLIN
    ATTN: DR. M. HEDLIN
    ATTN: PROF. F. VERNON
    ATTN: PROF. J. BERGER
    ATTN: PROF. J. ORCUTT
    ATTN: DR. G. D'SPAIN

UNIVERSITY OF CALIFORNIA SANTA CRUZ
INSTITUTE OF TECTONICS
SANTA CRUZ, CA 95064
    ATTN: DR. R. S. WU
    ATTN: PROF. T. LAY

UNIVERSITY OF COLORADO BOULDER
DEPT OF PHYSICS, CAMPUS BOX 390
BOULDER, CO 80309
      ATTN: DR. A. LEVSHIN
      ATTN: DR.R. ENGDAHL
      ATTN: M. RITZWOLLER
      ATTN: PROF. C. ARCHAMBEAU

COLUMBIA UNIVERSITY
LAMONT DOHERTY EARTH OBSEREVATORY
PALISADES, NY 10964
      ATTN: DR. J. XIE
      ATTN: DR. W. Y. KIM
      ATTN: PROF. P.G. RICHARDS
      ATTN: DR. M. TOLSTOY

UNIVERSITY OF CONNECTICUT
DEPARTMENT OF GEOLOGY & GEOPHYSICS
STOORS, CT 06269 2045
      ATTN: PROF. V.F. CORMIER, U-45,
          ROOM 207

CORNELL UNIVERSITY
DEPARTMENT OF GEOLOGICAL SCIENCES
3126 SNEE HALL
ITHACA, NY 14853
      ATTN: PROF. M.A. BARAZANGI

HARVARD UNIVERSITY
HOFFMAN LABORATORY
20 OXFORD STREET
CAMBRIDGE, MA 02138
      ATTN: PROF. A. DZIEWONSKI
      ATTN: PROF. G. EKSTROM

INDIANA UNIVERSITY
DEPARTMENT OF GEOLOGICAL SCIENCES
1005 10TH STREET
BLOOMINGTON, IN 47405
      ATTN: PROF. G. PAVLIS

IRIS
1200 NEW YORK AVENUE, NW SUITE 800
WASHINGTON, DC 20005
      ATTN: DR. D. SIMPSON
      ATTN: DR. G. E. VAN DER VINK

IRIS
1408 NE 45TH ST #201
SEATTLE, WA 98105
      ATTN: DR. T. AHERN

MASSACHUSETTS INSTITUTE OF TECHNOLOGY
EARTH RESOURCES LABORATORY
42 CARLETON STREET
CAMBRIDGE, MA 02142
      ATTN: DR. W. RODI
      ATTN: PROF. M.N. TOKSOZ

MICHIGAN STATE UNIVERSITY LIBRARY
450 ADMINISTRATION BUILDING
EAST LANSING, MI 48824
      ATTN: K. FUJITA

NEW MEXICO STATE UNIVERSITY
DEPARTMENT OF PHYSICS
LAS CRUCES, NM 88003
      ATTN: PROF. J. NI
      ATTN: PROF. T. HEARN

NORTHWESTERN UNIVERSITY
DEPARTMENT OF GEOLOGICAL SCIENCES
1847 SHERIDAN RD
EVANSTON, IL 60208
      ATTN: PROF. E. OKAL

PENNSYLVANIA STATE UNIVERSITY
GEOSCIENCES DEPARTMENT
403 DEIKE BUILDING
UNIVERSITY PARK, PA 16802
      ATTN: PROF. C. AMMON
      ATTN: PROF. S. ALEXANDER
      ATTN: DR. A. NYBLADE

SAN DIEGO STATE UNIVERSITY
DEPARTMENT OF GEOLOGICAL SCIENCES
SAN DIEGO, CA 92182
      ATTN: PROF. S. M. DAY

SOUTHERN METHODIST UNIVERSITY
DEPARATMENT OF GEOLOGICAL SCIENCES
P.O. BOX 750395
DALLAS, TX 75275
      ATTN: B. STUMP
      ATTN: E. HERRIN
      ATTN: H.L. GRAY
      ATTN: P. GOLDEN

UNIVERSITY OF HAWAII- MANOA
P.O. BOX 1599
KAILUA-KONA, HI 96745 1599
  ATTN: DR. M. A. GARCES

UNIVERSITY OF MISSISSIPPI
1 COLISEUM DRIVE
UNIVERSITY, MS 38677
  ATTN: PROF. H. BASS

UNIVERSITY OF SOUTHERN CALIFORNIA
520 SEAVER SCIENCE CENTER
UNIVERSITY PARK
LOS ANGELES, CA 90089 0483
  ATTN: PROF. C. G. SAMMIS
  ATTN: PROF. T. JORDAN

WASHINGTON UNIVERSITY
DEPARTMENT OF EARTH PLANT SCIENCE
ONE BROOKINGS DRIVE
SAINT LOUIS, MO 63130 4899
  ATTN: DR. G. SMITH

UNIVERSITY OF WISCONSIN MADISON
1215 W DAYTON ST
MADSION, WI 53706 1600
  ATTN: DR. C. THURBER

ST LOUIS UNIVERSITY
P.O. BOX 8148
PIERRE LACLEDE STATION
ST LOUIS, MO 63156 8148
  ATTN: PROF. B. J. MITCHELL
  ATTN: PROF. R. HERRMAN

UNIVERSITY OF MEMPHIS
3890 CENTRAL AVE
MEMPHIS, TN 38152
  ATTN: DR. J. PUJOL
  ATTN: DR. C. LANGSTON

UNIVERSITY OF TEXAS AUSTIN
P.O. BOX 7726
AUSTIN, TX 78712
  ATTN: DR. J. PULLIAM
  ATTN: DR. M. SEN

UNIVERSITY OF TEXAS EL PASO
DEPT OF GEOLOGICAL SCIENCES
EL PASO, TX 79901
  ATTN: PROF. G. KELLER
  ATTN: DR. D. DOSER
  ATTN: DR. A. VELASCO

FOREIGN

AUSTRALIAN GEOLOGICAL SURVEY
ORGANIZATION
CORNER OF JERRAGOMRRRA &
NINDMARSH DRIVE
CANBERRA, ACT 2609
AUSTRALIA
  ATTN: D. JESPOSN

GEOPHYSICAL INSTITUTE OF ISRAEL
POB 182
LOD, 7100 ISRAEL
  ATTN: DR. Y. GITTERMAN
  ATTN: DR. A. SHAPIRA

GEOLOGICAL SURVY OF CANADA
7 OBSERVATORY CRESCENT
OTTAWA K1A 0Y3 ONT
CANADA
  ATTN: C. WOODGOLD

I.R.I.G.M. B.P. 68
38402 ST. MARTIN D'HERES
CEDEX, FRANCE
  ATTN: DR. M. BOUCHON

MINISTRY OF DEFENSE
PROCUREMENT EXEUTIVE
BLACKNESS, BRIMPTON
READING FG7-4RS ENGLAND
  ATTN: DR. D. BOWERS

NTNF/NORSAR
P.O. BOX 51
N-2007 KJELLER, NORWAY
  ATTN: DR. F. RINGDAL
  ATTN: T. KVAERNA
  ATTN: S. MYKKELTVEIT

OBSERVATORIE DE GRENOBLE
I.R.I.G.M. - B.P. 53
38041 GRENOBLE, FRANCE
     ATTN: DR. M. CAMPILLO

OBSERVATORIO SAN CALIXTO
INDABURO #944
CASILLA 12656
LA PAZ
BOLIVIA
     ATTN: E. MINAYA

RESEARACH SCHOOL OF EARTH SCIENCES
INSTITUTE OF ADVANCED STUDIES
G.P.O. BOX 4
CANABERRA 2601, AUSTRALIA
     ATTN: PROF. B.L.N.KENNETT

PTS/CTBTO
VIENNA INTERNATIIONAL CENTRE
P.O. BOX 1200
VIENNA A-1400
AUSTRIA
     ATTN: P. BASHAM
     ATTN: DR. P. FIRBAS
     ATTN: DR. R. KEBEASY

RUHR UNIVERSITY/BOCHUM
INSTITUTE FOR FEOPHSIK
P.O. BOX 102148
463 BOCHUM 1, GERMANY
     ATTN: PROF. H.P. HARJES

SOCIETE RADIOMANA
27 RU CLAUDE BERNARD
75005 PARIS, FRANCE
     ATTN: DR.B. MASSINON
     ATTN: DR. P. MECHLER

UNIVERSITY OF BERGEN
INSTITUTE FOR SOLID EARTH PHYSICS
ALLEGATON 41
N-5007 BERGEN, NORWAY
     ATTN: E. HUSEBYE

UNIVERSITY OF CAMBRIDGE
DEPARTMENT OF EARTH SCIENCES
MADINGLEY RISE, MADINGLEY ROAD
CAMBRIDGE CB3 OEZ, ENGLAND
     ATTN: PROF. K. PRIESTELY

DEPARTMENT OF DEFENSE CONTRACTORS

BATTELLE MEMORIAL INSTITUTE
MUNITIONS & ORDANACE CTR
505 KINGS AVENUE
COLUMBUS, OH 43201 2693
     ATTN: TACTEC

BBN CORPORATION
1300 N 17TH STREET, SUITE 1200
ARLINGTON, VA 22209
     ATTN: DR. D. NORRIS
     ATTN: R. GIBSON
     ATTN: J. PULLI

CENTER FOR MONITORING RESEARCH
1300 N 17TH STREET,SUITE 1450
ARLINGTON, VA 22209 2402
     ATTN: DR. K. L. MCLAUGLHLIN
     ATTN: DR. R. WOODWARD
     ATTN: DR. R. NORTH
     ATTN: DR. V. RYABOY
     ATTN: DR. X. YANG
     ATTN: LIBRARIAN
     ATTN: DR. T. J. BENNETT
     ATTN: J. MURPHY
     ATTN: I. BONDAR
     ATTN: DR. N. KOHL

ENSCO, INC.
P.O. BOX 1346
SPRINGFIELD, VA 22151 0346
     ATTN: D. BAUMGARDT
     ATTN: Z. DER

WESTON GEOPHYSICAL CORPORATION
27 BEDFORD ST, SUITE 102
LEXINGTON, MA 02420
     ATTN: DR. D. REITER
     ATTN: J. LEWKOWICZ
     ATTN: DR. A. ROSCA
     ATTN: DR. I. TIBULEAC
     ATTN: M. JOHNSON

WESTON GEOPHYSICAL CORPORATION
917 ELLIS AVE SUITE 222
LUFKIN, TX 75904
    ATTN: DR.J. BONNER

WESTON GEOPHYSICAL CORPORATION
411 NW 26TH ST
GAINESVILLE, FL 32607
    ATTN: DR. S. RUSSELL

ITT INDUSTRIES
ITT SYSTEMS CORPORATION
1680 TEXAS STREET SE
KIRTLAND AFB, NM 87117 5669
2 CYS   ATTN: DTRIAC

JAYCOR
1410 SPRING HILL ROAD, SUITE 300
MCLEAN, VA 22102
    ATTN: DR. C. P. KNOWLES

MISSION RESEARCH CORPORATION
8560 CINDERBED ROAD, SUITE 700
NEWINGTON, VA 22122
    ATTN: DR. M. FISK
    ATTN: R. BURLACU

MULTIMAX,INC
1441 MC CORMICK DRIVE
LANDOVER, MD 20785
    ATTN: DR. I. N. GUPTA
    ATTN: DR. W. CHAN
    ATTN: W. RIVERS

MULTIMAX, INC
1090 N HIGHWAY A1A SUITE D
INDIANLATIC, FL 32903
    ATTN: DR. H. GHALIB

SCIENCE APPLICATIONS INT'L CORPORATION
10260 CAMPUS POINT DRIVE
SAN DIEGO, CA 92121 1578
    ATTN: DR. G. E. BAKER
    ATTN: DR. J. STEVENS
    ATTN: DR. D. ADAMS
    ATTN: DR.M. ENEVA

SCIENCE APPLICATIONS INTERNATINAL CORP
1227 S. PATRICK DR SUITE 110
SATELITTE BEACH, FL 32937
    ATTN: DR. M. FELIX
    ATTN: DR. H. GIVEN

URS CORPORATION
566 EL DORADO STREET
PASADENA, CA 91109 3245
    ATTN: DR.N.B. WOODS
    ATTN: DR. C. SAIKIA
    ATTN: DR. G. ICHINOSE